

# **MULTILAYER THIN FILM OPTICAL BIOSENSORS**

*by*

**Vinay K. M. Pampapathi**

*a thesis submitted to*

**University of London**

*for the degree of*

**Doctor of Philosophy**

*in*

**Electrical and Electronic Engineering**

Department of Electrical and Electronic Engineering

University College London

August 1994.

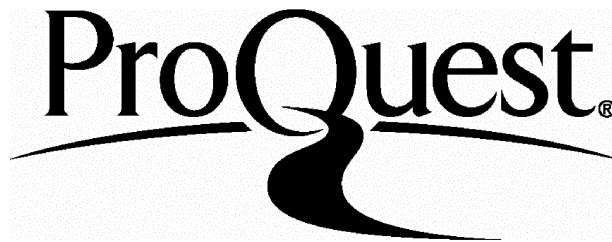
ProQuest Number: 10042827

All rights reserved

INFORMATION TO ALL USERS

The quality of this reproduction is dependent upon the quality of the copy submitted.

In the unlikely event that the author did not send a complete manuscript and there are missing pages, these will be noted. Also, if material had to be removed, a note will indicate the deletion.



ProQuest 10042827

Published by ProQuest LLC(2016). Copyright of the Dissertation is held by the Author.

All rights reserved.

This work is protected against unauthorized copying under Title 17, United States Code.  
Microform Edition © ProQuest LLC.

ProQuest LLC  
789 East Eisenhower Parkway  
P.O. Box 1346  
Ann Arbor, MI 48106-1346

## **ABSTRACT**

This thesis describes a planar optically resonant multilayer thin film device and discusses its application as an evanescent field fluorescence immunosensor. Previous workers have used multiple total internal reflection (TIR) techniques and both monomode and multimode waveguides for planar evanescent field fluorescence immunosensing. TIR methods give poor sensitivities (insufficient for many analytes of clinical interest) due to low evanescent field strengths and high background levels whereas efficient and reproducible exciting light coupling into planar waveguides presents a major instrument design problem. Optically resonant multilayer devices offer the high evanescent field strengths and low penetration depths of waveguide devices whilst retaining the ease of input coupling of TIR devices. Multilayer devices also offer the prospect (as do waveguide devices) of surface patterning using techniques such as photolithography, to allow multiple-analyte measurements on a single device.

The theory of multilayer systems is briefly described followed by the fabrication of the multilayer devices using sol-gel silica and iron phosphate thin films - chosen because they allowed the inexpensive deposition of thin films from solution by dip and spin coating techniques. The multilayer devices were characterised by combining theory with observed resonance measurements, which allowed the refractive indices of the thin film materials to be estimated.

The model assay was a fluorescence immunoassay for mouse-IgG in a buffer solution. The multilayer device gave a seven-fold sensitivity improvement over a TIR device. The assay was performed using a 633nm Helium-Neon laser and a 650nm semiconductor laser diode. The results showed that similar sensitivities could be obtained despite the five-fold lower optical power output of the laser diode.

The theory of multilayer devices was extended to model the multilayer immunosensor, thus allowing the analysis of the sources of the fluorescence and background signals. This modelling revealed the immobilised capture antibody layer to

be highly scattering and significant background signal contributions to be from scattered exciting light and from bulk solution fluorescence. The contribution to the background signal from scattering in the thin film layers was found to be insignificant.

## ACKNOWLEDGEMENTS

It is a pleasure to thank my supervisor, Dr. Michael T Flanagan for his support and excellent advice throughout this work. It was also a pleasure to have worked with Dr. Andrew N Sloper with whom I had many valuable discussions and whose help in the laboratory enabled me to perform my experiments. I am grateful, too, for the help of Maurice Gillet and his colleagues in the construction of some parts of the apparatus required for the experimental work.

I am very grateful to both Dr. Phelim Daniels and Dr. John Attridge at *Serono Diagnostics Ltd.* for their help, advice and support.

I would also like to thank the *Science and Engineering Research Council* and *Serono Diagnostics Ltd.* for their financial support.

There are many others who also helped towards the completion of this work, but I would like to thank Dr. Dominic Godwin in particular for taking the effort to proof read this thesis.

Finally, I wish to express my deep appreciation to my family for all their love, support, encouragement and understanding through all the trials and tribulations of a PhD.

To  
Pritheeva,  
for all your love and understanding

## **TABLE OF CONTENTS**

<b>ABSTRACT</b>	2
<b>ACKNOWLEDGEMENTS</b>	4
<b>ABBREVIATIONS</b>	14
<b>1 INTRODUCTION</b>	16
1.1 The medical diagnostics market	16
1.2 Biosensors	17
1.3 Biosensor applications	18
1.3.1 Health care	19
1.4 Biosensor requirements	20
1.5 Discussion	23
References	25
<b>2 BIOSENSOR TECHNOLOGY</b>	28
2.1 The biological sensing layer	28
2.1.1 The antibody	30
2.2 Immunoassays	32
2.3 Signalling of specific antibody-antigen binding	34
2.3.1 Labels used in indirect homogeneous immunoassays	35
2.3.2 No-label direct homogeneous immunoassays	37
2.4 Immunoassay performance	38
2.5 Transduction in immunosensors	40
2.5.1 Electrical immunosensors	40
2.5.2 Optical immunosensors	41
2.5.2.1 The evanescent field	42
2.6 Evanescent field immunosensors	45
2.6.1 Total internal reflection (TIR)	45
2.6.2 Surface plasmon resonance (SPR)	46

2.6.3	Optical waveguides	48
2.6.3.1	Optical fibre immunosensors	49
2.6.3.2	Planar waveguide immunosensors	50
2.6.4	Sensitivities of direct and indirect sensing methods	52
2.6.5	The fluorescence capillary fill device	52
2.7	Enhancing evanescent field immunosensors	53
2.7.1	Signal strength enhancement	53
2.7.2	Signal-to-background ratio enhancement	54
2.7.3	Signal-to-noise ratio enhancement	55
2.8	Conclusions	56
	References	57
<b>3</b>	<b>PROJECT OBJECTIVES AND MULTILAYER THIN FILM SENSORS</b>	<b>63</b>
3.1	Project objectives	63
3.2	Optically resonant multilayer thin film devices	64
3.3	Thin film fabrication methods and materials	68
3.3.1	Fabrication techniques	68
3.3.2	Materials	70
3.3.2.1	Sol-gel films	70
3.3.2.1	Metal phosphate films	72
3.4	Discussion	73
	References	74
<b>4</b>	<b>OPTICS OF MULTILAYER THIN FILM SYSTEMS</b>	<b>77</b>
4.1	Abbreviations	77
4.2	Plane waves	78
4.2.1	Reflection and transmission at a single interface	78
4.2.2	The fresnel reflection and transmission coefficients	79
4.2.3	Total internal reflection	80

4.2.4	Power flow across the interface	83
4.3	Thin layers and stratified systems	84
4.3.1	The method of successive field summations	84
4.3.2	The matrix method	88
	References	90
<b>5</b>	<b>EXPERIMENTAL MATERIALS AND METHODS</b>	<b>92</b>
5.1	Computer modelling	92
5.1.1	The multilayer thin film system	92
5.1.2	The immunosensor	92
5.1.3	Antibody-antigen binding	93
5.2	Thin film fabrication and characterisation	93
5.2.1	Chemicals	93
5.2.2	Substrates and substrate preparation	93
5.2.3	Coating solution preparation	95
5.2.4	Spin coating	95
5.2.4.1	The spinner	95
5.2.4.2	Thin film deposition	97
5.2.5	Curing	97
5.2.5.1	Silica films	98
5.2.5.2	Metal phosphate films	99
5.2.6	Deposition of multiple layers	99
5.2.7	Film thickness measurement	100
5.2.7.1	Metal phosphate films	100
5.2.7.2	Silica films	100
5.2.8	Capillary fill device (CFD)	103
5.2.9	Experimental apparatus	105
5.2.9.1	The light source	106
5.2.9.2	Prism/CFD arrangement	107
5.2.9.3	Fluorescence collection and measurement	108

5.2.9.4	Angular scans	109
5.2.10	Multilayer system characterisation	110
5.2.10.1	Thin film refractive index estimation	110
5.2.10.2	The Nile blue solution	112
5.3	Immunosensing experiments	115
5.3.1	The immunoassay	115
5.3.2	Chemicals	117
5.3.3	Multilayer thin film preparation	117
5.3.4	Capture IgG immobilisation	117
5.3.5	CFD assembly	119
5.3.6	The labelled antibody	119
5.3.6.1	Allophycocyanin	119
5.3.6.2	CY5.18	121
5.3.6.3	Labelling of antibody with CY5.18 dye	121
5.3.7	Immunosensing measurements	122
	References	124
<b>6</b>	<b>MULTILAYER THIN FILM SYSTEMS</b>	<b>127</b>
6.1	Multilayer thin film system modelling	127
6.1.1	Modelling considerations	128
6.1.2	Computer programming	129
6.1.2.1	Simplex maximum search routine	129
6.1.3	The single interface total internal reflection system	131
6.1.4	The four layer resonant system	133
6.1.4.1	Thin film thickness dependence	137
6.1.4.2	Thin film refractive index dependence	142
6.1.5	The five layer resonant system	144
6.1.6	Discussion	146
6.2	Multilayer thin film system characterisation	148
6.2.1	Sol-gel silica spin coating	148

6.2.2	Iron phosphate film spin coating	151
6.2.3	Film thickness uniformity	153
6.2.4	Optical resonance in the four layer system	154
6.3	Thin film refractive indices estimation	156
6.4	Discussion	160
	References	162
<b>7</b>	<b>MULTILAYER THIN FILM OPTICAL IMMUNOSENSORS</b>	<b>165</b>
7.1	Devices for immunosensing	165
7.1.1	Multilayer thin film sensor specification	165
7.1.2	Total internal reflection sensor specification	167
7.1.3	The capillary fill device	168
7.2	Capture antibody immobilisation	168
7.3	The model immunoassay	172
7.3.1	Fluorescence excitation, collection and measurement	172
7.3.2	The sample and reference solutions	173
7.3.2.1	The sample solution	173
7.3.2.2	The reference solution	174
7.3.2.3	Signal normalisation	174
7.4	Multilayer thin film immunosensors	175
7.4.1	Immunosensor signal time response	175
7.4.1.1	Immunosensor signal levels	176
7.4.2	Immunosensor angular scans	178
7.4.2.1	Multilayer thin film immunosensor	178
7.4.2.2	Total internal reflection immunosensor	187
7.4.3	Immunosensor dose response	190
7.5	Discussion	193
	References	196

<b>8</b>	<b>THEORETICAL MODELLING OF THE IMMUNOSENSOR</b>	<b>198</b>
8.1	Antibody-analyte binding	198
8.1.1	Theory	198
8.1.2	Application to observed data	200
8.2	Theoretical considerations	203
8.2.1	The incident light beam	203
8.2.2	The multilayer immunosensor system	204
8.2.2.1	The solution layer	204
8.2.2.2	The protein layer	206
8.2.2.3	The waveguide layer thin film thickness	208
8.2.3	The TIR immunosensor system	211
8.2.4	Fitting theory to the observed data	211
8.2.4.1	The immunosensor signal components	211
8.2.4.2	The theoretical immunosensing signal	213
8.2.5	Constraints on the distribution of scattering/fluorescing points	214
8.2.5.1	Constraints between the reference and sample cells	214
8.2.5.2	Constraints between separate devices	215
8.2.5.3	Exciting light input coupling efficiency	215
8.3	Fitting to the multilayer immunosensor data	216
8.3.2	Fitting results	216
8.3.2.1	Helium-neon (633nm) laser, allophycocyanin label	217
8.3.2.2	Laser diode (650nm), allophycocyanin label	221
8.4	Fitting to the TIR immunosensor data	225
8.4.1	Fitting results	225
8.4.1.1	Helium-neon (633nm) laser, allophycocyanin label	226
8.4.1.2	Laser diode (650nm), allophycocyanin label	230
8.5	Re-designing the immunosensor	233
8.6	Discussion	235
8.6.1	Antibody-analyte binding	235
8.6.2	Thin film fabrication	236
8.6.3	Comparison of multilayer and TIR immunosensors	236

8.6.4	Comparison of 633nm and 650nm lasers	238
8.6.5	Scope of the theoretical model	238
	References	240
<b>9</b>	<b>DISCUSSION</b>	<b>242</b>
9.1	Introduction	242
9.2	Multilayer thin films	244
9.2.1	Design considerations	244
9.2.1.1	Thin film refractive indices	244
9.2.1.2	Thin film layer thicknesses	245
9.2.2	Fabrication considerations	245
9.2.2.1	Thin film materials	245
9.2.2.2	Film thickness variations	247
9.2.2.3	Thin film deposition	247
9.3	Multilayer thin film optical immunosensors	248
9.3.1	The immobilised capture layer	248
9.3.2	Immunosensor performance	249
9.3.2.1	Sensor response	249
9.3.2.2	Sensor sensitivity	249
9.3.2.3	Signal referencing	253
9.3.3	Comparison of exciting laser light sources	253
9.3.4	Comparison of the fluorescent labels	254
9.3.5	General use of the multilayer sensor	254
9.4	Immunosensor modelling	255
9.4.1	Scope of model	255
9.4.2	Results of immunosensor modelling	256
9.4.2.1	Antibody-antigen binding	256
9.4.2.2	Signal sources	256
9.4.3	Achievements of modelling the immunosensor	258
9.5	Recommendations and further work	259

9.5.1 Planar thin film architecture	259
9.5.2 Immobilised capture antibody	259
9.5.3 The immunoassay	260
9.5.4 The multilayer immunosensor	260
References	262

## **APPENDIX 1**

<b>A1 ELECTROMAGNETIC WAVE THEORY OF PLANE WAVES</b>	<b>267</b>
A1.1 Abbreviations	267
A1.2 Basic electromagnetic theory	268
A1.2.1 Maxwells equations	268
A1.2.2 Time harmonic electromagnetic fields	268
A1.2.3 The electromagnetic wave equation	269
A1.2.4 Plane wave solutions	271
A1.2.5 Power flow in an electromagnetic wave	272
A1.3 Reflection and transmission at an interface	273
A1.3.1 Boundary conditions at a dielectric interface	273
A1.3.2 Reflection and transmission	273
A1.3.3 The reflection and transmission coefficients	275
A1.3.4 Total internal reflection	279
A1.3.5 Power flow across the interface	280

## ABBREVIATIONS

$\epsilon$	electric permittivity.
$\lambda_{ab}$	Absorption wavelength.
$\lambda_{ex}$	Excitation wavelength.
$\lambda_{em}$	Emission wavelength.
$\mu$	magnetic permeability.
<b>APC</b>	Allophycocyanin.
<b>BSA</b>	Bovine serum albumin.
<b>CFD</b>	Capillary fill device.
<b>CVD</b>	Chemical vapour deposition.
<b>DNA</b>	Deoxyribose nucleic acid.
<b>ELISA</b>	Enzyme linked immunosorbent assay.
<b>FET</b>	Field effect transistor.
<b>FCFD</b>	Fluorescence capillary fill device.
<b>hCG</b>	Human chorionic gonadotropin.
<b>HeNe</b>	Helium-Neon.
<b>IgG</b>	Immunoglobulin G.
<b>LED</b>	Light emitting diode.
<b>MW</b>	Molecular weight.
<b>PBS</b>	Phosphate buffered saline.
<b>PMT</b>	Photomultiplier tube.
<b>PTFE</b>	Polytetrafluoroethene.
<b>RI</b>	Refractive index.
<b>RNA</b>	Ribose nucleic acid.
<b>rpm</b>	Revolutions per minute.
<b>SPR</b>	Surface plasmon resonance.
<b>TE</b>	Transverse electric polarisation.
<b>TIR</b>	Total internal reflection.
<b>TM</b>	Transverse magnetic polarisation.
<b>TRIS</b>	Trizma - Tris(hydroxymethyl)aminoethane.

## CHAPTER 1

### INTRODUCTION

*This chapter provides an overview of biosensors - their applications and requirements. Considerations concerning the design and development of sensors are discussed and the PhD project objectives are very briefly outlined.*

#### 1.1 THE MEDICAL DIAGNOSTICS MARKET

There is an ever-increasing feeling in the medical community that prevention of the many physical ailments that affect people is better and more cost-effective than curing the problems [1]. This policy requires early detection of the symptoms (infection, hormone deficiency, etc.) or in some cases (such as congenital abnormalities and inherited diseases) detection of possible future problems before there are any visible symptoms. Thus, there is a great emphasis on the development of better diagnostic techniques that can give rapid, accurate analyses at ever-lower detection limits.

Clinical testing products for a wide range of analytes of medical interest are currently available (eg. glucose, human pregnancy hormone - hCG, whole blood analysis). The overwhelming majority of these products require considerable manipulation of the sample solutions (eg purification, addition of reagents, washing steps, or accurate measurement of sample volumes) to obtain accurate and reliable results. Hence, most hospitals have, or have access to, central laboratory facilities where clinical testing can be performed by personnel with the suitable qualifications or experience to conduct the tests. This centralisation, however, means that a sample (eg. urine, blood, etc.) taken from a patient needs to be transported to the laboratory, where

the test (assay) can then be performed, and the results conveyed back to the patient's doctor or the patient. It has been noted that, while an assay may take a few minutes, sorting and preparation of the sample and transport to and from the laboratory may take 2½ hours [2]. When the sample is taken by a GP, who has no direct access to any testing facilities, the delay may be of the order of days. These delays may, at worst, seriously compromise patient care, but it certainly does not help the 'prevention is better than the cure' objective. Ideally, a clinical testing instrument is required that needs minimal sample manipulation, provides rapid, accurate, reproducible results, can be used for a wide range of analytes and is relatively inexpensive.

The development of automated assay systems which remove the washing and reagent addition steps [4, 5] have made some progress towards simplifying the testing process. However, these instruments still require regular maintenance and calibration, and are certainly not cost-effective enough to be moved away from a central laboratory [5] and, hence, there is no real improvement in the delays involved in conducting the tests. Biosensors are initially being developed to fill this market niche and (considering medical applications) are particularly aimed at providing a cost-effective means of decentralizing clinical testing whilst attempting to retain the sensitivities of currently available products.

## **1.2 BIOSENSORS**

Biosensors are a class of chemical sensors which make use of a biological sensing component. Chemical sensors are often required to measure the presence or concentration of a particular chemical in a sample containing many other substances (eg. the measurement of the concentration of a hormone in a blood sample). This requires the sensor to be highly specific for the analyte whose concentration is being measured. Such a degree of specificity is rare in non-biological systems but common in biological systems (eg. enzymes, antibodies, chemical receptors) which makes them particularly

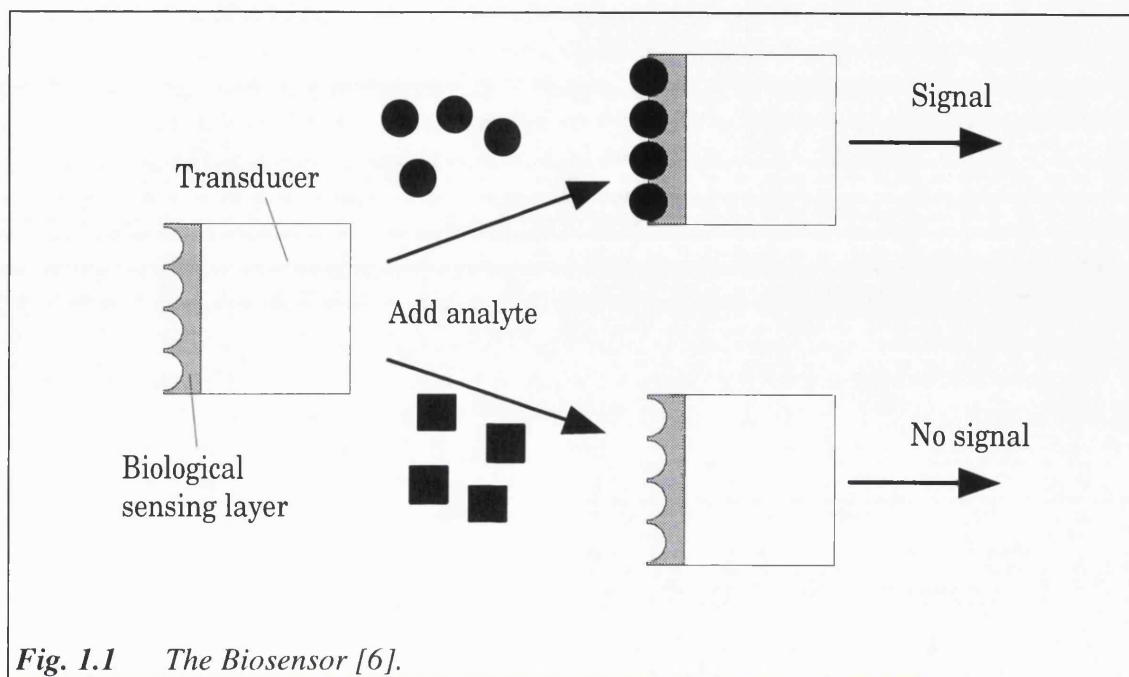


**Fig. 1.1** The Biosensor [6].

useful in sensor systems. It is, however, necessary to combine the biological component with a transducer (see fig.1.1) which produces a physical signal, corresponding to the concentration of the analyte, that can be easily quantified (eg. electrical, optical, acoustic).

### 1.3 BIOSENSOR APPLICATIONS

Although this thesis has opened with a brief look at the medical diagnostics market (which has been the catalyst for much of the current research work in biosensors), the future application of biosensors is not limited to the medical arena. Biosensors have a potentially large market and currently research is being undertaken for biosensor devices in all the areas listed in table 1.1. It should be emphasised that the number of biosensor products on the market is still very small and that table 1.1 gives an indication of both existing and possible applications. The largest projected market by far (with probably over a 50% market share [6], based on current diagnostics product sales), for biosensors is in the health care area, particularly in diagnostics and clinical

<b>Health care</b>	Diagnostics [8]. Clinical testing. Bedside/Doctor's surgery. Intensive care units [9]. Continuous monitoring [10]. Closed loop systems (eg. diabetic insulin administration) [10].
<b>Process Control</b>	Fermentation [11]. Closed loop production controls.
<b>Environmental</b>	Pollution control/monitoring [19]. Agriculture (fertiliser/pesticide control) [20]. Industrial waste management.
<b>Pharmaceutical</b>	Drug monitoring/control.
<b>Food and Drink</b>	Production control. Freshness testing [21]. Additives monitoring.
<b>Veterinary</b>	Diagnostics, etc.
<b>Military</b>	Infectious agent and toxin detection

*Table 1.1 Possible future biosensor applications.*

testing (a market that is currently estimated to be worth 4000 million US\$ in Europe alone in 1993 [6]). Veterinary and agricultural applications will also form an important market (up to a combined 25% share) followed by industrial process control and environmental monitoring applications. It has been estimated that the global biosensor market will be worth up to 350 million US\$ by 1996 [7].

### 1.3.1 Health care

Clinical testing products for a variety of analytes are currently available, mainly in the form of assay kits or as automated assay equipment [4] that require a certain degree

of skill, or experience to use. This is due to the fact that many of the kits and equipment require the addition of various reagents during the assay procedure or include washing steps that must be performed correctly and in the required order to obtain an accurate or correct result. Thus, most clinical testing is carried out in centralised laboratories by experienced personnel which places a time delay between taking a sample and obtaining a result.

Biosensors are, thus, being aimed at applications that would allow a nurse, GP or a patient to perform a measurement at the bedside, in the doctor's surgery or at home, reducing many of the delays. These biosensors will be used by relatively inexperienced personnel and therefore, need to be very simple to use; eg. requiring no more than the addition of the relevant sample and they will also need to incorporate any necessary reference or calibration measurements. This de-centralization of testing and the use of biosensors by inexperienced personnel places certain conditions on the design and requirements of a biosensor device (eg. safety aspects, instrument size and cost).

#### **1.4 BIOSENSOR REQUIREMENTS**

Table 1.2 lists the requirements that a commercial biosensor may be required to meet, some of which will be discussed in further detail below.

The typical media, in which a measurement is likely to be made, are blood, urine, saliva and mucus (for clinical applications), fermentation broth (industrial process control), or polluted water (environmental). These media are highly variable in their pH, metabolite, protein or chemical content and often depend on the person from whom (or the place from where) the sample was taken, and even on the time at which the sample was taken. The presence of chemicals other than the analyte of interest may give rise to interfering signals but, a biosensor still needs to operate without any pre-processing of the sample solution. It is, therefore, necessary for a commercial biosensor

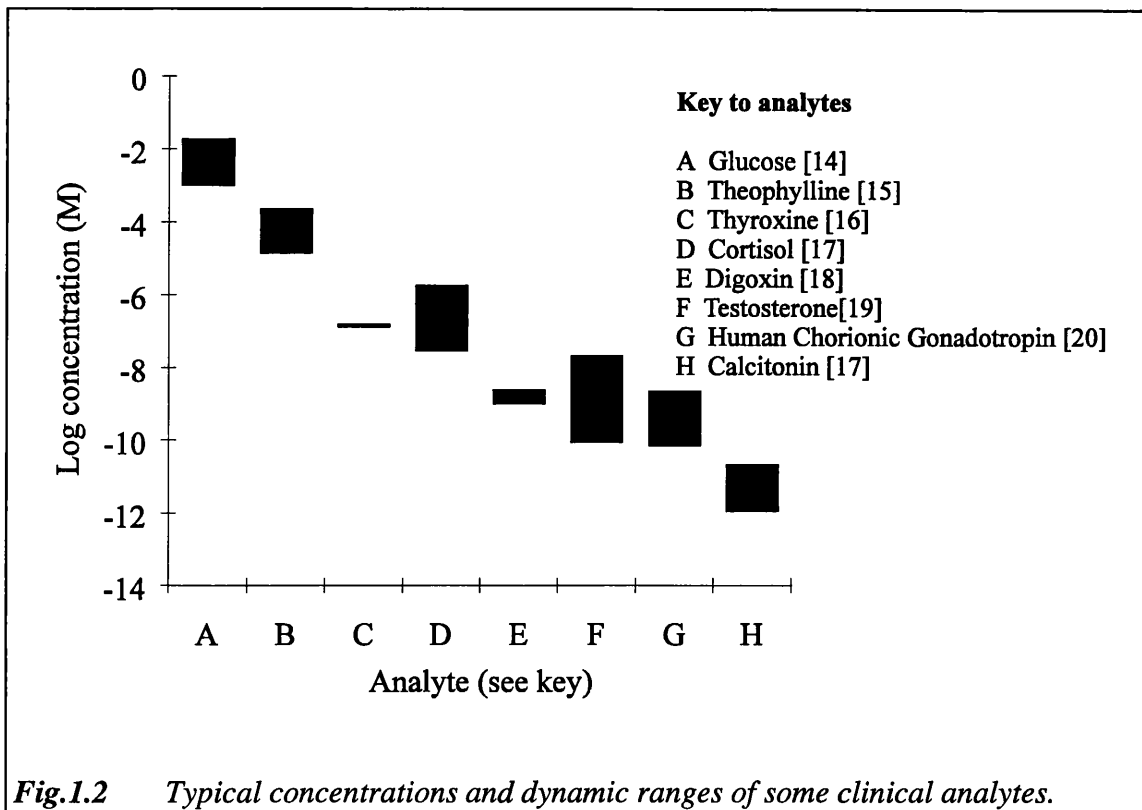
<b>Sensor device</b>	Environmental stability. Accuracy, reproducibility. Calibration/reference. Sensitivity. Dynamic range.  Speed of response.	eg. pH and temperature sensitivity Are variations significant? Automatic or user calibration? Is detectable limit sufficient for analyte? Is measurement range wide enough for all analyte concentrations.?  Ideally, a few minutes.
<b>Instrument</b>	Reliability.  Safety.  Ease of use. User-friendliness. Costs.	eg. maintenance requirements and lifetime. Risks of contamination, cross-infection, chances and consequences of false results. Sample manipulation or reagent addition? Is instrument operation straightforward? What are the capital and running costs?

**Table 1.2** Considerations when designing a marketable biosensor.

to be stable in a range of environments.

Typical analytes of clinical interest are: drugs; metabolites; hormones; enzymes; large proteins and even whole viruses, bacteria or cells. These vary considerably in their size from a molecular weight of ~100 daltons (eg. pesticides) to a few thousand daltons (hormones) to several hundred kilodaltons (eg. antibodies, DNA fragments). Analytes such as viruses and bacteria are very large and complex and are better measured in terms of their physical dimensions. It is conceivable that a single sensor technology could be used to detect all the above analytes but, more likely is that different sensor technologies will be more suited to different analytes.

The sensitivity and dynamic range required of a biosensor vary with the application and are very important when considering biosensor design and optimisation.



Typical sensitivities required for clinical analytes range from concentrations of 1mM to less than 1pM (see fig.1.2). Fig.1.2 also shows the dynamic ranges that are required of clinical analytes. These are typically about three orders of magnitude, but can be as low as a single order of magnitude or, sometimes, greater than four. It is, thus, unlikely that a single biosensor technology will be applicable for all analytes, but more likely that a biosensor can be 'tuned' for use on a range of analytes requiring similar sensitivities and dynamic ranges.

Biosensors for clinical applications are aimed at a mass market and are, therefore, likely to be used by inexperienced staff. This requires the biosensor equipment to be 'user-friendly' (ie. simple to understand and use, self-calibrating, self-testing, and reliable). Current laboratory based clinical testing kits and automated instruments are as cost effective as proposed biosensor technologies [22] and it is unlikely that biosensor instruments will make a large impact within a centralised laboratory environment. However, decentralisation requires greater numbers of biosensor instruments to be installed in separate wards, etc. and thus, capital (instrument) costs need to be low. In

addition, running costs need to be kept down as well because the sensors are likely to be single use disposable devices. Safety is also a prime consideration, not only in preventing physical harm to the user but also psychological harm. It has been shown that as many as 50% of the general population readily interpret the results of 'at home' pregnancy testing kits incorrectly [23]. The reasons for this were user error, misleading instructions or bad kit design, but false results, whether due to user or equipment error, may be highly stressful to the patient.

## **1.5 DISCUSSION**

When designing a biosensor there are a number of factors that need to be considered:

- what market is the biosensor aimed at?
- which analytes will the sensor be used for?
- what sensitivity and dynamic range will be required of the sensor?
- which media is the measurement to be made in?
- what are the safety aspects?
- what reference or calibration measurements are required?
- what will be the likely cost?

Once these questions have been answered, it is possible to design a biosensor to meet the requirements - for example, a biosensor for the clinical diagnostics market will need to be highly reliable, highly accurate and produce reproducible results, whilst a similar sensor for environmental applications may not be so heavily constrained.

The biosensors discussed in this thesis are aimed at the clinical testing market and at the higher sensitivity end required of biosensors. Inexpensive materials and fabrication techniques have been used as costs are likely to be an important factor in a

sensor that will be a single-use disposable device. Detection of the specific binding was done by measuring the fluorescence emitted by the sensing biological molecule labelled with an appropriate fluorophore. The biosensor incorporated only one reference measurement but it is possible to fabricate the sensor so that multiple reference measurement or multiple analyte detection can be done.

Chapter 2 will discuss the current biosensor technology, assessing the relative advantages and disadvantages of the various sensing systems, and chapter 3 will give a more in-depth description of the project objectives together with the reasons for the project.

## REFERENCES

- 1 **RASAI AH B**, Role of home and clinic testing in health care, *Clinical Biochemistry*, 1993, **26**, 15-17.
- 2 **ZALOGA G P**, Evaluation of bedside testing options for the critical care unit, *Chest*, 1990, **97**, 185S.
- 3 **ANONYMOUS**, Label-free technology visualizes biomolecular interactions in real time, *Biosensors & Bioelectronics*, **8(2)**, xi - xiv.
- 4 **CAMARA P D et al**, Evaluation of the Boehringer Mannheim ES300 immunoassay analyzer and comparison with enzyme immunoassay, fluorescence polarization immunoassay, and radioimmunoassay methods, *Clinical Biochemistry*, 1992, **25**, 251-254.
- 5 **McCANN J**, Exploiting biosensors, in **TURNER APF, KARUBE I, WILSON G S eds.**, *Biosensors: Fundamentals and applications*, Oxford University Press, New York, 1987, 1st ed., 737-746.
- 6 **HALL E A H**, *Biosensors*, Open University Press, Milton Keynes, 1990, 1st ed., pp 6, 3.
- 7 **ANONYMOUS - 'BIOELECTRONICS UPDATE'**, *Biosensors & Bioelectronics update*, *Biosensors & Bioelectronics*, 1992, **7(9)**, 606-607.
- 8 **BLUESTEIN B I, WALCZAK I M, CHEN S-Y**, Fiber optic evanescent wave immunosensors for medical diagnostics, *TIBTECH*, 1990, **8**, 161-168.
- 9 **ALCOCK S J, DANIELSSON B, TURNER A P F**, Advances in the use of in vivo sensors, *Biosensors & Bioelectronics*, 1992, **7**, 243-254.
- 10 **TURNER A P F, PICKUP J C**, Diabetes mellitus: biosensors for research and management, *Biosensors*, 1985, **1**, 85.
- 11 **SCHEPER T**, Biosensors for process monitoring, *Journal of Industrial Microbiology*, 1992, **9**, 163-172.
- 12 **YAO S H**, Chemistry and potential methods for in vivo glucose sensing, in **WISE D L ed.**, *Bioinstrumentation and Biosensors*, Marcel Dekker Inc., New York, 1991, 1st ed., pp229.
- 13 **St. LOUIS P J et al**, An evaluation of the Kodak Ektachem clinical chemistry slide for theophylline, *Therapeutic Drug Monitoring*, 1989, **11**, 93-96.
- 14 **JAFFE B M, BEHRMANN H R eds.**, *Methods of hormone radioimmunoassay*, Academic Press Inc., London, 1979, 2nd ed., pp1008.
- 15 Various immunoassay methods, *Biogenesis Ltd.*
- 16 **BOCHNER F et al**, *Handbook of clinical pharmacology*, Little, Brown & Co., Boston, 1983, 2nd ed.
- 17 **GOWER D B**, *Steroid hormones*, Croom Helm, London, 1979, 1st ed., pp61.
- 18 **YEN S S C, JAFFE R B**, *Reproductive endocrinology*, W B Saunders & Co. Ltd., 1978, 1st ed., 525-527.

- 19 **ROGERS K R, LIN J N**, Biosensors for environmental monitoring, *Biosensors & Bioelectronics*, 1992, 7, 317-321.
- 20 **BIER F F et al**, Use of a fiber optic immunosensor for the detection of pesticides, *Sensors and Actuators B*, 1992, 7, 509-512.
- 21 **WATANABE E, TANAKA M**, Determination of fish freshness with a biosensor system, in **WISE D L ed.**, Bioinstrumentation and Biosensors, *Marcel Dekker Inc., New York*, 1991, 1st ed., pp39.
- 22 **MANNING B, MALEY T**, Immunosensors in medical diagnostics - major hurdles to commercial success, *Biosensors & Bioelectronics*, 1992, 7, 391-395.
- 23 **DAVIAUD J et al**, Reliability and feasibility of pregnancy home tests: laboratory validation and diagnostic evaluation involving 638 volunteers, *Clinical Chemistry*, 1993, 39, 53-59.

## CHAPTER 2

### BIOSENSOR TECHNOLOGY

*Biosensors, referring to chapter 1, fig. 1.1, combine a biological sensing layer with a physical transducer. This chapter provides a critical assessment, in the context of the discussions of chapter 1, of the biological materials available for the sensing layer and also of the various transduction methods that are being employed. However, the emphasis is on evanescent field optical immunosensors as these are most directly relevant to the sensors that are the subject of this thesis. Finally, there is a discussion of some of the problems encountered with optical immunosensing systems and some of the improvements that could be considered or incorporated to tackle these problems.*

#### 2.1 THE BIOLOGICAL SENSING LAYER

Table 2.1 lists the possible biological components of a biosensor together with the analytes that they can be used to detect and their relative advantages or disadvantages.

**Cell and tissue based sensors [1].** Although these sensors have serious drawbacks in terms of sensitivity, specificity, response speed and shelf-life, they have the advantages that they are relatively inexpensive, simple and environmentally stable [2] (because the inside of the cell is isolated from the external environment). The use of such sensors may be limited to environmental applications (eg. effluent control or waste water monitoring) where the need for low cost is likely to outweigh any needs for high specificity, and to fermentation broth monitoring where the environmental stability of a cell-based sensor may be particularly attractive.

<b>Biospecific layer</b>	<b>Applicable for:</b>	<b>Relative merits</b>
<b>Tissues</b>	Factors affecting cell health.	Low specificity, low shelf-life.
<b>Whole cells and microbes</b>	Factors affecting cell health: eg. ethanol, oxygen and mutagens.	Inexpensive, environmentally stable. Low specificity, long response time, low shelf-life.
<b>Nucleic acids</b>	DNA and RNA	High specificity and long shelf-life. Limited analytes.
<b>Cell receptors</b>	Class specific: Drugs, toxins, hormones, etc..	High specificity, easily measured signal. Limited analytes, require immobilisation in lipid bilayers
<b>Enzymes</b>	Class-specific. Dependent on type of reaction the enzyme catalyses.	Good specificity. Direct detection by optical absorption or fluorescence methods or by electrochemical methods.
<b>Antibodies</b>	Can be produced for the detection of any large molecule (hapten) or macromolecule (antigen).	High specificity and affinity, wide range of analytes. Direct detection difficult and a label is usually required.

*Table 2.1 The biospecific component of a biosensor.*

**Nucleic acids and DNA fragments [3].** A single strand of DNA is highly specific for its complementary strand. This property can be very useful in the detection of genetic disorders or even in the detection of viruses (by RNA detection). Although DNA detection is a growing field, the more general application of DNA sensors is limited, outside of the medical arena.

**Cell receptor proteins [4].** Despite their high selectivity, affinity and the production of a readily measurable signal, these sensors have a major drawback in their stability. It has been difficult to isolate and immobilise the receptor proteins whilst retaining their activity. Most current receptor-based sensors need to immobilise the proteins in a lipid bilayer [5] or use the receptors present in their natural host. This factor may render receptor-based sensors commercially non-viable.

**Enzymes [6].** Enzymes act as catalysts for chemical reactions (changing a 'substrate' into its products) within living organisms and are class-specific (according to the type of reaction they catalyse). Enzymes have found widespread use in assays and biosensor devices because they are capable of producing a readily measurable signal (eg. electric current, colour changes, etc). Although enzymes can only be used directly for the detection of the presence of their substrate, they can be used indirectly as labels in other biosensing systems [7]. However, the limited range of analytes that enzymes can detect directly has prevented a more widespread use.

### 2.1.1 The antibody

Antibodies are part of the adaptive immune system of higher animals and are produced in response to the presence of foreign molecules within a host animal. The foreign molecules can be classed into two groups: 1) *antigens* (molecular weight >5000) - which induce an immune response and 2) *haptens* (molecular weight <5000) - which do not [8]. It is possible to induce an immune response to haptens by coupling the haptens to larger molecules. Antibodies are characterised by a high specificity and a high binding affinity for their respective antigen [8]. These properties, and the fact that antibodies can be raised against a wide range of antigens has led to their widespread use in conventional clinical tests (immunoassays) that have achieved femtomolar sensitivity [9]. Immunosensors make use of antibodies as the biospecific component. Antibodies were used as the biospecific layer in the biosensors described in this thesis.

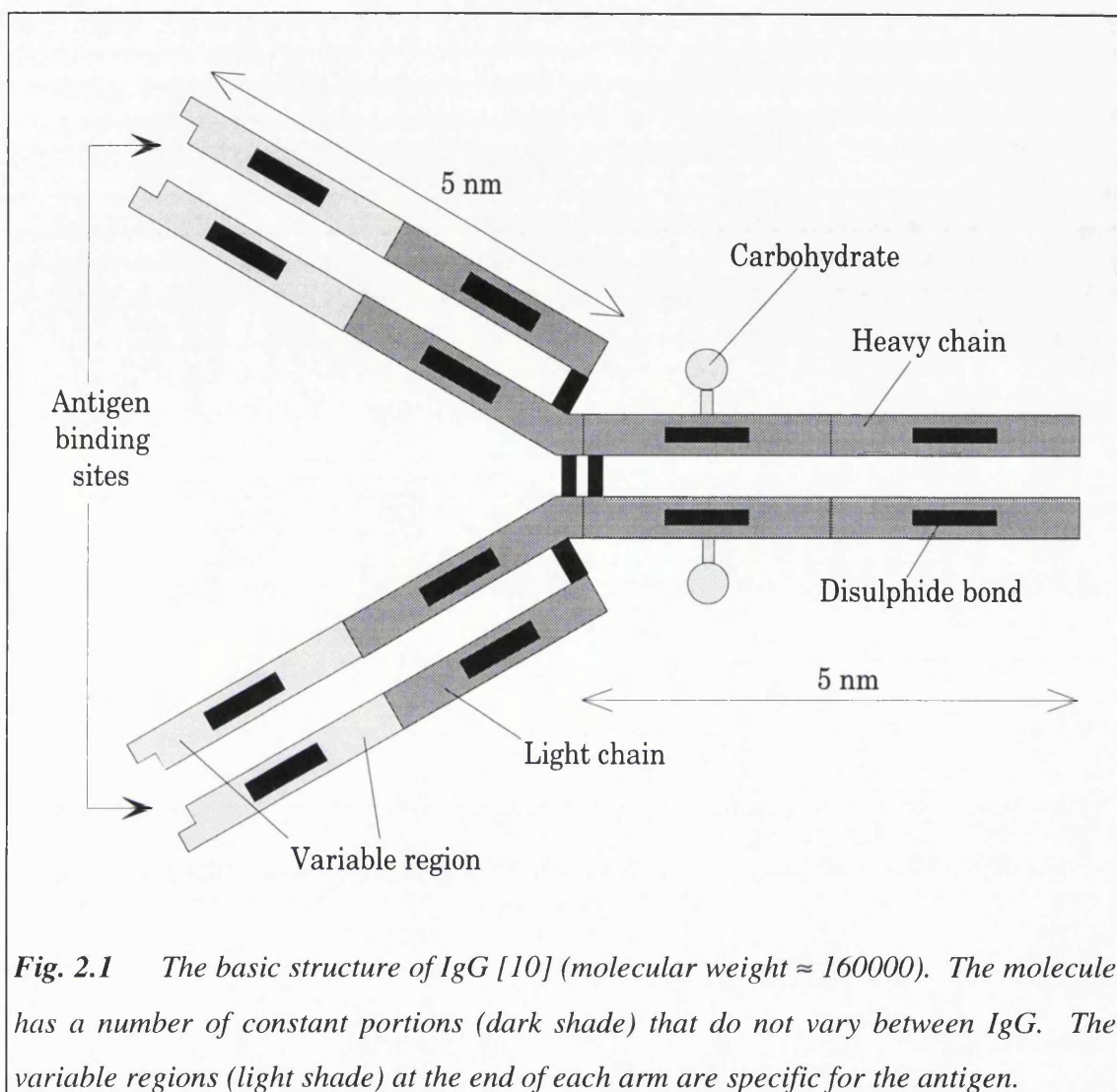


**Fig. 2.1** The basic structure of IgG [10] (molecular weight  $\approx 160000$ ). The molecule has a number of constant portions (dark shade) that do not vary between IgG. The variable regions (light shade) at the end of each arm are specific for the antigen.

There are five distinct classes of antibody present in most higher mammals [10] but the form most commonly used in assays is *Immunoglobulin G* (IgG), whose structure is illustrated in fig. 2.1. IgG is a 'Y'-shaped protein molecule which has two binding sites, at the end of each arm, that are specific for a particular antigen binding site. Antibodies can be artificially produced by immunising an animal towards the antigen. The animal will normally produce a range of antibodies with varying specificity and a wide range of binding affinities (association constants) in the range  $10^6$  to  $10^{12} \text{ M}^{-1}$  [10]. These antibodies are described as polyclonal. It is possible, however, to clone a single antibody line and produce these indefinitely in relatively large quantities [11]. Such antibodies are described as monoclonal, having a single

association constant typically in the range  $10^8$  to  $10^{11}$  M<sup>-1</sup>. Monoclonal antibodies are preferred to polyclonal antibodies in assays because of their well defined characteristics, high specificity and high binding affinity for the antigen, and also because of the inexhaustible production.

The dissociation rate constants of antibody-antigen complexes are generally very low ( $10^2$  to  $10^{-4}$  s<sup>-1</sup>) because of their high association constants, but it is possible to dissociate the antibody-antigen complex (which is performed, for example, during the production and purification of antibodies [12]). The process, however, is too complex, (sometimes reducing the activity of the antibody) for it to be incorporated into most commercial immunosensors, and so most immunosensors are likely to be single-use disposable devices. This is the case for the immunosensors described in this thesis.

## 2.2 IMMUNOASSAYS

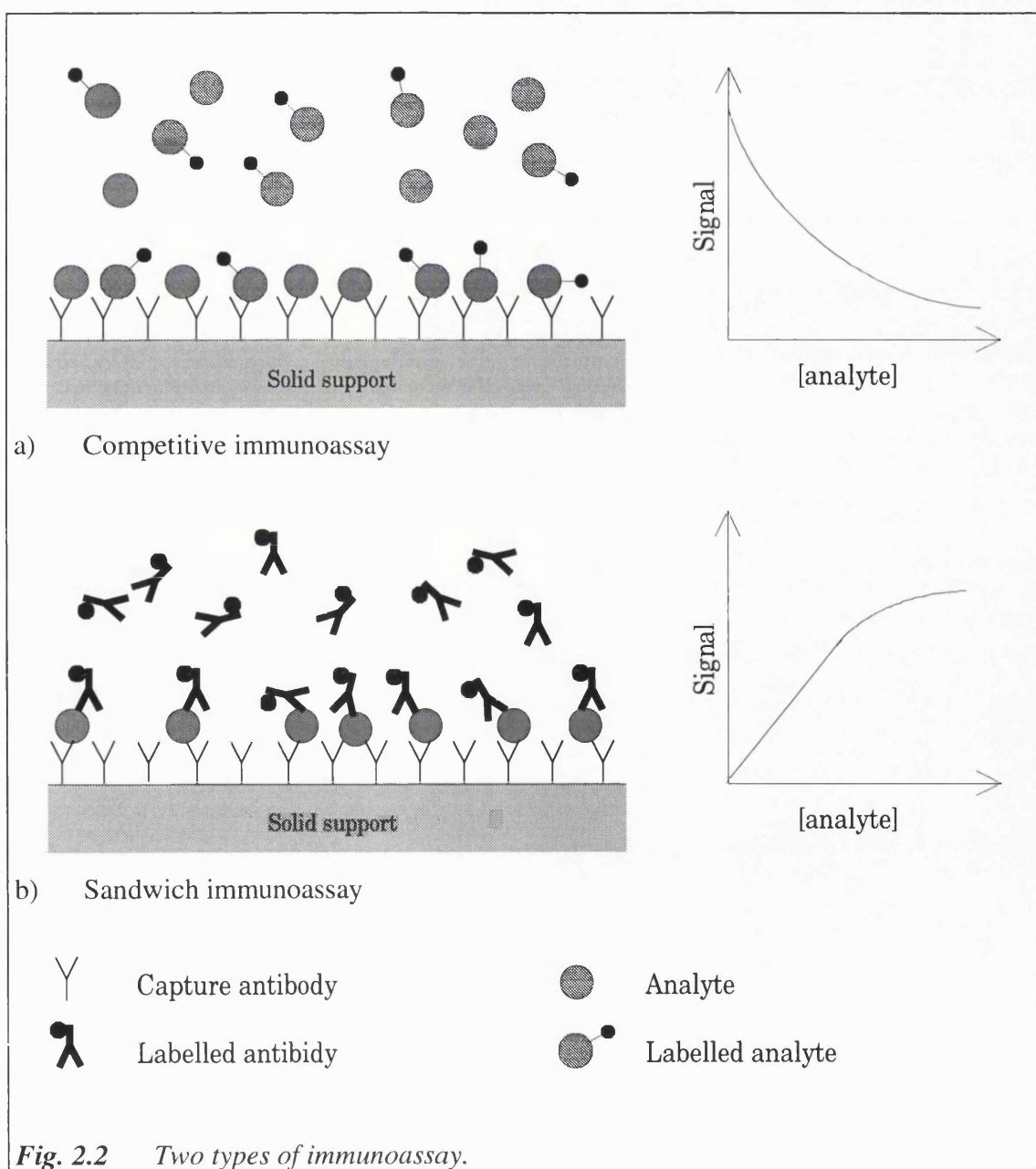
There are two major types of immunoassays that are applicable to and most commonly used in immunosensors. These are illustrated in fig. 2.2. Note that both techniques require the immobilisation, on a solid support, of an antibody specific for the analyte being quantified. The immobilised layer is typically termed the 'capture layer'.

**Competitive immunoassay.** A known quantity of labelled analyte is added to the sample solution and the labelled and sample analytes compete for binding sites on the capture antibody layer. The amount of labelled analyte binding to the capture antibodies is inversely proportional to the sample analyte concentration, giving a signal to sample analyte concentration curve as shown in fig. 2.2a.

**Sandwich immunoassay.** An excess of labelled antibody specific for the analyte is added to the sample solution. The capture antibody and the labelled antibody bind to the analyte at different sites on the analyte, thus forming a 'sandwich' layer. The

concentration of analyte in the sample solution can then be obtained by measuring the signal from the labelled antibody where the signal to analyte concentration curve is typically of the form shown in fig. 2.2b. This signal is approximately linear until saturation of the binding sites available on the capture layer is approached, whereupon the signal begins to plateau.

Sandwich assays are considered to have a number of advantages over competitive assays



(eg. linear response, wider working range, higher precision and sensitivity [13]). Sandwich assays also require shorter reaction times and the use of two different antibodies may give a higher specificity. One drawback of sandwich assays is the necessity for two binding sites on the analyte which limits its use in the assay of small haptens. A sandwich assay was used in the immunosensors described in this thesis, but competitive assay techniques could also have been used.

### 2.3 SIGNALLING OF SPECIFIC ANTIBODY-ANTIGEN BINDING

Immunoassays (both competitive and non-competitive) can be broadly classed into four categories under the terms: heterogeneous; homogeneous; direct and indirect as illustrated in table 2.2.

Signal measurement in a heterogeneous immunoassay is done after the sample solution (containing potentially interfering background proteins and labelled material) has been removed by washing steps, leaving the bound layer in a known environment. The signal, thus measured, would be free of any background signals from the sample solution. However, as discussed in chapter 1, many commercial immunosensors will require the elimination of any washing steps, and thus signal measurement will need to be performed in the presence of an interfering sample solution. Thus, heterogeneous immunoassays are not applicable to commercial immunosensors and so will not be

	<b>Heterogeneous</b>	<b>Homogeneous</b>
<b>Direct</b>	Requires washing/separation steps. No labelled reagent addition.	No washing/separation steps. No labelled reagent addition.
<b>Indirect</b>	Requires washing/separation steps. Requires labelled reagent addition.	No washing/separation steps. Requires labelled reagent addition.

*Table 2.2 Immunoassay classification.*

discussed further.

In homogeneous immunoassays, the signal measurement is made in the presence of the sample solution. The measurement can be 'direct' (no labels) or 'indirect' using appropriate labels.

### **2.3.1 Labels used in 'indirect' homogenous immunoassays**

The typical labels available for use in indirect immunoassays are listed in table 2.3.

**Radioisotopes.** Radioimmunoassays have achieved very high sensitivities (in the femtomolar range [9]) but have a number of drawbacks when considered for immunosensors. Radioimmunoassays, in general, require washing steps for the separation of the bound layer from the sample solution, although wash-free assays have been reported [14]. There are also many safety aspects involved in the handling of radioactive materials which, together with the costs of disposal, make them unsuitable for immunosensor use.

**Enzymes.** Enzyme immunoassays are usually colorimetric (measurement of optical absorption or colour changes) but it is also possible to use fluorescence, luminescence or electrochemical methods. Enzyme immunoassays can also be performed in a wash-free format [15]. However, such assays still require the addition of reagents such as the enzyme substrate or inhibitor, thus introducing extra steps that would need to be avoided when considering the commercial development of immunosensors.

**Fluorophores.** Fluorophores were originally used as alternatives to radio-isotopes because of their better safety aspects. They also have an advantage over enzyme labels in that the addition of reagents other than the labelled component is not required. Fluorophores that emit at long wavelengths (>520nm) are preferable so as to avoid the

intrinsic fluorescence of proteins which would contribute to background signal (this

LABELS	SIGNALS	RELATIVE MERITS IN IMMUNOSENSORS
<b>Radioactive isotopes</b>		
<sup>125</sup> I, <sup>3</sup> H, <sup>14</sup> C, etc	γ, β - rays.	Highly sensitive. Requires washing steps. Requires safe handling.
<b>Enzymes</b>		
<b>Colorimetric:</b> Alkaline phosphatase	λ <sub>ab</sub> = 405nm	Washing steps generally required although wash-free format possible but difficult. Requires addition of reagents.
<b>Fluorescent:</b> β - Galactosidase	λ <sub>ex</sub> = 490, λ <sub>em</sub> = 514nm	
<b>Luminescent:</b> Luciferin/Luciferase	λ <sub>em</sub> = 562nm	
<b>Fluorophores</b>		
<b>Short lived:</b> Fluorescein-ITC Allophycocyanin	λ <sub>ex</sub> = 485, λ <sub>em</sub> = 515nm λ <sub>ex</sub> = 650, λ <sub>em</sub> = 670nm	Very sensitive. Safe. Ease of coupling to antibodies. Weak signals.
<b>Long-lived (0.1 - 1 ms):</b> Lanthanide chelates	λ <sub>ex</sub> = 330, λ <sub>em</sub> = 613nm	
<b>Particles</b>		
<b>Light scattering:</b> Whole cells Antibody complexes		Simple. Safe. No reagent addition. Low sensitivity.
<b>Refractive index:</b> Large proteins Whole cells		

Table 2.3 Typical labels available for homogeneous immunoassay.

factor is particularly important in wash-free assay formats). The major problems with fluorescence immunoassay are caused by background fluorescence (from unbound labelled antibody), scattered exciting light and fluorescence quenching (by the sample solution) [16]. However, the advantages of using fluorophores in immunosensors has led to much interest being shown in their development. The optical immunosensors described in this thesis used fluorophores (allophycocyanin:  $\lambda_{\text{ex}} = 650\text{nm}$ ,  $\lambda_{\text{em}} = 660\text{nm}$ ; and CY5.18 cyanin dye:  $\lambda_{\text{ex}} = 650\text{nm}$ ,  $\lambda_{\text{em}} = 670\text{nm}$ ) as the labels. Allophycocyanin and CY5.18 were chosen because they can be excited by both a 632nm HeNe laser and a 650nm semiconductor diode laser thus allowing comparison of the two lasers as excitation sources.

Magnetic particles have been used as labels to aid the separation of the antibody-analyte complex from the bulk solution. However a second labelled antibody is still required to provide the measurable signal [17]. Antibodies bound to latex microspheres have been employed in light scattering immunoassays [68]. However, the application of this technique in a biosensor device has not been greatly investigated and it is unlikely that it will offer sufficient sensitivity.

### 2.3.2 No-label 'direct' homogeneous immunoassays

Direct immunoassays make use of effects that are intrinsic to the antibody-antigen binding reaction. Such assays are highly attractive to the development of immunosensors as they do not require the addition of a reagent, thus reducing the complexity and cost of immunosensor fabrication. Agglutination, precipitation, turbidimetric and nephelometric assays are all applicable to direct immunoassays, but the techniques most applicable to immunosensors are ones that rely on electrochemical changes [18], or changes in refractive index [19] or mass loading at a surface [20]. The two former methods have received considerable interest and have resulted in the development of various electrochemical and optical sensing systems respectively [21,

22]. However, intrinsic effects can often be too weak to measure effectively and immunosensors using direct detection methods are more likely to be affected by non-specific binding [23] which gives rise to a background signal that is often dependent on the sample solution environment. For example, the presence of any electroactive species will affect the results of an electrochemical sensor and the presence of large proteins or whole cells may greatly affect the results of the refractive index and mass loading methods.

## 2.4 IMMUNOASSAY PERFORMANCE

Prior to the discussion of immunosensors in general and immunosensor transduction methods in particular, the means by which the performance of a particular assay (or immunosensor) can be assessed are considered. There seems to be great deal of confusion in the definition of the terms by which an assay performance can be described: sensitivity, detection limit, precision, accuracy, dynamic (working) range are all used liberally in publications, often with inadequate or ambiguous definitions. Throughout the following text and the rest of the thesis, the following definitions (according to *Ekins* [24]) will be used.

**Precision.** This is equivalent to accuracy and can be defined as the minimum detectable difference (MDD) between two measurements. This is not only governed by the resolution of the measuring instrument but also by the scatter of repeated measurements at a single analyte concentration. Assuming that the instrument resolution is much better than the scatter of the measured points, then the precision can be defined as shown in fig. 2.3.

**Sensitivity.** This is equivalent to the detection limit (the lowest measureable analyte concentration) and is defined in a similar manner to precision (see fig. 2.3). Ideally all immunosensors would give a detection limit of zero, but noise, sample solution

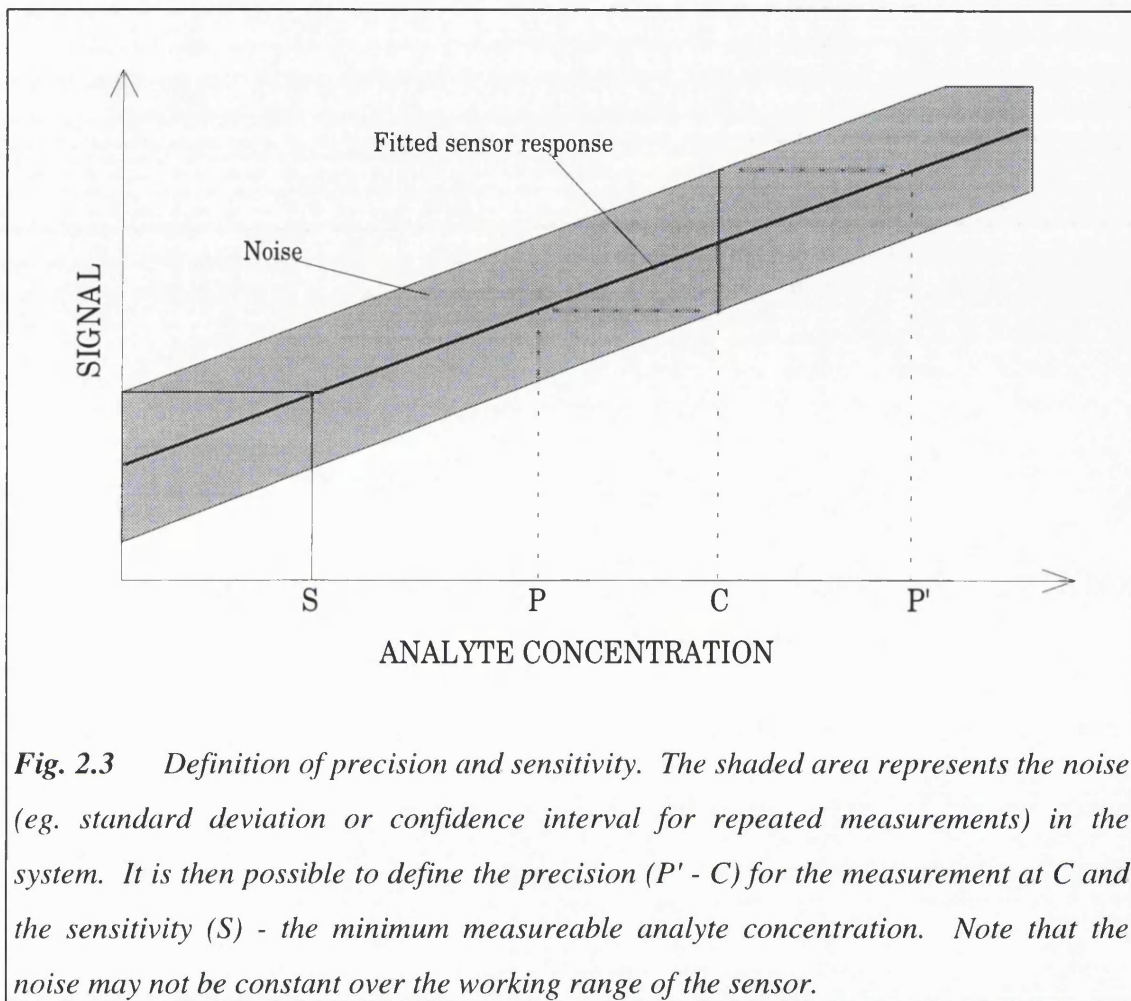


**Fig. 2.3** Definition of precision and sensitivity. The shaded area represents the noise (eg. standard deviation or confidence interval for repeated measurements) in the system. It is then possible to define the precision ( $P' - C$ ) for the measurement at  $C$  and the sensitivity ( $S$ ) - the minimum measurable analyte concentration. Note that the noise may not be constant over the working range of the sensor.

variations and other factors ensure that this is not possible. Sensitivity is a highly abused term being defined in many different ways by different workers, but *Ekins'* definition, that sensitivity is best described by the standard deviation of the zero analyte measurement, is used in this thesis. However, because it was not possible to fabricate a large number of devices, sufficient repetitions of the zero analyte measurement could not be made and the above definition was modified to the standard deviation of the measured points from a fitted straight line. The detection limit was then taken to be the analyte concentration that gave a signal that was two standard deviations from the zero analyte signal.

**Dynamic range.** This is the range of analyte concentrations from the detection limit to a maximum over which the sensor will give the desired precision.

## 2.5 TRANSDUCTION IN IMMUNOSENSORS

Enzyme redox reactions readily produce free electrons that can contribute to a measurable current in an electrode. Antibody-antigen reactions, however, cannot be so directly monitored but can be detected by a number of methods which may be grouped into three major categories:

- Acoustic
- Electrical
- Optical

**Acoustic.** The capture layer is immobilised onto a piezoelectric or surface acoustic wave device. The binding of the analyte increases the mass loading on the surface which alters the frequency of oscillation of the device [26]. This is a direct sensor which is simple to fabricate and operate and is particularly useful in the gaseous phase or for the detection of large analytes in complex liquid environments (eg. serum) [25] or small analytes in simple liquid environments (eg. water) [69]. Although sensitivities down to the nanomolar range are theoretically possible, the measurements are greatly affected by non-specific binding and are dependent on the viscosity of the sample solution [26], thus making acoustic sensors unsuitable for general use in complex environments.

### 2.5.1 Electrical immunosensors

This category can be further sub-divided into conductance [70], capacitance [71], amperometric, and potentiometric, of which only the last two have received widespread interest.

**Amperometric.** The oxidation-reduction reactions of enzymes can be detected by the

use of electrodes across which a potential has been applied. The current generated will be some function of the concentrations of the enzyme and its substrate [6]. The simplicity of the technique has led to the widespread use of amperometric assays, particularly for enzyme substrates such as glucose [73], oxygen [27] and even penicillin [72]. It is possible to fabricate an amperometric immunosensor by using an enzyme as the label on the antibody [28, 38]. Although nanomolar sensitivities have been obtained [6] using enzyme immunoassays, the requirement of such sensors for the addition of reagents (enzyme substrate, inhibitor, etc.) or the inclusion of washing steps increases their complexity making them less commercially viable.

**Potentiometric.** Most proteins, antibodies, antigens, etc. are electrically charged molecules and so it is feasible to fabricate an immunosensor device that is sensitive to changes in charge distribution. The most promising techniques currently being pursued make use of the semiconductor field-effect transistor (FET) device. The gate on a conventional electronic FET is replaced by a biological capture layer in the FET biosensor. The binding of the analyte onto the capture layer changes the surface charge distribution allowing current to flow in the device. The FET devices have many advantages. They are direct sensors that are simple to fabricate by modifying existing micro-electronic fabrication techniques and, hence, it is relatively inexpensive to fabricate an array of devices, allowing easy and cost-effective inclusion of reference and calibration measurements and also the possibility of multiple-analyte testing [29]. The major and limiting problem with potentiometric sensors, as with amperometric sensors, is one of sample solution dependence - any electro-active species present in the sample solution (eg.  $H^+$ ,  $Cl^-$  or charge carrying protein) can affect the signal [30].

### **2.5.2 Optical immunosensors**

The disadvantages of FET sensors has led workers to investigate alternative detection methods (eg. acoustic, optical), of which optical techniques, offering lower sample solution dependence and no electrical interference when compared to

potentiometric sensors, are receiving most attention. The bulk of conventional clinical immunoassays use optical techniques - fluorescence [31], luminescence [32], light scattering [33], etc.. It was, thus, a logical step to attempt to modify these for use in wash-free immunosensors with the possibility of achieving the same sensitivities as the conventional optical immunoassays. It is also possible to achieve multiple analyte testing by the use of multiple labels and multi-wavelength excitation, or by optical signal processing methods. Optical sensors are also more suitable as in-vivo sensors (using optical fibres) as they can be truly 'remote' from the measuring instrument.

The drawbacks are that signals from optical sensors are affected by ambient background light, scattered exciting light, or by unwanted signals from the sample solution or glass substrate (eg. background fluorescence and phosphorescence). Signal levels when measuring fluorescence can be very weak, thus requiring sensitive detection devices such as a photomultiplier tube (PMT) which adds to the cost of optical sensors. Commercially viable sensor technologies will require cheap disposable devices, moderately priced instrumentation and a wash-free assay format with detection limits similar to conventional optical immunoassays (ie. picomolar range). Thus, referring back to section 2.2, a suitable method is required whereby the signals from the bound layer can be discriminated from those in the bulk solution while retaining signal strength and without compromising instrument complexity. Evanescent field immunoassay techniques address this particular problem and so have received much attention. The evanescent field immunosensors that are the subject of this thesis aim to increase the signal-to-background and signal-to-noise ratios over a simple total internal reflection technique thus improving the sensitivity and detection limit.

### **2.5.2.1 The evanescent field**

An evanescent field (or evanescent wave) is associated with light totally internally reflected at a dielectric boundary or light confined within a dielectric waveguide. An evanescent wave is a non-propagating, oscillating electromagnetic wave present in the optically rarer medium whose field strength decays exponentially away from the

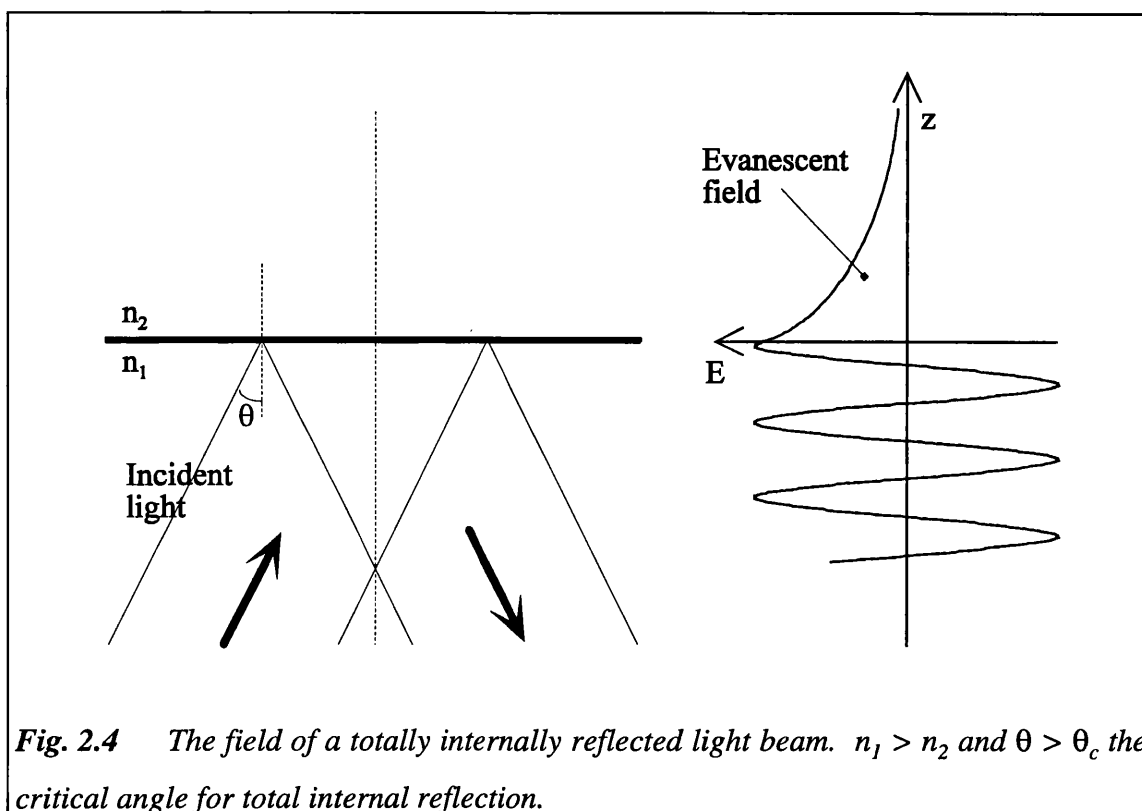


**Fig. 2.4** The field of a totally internally reflected light beam.  $n_1 > n_2$  and  $\theta > \theta_c$  the critical angle for total internal reflection.

interface at which total internal reflection has occurred (see fig. 2.4). Evanescent fields are, thus, also associated with waveguides (planar slab and optical fibre) and also with the oscillations of conduction band electrons at a metal/dielectric interface.

When time averaged, the evanescent field does not transfer energy away from the interface but energy does oscillate between the optically denser and rarer media. The presence of any optically absorbing or high refractive index material within the evanescent field, however, does allow energy to be transferred from the optically denser medium. This property can be used in evanescent field optical immunosensors (where the optically rarer medium is the sample solution) to excite fluorophores present within the evanescent field [34]. However, because the field decays exponentially away from the interface, fluorophores close to the interface (ie. in the bound layer for the immunoassays of section 2.2) are excited in preference to those in the bulk solution. Thus, an effective separation of the bound layer and the bulk sample solution is achieved. It is also possible to detect the emitted fluorescence by evanescently coupling the energy into the optically denser medium such that the angle of incidence,  $\theta$ , (see

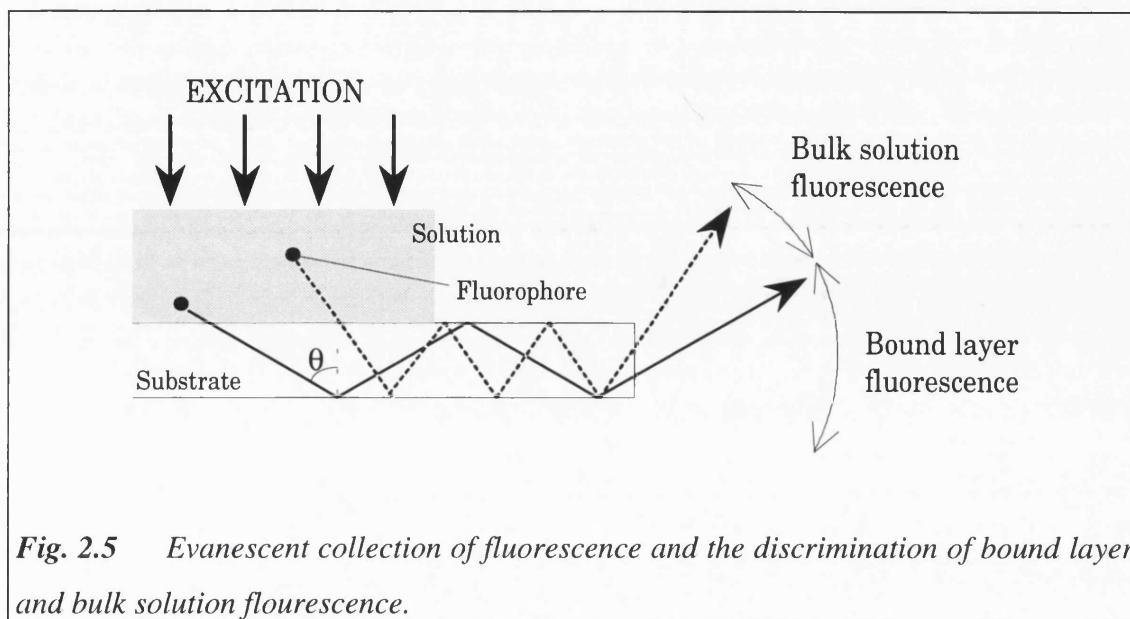


**Fig. 2.5** *Evanescent collection of fluorescence and the discrimination of bound layer and bulk solution fluorescence.*

fig. 2.5) is greater than the critical angle. Coupling into these angles is only possible for fluorophores lying close to the interface, whereas fluorophores in the bulk solution couple at lower angles of incidence. This can be used to separate bound layer and bulk sample solution fluorescence [35].

The two most important characteristics (as applied to sensors) of the evanescent field are the field strength and field penetration depth. The penetration depth of an evanescent field is defined as the distance from the interface at which the field strength falls to  $1/e$  of its value at the interface. The penetration depth is dependent on the wavelength and angle of incidence of the exciting light, the ratio of the dielectric refractive indices or (in a waveguide) the propagation vector of the confined wave. A high field strength will give a strong signal whereas a low penetration depth will give a better effective bound-layer to bulk-solution separation and so a better signal-to-background ratio. The typical penetration depths for evanescent field optical immunosensors are 50 - 200 nm and the typical bound layer thicknesses are 10 - 40 nm.

## 2.6 EVANESCENT FIELD IMMUNOSENSORS

### 2.6.1 Total internal reflection (TIR)

*Kronick and Little* [34] first demonstrated the concept of performing evanescent field excited, wash-free fluorescence immunoassays by using the evanescent field of a single reflection on the inside face of a quartz prism to excite fluorescein labelled antibody. The competitive assay they performed for the analyte (morphine) yielded a high detection limit concentration of 200nM because of low signal levels. The detection limit was too high for many analytes (chapter 1, fig. 1.1), which require measurement in the picomolar range, and so many workers have attempted to improve it.

*Sutherland et al* [36] used multiple internal reflections within a microscope slide and also within an optical fibre (0.6mm diameter) to improve the signal levels. They achieved a detection limit of 270nM for an assay of the drug methotrexate when using an optical absorption method. However, this was dramatically improved when an evanescently excited fluorescence assay for human IgG was performed, giving detection limits of 19nM and 9.5nM for the microscope slide and optical fibre respectively. *Sutherland et al* claimed that their fluorescence assays were limited by background fluorescence from unbound labelled antibody lying within the evanescent field. This, as will be demonstrated in this thesis, is only part of the problem and other background signal sources such as scattering of exciting light and phosphorescence of the glass may also be significant contributors.

Total internal reflection sensors have the advantages that they are relatively simple in design and it is easy to couple light into and out of the device. The drawback is the low signal level which gives a low signal-to-background ratio and therefore a poor sensitivity. Nevertheless, sensors based on total internal reflection techniques have been developed and are close to commercialisation [37].

### 2.6.2 Surface plasmon resonance (SPR)

A surface plasmon wave is a TM polarised electromagnetic wave, supported by oscillations in the density of the conduction band electron cloud, that propagates along a metal/dielectric interface. The oscillations are heavily attenuated and, therefore, the wave propagates for only a short distance (of the order of  $100\mu\text{m}$  [38]). Surface plasmons are excited when the propagation velocity of the exciting light matches that of the surface plasmon and, thus, a glass prism or a diffraction grating is required to reduce the propagation velocity of the exciting light. A surface plasmon can then be excited by varying the angle of incidence or the incident wavelength to allow the matching conditions to be met (fig. 2.6). When surface plasmon resonance occurs, most of the incident light energy is absorbed by the plasmons and then quickly lost through attenuation. Thus, the reflected light intensity shows a minimum at the angle of incidence for resonance (fig. 2.6). Fig. 2.6 shows a typical prism configuration, where the exciting light is reflected off a thin metal film (usually silver or gold). However, this configuration requires tight control over the film thickness to ensure that the evanescent

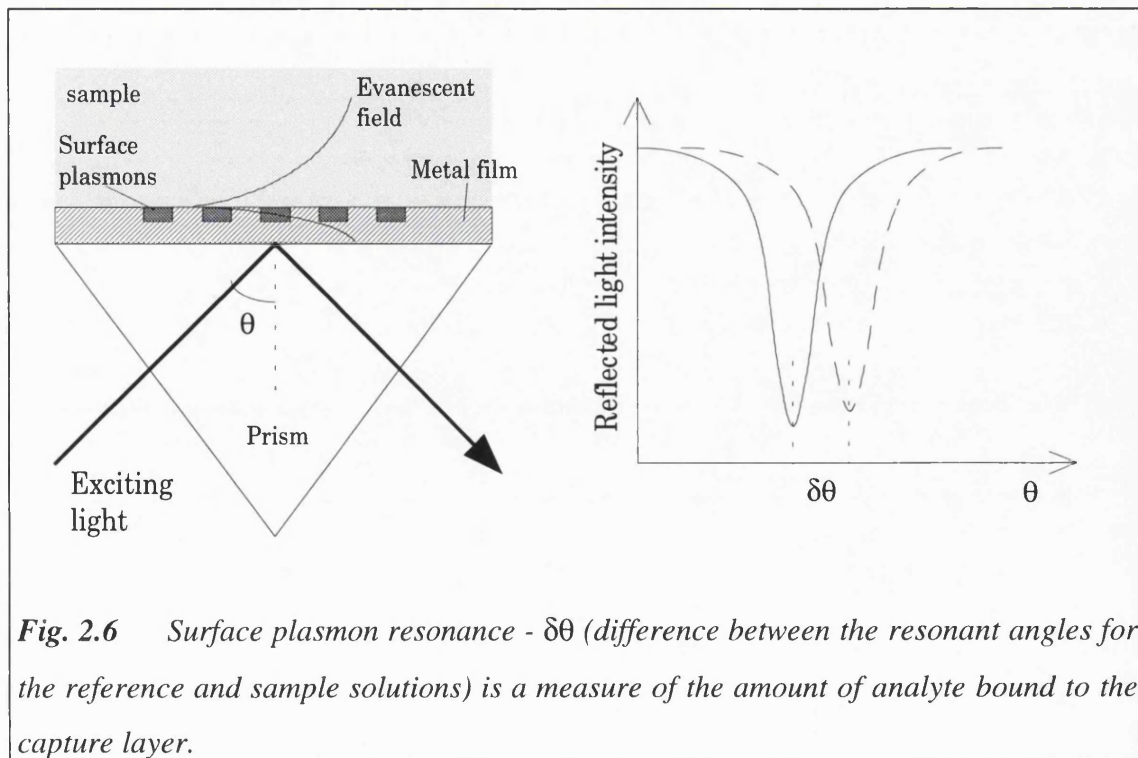


**Fig. 2.6** Surface plasmon resonance -  $\delta\theta$  (difference between the resonant angles for the reference and sample solutions) is a measure of the amount of analyte bound to the capture layer.

field of the incident light reaches the opposite face of the metal film so that SPR can be excited on this face. An alternative to prism coupling is to use a grating patterned on the metal surface in contact with the sample solution [39]. This has the advantages that a planar substrate (instead of a prism) can be used and that it requires a less rigorous control over film thickness, but, the surface plasmons now have to be excited through the sample solution and this may lead to greater sample solution dependence.

The resonant angle is dependent on the refractive index of the dielectric material within the evanescent field of the surface plasmon wave and any alteration in this refractive index will show as a shift in the resonant angle of incidence. Thus, if a capture antibody layer is immobilised on the metal film and a sample solution containing the analyte is added, the subsequent binding of the analyte will alter the refractive index and thus the minima in the reflected light beam will shift (fig. 2.6). The change in the angle is a measure of the amount of analyte bound to the capture antibody. Surface plasmon resonance has attracted a great deal of interest due to its inherent simplicity, because it is a direct sensing technique, and because it requires relatively cheap instrumentation (eg. a photodiode to monitor the intensity of the reflected light). *Daniels et al* [40] achieved a detection limit of 10nM for an immunoassay for  $\alpha$ -feto protein in phosphate buffered saline (PBS). Surface plasmon resonance based sensors have also had some, if limited, commercial success with systems such as PHARMACIA'S 'BIAcore' system [41]. However, these expensive systems still require manipulation and processing of the sample solution and as such are limited to laboratory environments.

The change in refractive index when the capture antibody binds the analyte is relatively small and so the SPR technique is limited to analytes that are large (ie. large proteins, viruses or whole cells). This factor means the system is sample solution dependent and is affected by non-specific binding especially with realistic sample solutions which may contain many large proteins or whole cells other than those of interest [42]. Another problem is the broadening of the resonance minimum (thus reducing angular resolution) caused by scattering from a rough immobilised or bound

protein layer [43]. To improve the performance of SPR sensors, a number of enhancements have been suggested such as the use of 'high refractive index labels', but suitable labels are not readily available, and their size and mass may unduly affect chemical kinetics. A more promising route is to use the enhanced evanescent field of a surface plasmon wave (~10 times more intense than the evanescent field for TIR) to excite fluorescent labels. Such enhanced excitation of fluorescence by SPR has been demonstrated previously [44] and the technique was used by *Attridge et al* [23] in an immunoassay for human chorionic gonadotropin (hCG) in serum which achieved a sensitivity of 240pM (a six-fold improvement on TIR).

### 2.6.3 Optical waveguides

Optical waveguide sensors were developed to improve on the performance of TIR and multiple-TIR sensors. Guided light is essentially in a resonant mode confined within the guide and so has a high associated field strength which gives rise to a high evanescent field strength outside the waveguide. The light also propagates (assuming a reflection model) at very high incident angles and, therefore, the evanescent field has a low penetration depth. The combination of a high evanescent field strength, low penetration depth and continuous interrogation (as opposed to discrete spots in TIR - see fig. 2.7) of the sensing surface should, in theory, improve the signal-to-background ratio of waveguide sensors over TIR systems. Waveguides can be fabricated by a large variety of methods borrowed from micro-electronics and thin-film fabrication techniques, but can be broadly classed into two categories: a) optical fibres; and b)

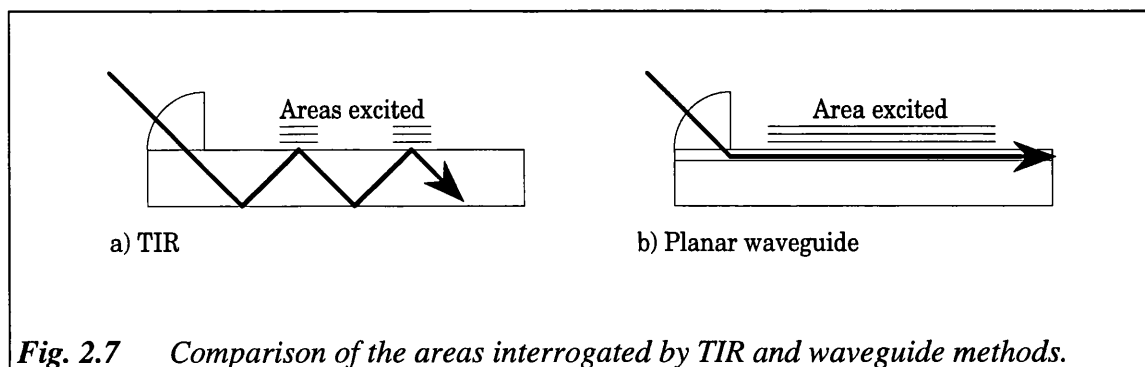
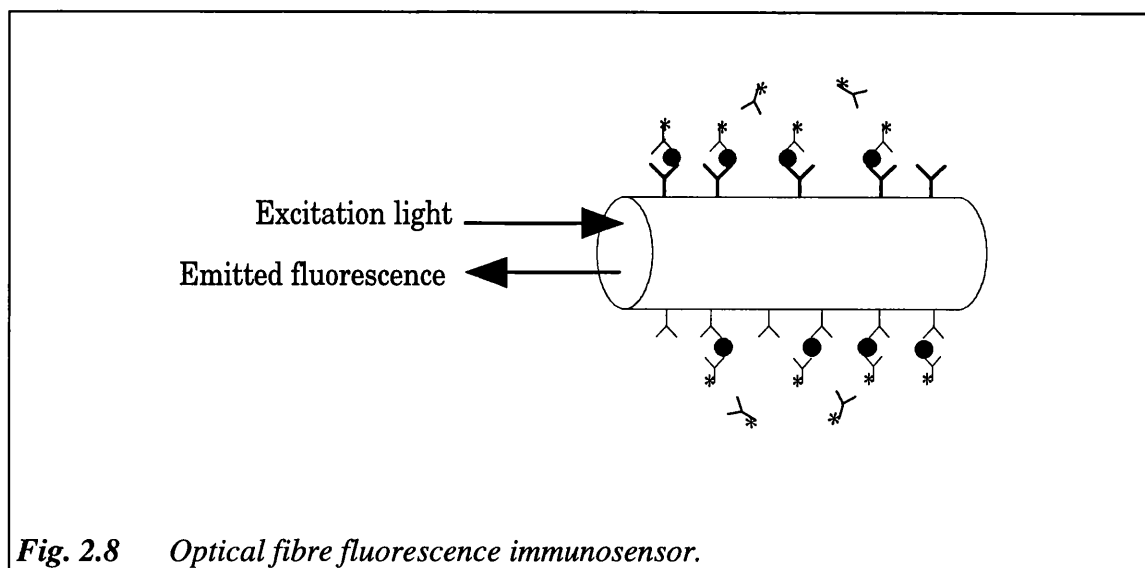


**Fig. 2.7** Comparison of the areas interrogated by TIR and waveguide methods.



planar waveguides.

### 2.6.3.1 Optical fibre immunosensors

The optical fibres used in evanescent field immunosensor devices are fabricated without a cladding layer or have their cladding removed so that the evanescent field of the guided light can directly interact with the bound layer (fig. 2.8). Optical absorption and fluorescence excitation techniques can be used but the latter gives much better sensitivities [36]. The full circumferential surface area of an optical fibre can be used for sensing but, because of the small diameters of optical fibres, the surface area available for immobilisation of the capture layer is limited, requiring the devices to have long active lengths (>10cm [45]). The surface area can be increased by using larger diameter fibres but this eventually leads to a TIR system and the advantages of high evanescent field strength are lost. Reference measurements cannot easily be incorporated onto the same length of fibre, and many current laboratory systems require a second length of fibre [46] or do not incorporate references. Efficient and reproducible coupling of light into the optical fibre is also a problem that could be the limiting factor concerning the commercial development of fibre sensors for the clinical diagnostics market where cheap, single-use disposable devices will dominate.

### 2.6.3.2 Planar waveguide immunosensors

Planar waveguides are usually thin-films of an optically dense medium on a suitable substrate of an optically rarer medium and can be fabricated by a wide variety of methods (ion-exchange [45], spin [46] and dip coating [47] from solution, chemical vapour deposition [48], sputtering [49], etc.). The choice of a suitable fabrication method for biosensor use will most likely be determined by cost. Planar guides, as with optical fibres, exhibit a high evanescent field strength and low penetration depth, but their planar geometry, greater surface area and more compact size and shape makes them more amenable as disposable immunosensor devices. A further advantage of planar waveguides is the possibility of surface patterning of the waveguide which would allow reference/calibration and multiple analyte measurements to be made on one device together with any optical signal processing that may be necessary [42, 50]. Cost of fabrication will limit the extent to which such ideas can be incorporated and thus, it is essential that cheap thin-film fabrication techniques are employed using materials that can be easily processed (ie. etching, photolithography, etc.).

Multiple analyte detection using patterned ion-exchanged waveguides has been demonstrated yielding a sensitivity down to  $0.1\mu\text{g/ml}$  ( $\sim 700\text{pM}$ ), but this included a washing step [51]. *Sloper et al* [50] have demonstrated the use of an indium phosphate monomode waveguide in an immunosensor for hCG (in serum) with a sensitivity of  $830\text{pM}$  giving an eight-fold improvement over a multiple internal reflection arrangement.

Waveguides can also be employed as direct sensors. *Lukosz et al* [52, 53] have fabricated, by an embossing technique, gratings in thin, sol-gel derived films that can be used as input and output waveguide couplers (see fig. 2.9). The efficiency of the couplers or the angle of incidence for maximum coupling of the light into the guide or the angle at which maximum light energy is coupled out of the guide is dependent on the properties of the material in direct contact with the grating coupler. Binding of antigen to a capture layer immobilised onto the grating can thus be detected. This technique has

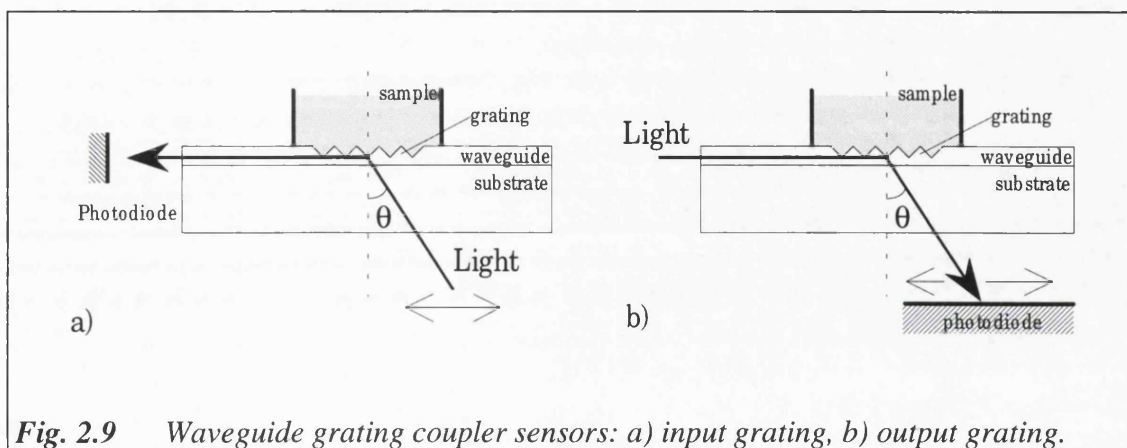


**Fig. 2.9** Waveguide grating coupler sensors: a) input grating, b) output grating.

not yielded a high sensitivity in experiments (4 - 5 nM) and theoretically is not expected to give better than 2nM performance [54]. However, a sensor based on the waveguide grating coupler is now being marketed [55].

A highly sensitive waveguide Mach-Zehnder interferometer technique, utilising a grating coupler with a claimed detection limit of 50pM has been described [56]. Considerable sample manipulation was required and the  $\text{Si}_3\text{N}_4$  waveguides on a thin silica film grown on a silicon wafer were fabricated by relatively expensive LPCVD and PECVD processes. The detection limit is somewhat ambiguous as there is no indication as to whether it was obtained by statistical analysis or if it was a one-off measurement.

However, the major drawback, as with optical fibers, is one of coupling the exciting light efficiently into the waveguide (coupling efficiency for TIR: ~80%, for thin-film waveguides: 5 - 25% [57]). Current laboratory systems use prism coupling techniques [58, 23, 40, 50] but these are not preferable for a commercial biosensor instrument where alternatives such as diffraction gratings will need to be used. The work by *Lukosz et al* [52-54] on diffraction grating waveguide couplers (fabricated using a simple embossing technique) on planar waveguides is promising, but problems still need to be addressed. For example, a large proportion of the light incident on a grating is transmitted straight through without being coupled into the guide, and film parameters (eg. thickness) and grating fabrication need to be tightly controlled to give reproducible coupling efficiencies.

#### 2.6.4 Sensitivities of direct and indirect sensing methods

The sensitivity of indirect sensing methods can be quoted simply as a molar analyte concentration. This is more difficult with direct sensing methods because the strength of the measured signal is highly dependent on the size of the analyte being quantified - the larger the analyte, the stronger the signal. Hence, it can be noticed in publications concerning direct methods that sensitivity figures are usually given in units such as mg/l, ng/cm<sup>2</sup>, etc.. It can thus be expected that the sensitivity offered by direct detection will be highly variable depending on the analyte being quantified. The sensitivity figures given in this chapter for direct sensing methods are based on the analyte that the researchers used in their experiments.

#### 2.6.5 The fluorescence capillary fill device

The competitive and sandwich indirect immunoassays described in section 2.2 require the addition of a labelled reagent to the sample solution. However, because immunosensors are likely to be used by inexperienced personnel, sample manipulation needs to be kept to a minimum and, ideally, the user should not be required to measure

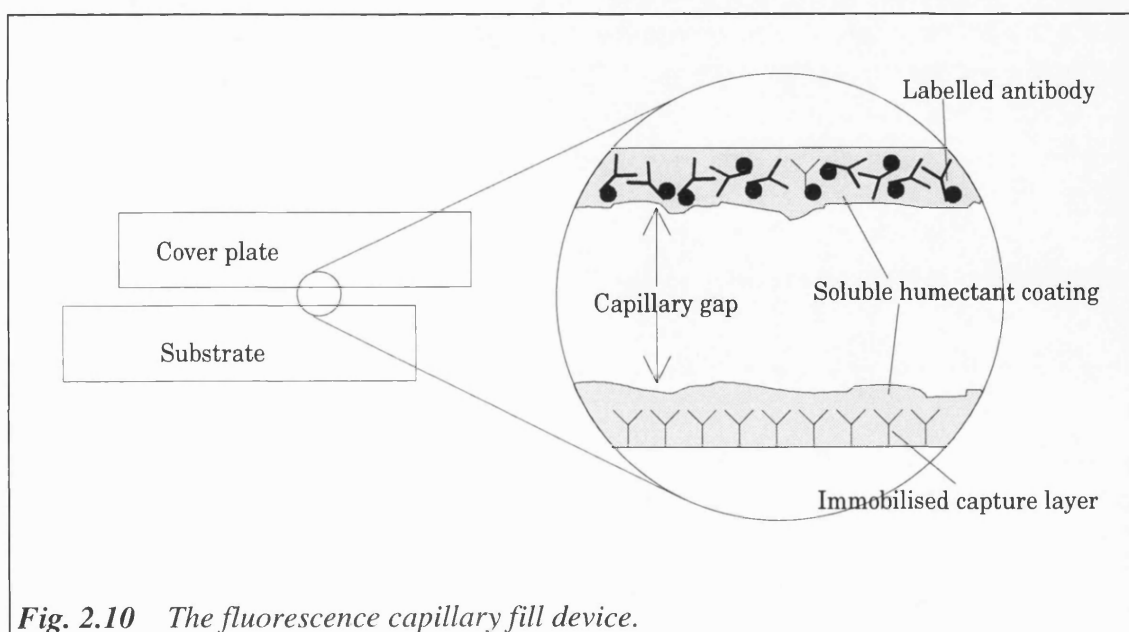


**Fig. 2.10** *The fluorescence capillary fill device.*

sample volumes accurately or to add a reagent. This particular problem was addressed by *Badley et al* [35] in their fluorescence capillary fill device (FCFD) [35, 59] shown in fig. 2.10. A drop of the sample solution placed at one end of the capillary gap (approximately 100 $\mu$ m wide) will fill the device by capillary action and, because the width of the capillary gap can be tightly controlled, the volume of the sample solution in the device is well defined. The capture antibody can then be immobilised on one of the glass plates and preserved by depositing a soluble humectant (eg. sucrose) layer, while on the opposite glass plate, a humectant layer containing the free labelled reagent can be deposited. When the sample solution is added, the humectant layer dissolves releasing the labelled reagent into solution. This particularly elegant system appears reagentless to the user who is simply required to add the relevant sample solution.

## 2.7 ENHANCING EVANESCENT FIELD IMMUNOSENSORS

The limitations of direct detection of analyte-antibody binding (ie. non-specific binding, high sample solution dependency), has led many workers to concentrate on evanescent field fluorescence excitation techniques. However, the performance (in terms of sensitivity) is still not good enough for many applications especially at very low analyte concentrations and, thus, many workers are currently investigating possible enhancements to existing methods.

### 2.7.1 Signal strength enhancement

A major problem of evanescent field fluorescence immunosensors is low signal strength, which requires rather sophisticated detection devices such as photomultiplier tubes, lock-in amplifiers, etc.. Although the reliance on PMT's for fluorescence detection is unlikely to be avoided, an increase in signal strength would decrease the significance of the electrical noise contribution from the PMT and the amplifiers. Possible improvements are:

- increasing the intensity of the exciting light by using lasers. This would be accompanied by an increase in the instrument cost - a cost that could be minimised by using semiconductor laser diodes. Increased scattering of the exciting light may offset any signal strength improvements.
- maximising the exciting light input coupling efficiency. This is a problem for waveguide sensors despite their sensitivity improvements over TIR systems.
- use high quantum yield fluorophore labels, eg. phycobiliproteins [60].
- maximising emitted fluorescence collection [61].

### 2.7.2 Signal-to-background ratio enhancement

Background signals (eg. PMT dark current, ambient light contamination) are relatively constant but become significant at weak signal levels (ie. at low analyte concentrations). The main sources of background signals are:

- fluorescence excited from unbound labelled reagent in the bulk of the sample solution [36]. Minimising this requires a reduction in the penetration depth of the evanescent field (by using high refractive index substrates or waveguides). Other techniques are polarisation [62] and time [63] resolved fluorimetry.
- scattering of the exciting light. The scattered exciting light may excite fluorescence in the bound layer and the bulk solution or may enter the PMT. Minimising scattering will require good device fabrication. A problem is that the immobilised antibody layer acts as an inherent scattering media [64], and this may be the limiting factor in the sensitivity of evanescent field sensors. Efficient filtering of the exciting light requires the excitation and emission wavelengths of the fluorophore to be well separated (Stokes' shift). The choice of fluorophores with a high Stokes' shift or the use of fluorescent

energy transfer techniques address this factor [65].

- phosphorescence from impurities in the glass substrate. Appropriate choice of a suitable substrate can avoid this problem but may add to the sensor cost.

### 2.7.3 Signal-to-noise ratio enhancement

The sensor precision and sensitivity are both dependent on the signal-to-noise ratio (see fig. 2.3), where noise can be defined as the signal variations between measurements at the same analyte concentration. An increase in this ratio would improve both the precision and the sensitivity. Signal-to-noise ratio can be improved by:

- increasing both the signal levels and the signal-to-background ratio.
- tightly controlled fabrication methods to minimise variations between different devices and ensure to uniformity.
- appropriate selection of reference and calibration measurements. A major source of variability in measurements is the biological binding layer and the analyte-antibody binding reaction which can often be sample solution dependent or be affected by non-specific binding - appropriate referencing measurements can compensate for these variations. Good choice of references can also compensate for variations caused by device handling (eg. fingerprints).

The immobilisation of the capture layer is another important factor in improving

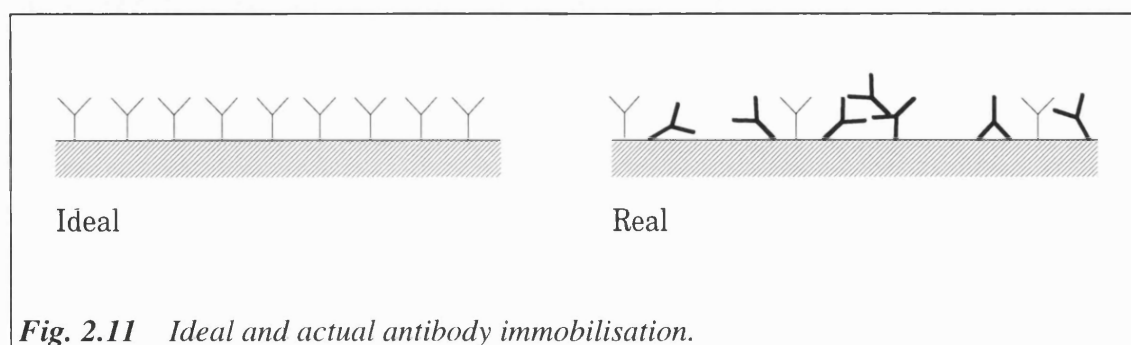


**Fig. 2.11** Ideal and actual antibody immobilisation.

sensor performance. Current immobilisation techniques can leave as little as 10% [50] of the possible sensor surface area with active antibodies (see fig. 2.11) which severely restricts the dynamic range because of the limited number of analyte molecules that can bind to the capture layer. The immobilisation may also not be uniform - instead of a uniform single layer of antibodies, there may be localised aggregates (fig. 2.11). Work on improving the immobilisation techniques is being pursued [66, 67].

Thin film waveguides provide a particular advantage in that it is possible, by patterning the film (using etching, photolithography, etc.), to incorporate a series of essentially separate waveguides onto the same sensor. This would allow the incorporation of reference measurements or multiple analyte testing on a single sample. It would also allow some optical signal processing structures, such as interferometers, directional couplers and optical gratings, to be incorporated. The inclusion of optical gratings on the sensor device would not only enable light coupling without the use of prisms, but by using gratings for wavelength selection, light reflection, etc., a host of optical signal processing can be performed on the device itself.

## **2.8 CONCLUSIONS**

This chapter has looked at current biosensor technology, its limitations and possible improvements. The emphasis has been on evanescent field immunosensing, as this is likely to provide the performance required for high sensitivity sensors at reasonable instrument prices. There are many problems, both optical and biological, to be solved to improve the sensitivity of evanescent field sensors and the following chapter (chapter 3) suggests the use of a multi-layer thin film sensor to improve the signal levels and signal-to-background ratios of current TIR sensors.

## REFERENCES

- 1 RAWSON D M, WILLMER A J, TURNER A P F, Whole-cell biosensors for environmental monitoring, *Biosensors*, 1989, 4, 299-311.
- 2 RECHNITZ G A, HO M Y, Biosensors based on cell and tissue material, *Journal of Biotechnology*, 1990, 15, 201-218.
- 3 BEATTIE K *et al*, Genosensor technology, *Clinical Chemistry*, 1993, 39(4), 719-722.
- 4 KIEFER H *et al*, Biosensors based on membrane transport proteins, *Biosensors & Bioelectronics*, 1991, 6, 233-237.
- 5 NIKOLELIS D P *et al*, Ion permeability through bilayer lipid membranes for biosensor development: control by chemical modification of interfacial regions between phase domains, *Analyst*, 1991, 116, 1221-1226.
- 6 KAUFMANN J M, GUILBAULT G G, Enzyme electrode biosensors: theory and applications, in SUELTER C H ed., Bioanalytical applications of enzymes, Volume 36, *John Wiley & Sons Inc., New York*, 1992, 63-113.
- 7 GHINDILIS A L *et al*, A new approach to the construction of potentiometric immunosensors, *Biosensors & Bioelectronics*, 1992, 7, 301-304.
- 8 CATTY D, Properties of antibodies and antigens, in CATTY D ed., *Antibodies. Volume 1: a practical approach*, IRL Press Ltd., Oxford, 1988, 1st ed., 7-18.
- 9 EDWARDS R, Radiolabelled immunoassay, in PRICE C P, NEWMAN D J eds., *Principles and practice of immunoassay*, Stockton Press, New York, 1991, 1st ed., 265-294.
- 10 ROITT I, BROSTOFF J, MALE D, *Immunology*, Gower Medical Publishing Ltd., London, 1988, 1st ed., pp5.1-5.10, pp8.4.
- 11 BROWN G, LING N R, Murine monoclonal antibodies, in CATTY D ed., *Antibodies. Volume 1: a practical approach*, IRL Press Ltd., Oxford, 1988, 1st ed., 81-104.
- 12 ARVIEUX J, WILLIAMS A F, Immunoaffinity chromatography, in CATTY D ed., *Antibodies. Volume 1: a practical approach*, IRL Press Ltd., Oxford, 1988, 1st ed., 113-136.
- 13 SIDDLE K, Properties and applications of monoclonal antibodies, in COLLINS W P ed., *Alternative immunoassays*, John Wiley & Sons Ltd., Chichester, 1985, 1st ed., 13-38.
- 14 HART H E, GREENWALD E D, Scintillation proximity assay (SPA) - a new method of immunoassay, *Molecular Immunology*, 1979, 16, 265-267.
- 15 JENKINS S H, Homogeneous enzyme immunoassay, *Journal of Immunological Methods*, 1992, 150, 91-97.
- 16 LAKOWICZ J R, MALIWAL B, OZINSKAS A, THOMPSON R B, Fluorescence lifetime energy-transfer immunoassay quantified by phase-modulation fluorometry, *Sensors and Actuators B*, 1993, 12, 65-70.
- 17 POLLEMA C H *et al*, Sequential injection immunoassay utilizing immunomagnetic beads,

- Analytical Chemistry*, 1992, **64**, 1356-1361.
- 18 **YAMAMOTO N Y et al**, Antigen-antibody reaction investigated with use of a chemically modified electrode, *Clinical Chemistry*, 1980, **26(11)**, 1569-1572.
  - 19 **LUKOSZ W**, Principles and sensitivities of integrated optical and surface plasmon sensors for direct affinity sensing and immunosensing, *Biosensors & Bioelectronics*, 1991, **6**, 215-225.
  - 20 **GIZELI E et al**, A Love plate biosensor utilising a polymer layer, *Sensors & Actuators B*, 1992, **6**, 131-137.
  - 21 **TAYLOR R F, MARENCHIC I G, SPENCER R H**, Antibody- and receptor-based biosensors for detection and process control, *Analytica Chimica Acta*, 1991, **249**, 67-70.
  - 22 **CUSH R et al**, The resonant mirror: a novel optical biosensor for direct sensing of biomolecular interactions Part I: principles of operation and associated instrumentation, *Biosensors & Bioelectronics*, 1993, **8**, 347-353.
  - 23 **ATTRIDGE J W et al**, Sensitivity enhancement of optical immunosensors by the use of a surface plasmon resonance fluoroimmunoassay, *Biosensors & Bioelectronics*, 1991, **6**, 201-214.
  - 24 **EKINS R**, Immunoassay design and optimisation, in **PRICE C P, NEWMAN D J eds.**, Principles and practice of immunoassay, *Stockton Press, New York*, 1991, 1st ed., 96-153.
  - 25 **PLOMER M, GUILBAULT G G, HOCK B**, Development of a piezoelectric immunosensor for the detection of enterobacteria, *Enzyme and Microbial Technology*, 1992, **14**, 230-235.
  - 26 **WALTON P W, BUTLER M E, O'FLAHERTY M R**, Piezoelectric-based biosensors, *Biochemical Society Transactions*, 1991, **19**, 44-48.
  - 27 **HENDRY S P, HIGGINS I J, BANNISTER J V**, Amperometric biosensors, *Journal of Biotechnology*, 1990, **15**, 229-238.
  - 28 **RISHPON J et al**, Immuno-electrodes for the detection of bacteria, in **MATHEWSON P R, FINLEY J W eds.**, Biosensor design and application, *ACS Symposium Series 511, American Chemical Society, Washington DC*, 1992, 59-72.
  - 29 **BLACKBURN G F**, Chemically sensitive field-effect transistors, in **TURNER A P F, KARUBE I, WILSON G S eds.**, Biosensors, *Oxford University Press, Oxford*, 1987, 1st ed., 481-530.
  - 30 **COLLINS S, JANATA J**, A critical evaluation of the mechanism of potential response of antigen polymer membranes to the corresponding antiserum, *Analytica Chimica Acta*, 1982, **136**, 93-99.
  - 31 **HEMMILA I**, Fluoroimmunoassays and immunofluorometric assays, *Clinical Chemistry*, 1985, **31**, 359-70.
  - 32 **BRONSTEIN I et al**, Chemiluminescent assay of alkaline phosphatase applied in an ultrasensitive enzyme immunoassay of thyrotropin, *Clinical Chemistry*, 1990, **35**, 1441-1446.
  - 33 **MARCHAND J et al**, Synthesis of new hydrophylic microspheres: optimized carriers for microparticle-enhanced nephelometric immunoassays, *Biopolymers*, 1992, **32**, 971-980.
  - 34 **KRONICK M N, LITTLE W A**, A new immunoassay based on fluorescence excitation by internal reflection spectroscopy, *Journal of Immunological Methods*, 1975, **8**, 235-240.

- 35 **BADLEY R A *et al***, Optical biosensors for immunoassays: the fluorescence capillary fill device, *Philosophical Transactions of the Royal Society of London B*, 1987, **316**, 143-160.
- 36 **SUTHERLAND R M *et al***, Optical detection of antibody-antigen reactions at a glass-liquid interface, *Clinical Chemistry*, 1984, **30(9)**, 1533-1538.
- 37 **SUTHERLAND R M *et al***, A disposable biosensor based on total internal reflection fluorescence, in **SCHMID R D ed.**, Biosensors international workshop 1987, *GBF Monographs*, VCH, New York, 1987, **10**, 305-306.
- 38 **HALL E A H**, Biosensors, *Open University Press, Milton Keynes*, 1990, 1st ed., pp327.
- 39 **CULLEN D C, BROWN R G W, LOWE C R**, Detection of immuno-complex formation via surface plasmon resonance on gold-coated diffraction gratings, *Biosensors*, 1987/88, **3**, 211-225.
- 40 **DANIELS P B *et al***, Surface plasmon resonance applied to immunosensing, *Sensors and Actuators*, 1988, **15**, 11-18.
- 41 **ANONYMOUS**, Label-free biosensor technology visualizes biomolecular interactions in real time, *Biosensors & Bioelectronics*, 8(2), xi-xiv.
- 42 **FLANAGAN M T, SLOPER A N, ASHWORTH R H**, From electronic to opto-electronic biosensors: an engineering view, *Analytica Chimica Acta*, 1988, **213**, 23-33.
- 43 **FLANAGAN M T, PANTELL R H**, Surface plasmon resonance and immunosensors, *Electronics Letters*, 1984, **20(23)**, 968-970.
- 44 **BENNER E, DORNHAUS R, CHANG R K**, Angular emission profiles of dye molecules excited by surface plasmon waves at a metal surface, *Optics Communications*, 1979, **30**, 145-149.
- 45 **RAMASWAMY R V, SRIVASTAVA R**, Ion-exchanged glass waveguides: a review, *Journal of Lightwave Technology*, 1988, **6(6)**, 984-1001.
- 46 **SLOPER A N, FLANAGAN M T**, Novel iron phosphate optical waveguides fabricated by low temperature process, *Electronics Letters*, 1988, **24(6)**, 353-355.
- 47 **HEWAK D W, LIT J Y W**, Standardization of a dip-coating procedure for optical thin films prepared from solution, *Canadian Journal of Physics*, 1988, **66**, 861-867.
- 48 **KERN W, BAN V S**, Chemical vapour deposition of inorganic thin films, in **VOSSEN J L, KERN W eds.**, Thin film processes, *Academic Press, New York*, 1978, 1st ed., 258-320.
- 49 **YIN Z, GARSIDE B K**, Low-loss GeO<sub>2</sub> optical waveguide fabrication using low deposition rate rf sputtering, *Applied Optics*, 1982, **21**, 4324-4328.
- 50 **SLOPER A N, DEACON J K, FLANAGAN M T**, A planar indium phosphate monomode waveguide evanescent field immunosensor, *Sensors and Actuators B*, 1990, **1**, 589-591.
- 51 **ZHOU Y *et al***, Multichannel evanescent fluorescence immunosensing using potassium and sodium ion-exchanged patterned waveguides, *Journal of Molecular Electronics*, 1991, **7**, 135-149.
- 52 **LUKOSZ W *et al***, Output grating couplers on planar optical waveguides as direct immunosensors, *Biosensors & Bioelectronics*, 1991, **6**, 227-232.
- 53 **NELLEN Ph M, LUKOSZ W**, Model experiments with integrated optical input grating couplers as

- direct immunosensors, *Biosensors & Bioelectronics*, 1991, 6, 517-525.
- 54 NELLEN Ph M, LUKOSZ W, Integrated optical input grating couplers as chemo- and immunosensors, *Sensors and Actuators*, 1991, B1, 285-295.
- 55 Manufactured by *Artificial Sensing Instruments (ASI) AG*, Austria.
- 56 HEIDEMAN R G, KOOYMAN R P H, GREVE J, Performance of a highly sensitive, optical waveguide Mach-Zehnder interferometer immunosensor, *Sensors and Actuators B*, 1993, 10, 209-217.
- 57 HUNSBERGER R G, Springer series in optical sciences: Integrated optics: theory and technology, *Springer-Verlag, New York*, 1984, 2nd ed., 88-105.
- 58 TAMIR T, Beam and waveguide couplers, in TAMIR T ed., Topics in applied physics Volume 7: Integrated optics, *Springer-Verlag, New York*, 1979, 2nd ed., 84-134.
- 59 ROBINSON G A *et al*, The fluorescent capillary fill device, *Sensors and Actuators B*, 1993, 11, 235-238.
- 60 KRONICK M N, The use of phycobiliproteins as fluorescent labels in immunoassay, *Journal of Immunological Methods*, 1986, 92, 1-13.
- 61 KOMIVES C, SCHULTZ J S, Fiber-optic fluorometer signal enhancement and application to biosensor design, *Talanta*, 1992, 39(4), 429-441.
- 62 RHYS WILLIAMS A T, Fluorescence polarisation immunoassay, in COLLINS W P ed., Complementary immunoassays, *John Wiley & Sons Ltd, Chichester*, 1988, 1st ed., 135-147.
- 63 DIAMANDIS E, Immunoassays with time-resolved fluorescence spectroscopy: principles and applications, *Clinical Biochemistry*, 1988, 21, 139-150.
- 64 SLOPER A N, FLANAGAN M T, Scattering in planar surface waveguide immunosensors, *Sensors and Actuators B*, 1993, 11, 537-542.
- 65 GLAZER A N, STRYER L, Fluorescent tandem phycobiliprotein conjugates: emission wavelength shifting by energy transfer, *Biophysical Journal*, 1983, 43, 383-386.
- 66 ALARIE J P, SEPANIAK M J, VO-DINH T, Evaluation of antibody immobilization techniques for fiber optic-based fluoroimmunosensing, *Analitica Chimica Acta*, 1990, 229, 169-176.
- 67 AHLUWALIA A *et al*, A comparative study of protein immobilization techniques for optical immunosensors, *Biosensors & Bioelectronics*, 1991, 7, 201-214.
- 68 CASTRACANE C E *et al*, Particle-counting immunoassay of human somatotropin, *Clinical Chemistry*, 1984, 30, 672-676.
- 69 GUILBAULT G G, HOCK B, SCHMID R, A piezoelectric immunobiosensor for atrazine in drinking water, *Biosensors & Bioelectronics*, 1992, 7, 411-419.
- 70 WATSON L D *et al*, A microelectronic conductimetric biosensor, *Biosensors*, 1987/88, 3, 101-115.
- 71 GARDIES F, MARTELET C, COLIN B, MANDRAND B, Feasibility of an immunosensor based upon capacitance measurements, *Sensors and Actuators*, 1989, 17, 461-464.

- 72 **FLANAGAN M T, CARROLL N J**, Thin-film antimony-antimony-oxide enzyme electrode for penicillin determination, *Biotechnology and Bioengineering*, 1986, **XXVIII**, 1093-1099.
- 73 **MOSCONE D, PASINI M, MASCINI M**, Subcutaneous microdialysis probe coupled with glucose biosensor for *in vivo* continuous monitoring, *Talanta*, 1992, **39(8)**, 1039-1044.

## CHAPTER 3

### PROJECT OBJECTIVES AND MULTI-LAYER THIN FILM SENSORS

*This chapter defines the project, the reasons and objectives, and states the case for the use of multi-layer thin film optically resonant structures in immunosensing systems. The theory of optical resonance within multi-layer thin films is discussed in chapter 4, whereas this chapter concentrates on the merits of using thin films, the materials available and the fabrication techniques.*

#### 3.1 PROJECT OBJECTIVES

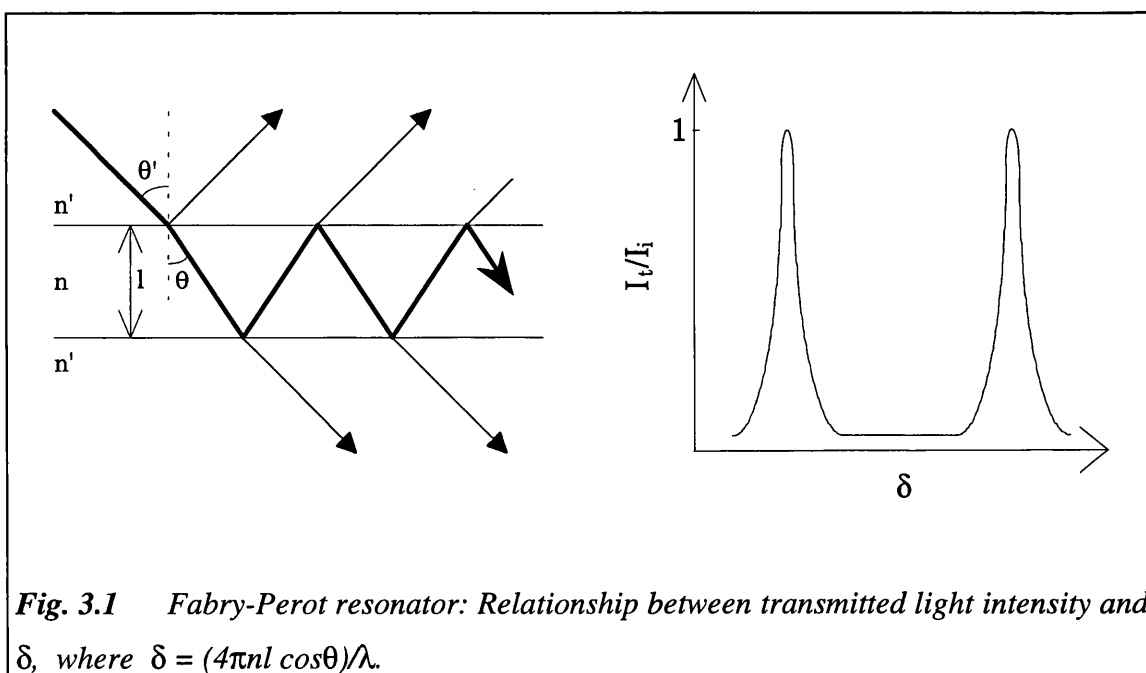
The total internal reflection (TIR) immunoassay of *Kronick and Little* [1] has a distinct advantage - simplicity. The evanescent field of a single totally internally reflected light beam is used to excite fluorescence. The drawbacks are the low signal levels giving rather poor sensitivities and only a discrete interrogation of the sensor surface (chapter 2, fig. 2.7). The signal levels could be improved by increasing the exciting light intensity but only at increased instrument cost, with the possibility that increased scattering of the exciting light and excitation of phosphorescence may offset any signal level improvements. Broadening of the exciting beam would allow a continuous interrogation of the sensing surface, but the decreased evanescent field strength may actually reduce signal levels. Waveguide sensors [2] improve the signal strength, and thus the sensitivities of evanescent field optical sensors by using an intense evanescent field and continuous sensor surface interrogation. Unfortunately, waveguide sensors suffer from a poor and variable exciting light input coupling efficiency (5 - 25 % [3]). High efficiency (80%) input coupling is possible [4] but the costs of incorporating such a system into a cheap, disposable sensor device will probably be too great to be

commercially viable.

The objective of this project was to design an evanescent field fluorescence optical immunosensing system that combined the advantages of a single spot TIR sensor (simplicity and high exciting light input coupling efficiency) together with the advantages of waveguide sensors (high signal levels and continuous sensor surface interrogation). Thus, the sensor was required to improve the signal-to-background ratios of current TIR sensors with a corresponding improvement in sensor sensitivity. The sensor is aimed mainly at medical applications and is likely to be a single use disposable device. Therefore, fabrication costs (both instrument and sensor) need to be kept down by using cost-effective fabrication techniques and inexpensive materials. Increased costs can be offset if a range of analytes can be tested on a single device.

### 3.2 OPTICALLY RESONANT MULTI-LAYER THIN FILM DEVICES

Optically thin films (films with a thickness of the order of the wavelength of light)



have been in use for some time: for example in interference filters [5], anti-reflection coatings [6], optical waveguides [2], Fabry-Perot resonators [7], etc.. Considering the Fabry-Perot resonator of fig. 3.1, it is possible, by choosing appropriate refractive indices, to excite a resonant optical wave confined within the thin film. Note that although

$$I = R + T$$

where  $I$ ,  $R$  and  $T$  are the incident, reflected and transmitted light intensities respectively, the light intensity within the thin film may be many times greater than the incident light intensity.

The example of fig. 3.1 transmits light but, with modifications, a resonant system that reflects the incident light can be designed. This is preferable in an evanescent field fluorescence sensor system to prevent light transmission through the sample solution. Such a reflective resonant system is illustrated in fig. 3.2. The incident light in the substrate is reflected off a low refractive index 'buffer' layer but some light energy is coupled into the high refractive index 'waveguide' layer by the penetration of the

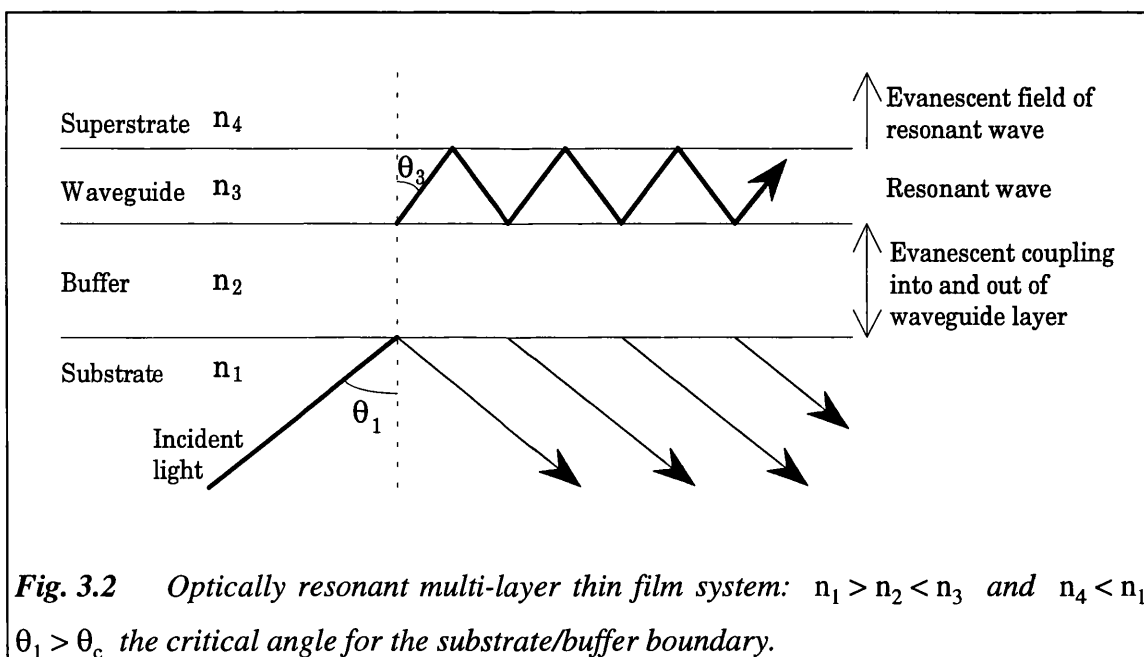


**Fig. 3.2** Optically resonant multi-layer thin film system:  $n_1 > n_2 < n_3$  and  $n_4 < n_1$   
 $\theta_1 > \theta_c$  the critical angle for the substrate/buffer boundary.

evanescent field into the waveguide layer. The waveguide layer is sandwiched between two low refractive index media (the superstrate and the buffer layer), such that light energy coupled into the waveguide layer is confined and, thus, a resonant wave can be excited in this layer. The term 'waveguide' layer is used as there are similarities with a waveguide system: a) the evanescent coupling of light energy into the 'waveguide' layer is similar to waveguide prism coupling techniques [4]; b) waveguiding probably occurs over short distances but all the light energy coupled into the waveguide layer is coupled back out to form the reflected wave. Light transmission into the superstrate is prevented by choosing appropriate refractive indices and by keeping the angle of incidence greater than the critical angle for total internal reflection (see fig. 3.2).

The resonant wave confined within the waveguide layer has the characteristics of a high field strength and thus a high intensity. This means that the evanescent field (in the superstrate layer) will have a correspondingly high field at resonance. The angle of incidence for resonance, as with the Fabry-Perot resonator, is dependent on film

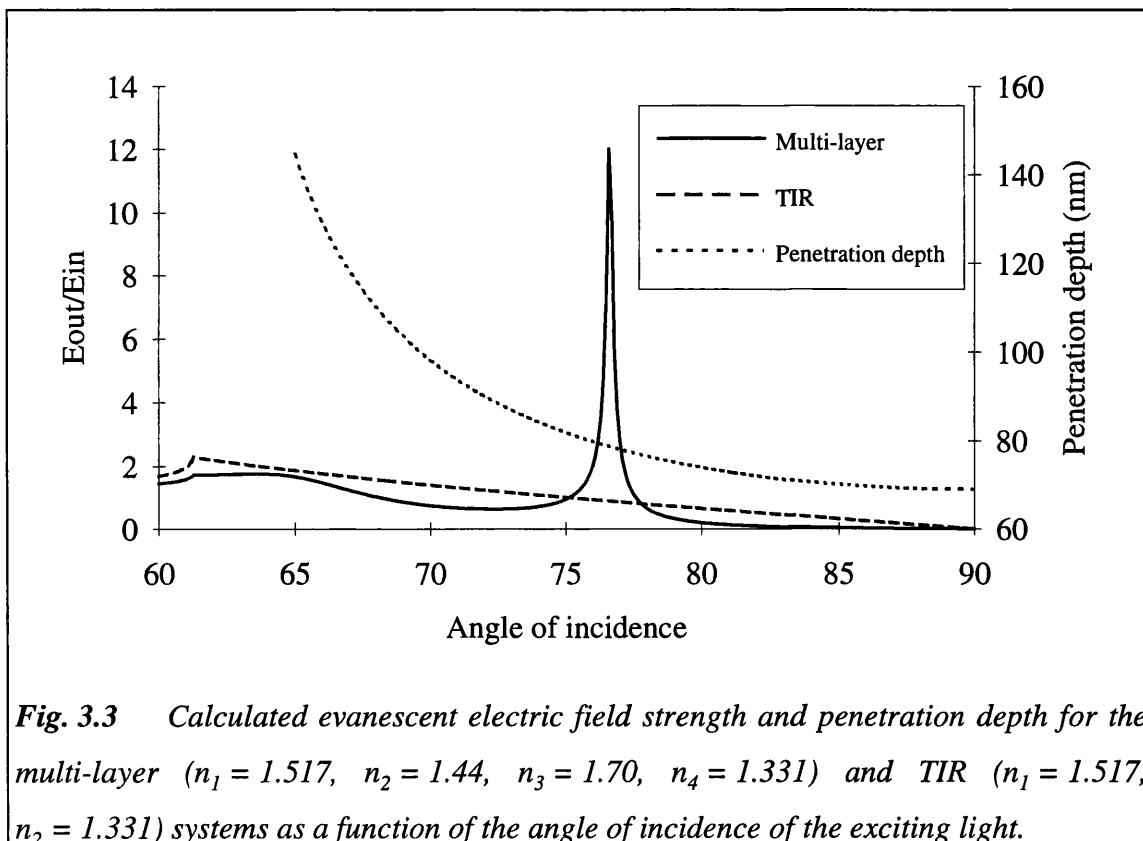


**Fig. 3.3** Calculated evanescent electric field strength and penetration depth for the multi-layer ( $n_1 = 1.517$ ,  $n_2 = 1.44$ ,  $n_3 = 1.70$ ,  $n_4 = 1.331$ ) and TIR ( $n_1 = 1.517$ ,  $n_2 = 1.331$ ) systems as a function of the angle of incidence of the exciting light.

thicknesses and refractive indices, and the wavelength of the incident light. The electromagnetic theory and modelling of the multilayer system will be discussed in later chapters but fig. 3.3 illustrates how the evanescent electric field strength in the superstrate layer of the system of fig. 3.2 behaves with the angle of incidence of the exciting light. The evanescent field of a TIR system is also shown for comparison together with the variation of the penetration depth of the evanescent field with angle of incidence. Note that for the multilayer and TIR systems considered, the penetration depths of the evanescent field are the same. It can be seen that at the angle of incidence for resonance, the evanescent field strength is greatly enhanced, especially over that of the TIR system. The maximum evanescent field strength for the TIR system is at the critical angle where the penetration depth is very high, whereas the resonant field enhancement for the multilayer system occurs at a much lower penetration depth. The combination of a high evanescent field strength and low penetration depth should improve the signal-to-background characteristics of the multilayer sensor over the TIR sensor in a manner similar to that of the waveguide fluorescence sensor [2].

The major drawback with the multilayer system is likely to be one of cost. The resonance in the multilayer system is very sharply dependent on the angle of incidence and other parameters such as film thickness, thus making the efficient coupling of the exciting light into the resonant mode difficult. Hence, tight control of thin film fabrication and instrument design would be required, increasing the instrument and sensor device manufacturing cost. However, if sufficient field enhancement is obtained, the instrument can be designed such that the exciting light is incident over a small range of angles, thus relaxing some of the fabrication requirements. A second problem is the requirement of at least two thin films to obtain the required evanescent field strength enhancement. However, by suitably patterning the thin films it would be possible to incorporate reference or calibration measurements, or to perform multiple-analyte measurement [2] on the same device. This would offset some of the costs of production but inexpensive thin film fabrication techniques would still be required.

### **3.3 THIN FILM FABRICATION METHODS AND MATERIALS**

Thin film materials for application in biosensors need to have the following characteristics:

- low optical absorption at the wavelengths of interest (>500nm).
- chemical resistance to the solutions likely to be used in the biosensor.
- impermeability to the solutions to prevent sample solution dependence.
- immobilisation of biomolecules on the film surface should be possible.
- a low tendency for non-specific binding of biomolecules on the film surface.

The thin film fabrication methods should:

- give reproducible film characteristics (eg. refractive index, thickness, etc.).
- allow easy patterning of the film surface (eg. for the incorporation of grating couplers, multiple analyte detection, integrated optical devices etc.). This will require materials that lend themselves easily to processing methods such as photolithography and embossing.

Finally, an immunosensor device will most likely be a single use, disposable device and as such will require both inexpensive materials and fabrication techniques.

#### **3.3.1 Fabrication techniques**

**Sputtering.** The sputtering process can be used to grow thin films from a wide variety and mixture of materials allowing fine control over the thin film characteristics. Generally, the technique can produce very pure, durable, uniform and optically low loss films [8] with a wide range of refractive indices. However, the process is expensive, requiring high vacuum pressures, high processing and annealing temperatures to obtain good quality films. Also, due to equipment constraints, large batch production, which

would reduce fabrication costs, is not possible.

**Ion-exchange.** The refractive index of a substrate can be modified by the introduction of various ions in exchange for ions already present in the crystal structure of the substrate. This can be done by immersing the substrate in a molten bath (temperatures required are dependent on the salt used but are typically 200 - 400 °C) containing the ions (eg. Li<sup>+</sup>, Na<sup>+</sup>, Al<sup>3+</sup>, K<sup>+</sup>, Ag<sup>+</sup> etc.) that need to be incorporated into the substrate [9]. The ion exchange is assisted by applying an electric potential across the molten bath/substrate interface. The ion exchange process produces a graded index profile waveguide but the refractive index increment obtained is very small (~0.1) and as such is unsuitable for resonant multilayer devices where a much greater refractive index difference would be required.

**Chemical Vapour Deposition (CVD).** The CVD process is widely used in micro-electronics because of the flexibility the process offers in terms of chemical composition, and thin film characteristics. The process can be used to deposit films of silica, silica-titania, alumina, etc., as well as more conventional electronic films such as GaAlAs. High processing temperatures are again required (600 - 900 °C), but the CVD process is better suited to large scale production than the sputtering process. However, the CVD process is probably still too expensive for general use in biosensor device fabrication.

**Dip coating.** The substrate is immersed into a solution of the material that is to be deposited and withdrawn at a controlled rate, the rate of withdrawal determining the film thickness [10]. This process is very low cost and can be used to deposit on relatively large substrates allowing further cost reductions. However, the technique is limited to materials or precursors of the required material that can be dissolved in a suitable solvent. It is also difficult to control accurately the film thickness or uniformity and usually annealing of the dried film is required (at varying temperatures depending on the deposited material) to give reproducible film characteristics. The technique, nevertheless, has been used successfully to produce a commercially viable sensor

device [11].

**Spin coating.** A solution of the material to be deposited can be placed on a substrate and spun off to leave a thin coating which can be dried and cured to give the required thin film, with the thickness of the thin film being inversely proportional to the spin speed [12]. Although not as cost-effective as dip coating, the spin coating technique of fabricating thin films offers greater control over film thickness and uniformity. However, as with dip coating, the technique is limited to soluble materials and the processing of large substrate sizes is limited to some extent by the stresses encountered by the substrate during spinning. Spin coating was the technique used to deposit the thin films for the sensor devices described in this thesis, although dip coating techniques could also have been used.

Dip and spin coating techniques are the most cost-effective and probably the most appropriate techniques for thin film fabrication for disposable biosensor devices. CVD may produce more uniform films but the technique is unlikely to be suitably cost effective. The following section will look at some materials for thin film fabrication by dip and spin coating methods.

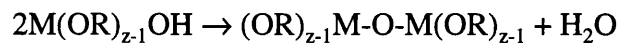
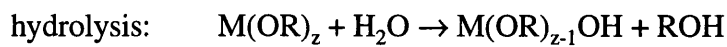
### **3.3.2 Materials**

**Polymer films.** Polymer films can be deposited using the inexpensive dip and spin coating processes [13] and can be easily patterned by etching with various solvents. However, it may be difficult to control the thickness and uniformity of films over large surface areas, which would make the incorporation of integrated optical components (eg. gratings) difficult [14].

#### **3.3.2.1 Sol-gel films.**

The sol-gel process involves the hydrolysis and condensation of metal alkoxide

compounds to form inorganic metal oxide polymers [15]. The metal alkoxide is usually dissolved in an alcoholic solvent and the hydrolysis is initiated by the addition of water under the required pH conditions, after which the reaction proceeds spontaneously. The actual process is complex with several steps being involved in both the hydrolysis and condensation reactions and additives are usually required to control the formation of the metal oxide polymers [16]. However, the basic reactions can be simplified as follows [15] (where M represents a metal or silicon and R represents an alkyl group):



The final structure of the inorganic polymers depends on the alkyl group, the pH and the molar ratio of H<sub>2</sub>O:M. These factors can be used to control the properties of the resulting metal oxide.

The sol-gel technique has been used to produce bulk glasses [17] and optical fibres as well as thin films [10, 15, 18, 19] on a variety of substrates such as metals, glasses and silicon. Considering optical applications, the two oxides of most interest that can be easily synthesised by the sol-gel process are silica and titania which have been used in the fabrication of anti-reflection coatings [18] and interference filters [19]. This is because both materials are transparent in the visible region and high quality thin films can be obtained by the sol-gel route. In addition, the two materials can be mixed in varying molar ratios to give refractive indices in the range 1.4 to 1.9 [10]. Sol-gel silica thin films were used as the low refractive index buffer layer in the multi-layer devices that are discussed in this thesis.

The major advantage of the sol-gel process is the flexibility that it offers. The sol-gel mixture is initially a solution which allows the easy incorporation of dopants into the finished glass. This, combined with the fact that many sol-gel mixtures can be cured at temperatures from room temperature to over 900°C, has allowed a wide range of

dopants to be used, from pH sensitive dyes [20] and enzymes [21] (which will be destroyed at high temperatures) to laser dye materials [22]. A sol-gel film remains pliable immediately after deposition and before it is dried or cured thus allowing surface patterning through embossing - a technique that has been used successfully to fabricate diffraction gratings in silica/titania waveguides [23]. There is also a cost advantage over other thin-film fabrication techniques such as CVD and sputtering, as the sol-gel process allows cheaper spin and dip coating techniques to be employed whilst still giving comparable thin-film qualities and properties [24].

The major disadvantage with the sol-gel process for fabricating glasses is that the finished glass is micro-porous with the porosity being inversely proportional to the curing temperature [10, 25]. Full densification is obtained at high curing temperatures (>900°C for silica), but only at a cost penalty. The porosity is not a problem when the glass is used in dry optical components but becomes significant when the glass is in contact with liquids (as will be the case for biosensor applications), where the optical properties of the glass will be affected by the liquid permeating into the pores. The porosity of sol-gel glass was cited as a possible cause of a signal drift that was observed in a silica/titania waveguide biosensor [26]. However, the porosity has been used to an advantage in some pH [20] and enzyme [21] sensors where the pores allowed the transport of the analyte to the dye or protein trapped within the sol-gel glass. Porous thin films would be a great disadvantage in the optically resonant multi-layer sensors that are the subject of this thesis because the optical resonance is highly dependent on the properties of the thin films. However, by coating the sol-gel film with a thin film of a non-porous material (such as metal phosphate glass), the problems due to porosity can be avoided.

### **3.3.3.2 Metal phosphate films**

Iron III, aluminium and chromium phosphate films which were deposited by dip-coating were first investigated as protective coatings on glassware and anodised aluminium [27]. These phosphates, together with gallium, indium and vanadium

phosphates, were further investigated by *Sloper and Flanagan* for use in waveguide immunosensors [28, 29]. Metal phosphate films have several advantages for use as thin films in biosensors:

- they can be deposited from solution using cost-effective dip and spin coating techniques to form hard, glassy films.
- refractive index can be controlled in the range 1.49 to 1.78 by varying the film composition and by mixing the metal cations.
- a wide range of film thicknesses can be obtained.
- curing temperatures are low (200°C).
- the films are non-porous, and are chemically resistant to physiological saline, serum, blood and urine.
- gratings can be incorporated by using a simple embossing technique.

However, the films are attacked by strongly acidic or alkaline solutions, although such solutions are unlikely to be encountered in medical diagnostics applications. Iron phosphate films, because they offer the highest refractive index of the metal phosphates, were used for the high refractive index waveguide layer in the multi-layer thin film immunosensors.

### **3.4 DISCUSSION**

This chapter has considered the possible advantages of using multilayer thin film optically resonant devices as immunosensors together with some of the techniques that could be used in the fabrication of the thin films. The chosen method was the spin coating of sol-gel silica and iron phosphate thin films. However, in a large scale production environment, a technique such as CVD may offer better film thickness uniformity and reproducibility at comparable costs.

## REFERENCES

- 1 **KRONICK M N, LITTLE W A**, A new immunoassay based on fluorescence excitation by internal reflection spectroscopy, *Journal of Immunological Methods*, 1975, 8, 235-240.
- 2 **SLOPER A N, DEACON J K, FLANAGAN M T**, A planar indium phosphate monomode waveguide evanescent field immunosensor, *Sensors and Actuators B*, 1990, 1, 589-591.
- 3 **HUNSBERGER R G**, Springer series in optical sciences: Integrated optics: theory and technology, *Springer-Verlag, New York*, 1984, 2nd ed., 88-105.
- 4 **TAMIR T**, Beam and waveguide couplers, in **TAMIR T ed.**, Topics in applied physics Volume 7: Integrated optics, *Springer-Verlag, New York*, 1979, 2nd ed., 84-134.
- 5 **MACLEOD H A**, Thin-film optical filters, *Adam Hilger Ltd., Bristol*, 1986, 2nd ed..
- 6 **BORN M, WOLF E**, Principles of optics, *Pergamon Press, Oxford*, 1980, 6th ed., 61-70.
- 7 **YARIV A**, Optical electronics, *Holt, Rinehart and Winston, New York*, 1989, 3rd ed., 87-92.
- 8 **YIN Z, GARSIDE B K**, Low-loss GeO<sub>2</sub> optical waveguide fabrication using low deposition rate rf sputtering, *Applied Optics*, 1982, 21, 4324-4328.
- 9 **RAMASWAMY R V, SRIVASTAVA R**, Ion-exchanged glass waveguides: a review, *Journal of Lightwave Technology*, 1988, 6(6), 984-1001.
- 10 **HEWAK D W, LIT J W Y**, Standardization and control of a dip-coating procedure for optical thin films prepared from solution, *Canadian Journal of Physics*, 1988, 66, 861-867.
- 11 **NELLEN Ph M, TIEFENTHALER K, LUKOSZ W**, Integrated optical input grating couplers as biochemical sensors, *Sensors and Actuators*, 1988, 15, 285-295.
- 12 **WASHO B D**, Rheology and modelling of the spin coating process, *IBM Journal of Research and Development*, 1977, 21(1), 190-198.
- 13 **RAMASWAMY V, WEBER H P**, Low-loss polymer films with adjustable refractive index, *Applied Optics*, 1973, 12, 1581-1583.
- 14 **LEE D L**, Electromagnetic principles of integrated optics, *J Wiley & Sons, New York*, 1986, 1st ed., 174-6.
- 15 **BRINKER C J, FRYE G C, HURD A J, ASHLEY C S**, Fundamentals of sol-gel dip coating, *Thin Solid Films*, 1991, 201, 97-108.
- 16 **LIVAGE J, SANCHEZ C**, Sol-gel chemistry, *Journal of Non-Crystalline Solids*, 1992, 145, 11-19.
- 17 **TOKI M, TAKEUCHI T, MIYASITA S, KANBE S**, Fabrication of high-purity silica glass through WSPA-sol-gel process, *Journal of Materials Science*, 1992, 27, 2857-2862.
- 18 **MUKHERJEE S P, LOWDERMILK W H**, Gel-derived single layer antireflection films, *Journal of Non-Crystalline Solids*, 1982, 48, 177-184.
- 19 **KOZHUKHAROV V, et al**, Sol-gel processing of multilayer thin coatings, *Journal of Materials*

*Science Letters, 1992, 11, 1206-1208.*

- 20 **ROTTMAN C, et al**, Doped sol-gel glasses as pH sensors, *Materials Letters, 1992, 13, 293-298.*
- 21 **YAMANAKA S A, et al**, Enzymatic activity of glucose oxidase encapsulated in transparent glass by the sol-gel method, *Chemistry of Materials, 1992, 4(3), 495-497.*
- 22 **BERRY A J, KING T A**, Characterisation of doped sol-gel derived silica hosts for use in tunable glass lasers, *Journal of Physics D: Applied Physics, 1989, 22, 1419-1422.*
- 23 **LUKOSZ W, TIEFENTHALER K**, Sensitivity of integrated optical grating and prism couplers as (bio)-chemical sensors, *Sensors and Actuators, 1988, 15, 273-284.*
- 24 **OZER N, DEMIRYONT H, SIMMONS J H**, Optical properties of sol-gel spin-coated TiO<sub>2</sub> films and comparison of the properties with ion-beam-sputtered films, *Applied Optics, 1991, 30(25), 3661-3666.*
- 25 **SAKKA S, YOKO T**, Sol-gel derived coating films and applications, in **REISFELD R, JØRGENSEN C K** eds., *Structure and Bonding 77, Springer-Verlag, Berlin, 1992, 90-118.*
- 26 **NELLEN Ph M, LUKOSZ W**, Integrated optical input grating couplers as direct affinity sensors, *Biosensors & Bioelectronics, 1993, 8, 129-147.*
- 27 **ROTHON R N**, Solution-deposited metal phosphate coatings, *Thin Solid Films, 1981, 77, 149-153.*
- 28 **SLOPER A N, FLANAGAN M T**, Novel iron phosphate optical waveguides fabricated by a low temperature process, *Electronics Letters, 1988, 24(6), 353-355.*
- 29 **SLOPER A N, FLANAGAN M T**, Metal phosphate planar waveguides for biosensors, *Applied Optics, 1994, 33(19), 4230-4240.*

## CHAPTER 4

### OPTICS OF MULTILAYER THIN FILM SYSTEMS

*The optical theory of multilayer thin film structures is considered in this chapter. The theory is developed from a statement of the Fresnel reflection and transmission coefficients for a single interface, and then expanded to the case where the single interface is replaced with a stratified system of thin layers. A more detailed development of the theory from Maxwell's equations can be found in Appendix 1 or in the many texts on the subject of electromagnetic waves [1, 2]*

#### 4.1 ABBREVIATIONS

$\epsilon$	electric permittivity.
$\mu$	magnetic permeability. ( $\epsilon$ and $\mu$ describe the electromagnetic properties of a given medium).
$\omega$	angular frequency: $\omega = 2\pi f$ , where $f$ is the frequency.
<b>TE</b>	transverse electric polarised wave - the electric field vector is perpendicular to the plane of incidence (see fig. 4.1).
<b>TM</b>	transverse magnetic polarised wave - the magnetic field vector is perpendicular to the plane of incidence. An arbitrarily polarised wave can be expressed as a linear combination of a TE and a TM wave.
<b>Plane wave</b>	a wave whose uniform phase wave front is planar.
<b>Uniform wave</b>	a wave whose wave front is a surface with uniform phase and amplitude.

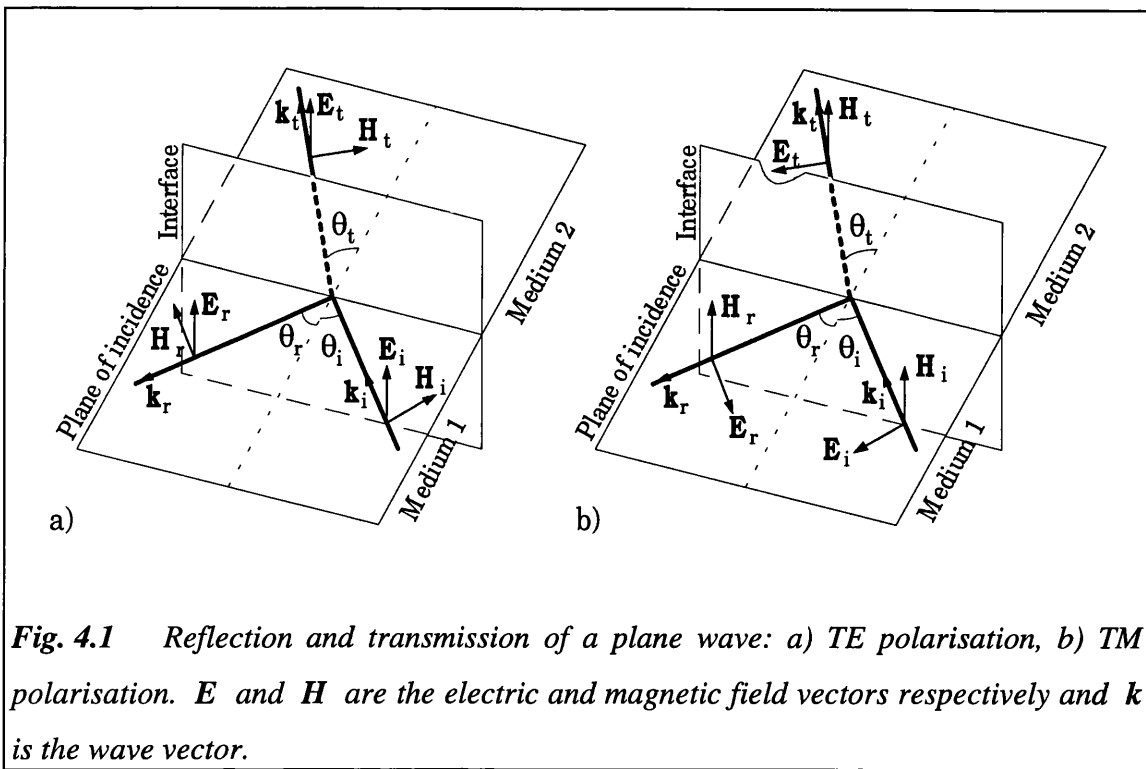


**Fig. 4.1** Reflection and transmission of a plane wave: a) TE polarisation, b) TM polarisation.  $E$  and  $H$  are the electric and magnetic field vectors respectively and  $k$  is the wave vector.

## 4.2 PLANE WAVES

### 4.2.1 Reflection and transmission at a single interface

Consider a plane, uniform light wave incident on an interface between medium 1 ( $\epsilon_1, \mu_1$ ) and medium 2 ( $\epsilon_2, \mu_2$ ) as shown in fig. 4.1. The incident, reflected and transmitted waves all lie in the same plane (the plane of incidence), and the angles  $\theta_i, \theta_r$  and  $\theta_t$  (formed by the incident, reflected and transmitted waves respectively with the normal to the interface) are related by [1]:

$$\sin \theta_r = \sin \theta_i \tag{4.1}$$

and

$$k_1 \sin \theta_i = k_2 \sin \theta_t \tag{4.2}$$

where  $k$  is the wave number:

$$k_i = \omega \sqrt{\epsilon_i \mu_i} \quad (4.3)$$

Equation 4.2 is a more general form of Snell's law.

#### 4.2.2 The Fresnel reflection and transmission coefficients

The reflection and transmission coefficients (or Fresnel coefficients) [1, 2, 4] provide information on the amplitude and phase of the reflected and transmitted waves relative to the incident wave's amplitude and phase. There are two reflection and two transmission coefficients (one for each plane of polarisation) and are simply stated here (a brief derivation can be found in appendix 1). The coefficients for a TE polarised wave are:

$$r_{\text{TE}} \equiv \left( \frac{E_r}{E_i} \right)_{\text{TE}} = \frac{\mu_2 k_1 \cos \theta_i - \mu_1 k_2 \cos \theta_t}{\mu_2 k_1 \cos \theta_i + \mu_1 k_2 \cos \theta_t} \quad (4.4)$$

$$t_{\text{TE}} \equiv \left( \frac{E_t}{E_i} \right)_{\text{TE}} = \frac{2\mu_2 k_1 \cos \theta_i}{\mu_2 k_1 \cos \theta_i + \mu_1 k_2 \cos \theta_t} \quad (4.5)$$

where,  $E_i$ ,  $E_r$  and  $E_t$  are the complex amplitudes of the incident, reflected and transmitted wave electric field strengths respectively. The coefficients for a TM polarised wave are:

$$r_{\text{TM}} \equiv \left( \frac{H_r}{H_i} \right)_{\text{TM}} = \frac{\epsilon_2 k_1 \cos \theta_i - \epsilon_1 k_2 \cos \theta_t}{\epsilon_2 k_1 \cos \theta_i + \epsilon_1 k_2 \cos \theta_t} \quad (4.6)$$

$$t_{\text{TM}} \equiv \left( \frac{H_t}{H_i} \right)_{\text{TM}} = \frac{2\epsilon_2 k_1 \cos \theta_i}{\epsilon_2 k_1 \cos \theta_i + \epsilon_1 k_2 \cos \theta_t} \quad (4.7)$$

where,  $H_i$ ,  $H_r$  and  $H_t$  are the complex amplitudes of the incident, reflected and transmitted wave magnetic field strengths respectively.

Using the relation (see appendix 1):

$$\eta \equiv \frac{|\mathbf{E}|}{|\mathbf{H}|} = \sqrt{\frac{\mu}{\epsilon}} \quad (4.8)$$

the ratios of the reflected and transmitted electric field strengths to the incident electric field strength can be obtained for a TM polarised wave:

$$\left( \frac{E_r}{E_i} \right)_{\text{TM}} = r_{\text{TM}} \quad \left( \frac{E_t}{E_i} \right)_{\text{TM}} = \frac{\eta_2}{\eta_1} t_{\text{TM}} \quad (4.9)$$

### 4.2.3 Total internal reflection

It is clear from equation 4.2 that when a plane wave in medium 1 is incident on an interface with an optically less dense medium 2, (as in fig. 4.1) there exists a range of incident angles such that:

$$\sin \theta_t = \frac{k_1}{k_2} \sin \theta_i > 1 \quad (4.10)$$

The angle of incidence ( $\theta_i$ ) at which equation 4.10 becomes true is known as the critical angle. At angles of incidence greater than the critical angle, the angle  $\theta_t$  becomes complex and  $|r_{\text{TE}}| = |r_{\text{TM}}| = 1$ , ie. all incident light energy is reflected back into medium 1 (total internal reflection).

Although all the light energy is reflected, the electromagnetic field in medium 2 does not disappear and it can be shown (appendix 1) that the field decays exponentially as the perpendicular distance from the interface increases (see fig. 4.2) [1, 2]. The wave in medium 2 is described as an evanescent wave and it is also non-uniform - ie. the planes of constant phase and constant amplitude are not co-incident. In this case, the planes of constant phase are perpendicular to the interface and the planes of constant amplitude are parallel to the interface. An important figure when considering evanescent field optical biosensors is the evanescent field penetration depth - the distance from the interface at which the field strength of the evanescent wave in medium 2 falls to  $1/e$  of its value at the interface (fig. 4.2). The penetration depth is given by [1, 2]:

$$d_{\text{pen}} = \frac{1}{k_1 \sqrt{\sin^2 \theta_i - (\epsilon_2/\epsilon_1)}} \quad (4.11)$$

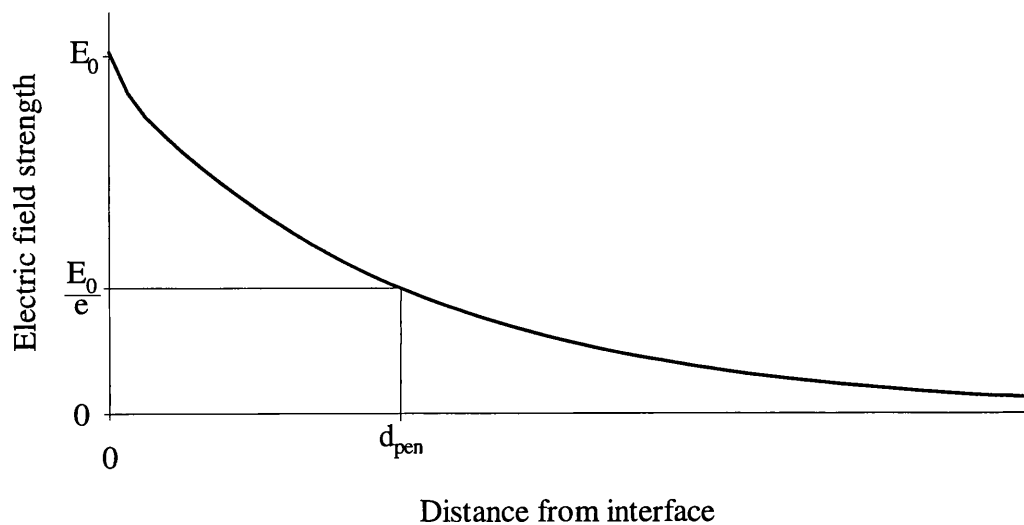


**Fig. 4.2** The evanescent field of a totally internally reflected plane wave. The penetration depth is given by  $d_{\text{pen}}$ .

When designing an evanescent field optical biosensor, it is important to minimise the penetration depth and maximise the transmitted field strength. Equation 4.11 indicates that to minimise the penetration depth, it is required that the ratio  $\epsilon_1/\epsilon_2$  is large and that the angle of incidence is also large.

It can be shown [2] that, for a TE wave, the transmitted electric field vector remains polarised perpendicular to the plane of incidence and the magnetic field vector rotates in the plane of incidence with its axis of rotation parallel to the electric field vector (fig. 4.3). The converse is true for a TM wave. This phenomenon can be useful in an evanescent field biosensor because the absorption of many fluorescent molecules (when immobilised) is highly dependent on the polarisation of the exciting light. Thus, because electron transition is mainly dependent on the electric field strength, it is useful to use TM polarised exciting light as the rotating electric vector in the evanescent field will excite a greater number of fluorescent molecules bound to the tagged antibodies. In a simple total internal reflection sensor, it would be possible to use unpolarised light

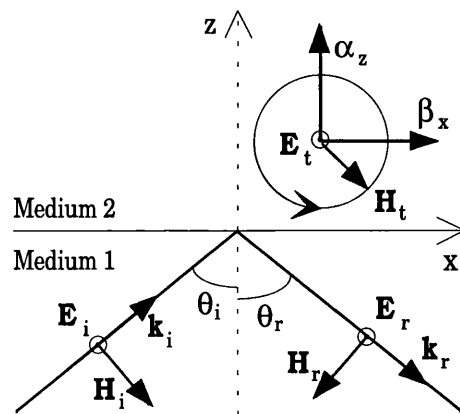


**Fig. 4.3** Total internal reflection of a TE polarised plane wave. The transmitted wave remains TE polarised but the magnetic field vector ( $H$ ) rotates with respect to time in the plane of incidence. The transmitted  $k$  vector breaks down to a real  $x$ -component ( $\beta$ ) and an imaginary  $z$ -component ( $\alpha$ ) indicating that there is a time averaged energy flow in the  $x$ -direction but not in the  $z$ -direction.

but, in the resonant multilayer thin film devices relevant to this thesis, this is not possible as the resonance is dependent on the polarisation of the incident light.

#### 4.2.4 Power flow across the interface

It is useful to know the power that is transferred from medium 1 into medium 2 and to calculate this it is required to know the Poynting vectors [1, 2] for the incident, reflected and transmitted waves, and to calculate the power flow perpendicular to the interface. The ratios of the reflected and transmitted power flowing normal to the interface relative to the incident normal power flow are given, respectively, for a TE polarised wave by (see appendix 1):

$$\mathfrak{R}_{\text{TE}} = |r_{\text{TE}}|^2 \quad (4.12)$$

$$\mathfrak{S}_{\text{TE}} = \frac{\mu_1 k_2 \cos \theta_t}{\mu_2 k_1 \cos \theta_i} |t_{\text{TE}}|^2 \quad (4.13)$$

Similarly, for a TM wave:

$$\mathfrak{R}_{\text{TM}} = |r_{\text{TM}}|^2 \quad (4.14)$$

$$\mathfrak{S}_{\text{TM}} = \frac{\epsilon_1 k_2 \cos \theta_t}{\epsilon_2 k_1 \cos \theta_i} |t_{\text{TM}}|^2 \quad (4.15)$$

$\mathfrak{R}$  and  $\mathfrak{S}$  are known as the reflectivity and the transmittivity respectively. The law of conservation of energy means:  $\mathfrak{R} + \mathfrak{S} = 1$ .

### 4.3 THIN LAYERS AND STRATIFIED SYSTEMS

The theory briefly described in section 4.2 can be applied not only to semi-infinite slabs, but also to thin films and to multiple layers of thin films. An optically thin film is one which has a film thickness of the order of the wavelength of light.

#### 4.3.1 The method of successive field summations

Consider the system of fig. 4.4 where there is a thin film medium 2, ( $\epsilon_2, \mu_2$ ) and thickness  $h_2$ , sandwiched between two semi-infinite slabs - medium 1, ( $\epsilon_1, \mu_1$ ) and medium 3, ( $\epsilon_3, \mu_3$ ). The interfaces are planar and smooth and the light is incident on the medium (1,2) boundary as shown in fig. 4.4. Using the formulae of equations 4.4 - 4.7, the reflection and transmission coefficients can be calculated for each of the interfaces. Assume that the reflection coefficients for the interfaces are  $r_{12}$ ,  $r_{21}$ ,  $r_{23}$  and the transmission coefficients are  $t_{12}$ ,  $t_{21}$ ,  $t_{23}$  (where, for example, the subscript '12' implies that the coefficient is for a wave travelling from medium 1 to medium 2). The

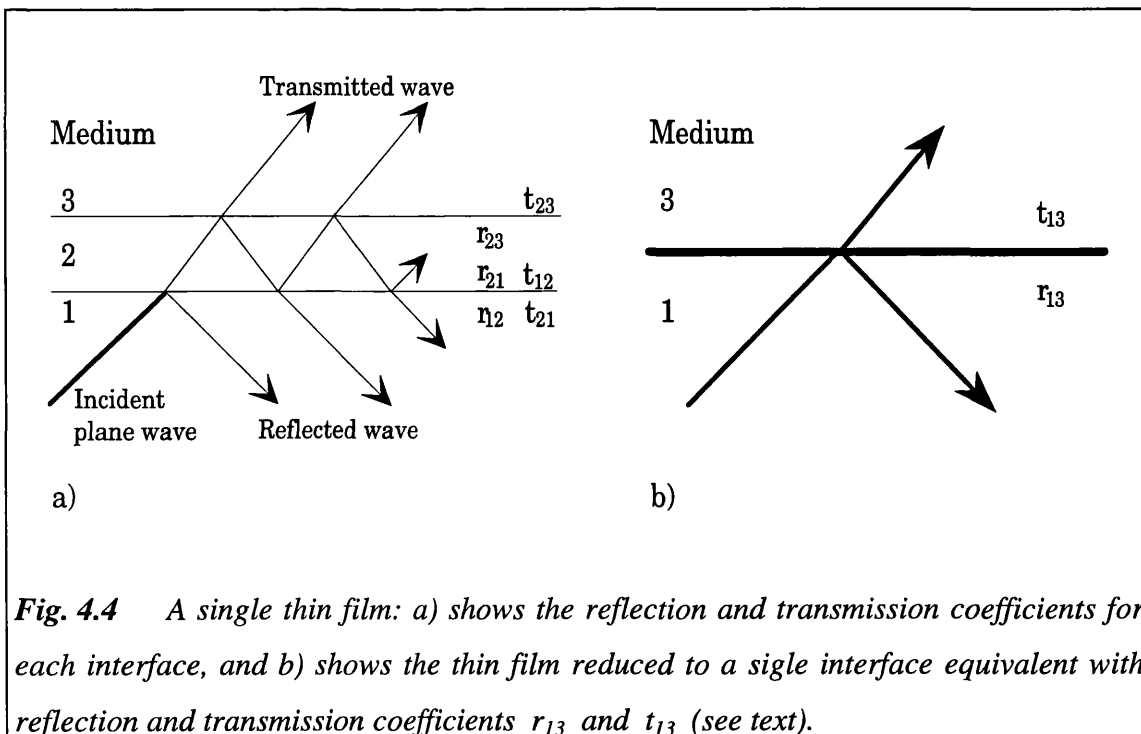


**Fig. 4.4** A single thin film: a) shows the reflection and transmission coefficients for each interface, and b) shows the thin film reduced to a single interface equivalent with reflection and transmission coefficients  $r_{13}$  and  $t_{13}$  (see text).

reflected wave is then composed of an initial reflection at the (1,2) interface and subsequent multiple reflections at the (2,3) and the (2,1) interfaces that are transmitted through the (2,1) interface (see fig. 4.4). Hence, defining a reflection coefficient  $r_{13}$  for the thin film, it can be seen that [3]:

$$r_{13} = r_{12} + t_{12} e^{j\beta_2} r_{23} e^{j\beta_2} t_{21} + t_{12} e^{j\beta_2} r_{23} e^{j\beta_2} r_{21} e^{j\beta_2} r_{23} e^{j\beta_2} t_{21} + \dots \quad (4.16)$$

where

$$\beta_2 = k_2 h_2 \cos \theta_2 \quad (4.17)$$

represents the phase change in traversing the thickness of the thin film layer. Simplifying gives:

$$r_{13} = r_{12} + t_{12} t_{21} r_{23} e^{2j\beta_2} (1 + r_{21} r_{23} e^{2j\beta_2} + r_{21}^2 r_{23}^2 e^{4j\beta_2} + \dots) \quad (4.18)$$

The term within the brackets is of the form  $S = a + ax + ax^2 + \dots$  whose sum is given by:

$$S = \frac{a}{1 - x}$$

provided  $|x| < 1$ . Thus, using the relation  $1 + r = t$  (see appendix 1) and knowing

$$r_{21} = -r_{12} \quad (4.19)$$

the following equation is obtained:

$$r_{13} = \frac{r_{12} + r_{23} e^{2j\beta_2}}{1 + r_{12} r_{23} e^{2j\beta_2}} \quad (4.20)$$

Similarly, defining  $t_{13}$  as the transmission coefficient across the thin film, it is found that:

$$t_{13} = \frac{t_{12}t_{23} e^{j\beta_2}}{1 + r_{12}r_{23} e^{2j\beta_2}} \quad (4.21)$$

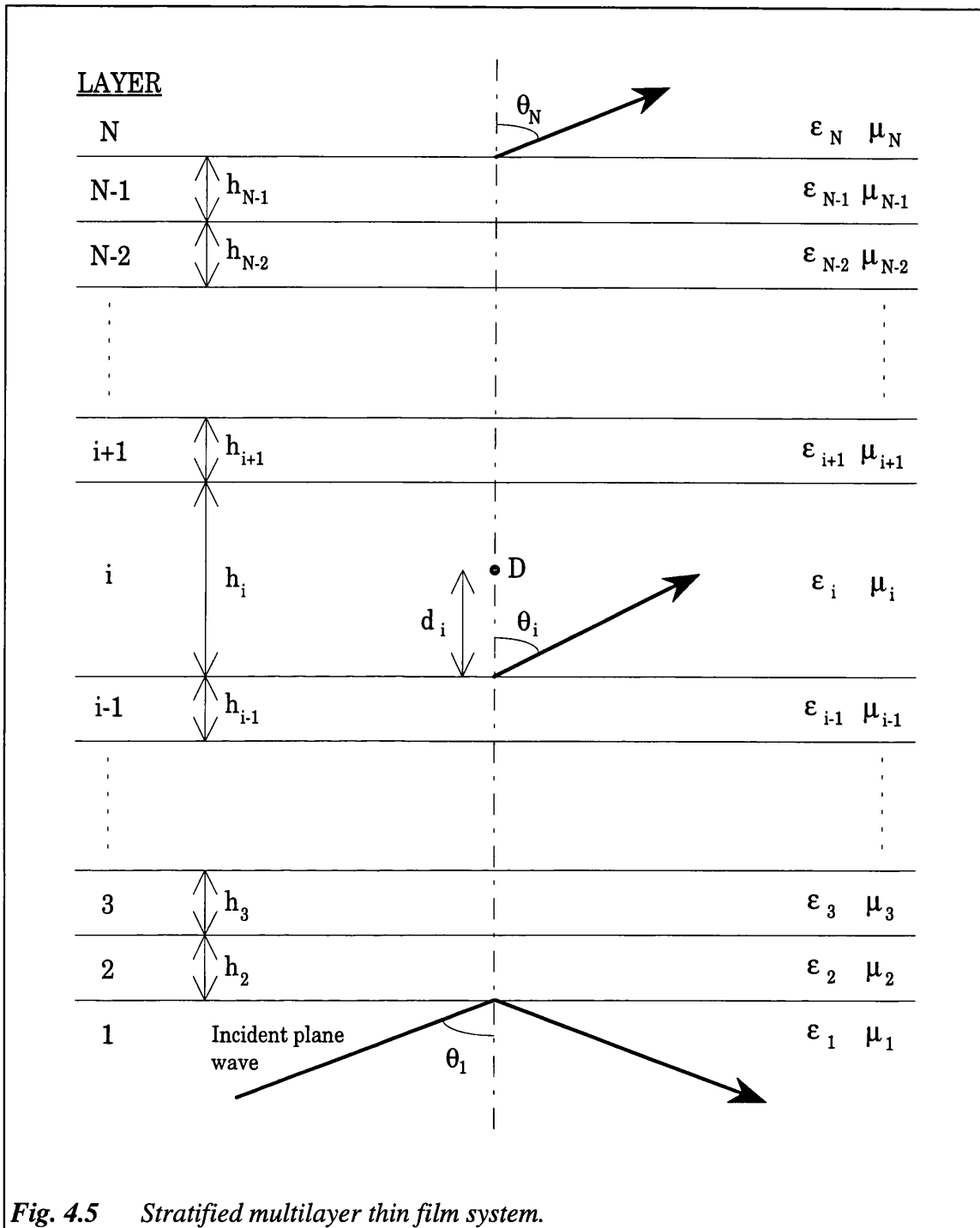
The equations 4.20 and 4.21 give the reflection and transmission coefficients of a thin film and allow the thin film to be treated as single interface with reflection and transmission coefficients  $r_{13}$  and  $t_{13}$  respectively.

This technique can be expanded to a multilayer thin film system by successively incorporating each thin film layer to a single interface equivalent thus reducing the multilayer system to a single interface. However, when considering thin films, it must be noted that, unlike the relation given in equation 4.19,

$$r_{31} \neq -r_{13} \quad (4.22)$$

The technique of summing the fields produced by successive reflections can be used to calculate the field strength distribution across the thickness of an arbitrary thin film relative to the incident field strength. Consider the N-layer structure of fig. 4.5 with N-2 thin film layers. Assuming that  $t_{ii}$  (the transmission coefficient for layers 2, ..., i-1),  $r_{i1}$  (the reflection coefficient for layers i-1, ..., 2) and  $r_{iN}$  (the reflection coefficient for layers i+1, ..., N-1) are known, then it is easily shown that the ratio of the field strength at a point D in layer i to the incident field strength in layer 1 is given by:

$$t_i(d_i) = \frac{t_{ii} (e^{j\delta_i} + r_{iN} e^{2j\beta_i} e^{-j\delta_i})}{1 - r_{iN}r_{i1} e^{2j\beta_i}} \quad (4.23)$$



where  $\beta_i = k_i h_i \cos \theta_i$  represents the phase change in traversing layer  $i$  and  $\delta_i = k_i d_i \cos \theta_i$  represents the phase change in traversing the distance  $d_i$  normal to the interface.

Equation 4.23 can be applied to each of the layers  $1, \dots, N$  and it is, thus, possible

to build up a picture of the field strength distribution throughout the multilayer structure relative to the incident wave field strength.

### 4.3.2 The matrix method

The method outlined in section 4.3.1 is useful when there are less than two or three thin films but if there are more, it can be seen that the calculation burden rapidly increases. In these cases it is easier to use the matrix method. This method is not derived here but a full derivation can be found in *Born & Wolf* [4].

Consider the stratified system of fig. 4.5 where the incident light is TE polarised. The characteristic matrix,  $\mathbf{M}_i$ , for layer  $i$  is then given by:

$$\mathbf{M}_i = \begin{pmatrix} \cos \beta_i & -\frac{j}{p_i} \sin \beta_i \\ -jp_i \sin \beta_i & \cos \beta_i \end{pmatrix} \quad (4.24)$$

where

$$p_i = \sqrt{\frac{\epsilon_i}{\mu_i}} \cos \theta_i \quad (4.25)$$

$$\beta_i = k_i h_i \cos \theta_i \quad (4.26)$$

$\mathbf{M}_i$  and  $\beta_i$  are calculated for  $i = 2, \dots, N-1$  and  $p_i$  for  $i = 1, \dots, N$ . The characteristic matrix,  $\mathbf{M}$ , for the whole stratified system is then:

$$\mathbf{M} = \prod_{i=2}^{N-1} \mathbf{M}_i \quad (4.27)$$

The reflection and transmission coefficients for the stratified system are obtained from the characteristic matrix as follows:

$$r_{\text{TE}} = \frac{(m_{11} + m_{12}p_N)p_1 - (m_{21} + m_{22}p_N)}{(m_{11} + m_{12}p_N)p_1 + (m_{21} + m_{22}p_N)} \quad (4.28)$$

$$t_{\text{TE}} = \frac{2p_1}{(m_{11} + m_{12}p_N)p_1 + (m_{21} + m_{22}p_N)} \quad (4.29)$$

where  $m_{ij}$  are the elements of the matrix  $\mathbf{M}$ .

The reflection and transmission coefficients for a TM polarised plane wave are obtained by replacing  $p_i$  in the equations above with

$$q_i = \sqrt{\frac{\mu_i}{\epsilon_i}} \cos \theta_i \quad (4.30)$$

The reflection and transmission coefficients will now be the ratios of the magnetic field strengths and not the electric field strengths.

The values obtained for the reflection and transmission coefficients may be substituted into equations 4.12 - 4.15 to obtain the power flow across the stratified medium.

**REFERENCES**

- 1 **LEE D L**, Electromagnetic principles of integrated optics, *J Wiley & Sons, New York, 1986, 1st ed., 13-67.*
- 2 **LORRAIN P, CORSON D R, LORRAIN F**, Electromagnetic fields and waves, *W H Freeman & Co., New York, 1988, 3rd ed., 492-593.*
- 3 **ANDERS H**, Thin films in optics, *The Focal Press, London, 1967, 18-59.*
- 4 **BORN M, WOLF E**, Principles of optics, *Pergamon Press, London, 1975, 5th ed., 36-41, 51-62.*

## CHAPTER 5

### EXPERIMENTAL MATERIALS AND METHODS

*This chapter describes the materials and the methods that were used at each stage of the multilayer thin film immunosensor development. The chapter is in three parts, describing the multilayer modelling, the multilayer thin film device fabrication and characterisation, and the immunosensor device fabrication and performance of an assay for mouse-IgG. Note that this chapter concentrates on the materials and methods while the experimental results will be described in chapters 6, 7 and 8.*

#### 5.1 COMPUTER MODELLING

##### 5.1.1 The multilayer thin film system

The multilayer thin film system was modelled by computer prior to the fabrication of the devices. The modelling was performed on a 386 PC-compatible computer using the *Microsoft 'C'* language. Basic routines to handle complex numbers were obtained from *Numerical Recipes in C* [1] to which further routines (eg. to calculate the sine and cosine of a complex number) were added. The simplex minimisation routine due to *Nelder and Mead* [2] was also obtained from *Numerical Recipes in C*.

##### 5.1.2 The immunosensor

The sandwich immunoassay that was performed using the multi-layer immunosensor was subsequently modelled to determine the major noise and background

signal sources. The programs for this were also written in *Microsoft 'C'* on a 386 PC-compatible computer.

### 5.1.3 Antibody-antigen binding

The programs for the modelling of the antibody-antigen binding reaction using a Sipsian distribution function [3] were written in *Microsoft BASIC* on an *Apple* Macintosh computer by *Dr. M T Flanagan*.

## 5.2 THIN FILM FABRICATION AND CHARACTERISATION

### 5.2.1 Chemicals

Table 5.1 lists all the reagents that were used in the fabrication of the thin films. The water was purified and de-ionised using an 'Elgastat Spectrum' reverse osmosis water purifier (*Elga Ltd.*).

### 5.2.2 Substrates and substrate preparation

The glass substrates, onto which the thin films were deposited, were soda-lime float glass plates (sold by *Pilkington Micronics Ltd., UK* under the trade name of PERMABLOC). The plates are 1.1mm thick and possess an intrinsic ion-exchanged waveguide on the face of the plate that was in contact with molten tin during production. Thus, thin film deposition on this face was avoided. The refractive index of the plates was ascertained to be  $1.517 \pm 0.0002$  (after measuring 10 samples) at the wavelength of 632.8nm by using an ABBE refractometer (*Bellingham-Stanley Ltd., UK*) with a helium-neon laser (*Melles-Griot, US*) as the light source.

Material	Formula	Supplier	Code	Grade
<b>Solvents</b>				
methanol	CH <sub>3</sub> OH	BDH Ltd.	10158	AnalaR
ethanol (96%)	C <sub>2</sub> H <sub>5</sub> OH	BDH Ltd.	28719	GPR
acetone	CH <sub>3</sub> COCH <sub>3</sub>	BDH Ltd.	10003	GPR
iso-propanol	C <sub>3</sub> H <sub>7</sub> OH	BDH Ltd.	10224	AnalaR
<b>Phosphate glass constituents</b>				
iron (III) nitrate	Fe(NO <sub>3</sub> ) <sub>3</sub> ·9H <sub>2</sub> O	BDH Ltd.	10300	AnalaR
aluminium nitrate	Al(NO <sub>3</sub> ) <sub>3</sub> ·9H <sub>2</sub> O	BDH Ltd.	10306	AnalaR
ortho-phosphoric acid	H <sub>3</sub> PO <sub>4</sub>	BDH Ltd.	10173	AnalaR
<b>Silica glass constituents</b>				
LIQUICOAT Si	Si(OC <sub>2</sub> H <sub>5</sub> ) <sub>4</sub>	Merck Ltd.	ZLI-2132	
<b>Miscellaneous</b>				
Decon 90 detergent		BDH Ltd.	56022	

**Table 5.1** Chemicals used in the fabrication of the thin films.

Some experiments were performed using silica coated PERMABLOC substrates that were donated by *Serono Diagnostics Ltd., UK*. The silica was deposited by a CVD process by *Pilkington Micronics Ltd.*

The substrates were first cut into plates of dimensions 90mm or 50mm square (the smaller size was necessary to fit inside a tube furnace), and cleaned by soaking overnight in an aqueous detergent solution (3 - 4 % v/v Decon 90). The plates were then rinsed and left to soak in purified water for approximately one hour. Immediately before thin film deposition, each plate was rinsed with purified water, then with ethanol and then spun dry.

### 5.2.3 Coating solution preparation

**Sol-gel silica.** A commercially available tetraethylorthosilicate sol-gel solution (LIQUICOAT Si, ZLI-2132, obtained from *Merck Ltd., UK*) was used. The solution was 0.2 $\mu$ m filtered using a PTFE syringe filter immediately before deposition and was used without dilution.

**Metal phosphate.** The metal phosphate solutions were prepared, as described by *Sloper and Flanagan* [4, 5], within 24 hours of deposition. The required metal (iron(III) or aluminium) nitrate was dissolved in a solution of orthophosphoric acid and methanol, and the required metal phosphate solution molarity was obtained by dilution with methanol. The metal:phosphate ratio was always 1:1. Metal phosphate solution molarities used were 1M, 0.5M and 0.25M, and typically contained some water introduced as water of hydration in the metal nitrate and by water present in the orthophosphoric acid solution. The solutions were 0.2 $\mu$ m filtered using a PTFE syringe filter prior to deposition.

### 5.2.4 Spin coating

#### 5.2.4.1 The spinner

Thin film deposition was done by employing a spin-coating technique for which a

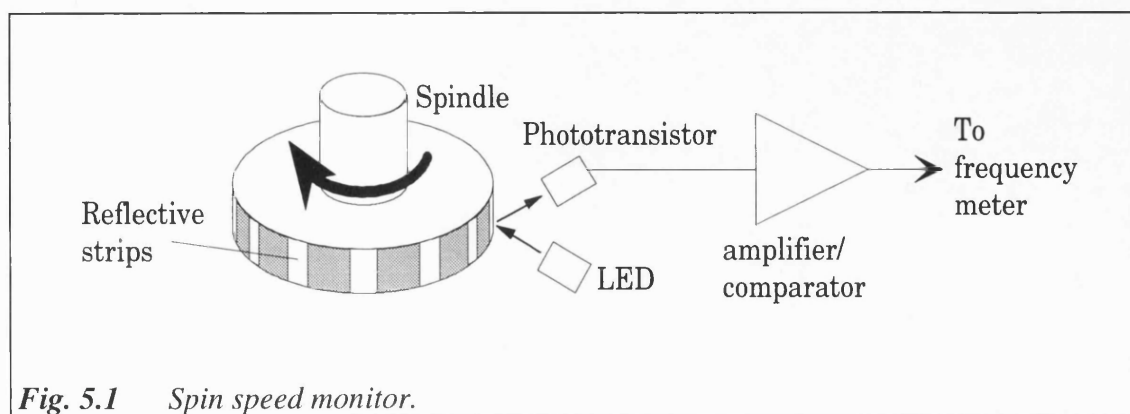


**Fig. 5.1** Spin speed monitor.

spinner instrument (type TP6000, *Micro-Contrôle SET, France*) intended for spinning photoresist onto silicon substrates was used. The spinner had a speed range from 0 to 10000 rpm in 100rpm increments and variable acceleration in the range 100 to 20000 rpm/s in 100rpm/s increments. The substrates were held on the chuck by a vacuum applied to the underside of the substrate via grooves in the surface of the chuck.

Although, the instrument allowed speed, acceleration and spin time to be set via a keypad and digital display, an auxiliary spin speed monitor was built to cross-check the indicated spin speed. The spin speed monitor consisted of an LED/phototransistor pair whereby the light emitted by the LED could be reflected onto the phototransistor by an aluminium foil strip attached to the spindle of the spinner (see fig. 5.1). Twelve such reflective foil strips were placed around the spindle so the output of the phototransistor was a square wave whose frequency was twelve times the spinner rotation frequency. The output of the phototransistor was fed to a hand-held frequency meter (supplied by *RS Components Ltd., UK*, stock no. 610-972) which gave a reading to the nearest unit Hz. This allowed the spin speed to be determined to an accuracy of  $\pm 2.5$ rpm (the

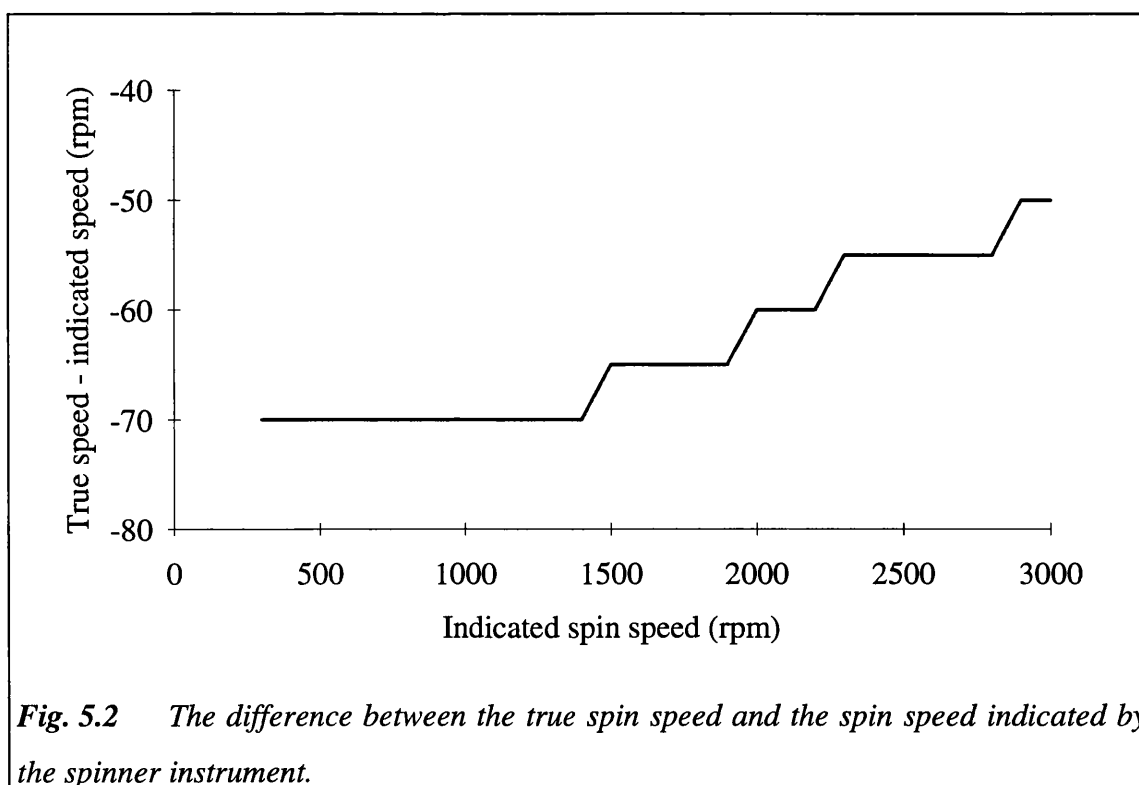


*Fig. 5.2 The difference between the true spin speed and the spin speed indicated by the spinner instrument.*

accuracy being determined by the number of reflective strips used). It was found that there was a large discrepancy between the spin speed measured by the auxiliary speed monitor and the speed indicated on the spinner as shown in fig. 5.2. Subsequently, only the readings from the auxiliary speed monitor were used.

#### 5.2.4.2 Thin film deposition

The thin films were deposited by first flooding the surface of the substrate with the required coating solution while the substrate was mounted on the spinner chuck but was stationary. The substrate was then spun for one minute at the required spin speed. The spinning was performed at the ambient temperature but the atmosphere immediately above the substrate was controlled by placing a small volume of a solvent in the drip tray of the spinner. It has been found that the thickness of the thin films can be controlled more accurately by ensuring that atmospheric conditions immediately above the substrate are constant [5]. For the metal phosphate solution, the solvent in the drip tray was some excess metal phosphate solution. For the sol-gel solution, propan-2-ol (which was recommended as a diluent for the sol-gel solution by *Merck Ltd.*) was used not only to control atmospheric conditions but also to prevent the excess sol-gel solution from drying out, which would have given silica dust particles that could contaminate the thin film.

Clean room conditions were not available, and so all spin coating was performed within a laminar flow hood (*Bassaire Ltd., UK*), through which filtered air circulated to minimise dust contamination of the thin films.

#### 5.2.5 Curing

Thermal curing, in all cases, was performed immediately after the spin coating procedure.

### 5.2.5.1 Silica films

The silica films were first dried for a minimum of 1 hour at 100°C by placing the substrates flat on aluminium plates (pre-heated) in an oven (UM series from *Memmert, Germany*) where the temperature was controlled to  $\pm 2^\circ\text{C}$ . The oven was placed inside the laminar flow hood so that the films could be dried before they were exposed to a dusty atmosphere. The substrates were then removed, placed vertically in silica carriers and transferred to a tube furnace for curing at 500°C for 2 hours. The temperature of the furnace was ramped from ambient to 500°C, and was accurately controlled to within 1°C by a *Eurotherm 818P* controller. After curing, the substrates were allowed to cool inside the furnace (to prevent excessive thermal stress being induced on the substrate) until the the temperature was less than 100°C before they were removed. The temperature profile for the curing is shown graphically in fig. 5.3. Some silica films (deposited on 90mm square substrate plates) were cured flat on aluminium plates at  $300 \pm 4^\circ\text{C}$  for 2 hours in a fan oven (300 plus series from *Gallenkamp Ltd., UK*). These plates were removed from the oven whilst still lying on the aluminium plates immediately after curing and were allowed to cool at room temperature

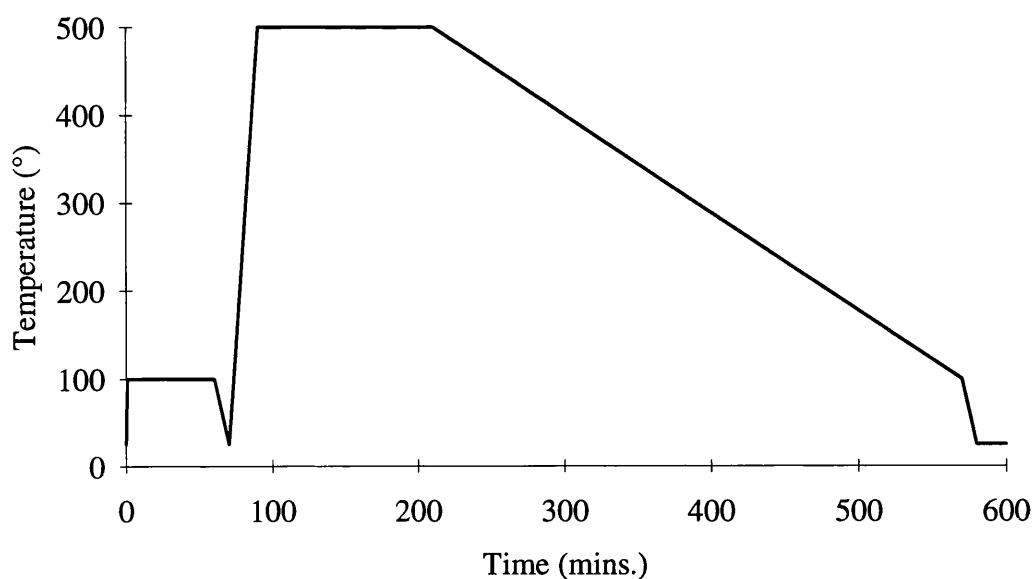


**Fig. 5.3** Temperature profile for the curing of sol-gel deposited silica films.

### 5.2.5.2 Metal phosphate films

All metal phosphate films were dried at  $70\pm 2$  °C for between 5 and 15 mins. in a similar manner to that described above for silica. They were then cured at  $200\pm 2$  °C for 1 hour by transferring the aluminium plates holding the substrates to the larger oven (300 plus series from, *Gallenkamp Ltd., UK*). The substrates were removed from the oven immediately after curing and allowed to cool at room temperature.

### 5.2.6 Deposition of multiple layers

Deposition of the first thin film layer was performed by following the procedures described in sections 5.2.2 to 5.2.5. The deposition of further thin layers was required to: a) increase the thickness of the thin film layer; or b) to deposit a thin film layer of a different refractive index material. The deposition of multiple layers was achieved by repeating the procedures of sections 5.2.2 to 5.2.5 for each of the subsequent thin film depositions.

It was found that both the sol-gel and metal phosphate solutions did not wet the surface of a previously deposited sol-gel silica or metal phosphate film. The result of this was that droplets would form on the surface after spinning instead of a uniform thin film. The problem could not be solved by rinsing the plates in a solvent (ethanol or methanol) or by soaking overnight in water but could be overcome by cleaning the plates with the detergent solution as described in section 5.2.2. However, the high pH of the Decon90 detergent solution (approximately 11 - 11.5) etched away any metal phosphate film present (the etch rate was sufficient to etch a 1000nm  $\text{AlPO}_4$  film in 2 - 3 hours). This was the major reason for using a sol-gel derived silica layer as the first thin film layer.

### 5.2.7 Film thickness measurement

The thin film thickness was measured by traversing the stylus of a surface profiling instrument (Taly-Step 1, manufactured by *Rank Taylor Hobson Ltd., UK*) across a step cross-section of the film.

#### 5.2.7.1 Metal phosphate films

The step required by the surface profiling instrument was prepared by etching the metal phosphate films after masking a small portion of the film with photoresist. The photoresist (S1818 SP16, from *Shipley Europe Ltd., UK*) was painted on the film and dried at 80°C for 20 mins.. The etchant was a standard metallic aluminium etchant (Isoform aluminium etch, from *MicroImage Technology Ltd., UK*). The etching was performed by holding the substrate for approximately 2 mins. [4, 5] in a 100ml tall form beaker containing a quantity of the aluminium etchant stirred by a double star magnetic flea. The etchant was renewed after every 15 - 20 uses. The film thickness was then measured after removing the photoresist with acetone.

The silica layer present under the iron phosphate layer in the multilayer systems was not etched by exposure to the aluminium etchant. This was ascertained by measuring the thickness of the silica film before and after placing the silica film in the aluminium etchant for five minutes. No change in the silica film thickness was observed.

#### 5.2.7.2 Silica films

Preparation of a step in the silica films proved to be more difficult, as a suitable etchant that could discriminate between the silica film and the float glass substrate could not be found. Ellipsometry was considered as an alternative to surface profiling but the large number of samples requiring thickness measurement and the lack of an available instrument led to two other methods being considered.

**METHOD A - Etch rate method.**

This method was used to measure the silica film thickness by looking for the change in etch rate that occurs as the silica film is completely etched, thus exposing the float glass substrate to the silica etchant.

The use of silica etchant reduced the adhesion of the photoresist to the substrate, and so a primer (hexamethyldisilazane, from *Shibley Europe Ltd., UK*) was used to improve adhesion. The substrates incorporating the silica film were vapour primed by placing the substrates in a rack which was placed proud of the surface of a small volume of the primer in a container. Ten minutes were sufficient for priming. The reverse of the substrate (ie. the face not having a silica film) was then spin coated with photoresist and dried at 80°C for 20mins. This was necessary to prevent the back of the substrate being etched. Each substrate plate was then cut to give about 30 slides of dimensions 1x3 cm, and the face with the silica film was primed as described above. A photoresist strip was then painted on each slide and dried, again as described above. The slides were now ready for etching.

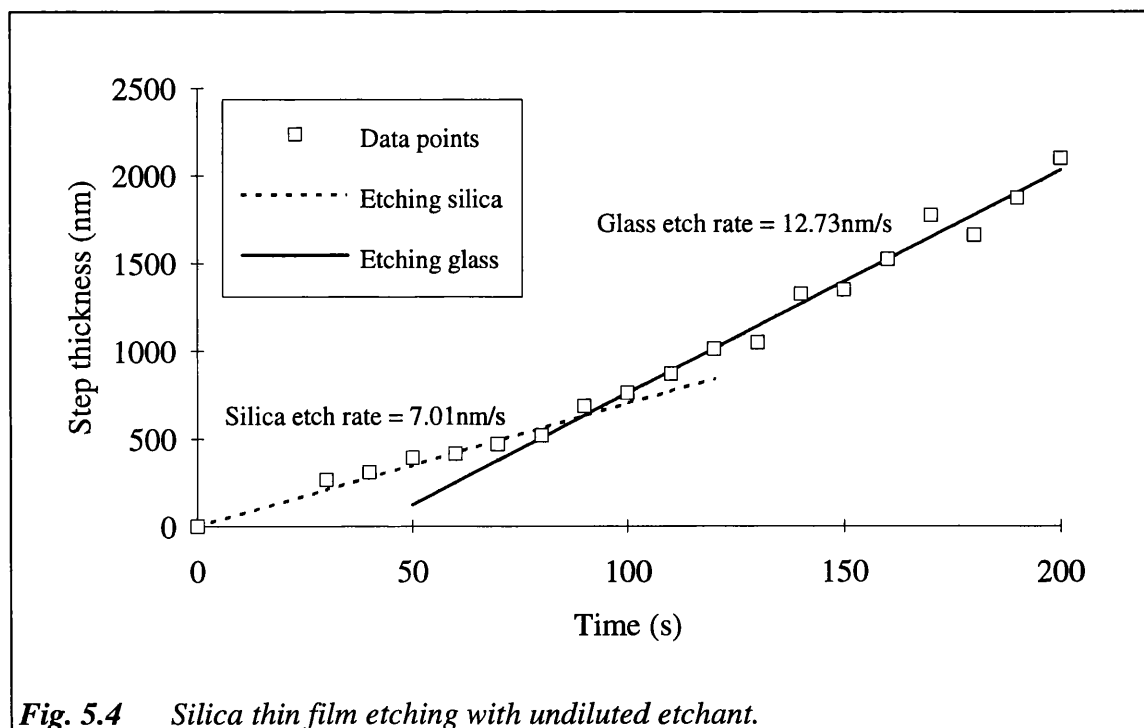


**Fig. 5.4** Silica thin film etching with undiluted etchant.

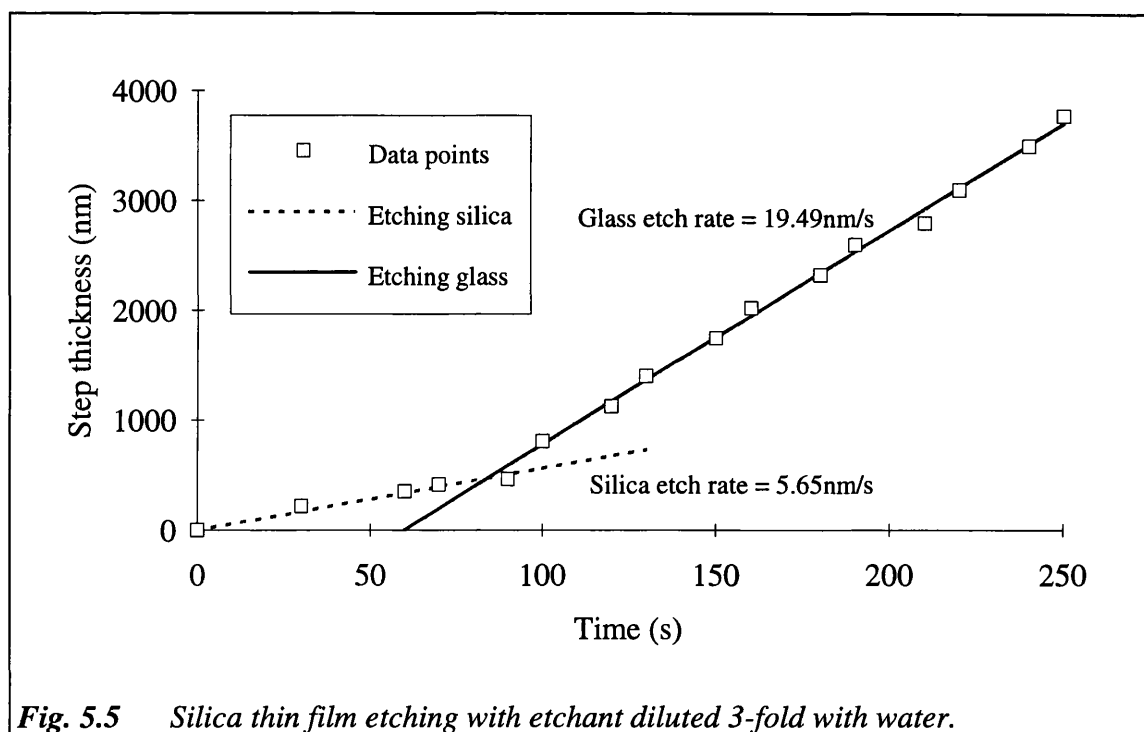


**Fig. 5.5** Silica thin film etching with etchant diluted 3-fold with water.

The 30 slides, from a single substrate, were placed in a rack and submerged in the silica etchant (silicon dioxide etch 7:1 - a mixture of 7 parts 50%  $\text{NH}_4\text{F}$  solution and 1 part 49% HF solution, from *MicroImage Technology Ltd., UK*) which was in a polypropylene container placed on a shaker. The slides were removed singly from the etch at 10s intervals, rinsed in purified water, rinsed in ethanol and allowed to air dry. After removal of the photoresist with acetone, the depth of the etched step was measured. Figs. 5.4 and 5.5 show the step thickness as a function of etching time for CVD deposited silica plates. Fig. 5.4 is for undiluted etchant and fig. 5.5 for etchant diluted 3-fold with purified water. The reasons for the increase in the PERMABLOC substrate etch rate when diluted etchant is used are unclear.

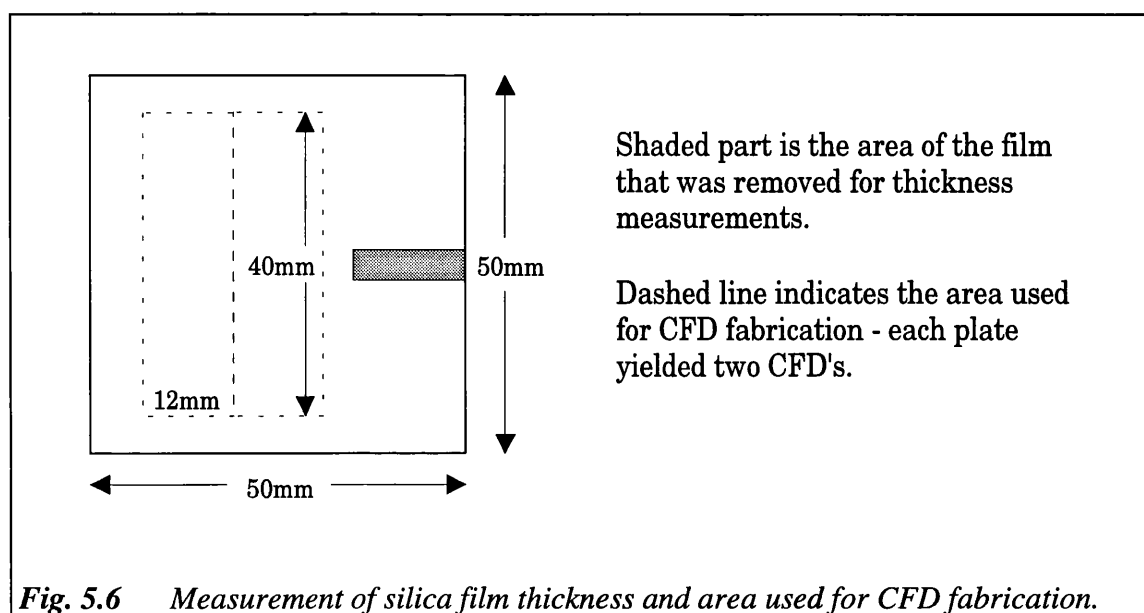
This method was sufficient to correctly identify the CVD deposited silica film thickness of 500nm on the PERMABLOC substrates. However, probably due to the porous nature of the sol-gel silica films, and, therefore, the much higher etch rates, the technique was not useful for determining sol-gel deposited silica film thicknesses.

### **METHOD B - wiping method**

Immediately after spin coating the sol-gel silica layer and before drying or curing, the film can be wiped off with a tissue dampened with a suitable solvent (eg. acetone) [6]. This method proved to be particularly useful for obtaining a step in the sol-gel deposited silica films that would be suitable for using in film thickness measurement. A small area of the film was removed by wrapping a lens cleaning tissue dampened with acetone around a flat edged spatula and wiping this from centre to edge in a smooth movement. The area removed from a typical 50mm square plate is shown in fig. 5.6. When multiple silica layers were deposited, the thickness of each layer was measured before the deposition of the next layer.

#### **5.2.8 Capillary fill device (CFD)**

The capillary fill device (CFD), as described by *Badley et al* [7] and *Robinson et al* [8], and in chapter 2, section 2.6.4, allows accurate control of the volume of the sample liquids introduced into the capillary gap. The capillary cell also provides a useful means by which test solutions and fluorescent solutions can be held next to the thin films devices that are the subject of this thesis.



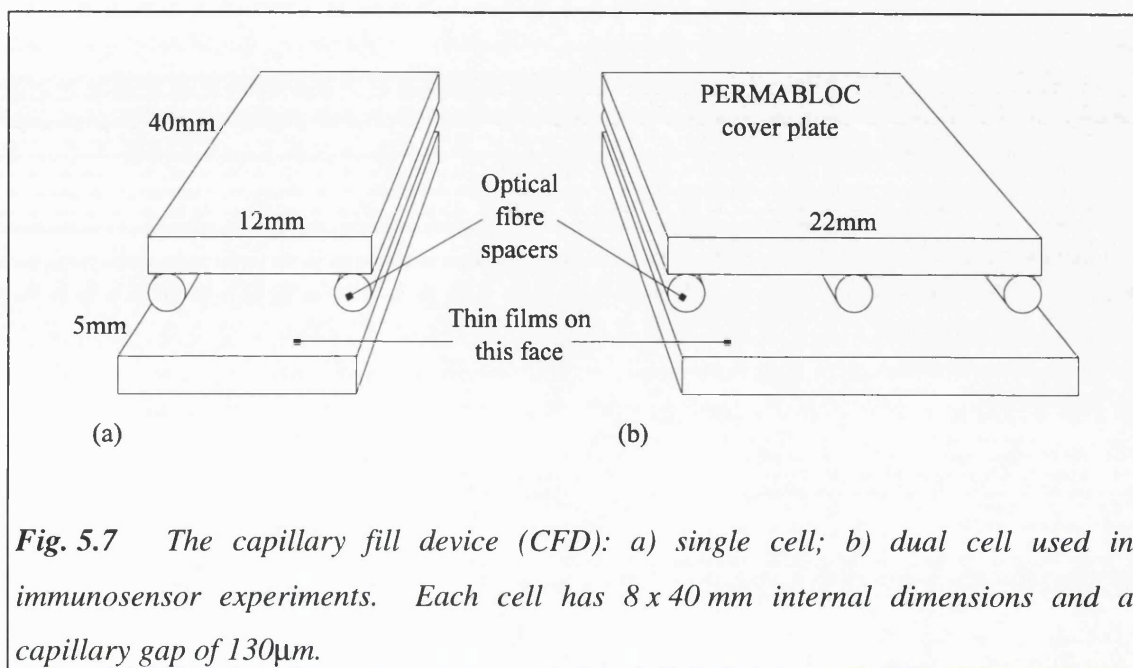


**Fig. 5.7** The capillary fill device (CFD): a) single cell; b) dual cell used in immunosensor experiments. Each cell has 8 x 40 mm internal dimensions and a capillary gap of 130µm.

Capillary cells, as illustrated in fig. 5.7, were fabricated using 125µm optical fibres (stripped of their protective plastic coating) as spacers, and PERMABLOC float glass cover plates. UV curing glue was used to hold the plates and spacers together. The UV glue, after curing, was resistant to water but was easily dissolved by organic solvents such as ethanol, methanol or acetone. The size of the capillary gap was  $130 \pm 5 \mu\text{m}$  after measuring the thickness of 25 cells with a micrometer (*Mitutoyo, Japan*). The lip present on one end of the cell was used to introduce the sample solution

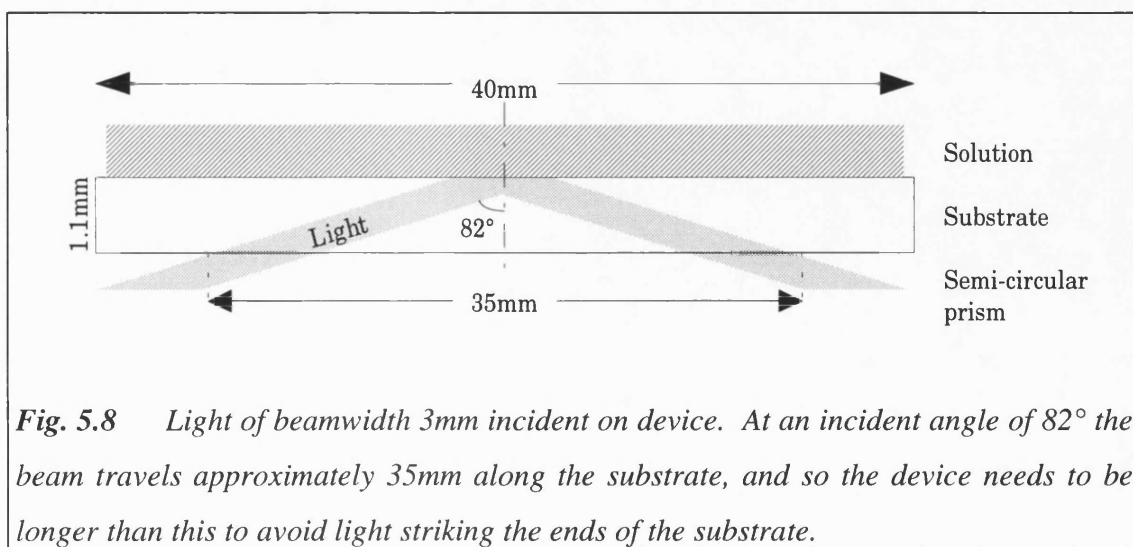


**Fig. 5.8** Light of beamwidth 3mm incident on device. At an incident angle of 82° the beam travels approximately 35mm along the substrate, and so the device needs to be longer than this to avoid light striking the ends of the substrate.

into the capillary gap. Fig. 5.7b shows a CFD with two capillary cells. These were used in immunosensor experiments where one cell contains a reference solution and the other contains the sample solution. The length of the capillary cell (40mm) was chosen so that light could be coupled into and out of the device, without striking the ends, at angles of incidence up to 82° (see fig. 5.8). Any light striking the ends of the device would be scattered and would give rise to a high background signal. The length of the capillary cell was limited by the size of the substrates onto which the thin films were spun (50mm square).

### 5.2.9 Experimental apparatus

The experimental apparatus illustrated in fig. 5.9 was designed and assembled to measure evanescently excited fluorescence to: a) allow the characterisation of the multilayer thin film system; and b) perform immunoassay measurements. Note that all interference filters used in the experimental apparatus were obtained from *Ealing*

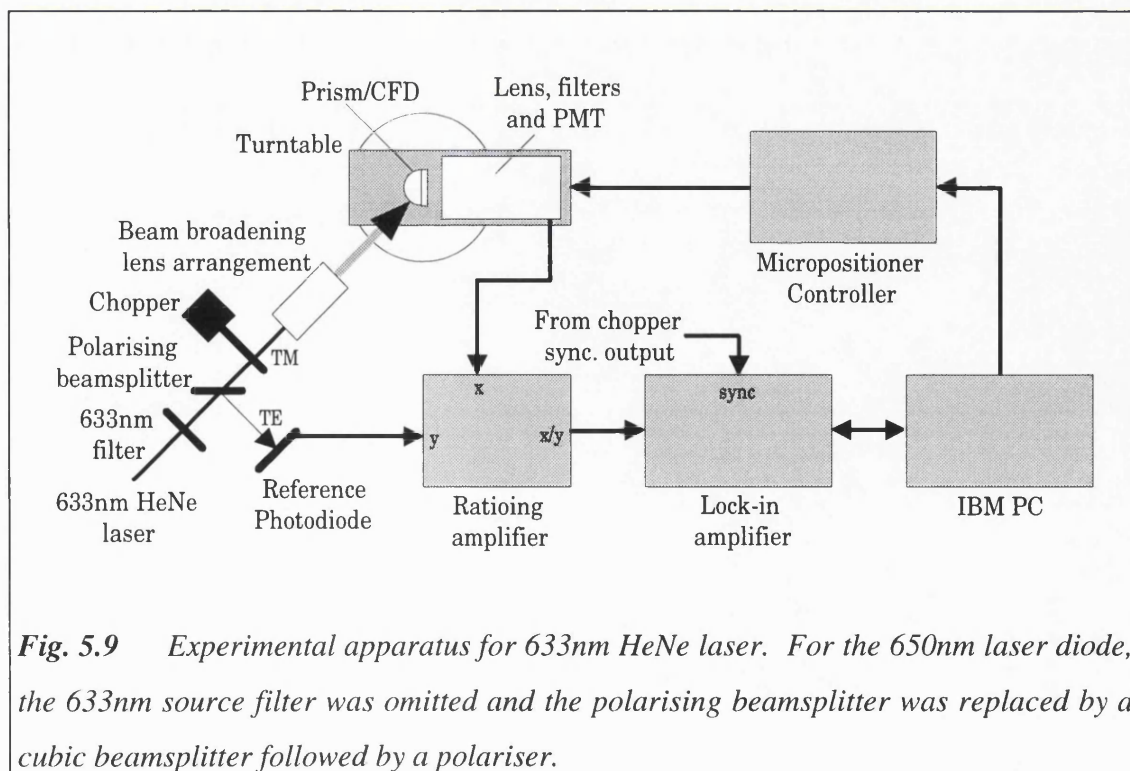


**Fig. 5.9** Experimental apparatus for 633nm HeNe laser. For the 650nm laser diode, the 633nm source filter was omitted and the polarising beamsplitter was replaced by a cubic beamsplitter followed by a polariser.

*Electro-Optics Ltd., UK* and lenses were either obtained from *Ealing* or *Spindler & Hoyer Ltd., UK*.

### 5.2.9.1 The light source

Two laser sources were used for most of the immunosensor measurements, but initially, only a single source (the helium-neon laser) was available for the multilayer thin film system characterisation.

**Helium-Neon laser.** The laser was a 5mW, 632.8nm output Helium-Neon laser (*Melles-Griot, US*) whose output was filtered by a 633nm bandpass interference filter to remove any spurious laser emission at different wavelengths. Any power fluctuations in the output of the laser were compensated by using a monitor photodiode and a ratioing amplifier. A polarising beamsplitter directed the TE polarised light from the laser to the monitor photodiode and the TM polarised light was used as the exciting light. The ratioing amplifier was built around the AD524 instrument amplifier and AD534JH analogue multiplier IC's (*Analogue Devices*). The TM polarised beam was then chopped (using a chopper from *Mono-Light Instruments Ltd., UK*) at a frequency of 400Hz synchronised to the output of a *Hewlett-Packard HP3325A* function generator. The chopped TM beam was then broadened and collimated in the horizontal plane using the lens arrangement of fig. 5.10 such that the beam excited an area on the capillary fill

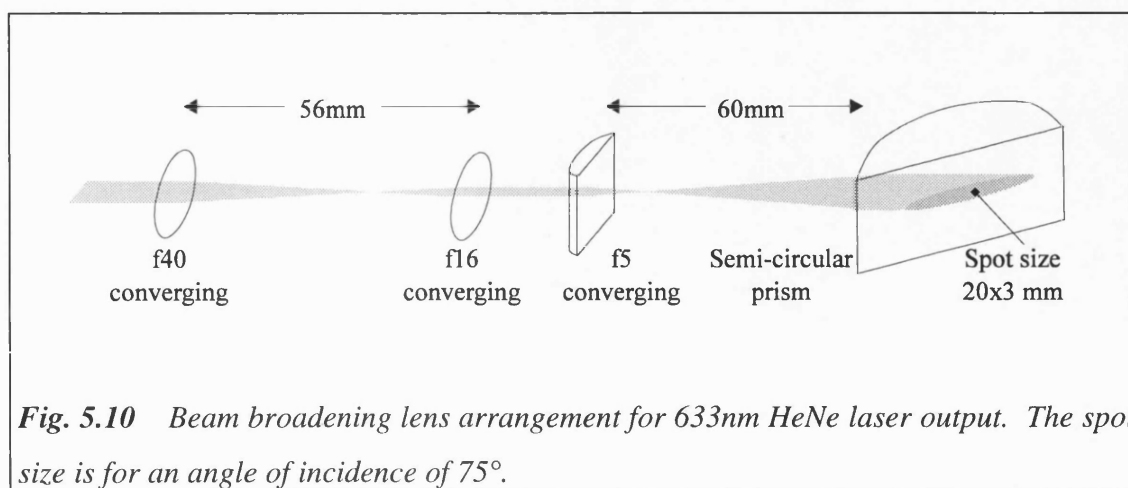


**Fig. 5.10** Beam broadening lens arrangement for 633nm HeNe laser output. The spot size is for an angle of incidence of  $75^\circ$ .

device measuring approximately 20 x 3 mm, at an angle of incidence of approximately 75°. However, due to the lack of appropriate lenses, the final, broadened beam had a slight convergence of approximately 0.12°.

**Laser Diode.** The second laser source was a 1mW, 650nm output laser diode module (LDM145/650/1 from, *Imatronic Ltd., UK*). The output of this laser was not filtered because a suitable 650nm bandpass filter was not available. Any output power fluctuations were minimised, as described for the helium-neon laser above, but a non-polarising beamsplitter was used in the case of the laser diode. The beam was then chopped (as for the 633nm source), TM polarised, broadened and collimated using the lens arrangement of fig. 5.11 to excite an area approximately 20 x 4 mm at a 75° angle of incidence. The estimated divergence of the beam was approximately 0.5°.

The exciting light beam was broadened to excite fluorescence from a large proportion of the surface area of the thin films. This would allow the averaging of the fluorescence signals, and would help to compensate for minor variations in the thicknesses or properties of the thin films, or in the distribution of the fluorophores close to the surface of the thin films.

### 5.2.9.2 Prism/CFD arrangement

The prism and CFD arrangement is illustrated in fig. 5.12. The prism (donated by

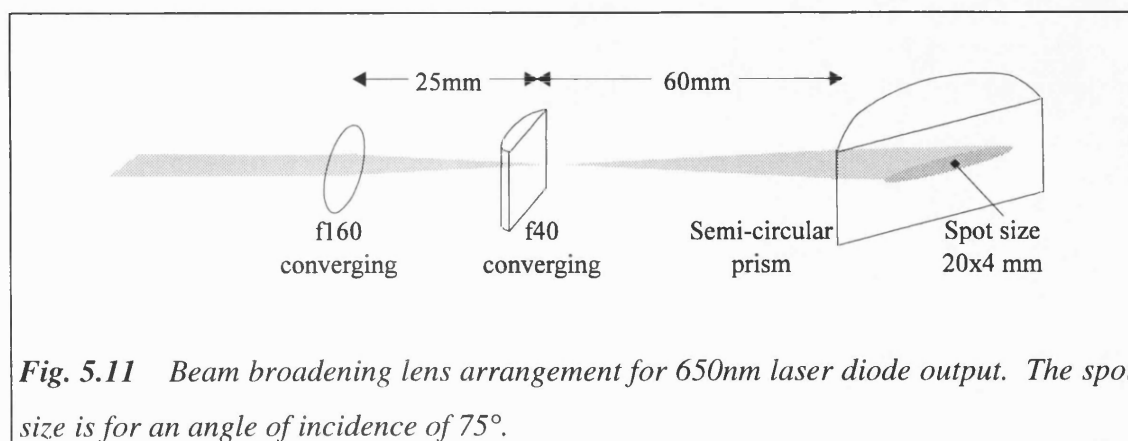


**Fig. 5.11** Beam broadening lens arrangement for 650nm laser diode output. The spot size is for an angle of incidence of 75°.

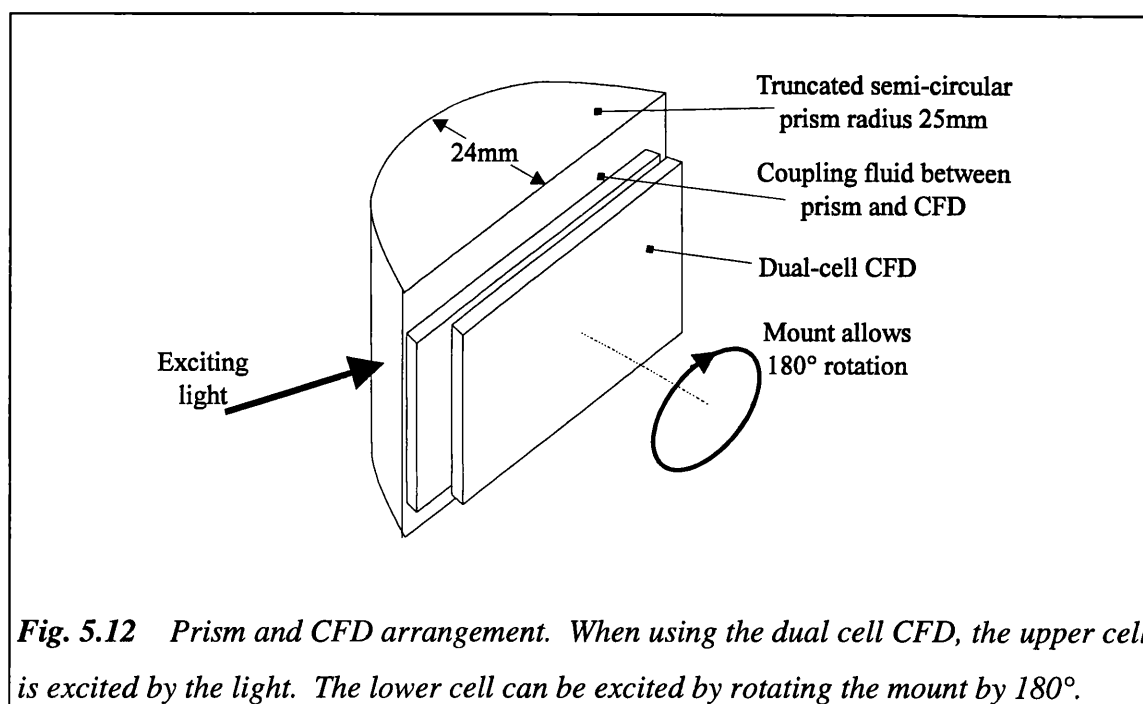


**Fig. 5.12** Prism and CFD arrangement. When using the dual cell CFD, the upper cell is excited by the light. The lower cell can be excited by rotating the mount by 180°.

*Serono Diagnostics Ltd.*) is a semi-circular prism truncated by 1mm to allow for the thickness of the substrate on the CFD. The refractive index (measured with an ABBE refractometer) of the prism is equal to the float glass substrate refractive index, ie. 1.517 at 633nm. A fluid of refractive index 1.520 (*Cargille Laboratories Inc., US*) was used between the prism and CFD. This fluid was chosen to closely match the refractive indices of the prism and CFD substrate to minimise partial reflections at the interfaces.

A mount was built to hold the prism and CFD arrangement securely, with minimal lateral movement. When using the two cell CFD (fig. 5.7b) in immunosensor experiments, the mount was designed so that it could be rotated by 180° to allow fluorescence measurements to be made on both cells.

### 5.2.9.3 Fluorescence collection and measurement

The emitted fluorescence was collected by the lens arrangement of fig. 5.13 giving a collection angle of ~60° and an observation area of 25 x 10 mm. Scattered exciting and background light were filtered by two interference filters. One filter (a 700±40nm bandpass filter) was used for both the 633nm and 650nm light sources. The second

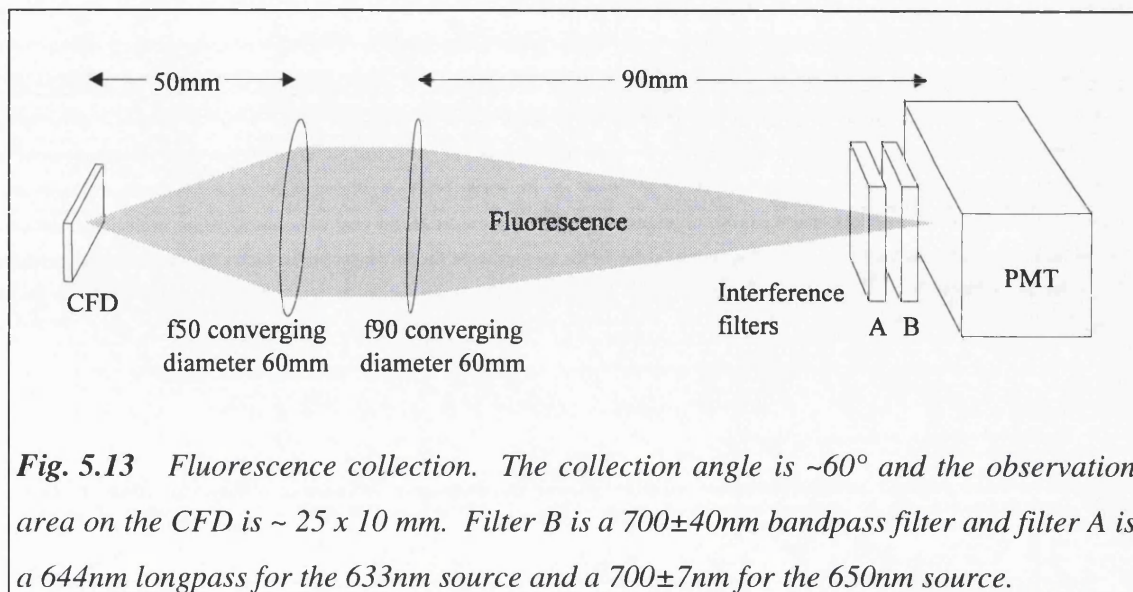


**Fig. 5.13** Fluorescence collection. The collection angle is  $\sim 60^\circ$  and the observation area on the CFD is  $\sim 25 \times 10$  mm. Filter B is a  $700 \pm 40$  nm bandpass filter and filter A is a 644 nm longpass for the 633 nm source and a  $700 \pm 7$  nm for the 650 nm source.

filter was a 644 nm longpass filter for the 633 nm source and a  $700 \pm 7$  nm bandpass filter for the 650 nm source (see fig. 5.13). The fluorescence signal was measured by a photomultiplier tube, PMT (type R928 from, *Hamamatsu Ltd., UK*) with an anode-cathode voltage of 650V and a load resistor of  $1\text{M}\Omega$ . The signal was then high pass filtered (using a simple RC filter with a 3dB cutoff at 150Hz) to remove the dc component of the PMT output, thus reducing background light and PMT dark current interference. As illustrated in fig. 5.9, the PMT signal was then fed into the ratioing amplifier (see section 5.2.9.1) and divided by the reference photodiode signal to compensate for any power fluctuations in the output of the laser. The amplitude of the ratioed signal was then measured by a lock-in amplifier (EG&G 5206 from, *Princeton Applied Research, US*) synchronised with the chopper frequency.

#### 5.2.9.4 Angular scans

To allow the measurement of the angle of incidence for resonance in the multilayer thin film system (ie. when there is peak fluorescence emission), it was necessary to measure the emitted fluorescence at varying angles of incidence of the exciting light. This was achieved by placing the prism/CFD arrangement (fig. 5.12) and the fluorescence collection arrangement (fig. 5.13) on a micropositioner turntable with

an angular resolution of  $0.001^\circ$  (*Micro-Controle, France*) with the CFD lying vertically on the axis of rotation of the turntable (see fig. 5.9). The turntable was controlled by a micropositioner controller (type IT6D CA2 from, *Micro-Controle, France*).

The micropositioner controller and the lock-in amplifier were linked to a PC compatible computer (PC III, *Opus Ltd., UK*) via an IEEE interface board (*Brain Boxes Ltd., UK*). Software routines for controlling the interface board, micropositioner controller and the lock-in amplifier were written in 'C' (*Microsoft 'QuickC'*) and these routines could then be incorporated into any 'C' program. A 'C' program utilising these routines was written to automatically perform angular scans (with input initial and final angles of incidence and angle step size) and record and save the signal levels measured by the lock-in amplifier. The resulting text file could then be imported into a commercial spreadsheet or charting application (eg. *Microsoft EXCEL*) or into another program for data manipulation.

### **5.2.10 Multilayer system characterisation**

To optimise the multilayer thin film system for immunosensor device fabrication, it was necessary to ascertain the refractive indices of the thin films and to obtain the variation of resonant angle of incidence with film thicknesses or refractive indices.

#### **5.2.10.1 Thin film refractive index estimation**

Ellipsometry [9] and, a simpler method, waveguide mode analysis [4, 5, 11] are common techniques used for the determination of thin film parameters such as refractive index and film thickness. Even surface plasmon resonance has been used for thin film characterisation [10]. Waveguide mode analysis becomes more difficult if multiple layers are involved (ie. the standard single slab waveguide model cannot be applied) and is impossible if the film refractive index is less than that of the substrate (because the thin film is then not a waveguide). Although ellipsometry can provide accurate results,

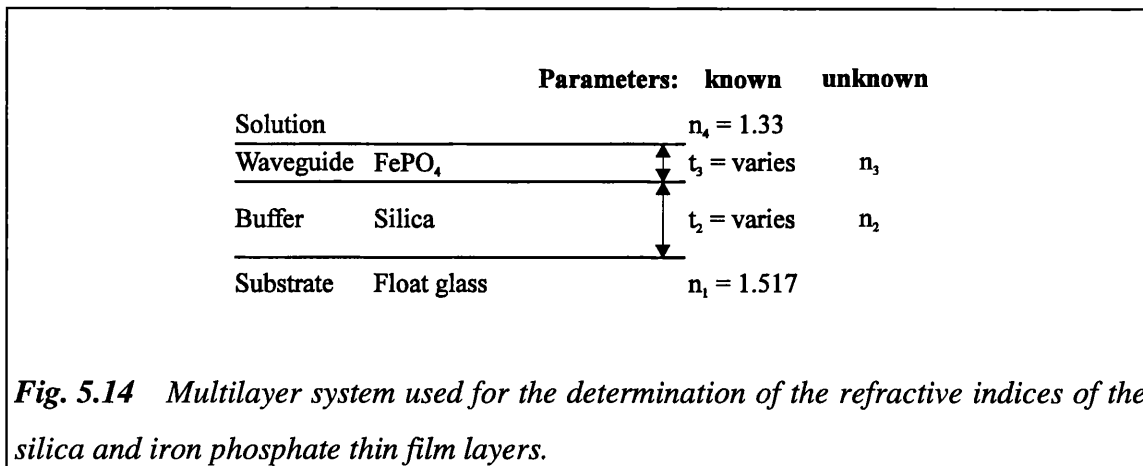


**Fig. 5.14** Multilayer system used for the determination of the refractive indices of the silica and iron phosphate thin film layers.

it requires complex instrumentation and, due to the lack of availability of a suitable ellipsometry instrument, a different method was attempted.

Researchers have used the optical properties of thin films (ie. optical interference, resonance, etc) to estimate the refractive indices of the thin films [12]. It was therefore decided that the software programs developed for the modelling of the multilayer system could be used to estimate the refractive indices of the thin films by fitting experimental data to the theoretical model.

Multilayer thin films devices (as shown in fig. 5.14) were fabricated as described in sections 5.2.1 to 5.2.6 with varying silica and iron phosphate film thicknesses. Single cell capillary fill devices (as shown in fig. 5.7a) were then assembled as described in section 5.2.8. The capillary cells were filled with a solution of Nile blue fluorescent dye and an angular scan to measure the emitted fluorescence as a function of the angle of incidence of the exciting light was performed. This gave a typical fluorescence vs. angle of incidence curve as shown in fig. 5.15. The angular resolution on all the scans was 0.1°.

The angle of incidence for peak fluorescence emission was fitted to a theoretical calculation of the angle of incidence for peak evanescent field strength using estimated silica and iron phosphate refractive indices. Note: all other parameters required in the calculation (eg. film thicknesses, etc) were measured or known. The fitting was done by

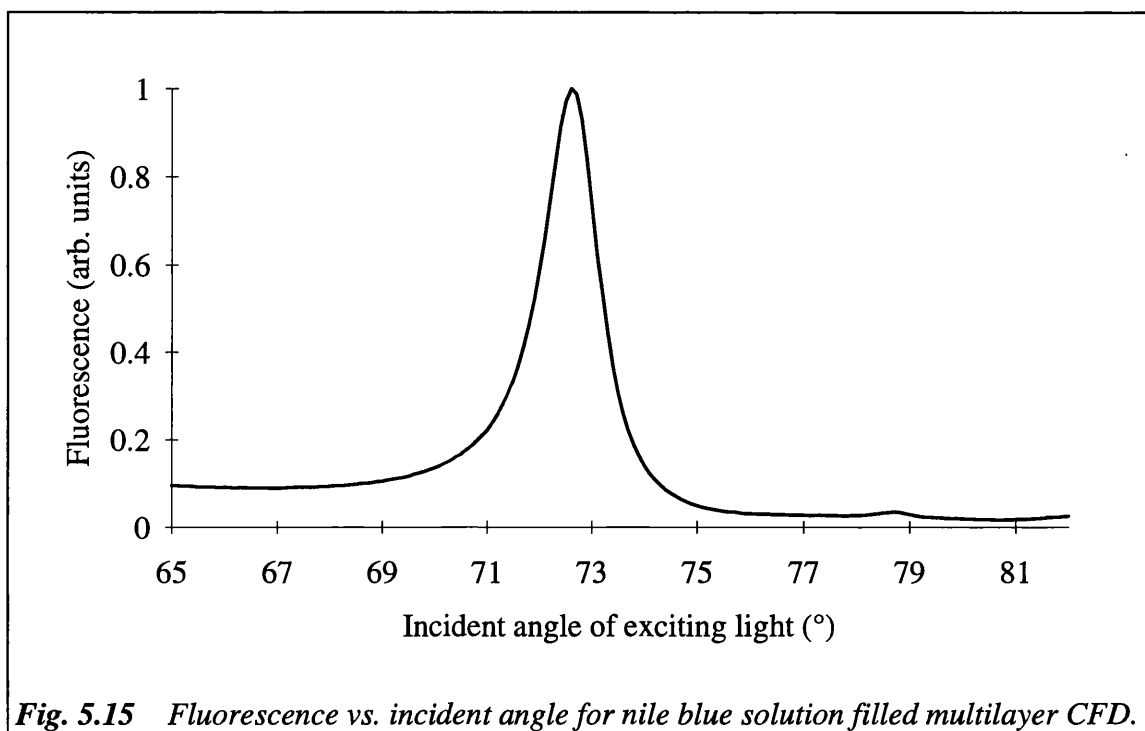


Fig. 5.15 Fluorescence vs. incident angle for Nile blue solution filled multilayer CFD.

a least squares minimisation technique using a two-dimensional simplex minimisation routine due to *Nelder & Mead* [2]. The 'C' language code for the simplex routine was obtained from Numerical Recipes in C [1].

### 5.2.10.2 The Nile blue solution

Nile blue (see fig. 5.16), from *Lambda Physik, Germany*, was used as the fluorescent dye as it had an absorption peak near 633nm [13] and thus fluorescence could easily be excited by using a 633nm HeNe laser. The absorption spectra (taken

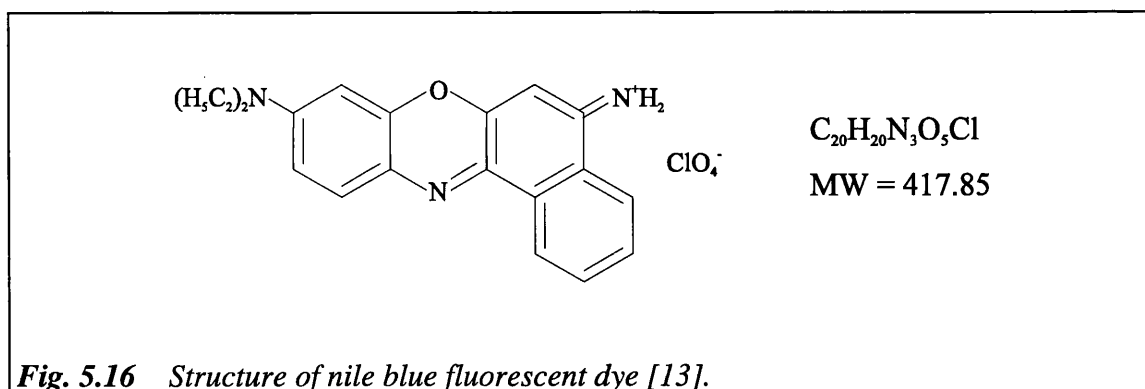
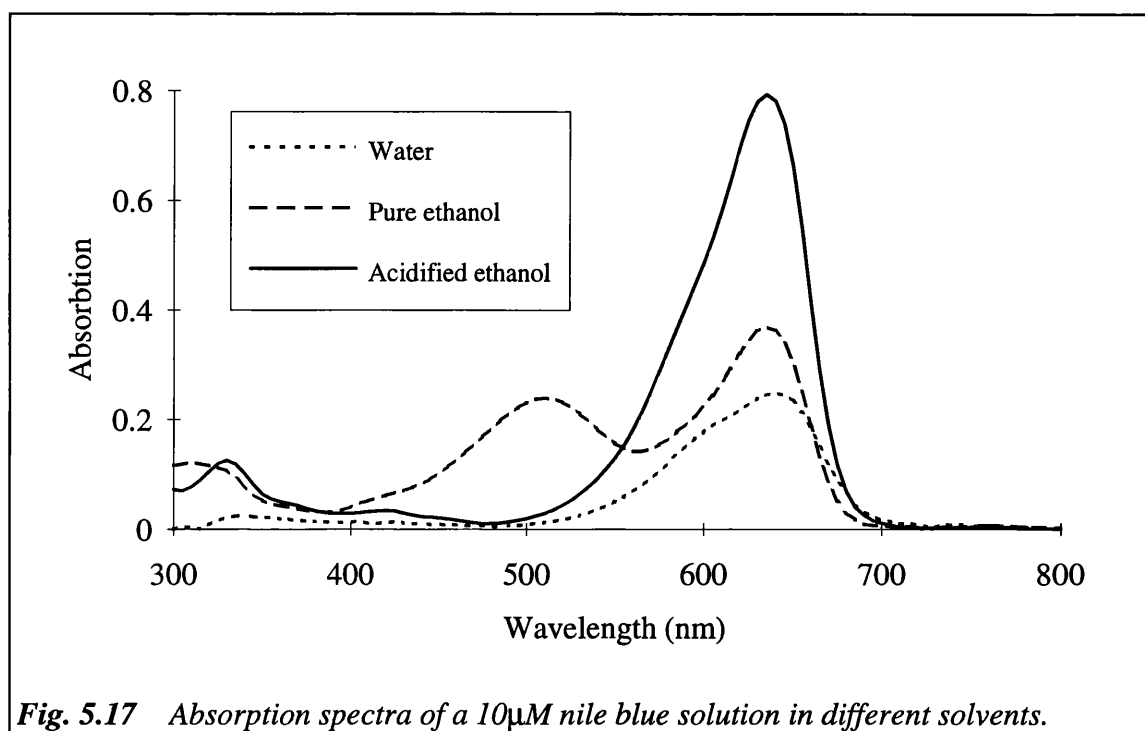
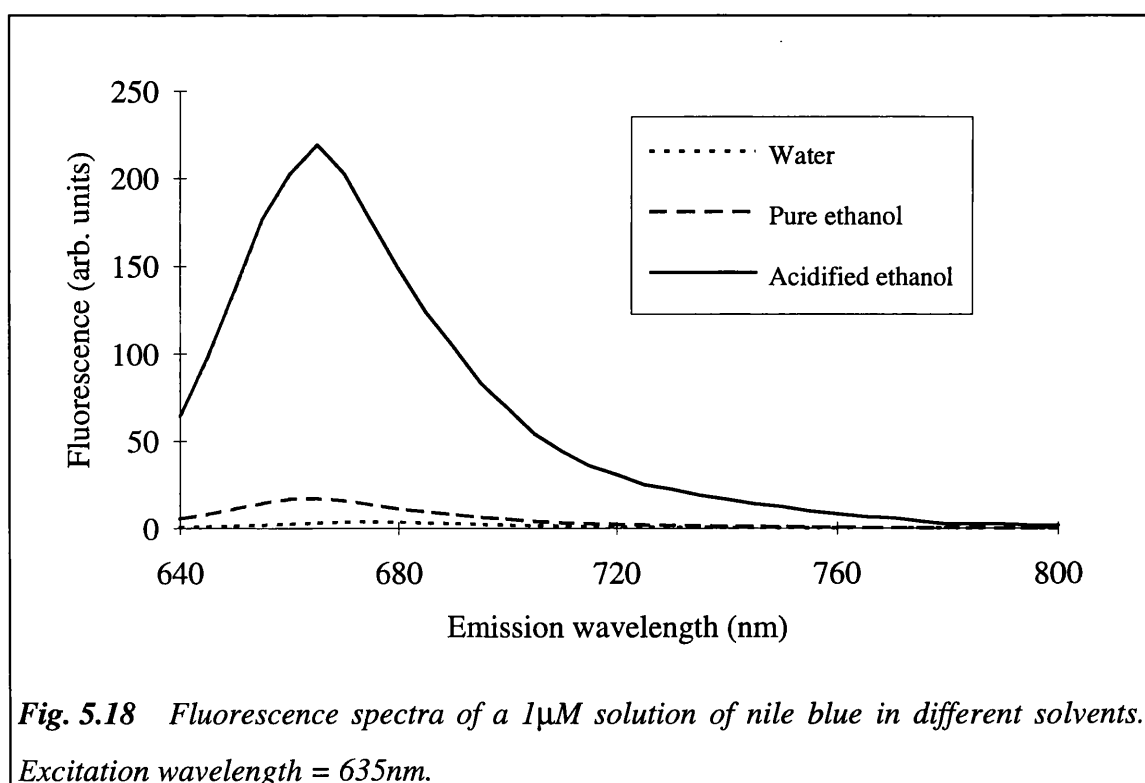
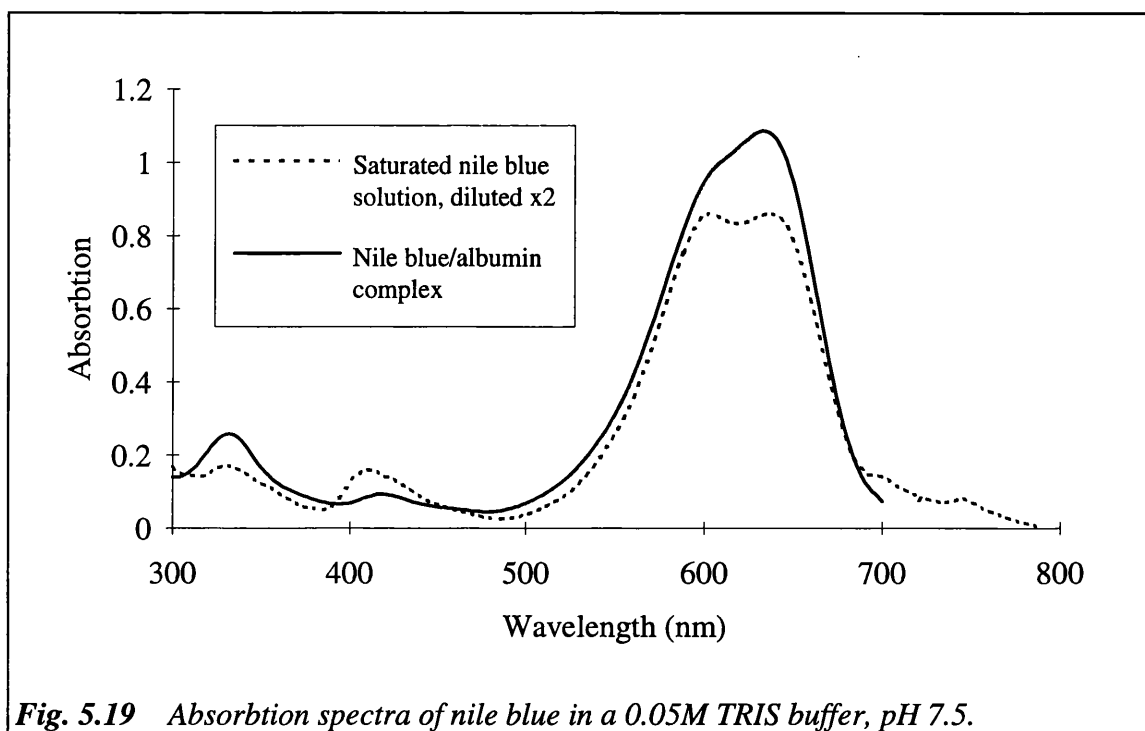


Fig. 5.16 Structure of Nile blue fluorescent dye [13].



with a PU8625 Spectrophotometer, *Philips Analytical Ltd, UK*) and fluorescence spectra (taken with a MPF-44A Fluorescence Spectrophotometer, *Perkin-Elmer, UK*)





**Fig. 5.19** Absorbance spectra of Nile blue in a 0.05M TRIS buffer, pH 7.5.

for solutions of Nile blue in different solvents are shown in Figs. 5.17-5.18. Solutions of Nile blue in ethanol could not be used, as ethanol destroys the UV-curing glue used in

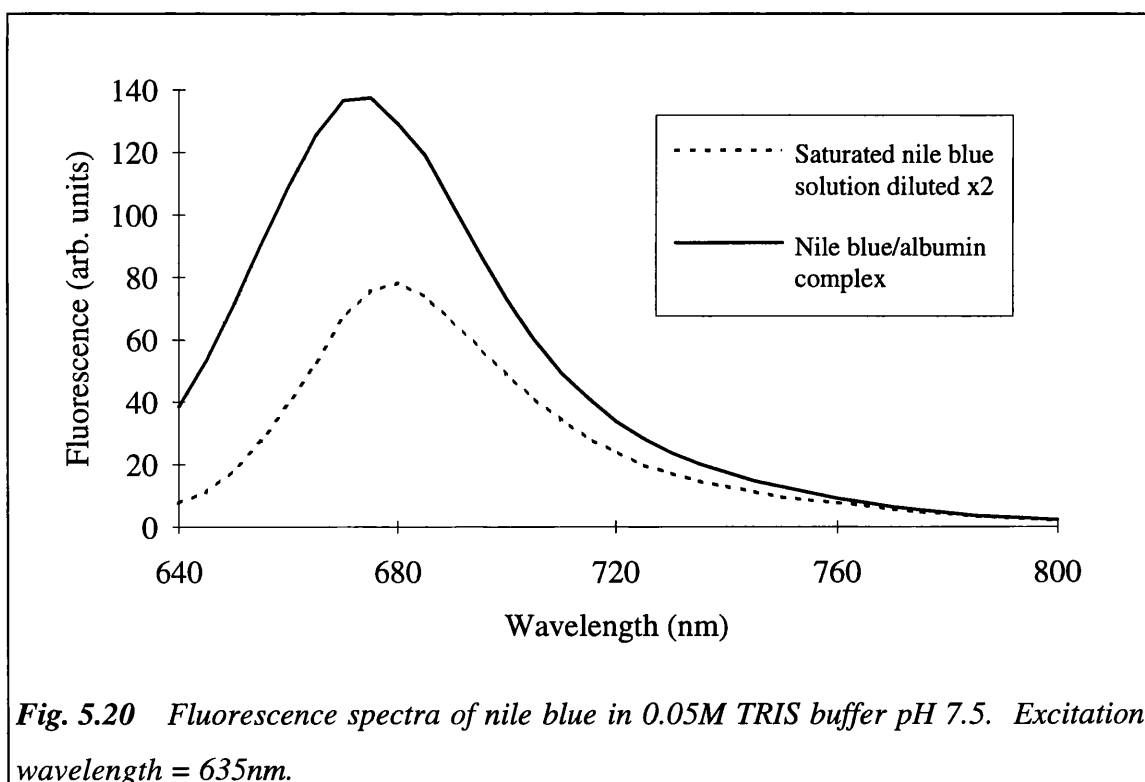


**Fig. 5.20** Fluorescence spectra of Nile blue in 0.05M TRIS buffer pH 7.5. Excitation wavelength = 635nm.

the CFD's. However, the solutions in water were only weakly fluorescent. The two absorption peaks on the spectra for Nile blue in pure ethanol (*BDH Ltd., UK*, SpectroSol grade) may be due to the dye existing in two forms and decreasing the pH allows one of the two forms to predominate [14].

It was decided to complex the dye with a protein in a buffer solution to stabilise the pH and to make the Nile blue dye more fluorescent in water. This would allow the dye/protein complex to be dissolved in water but retain an organic environment immediate to the Nile blue molecule. A saturated solution of Nile blue in a 0.05M TRIS buffer (*Sigma Chemical Co., UK*), pH 7.5, was prepared and any undissolved material was filtered out with a 0.2µm syringe filter. A 1% solution of bovine serum albumin (*Sigma*) was also prepared in 0.05M TRIS buffer, pH 7.5 and filtered using qualitative filter paper No.1 (*Whatman Ltd., UK*). The two solutions were then mixed in a 1:1 volume ratio to yield a Nile blue/0.5% albumin solution in 0.05M TRIS buffer pH 7.5. The absorption and fluorescence spectra are given in figs. 5.19 - 5.20.

## 5.3 IMMUNOSENSING EXPERIMENTS

### 5.3.1 The immunoassay

A straightforward sandwich immunoassay for mouse-IgG (the analyte) in a phosphate buffered saline solution was chosen to evaluate the multilayer thin film immunosensor. The choice was largely based on the simplicity of the assay, the availability of the reagents and the expense of performing repeated assays. The capture antibody that was immobilised on the sensor surface was affinity purified polyclonal sheep anti-mouse IgG antibody (*Binding Site Ltd., UK*). The analyte was mouse serum, calibrated for IgG content, (*Binding Site Ltd.*) which was serially diluted with phosphate buffered saline to give the required mouse IgG concentration. Two differently labelled anti-mouse IgG antibodies were used to complete the assay. The

first was a polyclonal goat anti-mouse IgG antibody conjugated to a fluorescent allophycocyanin label (*Molecular Probes, US*). The second was polyclonal sheep anti-mouse IgG antibody (*Binding Site Ltd.*) that was labelled with a fluorescent sulphoindocyanine dye - CY5.18 (*Biological Detection Systems, US*). The two fluorescent dyes were chosen as both can be used with either a 633nm HeNe laser or a 650nm semiconductor laser diode. The allophycocyanin label is a large, high quantum yield fluorescent [15] protein with a molecular weight of ~104000 whereas the CY5.18 label is much smaller (molecular weight of 937) [16].

Material	Formula	Supplier	Code	Grade
<b>Solvents</b>				
N,N-dimethylformamide	HCON(CH <sub>3</sub> ) <sub>2</sub>	Aldrich Ltd.	22,705-6	
<b>Immobilisation</b>				
glycidyl oxypropyl-trimethoxysilane	C <sub>9</sub> H <sub>20</sub> O <sub>5</sub> Si	Fluka.	50040	
N,N'-carbonyl diimidazole	C <sub>7</sub> H <sub>6</sub> N <sub>4</sub> O	Lancaster Synthesis.	0223	
Brij-35		Aldrich Ltd.	85,836-6	
TRIZMA buffer		Sigma Ltd.		
<b>Antibody labelling</b>				
dimethyldichlorosilane solution (2%)		BDH	33164	
hydroxylamine monohydrochloride		Sigma Ltd.	H-9876	1

**Table 5.2** Some chemicals used in performing the immunosensor experiments

### **5.3.2 Chemicals**

The chemicals used in preparing for and performing the immunosensor experiments were generally obtained from *BDH Ltd, UK* and were of AnalaR grade. The chemicals that were not obtained from BDH, or that were of a special grade are listed in table 5.2.

### **5.3.3 Multilayer thin film preparation**

The multilayer thin films on 50mm square substrates were prepared as described in section 5.2. Two coats of silica (deposited at a spin speed of 800rpm and cured at 500°C) were used to obtain a silica film with a thickness between 750 - 800nm. The iron phosphate film was deposited using a 0.25M solution and spun at 800rpm to give a film thickness between 150 - 170nm. Thus the angle of incidence of the exciting light required for resonance was between 75 - 77°. The film thicknesses quoted are estimates based on previous measurements of film thickness as a function of spin speed. The rather destructive method of film thickness measurement was avoided to minimise non-uniformities in the thin films and to allow the use of most of the surface area. The substrates were then scribed on the reverse face (as shown in fig. 5.21) to allow the substrate to be cut to fabricate capillary cells after protein immobilisation.

### **5.3.4 Capture IgG immobilisation**

A standard method [17, 18] for the covalent coupling of proteins to a glass surface was used. The substrates bearing the multilayer surface and scribed on the reverse face were soaked in a 1% v/v DECON90 detergent solution for 10mins., then rinsed with purified water and left to soak in purified water for 1 hour. The plates were then placed in a 350mM glycidyl oxypropyltrimethoxysilane solution (unbuffered pH of 3.5) for two hours, followed by a rinse and then blown dry. The plates were transferred to a dry rack and immersed in a 0.125M 1,1'-carbonyldiimidazole solution in dry acetone for 15mins.,

followed by a rinse in dry acetone and then blown dry. The plates were then incubated in contact with a 1 $\mu$ M solution of sheep anti-mouse IgG antibody in phosphate buffered saline (PBS - 10mM phosphate buffer, 100mM saline) pH 7.4 for four hours. The plates were then rinsed in PBS followed by a rinse in PBS containing 1% w/v Brij 35. A 300mM sucrose solution with 5mM sodium azide in a 50mM TRIS buffer pH 7.5 was spun onto the immobilised surface and dried at room temperature to preserve the activity of the immobilised antibodies. The sucrose layer thickness was approximately 10 $\mu$ m. The plates were then stored with desiccant at 4°C. The density of active binding sites for antibodies immobilised on a phosphate glass following the above procedure has been previously determined [19, 20] to be approximately 3 fmol/mm<sup>2</sup>. This represents about 8% of the possible active sites assuming that the antibodies would be hexagonally close packed.

The above procedure was also performed for a batch of float glass substrates, not bearing any thin films, that were used to make some straightforward total internal reflection immunosensing measurements, as a comparison for the multilayer system. Immobilisation, in this case, was on the face that had not been in contact with the molten tin during the production of the float glass.

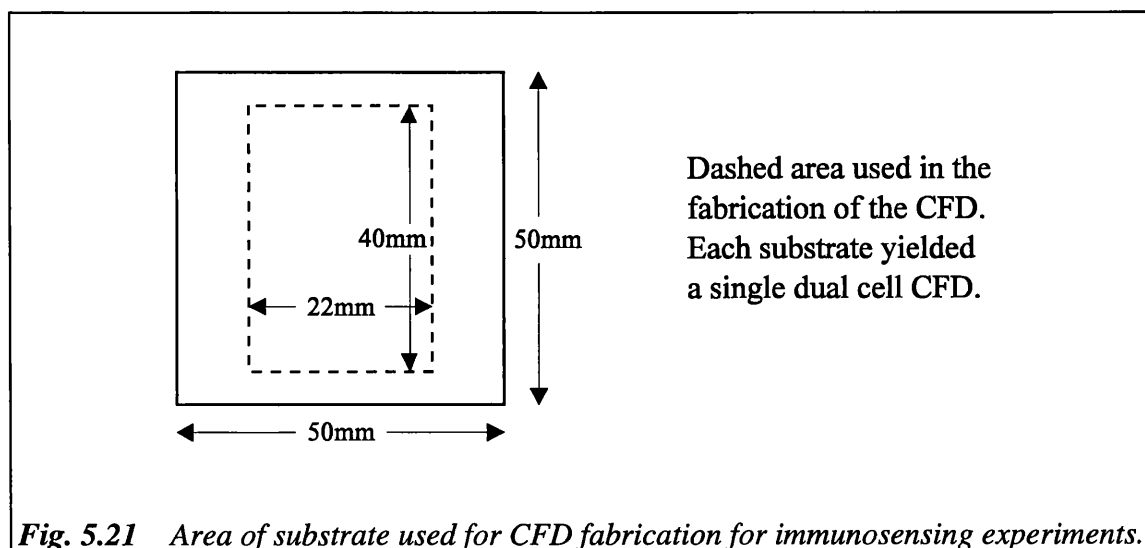


**Fig. 5.21** Area of substrate used for CFD fabrication for immunosensing experiments.

### 5.3.5 CFD assembly

Dual cell (see fig. 5.7) capillary fill devices were assembled as described in section 5.2.8 using the area of the substrate indicated by the dashed line in fig. 5.21.

### 5.3.6 The labelled antibody

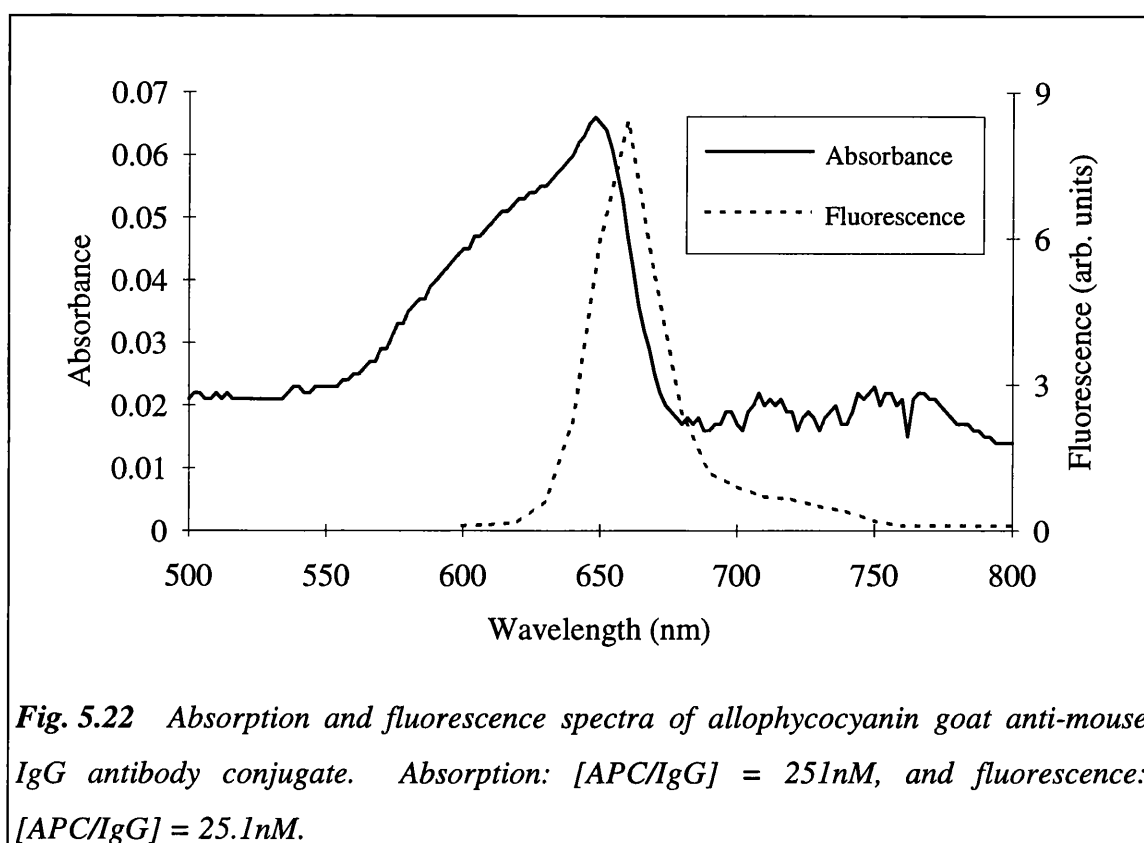
Two different labelled antibodies were used: an allophycocyanin labelled goat anti-mouse IgG antibody and a CY5.18 dye labelled sheep anti-mouse IgG antibody.

#### 5.3.6.1 Allophycocyanin

Allophycocyanin is one of the phycobiliproteins [15] used in the light harvesting process in species of blue-green algae. Phycobiliproteins have, therefore, been evolved to maximise light absorbance and fluorescence, whilst minimising susceptibility to fluctuations in the internal or external environment. Hence, phycobiliproteins make ideal candidates for use as fluorescent labels in immunoassays, but there are drawbacks. They are relatively large proteins (of the order of the size of an antibody) and, thus, are susceptible to non-specific binding, and when conjugated to an antibody can sterically

	<b>Allophycocyanin</b>	<b>CY5.18</b>	<b>Sheep antibody</b>	<b>Goat antibody</b>
Molecular weight	104000	937	160000	160000
Absorption max. (nm)	650	650	280	280
Extinction coeff. at 280nm ( $M^{-1}cm^{-1}$ )	125000	12500	240000	224000
Extinction coeff. at max. absorbance ( $M^{-1}cm^{-1}$ )	700000	250000	-	-
Emission max. (nm)	660	668	-	-

*Table 5.3 Optical characteristics of the antibodies and fluorescent labels.*



hinder the binding of the antibody to its antigen [21].

One of the aims of this project was the use of inexpensive methods and components and thus there was a need to avoid the use of a Helium-Neon laser excitation source and use, instead, a semiconductor laser diode. The ready availability of allophycocyanin conjugated antibody and possibility of exciting allophycocyanin with both a 633nm HeNe laser and a 650nm laser diode, would thus allow comparison between the two excitation sources.

The allophycocyanin label:antibody ratio was determined spectrophotometrically to be 1:2.66, using the data given in table 5.3. The absorption and fluorescence spectra of the allophycocyanin-antibody conjugate are shown in fig. 5.22.

### 5.3.6.2 CY5.18

This dye has very similar characteristics to allophycocyanin (see table 5.3) but it is not a protein and has a much lower molecular weight than allophycocyanin. This dye became commercially available late in the project and was used as a comparison for the allophycocyanin label.

### 5.3.6.3 Labelling of antibody with CY5.18 dye

A reactive form of the CY5.18 dye (CY5.18 succinimidyl ester) was obtained from *Biological Detection Systems, US* and used to label sheep anti-mouse IgG antibody (*Binding Site Ltd., UK*). The procedure adopted was very similar to that suggested by *Biological Detection Systems*.

The antibody (in a TRIS buffer pH 7.4) was dialysed against 3.5 l carbonate buffer pH 8.5 to obtain a solution in carbonate buffer. A *Pierce* Microdialyser with a preframed dialysis membrane (molecular weight cut off of 8000 or greater) was used.

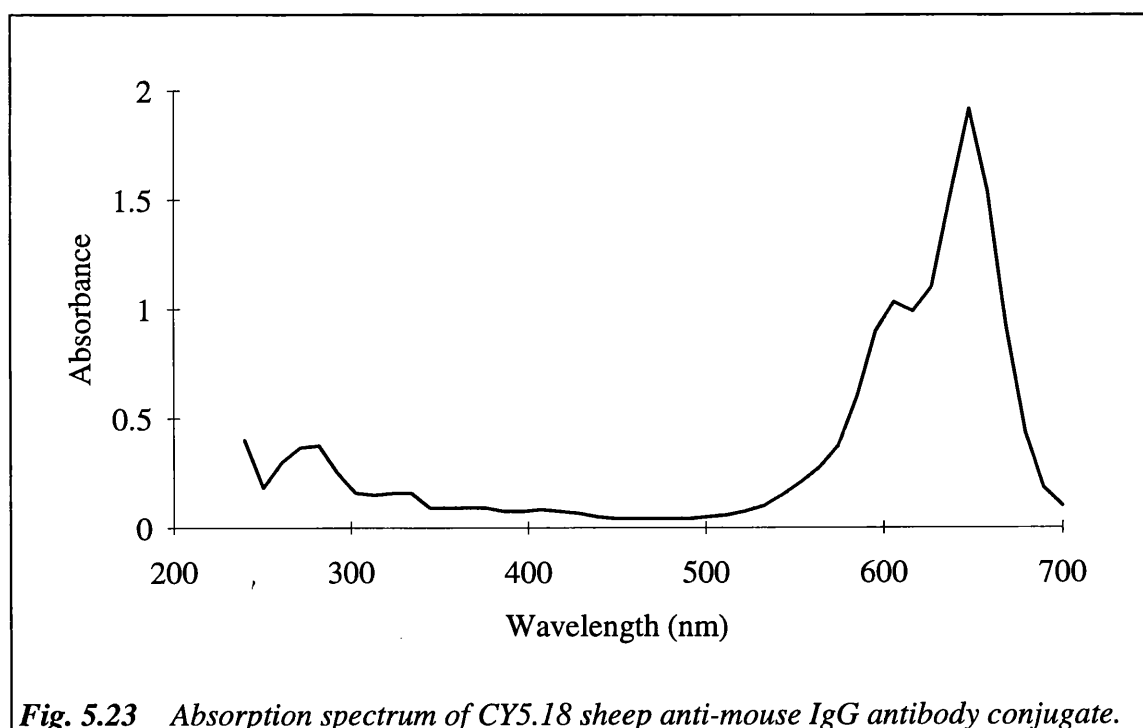


**Fig. 5.23** Absorption spectrum of CY5.18 sheep anti-mouse IgG antibody conjugate.

The CY5.18 reactive dye was dissolved in dimethylformamide (DMF) which was then added to the stirred antibody solution, and the mixture was incubated for one hour at 4 °C. The labelling reaction was stopped by adding hydroxylamine monohydrochloride dissolved in 2M sodium hydroxide, after which the mixture was incubated for ½ hour at 4 °C. The mixture was then dialysed against 3.5 l of 10mM phosphate buffer with 100mM saline to obtain a CY5.18 labelled antibody solution in phosphate buffered saline. The dye:protein ratio was determined spectrophotometrically to be 6.5:1. The absorption spectrum of the CY5.18 dye-antibody conjugate is shown in fig. 5.23.

### 5.3.7 Immunosensing measurements

The density of active binding sites on the immobilised antibody layer was estimated at  $\sim 3$  fmol/mm<sup>2</sup> (see section 5.3.4). When used in a CFD with a capillary gap of 130µm, the binding sites will be saturated when the analyte concentration exceeds  $\sim 25$ nM (assuming that all the analyte binds to the capture antibody). To ensure that all the analyte binds to the labelled antibody, an excess concentration (over the maximum analyte concentration) of the of the labelled antibody is normally used [22]. The labelled antibody concentration used in the immunassays performed was 250nM (a 10-fold excess).

The analyte solution was diluted mouse serum calibrated for mouse IgG content (*Binding Site Ltd., UK*), the diluent being 0.1M phosphate buffered saline. The required concentration of mouse IgG was obtained by serial dilution. Note that both the labelled antibody and analyte solutions were diluted to twice the required concentration which, on mixing in equal volumes, would yield the required concentrations.

The analyte and labelled antibody solutions were pre-mixed (for experimental convenience) 10 mins. before use and allowed to reach ambient temperature. The dual cell CFD was also allowed to reach ambient temperature before use and then assembled in the mount. The capillary cells on the CFD were then filled with a reference (a 250nM

solution of labelled antibody in 0.1M PBS) and a sample (250nM labelled antibody and analyte in 0.1M PBS) solution respectively and the mount was inserted into the experimental apparatus described in section 5.2.9. The reaction kinetics were then monitored on one of the cells (both cells could not be observed simultaneously) using either the 633nm or 650nm laser at a fixed angle of incidence. The reaction was allowed to proceed for 30 mins. (allophycocyanin label) or 20 mins. (CY5.18 label) to reach equilibrium after which angular scans were taken (to obtain the resonant angle and peak signal) for both the reference and sample cells with both the 633nm and 650nm lasers (this process took a further 15 mins.).

## REFERENCES

- 1 **PRESS W H et al**, Numerical recipes in C, *Cambridge University Press, Cambridge, 1992, 2nd ed.*, 408-412.
- 2 **NELDER J A, MEAD R**, A simplex method for function minimization, *Computer Journal, 1965, 7, 308-313*.
- 3 **DAY E D**, Advanced immunochemistry, *Wiley-Liss Inc., New York, 1990, 2nd ed.*, 259-350.
- 4 **SLOPER A N, FLANAGAN M T**, Novel iron phosphate optical waveguides fabricated by a low temperature process, *Electronics Letters, 1988, 24(6), 353-355*.
- 5 **SLOPER A N, FLANAGAN M T**, Metal phosphate planar waveguides for biosensors, *Applied Optics, 1994, 33(19), 4230-4240*.
- 6 **HEWAK D W, LIT J W Y**, Standardization and control of a dip-coating procedure for optical thin films prepared from solution, *Canadian Journal of Physics, 1988, 66, 861-867*.
- 7 **BADLEY R A, et al**, Optical biosensors for immunoassays: the fluorescence capillary fill device, *Philosophical Transactions of the Royal Society of London B, 1987, 316, 143-160*.
- 8 **ROBINSON G A, ATTRIDGE J W, DEACON J K, WHITELEY S C**, The fluorescent capillary fill device, *Sensors and Actuators B, 1993, 11, 235-238*.
- 9 **AZZAM R M A, BASHARA N M**, Ellipsometry and polarized light, *North Holland Publishing Company, Amsterdam, 1979, 1st ed.*.
- 10 **de BRUIJN H E, ALTENBERG B S F, KOOYMAN R P H, GREVE J**, Determination of thickness and dielectric constant of thin transparent dielectric layers using surface plasmon resonance, *Optics Communications, 1991, 82(5,6), 425-432*.
- 11 **ITZKOVITZ M, et al**, Guided-wave method for measuring optical parameters in moderately lossy thin films, *Thin Solid Films, 1985, 125, 193-198*.
- 12 **KITAJIMA H, HIEDA K, SUEMATSU Y**, Various light resonance mechanisms in dielectric and metallic layers and a measurement procedure for optical constants, *Japanese Journal of Applied Physics, 1981, 20(1), 103-112*.
- 13 **BRACKMANN U**, Lambdachrome laser dyes - Lambda Physik handbook, *Lambda Physik, 1986, 1st ed.*.
- 14 **LILLIE R D, ed., CONN H J**, Biological stains, *Waverley Press Inc, Baltimore, 1977, 9th ed.*, 409-410.
- 15 **HAUGLAND R P**, Molecular probes: Handbook of fluorescent probes and research chemicals, *Molecular Probes Inc., 1992, 5th ed.* 77-79.
- 16 **MUJUMDAR R B et al**, Cyanine dye labeling reagents: sulfoindocyanine succinimidyl esters, *Bioconjugate Chemistry, 1993, 4(2), 105-111*.
- 17 **HEARN M T W**, 1,1'-carbonyldiimidazole-mediated immobilization of enzymes and affinity ligands, in **MOSBACH K ed.**, Immobilised enzymes and cells, Part B, *Methods in Enzymology*,

1987, **135**, 102-117.

- 18 **ALARIE J P, SEPANIAK M J, VO-DINH T**, Evaluation of antibody immobilization techniques for fiber optic-based fluoroimmunosensing, *Analytica Chimica Acta*, 1990, **229**, 169-176.
- 19 **SLOPER A N, DEACON J K, FLANAGAN M T**, A planar indium phosphate monomode waveguide evanescent field immunosensor, *Sensors and Actuators*, 1990, **B1**, 589-591.
- 20 **SLOPER A N**, Optical waveguide biosensors, *PhD Thesis*, April 1991, University of London, 187-191.
- 21 **KRONICK M N, GROSSMAN P D**, Immunoassay techniques with fluorescent phycobiliproteins conjugates, *Clinical Chemistry*, 1983, **29(9)**, 1582-1586.
- 22 **MIYAI K**, Classification of immunoassay, in **PRICE C P, NEWMAN D J eds.**, Principles and practice of immunoassay, *Stockton Press, New York*, 1991, *1st ed.*, 246-264.

## CHAPTER 6

### MULTILAYER THIN FILM SYSTEMS

*The characterisation of the multilayer system is described in this chapter. The results of the modelling of the system are given, and these were used as a guideline to the parameters required for a practical multilayer immunosensor. The silica and iron phosphate multilayer system is then described, looking at the spin coating, curing and the problems that were encountered. The programming for, and the estimation of, the refractive indices of the thin films is finally described.*

#### 6.1 MULTILAYER THIN FILM SYSTEM MODELLING

The modelling of the multilayer system can be divided into two parts. The second part, which concerns the modelling and assessment of the immunosensor measurements, is discussed in chapter 8. This part deals with the modelling prior to the design and fabrication of a practical multilayer system.

The reflection and transmission coefficients derived for a single interface and for multilayer thin film structures in chapter 4 are sufficient to undertake an analysis of multilayer structures. However, to simplify the modelling, a number of assumptions were made:

- all media were homogeneous, isotropic, linear, non-magnetic, non-conductors. They were also neither lossy nor absorbing.
- the interfaces were smooth, planar, and parallel to each other. Thus scattering effects were ignored.

- the incident light was a plane, homogeneous and uniform wave.

The first assumption allows a simplification to be made. The media are non-magnetic ( $\mu = 0$ ) and thus, the refractive index is given by

$$n = \sqrt{\epsilon\mu} = \sqrt{\epsilon} \quad (6.1)$$

and so it can be shown that the wave number is given by:

$$k = \frac{2\pi}{\lambda_0} n \quad (6.2)$$

where,  $\lambda_0$  is the free space wavelength of the exciting light.

### 6.1.1 Modelling considerations

Modelling of a system is carried out to optimise as many parameters as possible prior to fabrication and testing. In the case of this multilayer resonant system, the parameters that may mainly affect the resonance are:

- The angle of incidence of the incident exciting light.
- The polarisation state of the incident light.
- The wavelength of the incident light.
- The thicknesses of the thin film layers.
- The refractive indices of the media.
- The number of thin film layers.

The excitation probability of a fluorophore is dependent on the square of the electric field strength [1] and, thus, all modelling will have to consider the electric field strength or the square of the electric field strength.

## 6.1.2 Computer programming

The programming was done initially in *Microsoft* QuickC, and later updated and improved in *Microsoft* 'C' on an 386 PC-compatible computer. Complex number handling routines were obtained from *Numerical recipes in C* [2]. Routines to perform further complex number operations (eg. conversion from cartesian to exponential notation, complex trigonometric functions, etc.) were added by the author and by *Dr. A Sloper*. All the calculations were performed using the 'C' language data type 'float' for the variables.

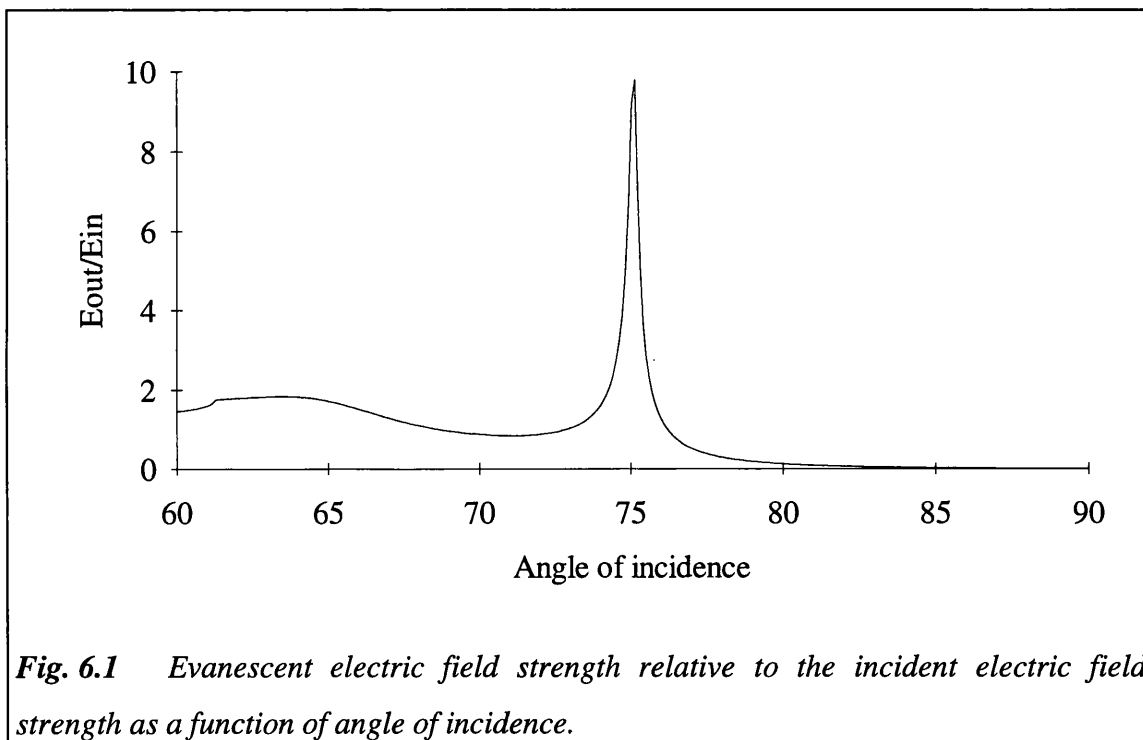
The data obtained from the calculations were saved in an ASCII file which could be imported into a spreadsheet such as *Microsoft* EXCEL to produce a graphic output.

### 6.1.2.1 Simplex maximum search routine

It was necessary in much of the modelling to obtain the angle of incidence at which resonance occurred and for this a 'Simplex' maximum search routine (by *Nelder and Mead* [3]) was used for which a 'C' language routine was obtained from *Numerical Recipes in C*. Fig. 1 shows a typical curve for which the simplex routine was used to find the angle of incidence required for resonance. The resonance could occur at angles of incidence from 65 - 90° (depending on the multilayer system parameters) and, as can be seen in fig. 6.1, could produce a sharp peak. The simplex routine therefore required a large step size to search the angular range rapidly but also required accuracy to detect the sharp resonance peak. The routine obtained from *Numerical recipes in C* was, thus, modified such that the step size and accuracy could be changed during the search to allow both the rapid and accurate detection of the resonance peak.

One problem associated with the use of maximum (or minimum) search routines is that a local maximum may be found instead of a global maximum. The success of a search routine is, therefore, highly dependent on the initial search start points and step size that are fed into to the routine. When it was attempted to start the search routine

with values for the angle of incidence that were known to be on either side of the maximum, the search routine commonly returned values for local maxima that were present below the angle required for resonance (fig. 6.1). A closer examination of the variation of the field strength against angle of incidence (fig. 6.1) revealed that the curve fell off smoothly with angles of incidence greater than that required for resonance. It was, thus, decided to start off the search with initial points that were known to be greater than the resonant angle. However, the search routine could still miss the maximum due to the sharpness of the resonant peak. The problem was solved by placing a lower limit



(known to be below the resonant angle) on the angle of incidence which, if it was reached, would restart the search with modified initial search points. The lower limit was removed if the routine consistently failed to locate a maximum within the set bounds. The success of the routine was tested by comparing results with those obtained from a program that only calculated field strength against angle of incidence (with all other parameters fixed). The agreement between the two was 100% for the test cases.

### 6.1.3 The single interface total internal reflection system

The single interface total internal reflection (TIR) immunosensor, as shown in chapter 2, fig. 2.4, was used as a benchmark to assess the performance of the multilayer thin film immunosensor. The optical characteristics of the single interface system were known or could be easily ascertained and so provided a means by which the multilayer

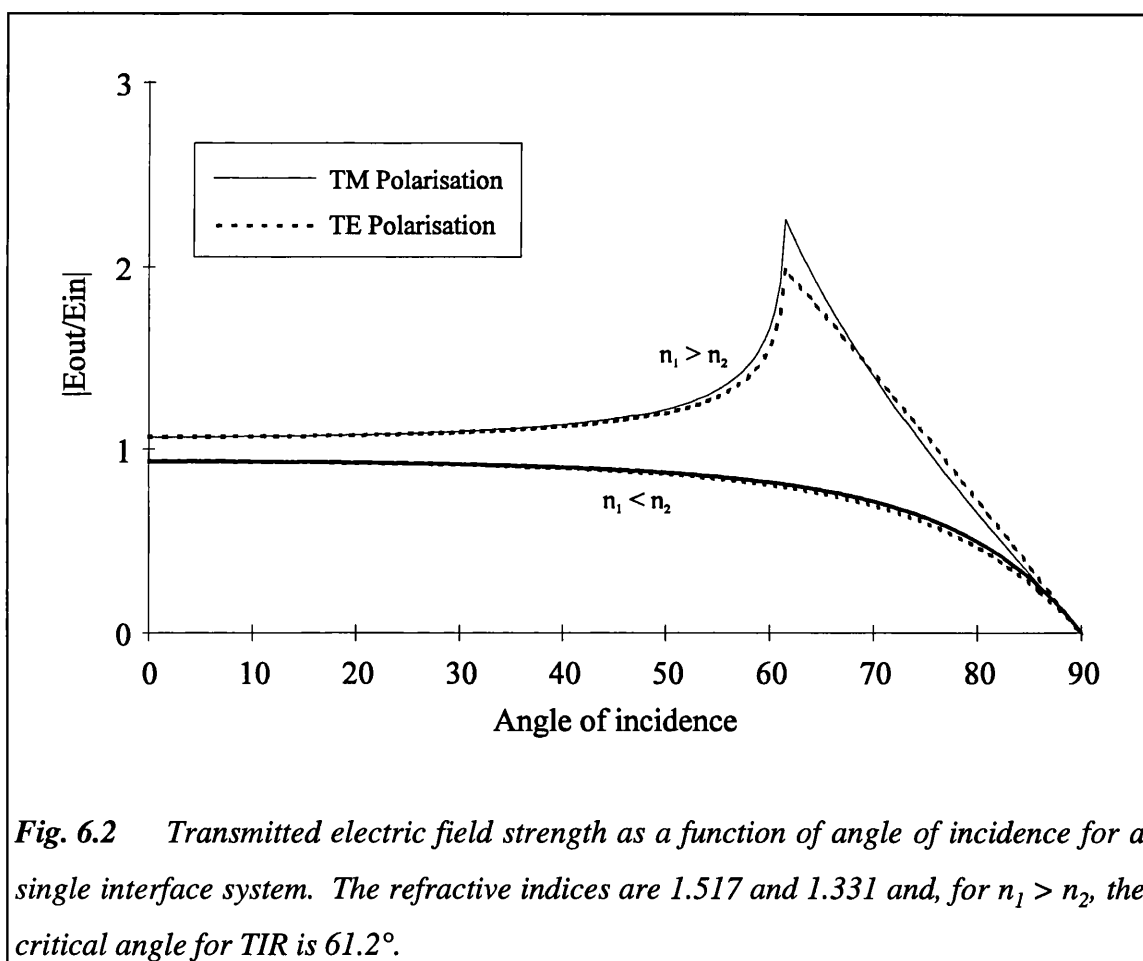


**Fig. 6.2** Transmitted electric field strength as a function of angle of incidence for a single interface system. The refractive indices are 1.517 and 1.331 and, for  $n_1 > n_2$ , the critical angle for TIR is 61.2°.

thin film modelling programs could be tested. This section briefly illustrates the modelling of the single interface system.

Fig. 6.2 illustrates the transmitted electric field strength as a function of angle of incidence. Note that in the total internal reflection case ( $n_1 > n_2$ ), the maximum evanescent field strength occurs at the critical angle. However, the penetration depth of

the evanescent field tends to infinity near the critical angle (see fig. 6.4) and, thus, the TIR system is used at angles of incidence well above the critical angle.

Fig. 6.3 shows a profile of the electric field strength through the two media (for  $n_1 > n_2$ , the TIR case is shown). A standing wave is established in medium 1 by the partial reflection of the incident light at the interface and, in medium 2, the field strength decays exponentially for the TIR case. Note that, for the TM polarised wave, the

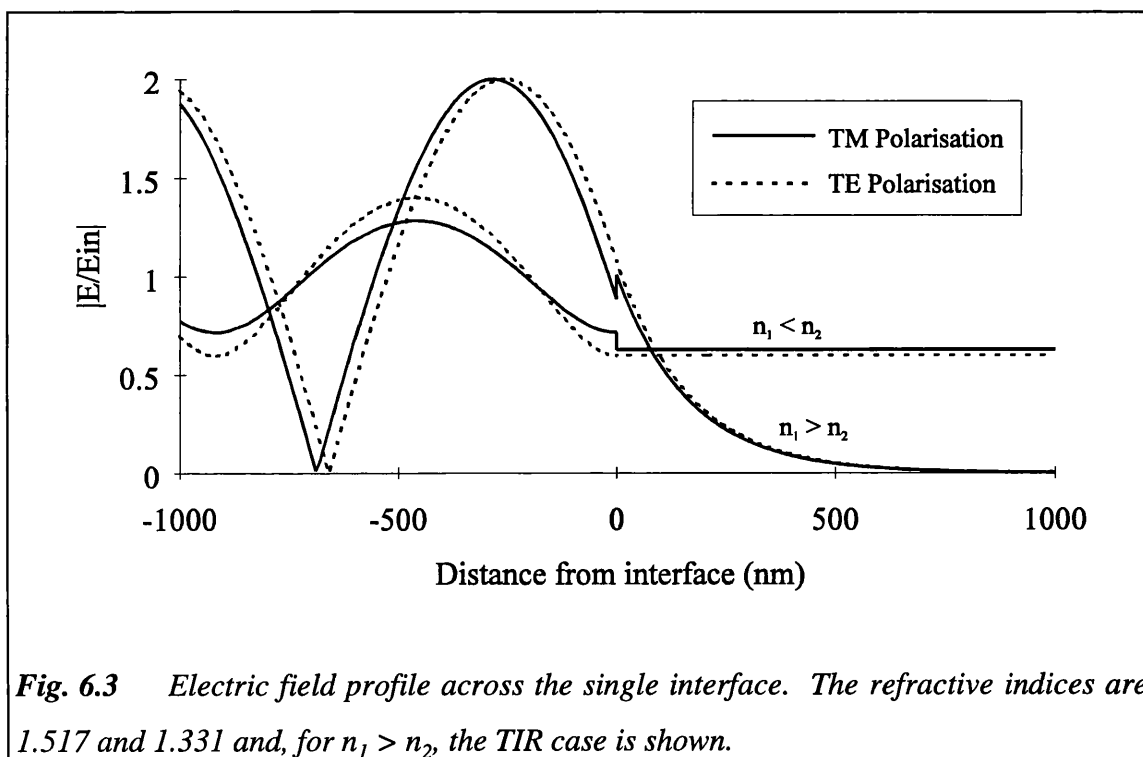


**Fig. 6.3** Electric field profile across the single interface. The refractive indices are 1.517 and 1.331 and, for  $n_1 > n_2$ , the TIR case is shown.

electric field strength is discontinuous across the interface.

The probability of exciting a fluorophore is proportional to the intensity of the exciting light [1], and intensity, in general, is proportional to the square of the field strength. The concept of intensity is difficult when considering an evanescent field because the Poynting vector becomes complex. Hence, the term 'intensity', when applied to the evanescent field, will be assumed to be proportional to the square of the

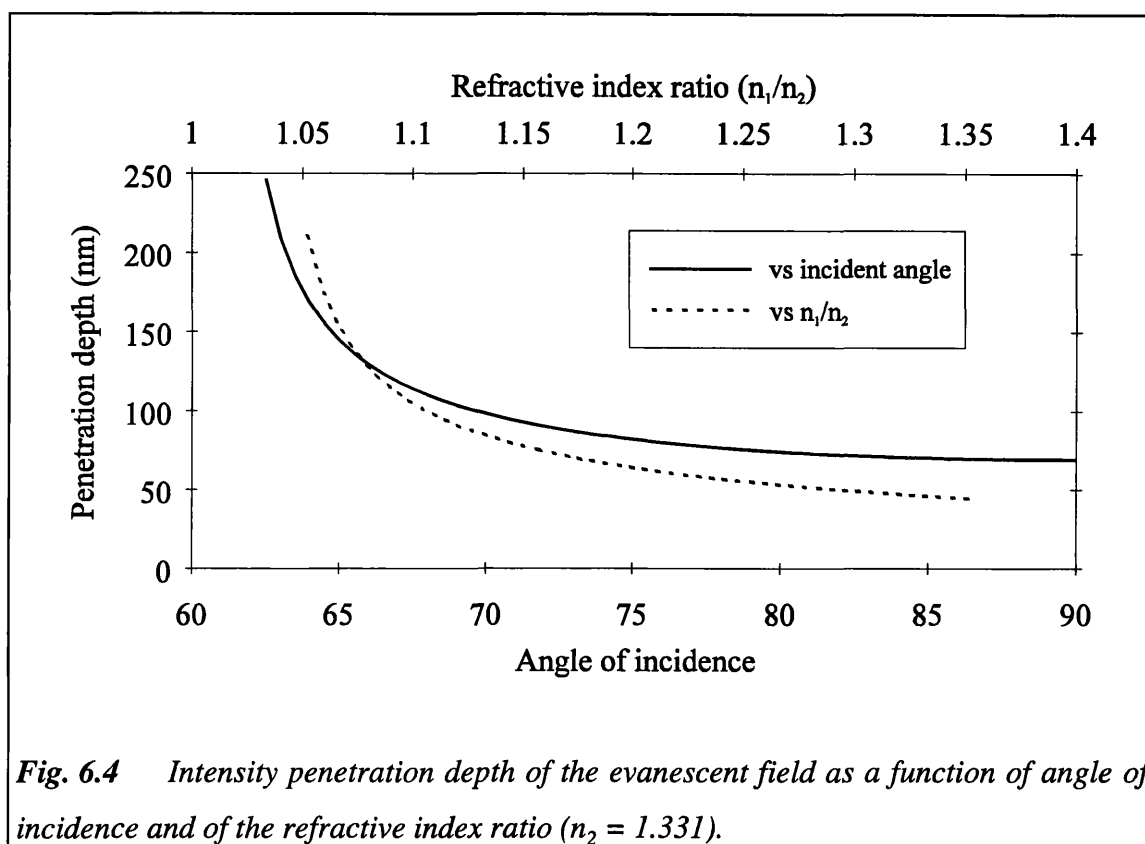


**Fig. 6.4** Intensity penetration depth of the evanescent field as a function of angle of incidence and of the refractive index ratio ( $n_2 = 1.331$ ).

electric field strength. Fig. 6.4 shows the intensity penetration depth of the evanescent field. Minimisation of the penetration depth and maximisation of the evanescent field 'intensity' are essential to improving the sensitivity of evanescent field immunosensors [4]. Fig. 6.4 suggests that a high  $n_1:n_2$  ratio and a high angle of incidence are required for low penetration depth.

#### 6.1.4 The four layer resonant system

The simplest resonant system is the basic four layer system illustrated in fig. 6.5. Prior to the fabrication of the multilayer devices, the four layer system was modelled to determine what factors the resonance was dependent on, and how these factors affected the resonance characteristics. The modelling was used in the choice of the thin film parameters (eg. film thickness) and in the choice of experimental conditions. In the discussion that follows, the figures stated for refractive index, etc. in fig. 6.5 will be the

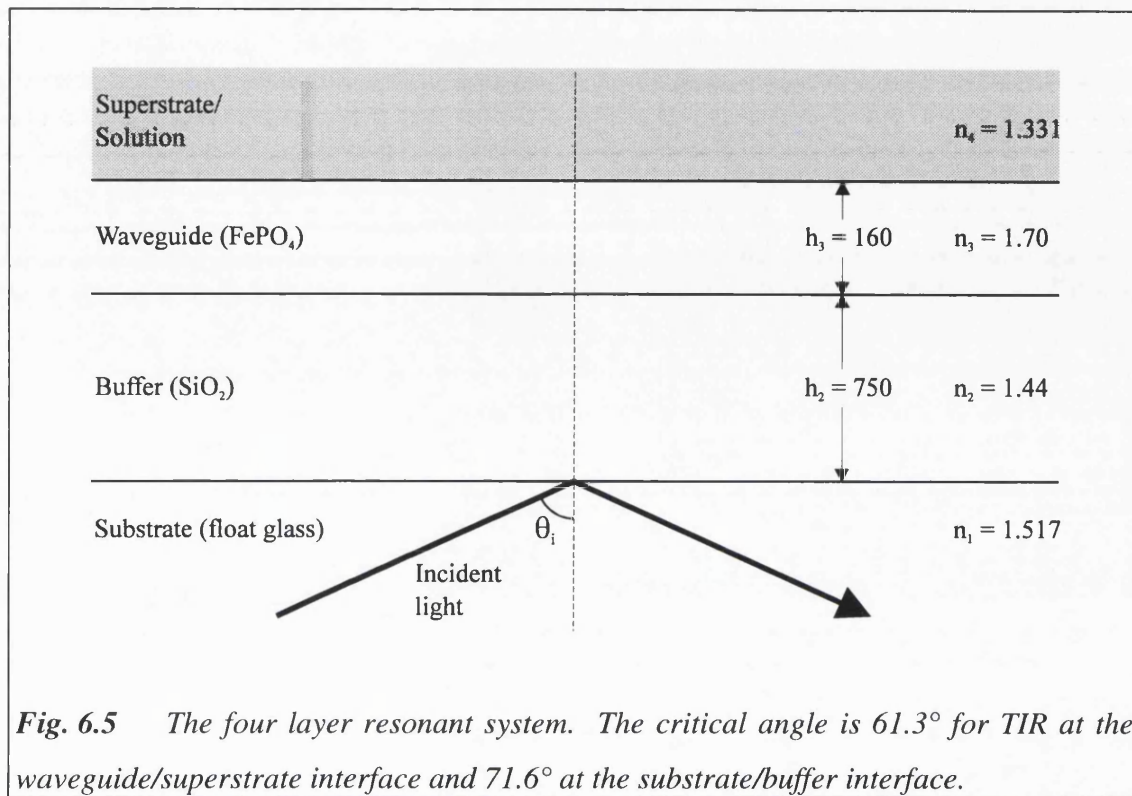


**Fig. 6.5** The four layer resonant system. The critical angle is  $61.3^\circ$  for TIR at the waveguide/superstrate interface and  $71.6^\circ$  at the substrate/buffer interface.

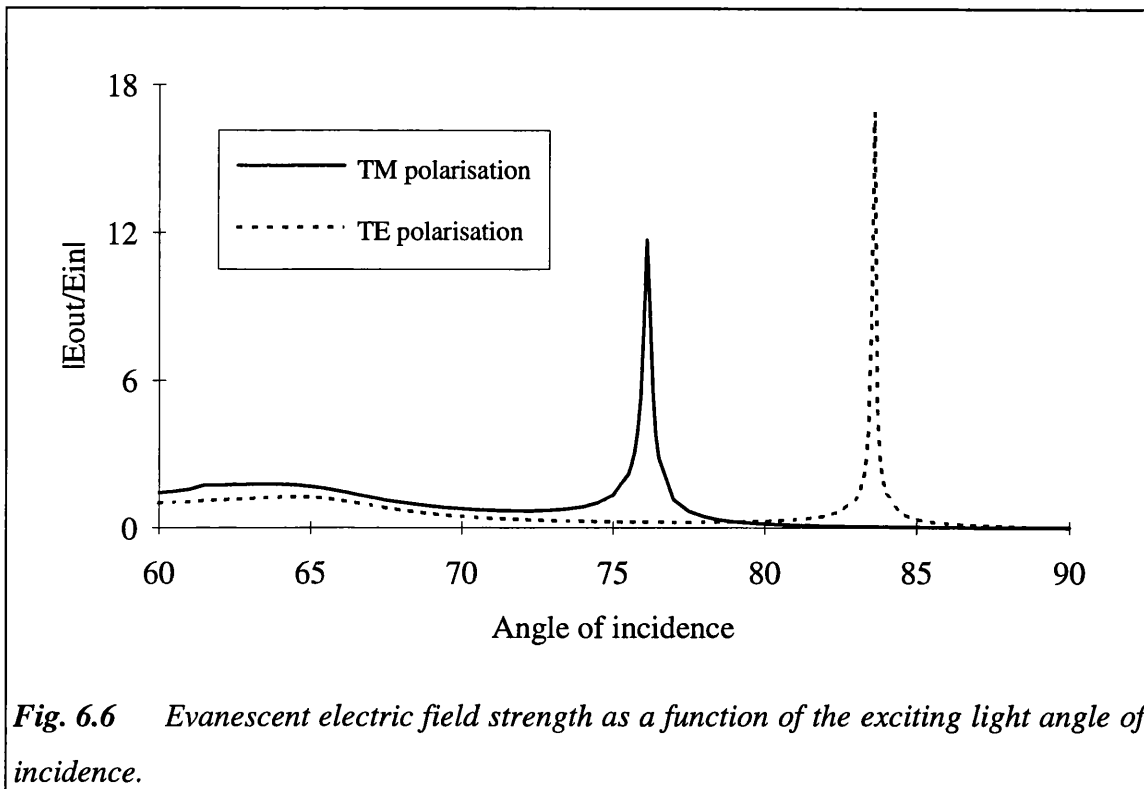
values used (unless otherwise stated) along with an incident light wavelength of 632.8nm. Fig. 6.5 illustrates the system that was eventually fabricated, and the reasons for the choice of the indicated parameters will be discussed at the end of this chapter.

The resonance is mainly dependent on:

- The angle of incidence ( $\theta_i$ ) of the exciting light.
- The wavelength of the exciting light.
- The thicknesses of the thin film layers.
- The refractive indices of the thin film layers.

The modelling was required to obtain a resonant system that was optimised to give a low evanescent field penetration depth and a high evanescent field strength.

Fig. 6.6 shows the evanescent field strength as a function of the angle of incidence ( $\theta_i$ ) of the exciting light for both TM and TE polarisations for the multilayer system of

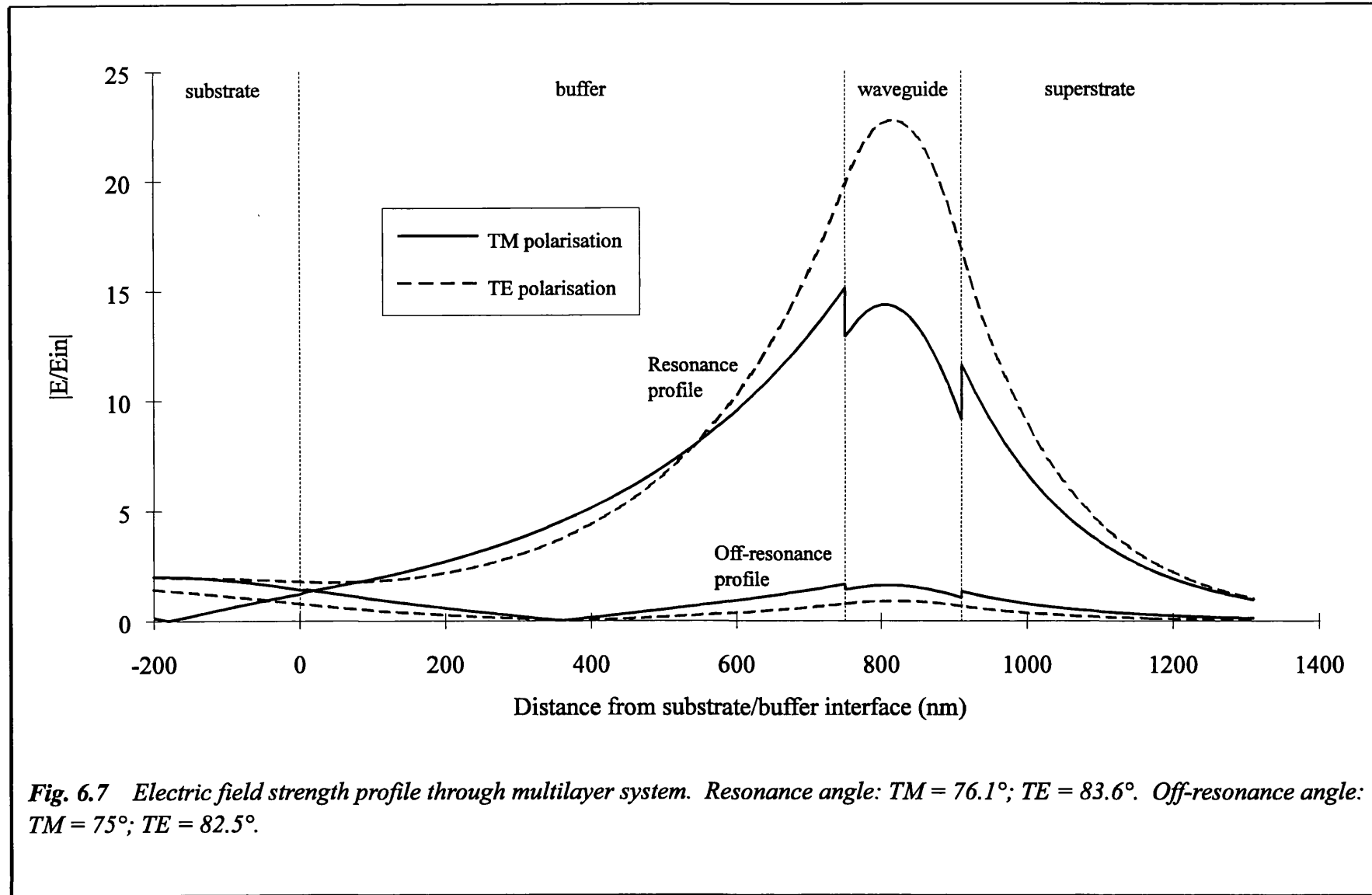


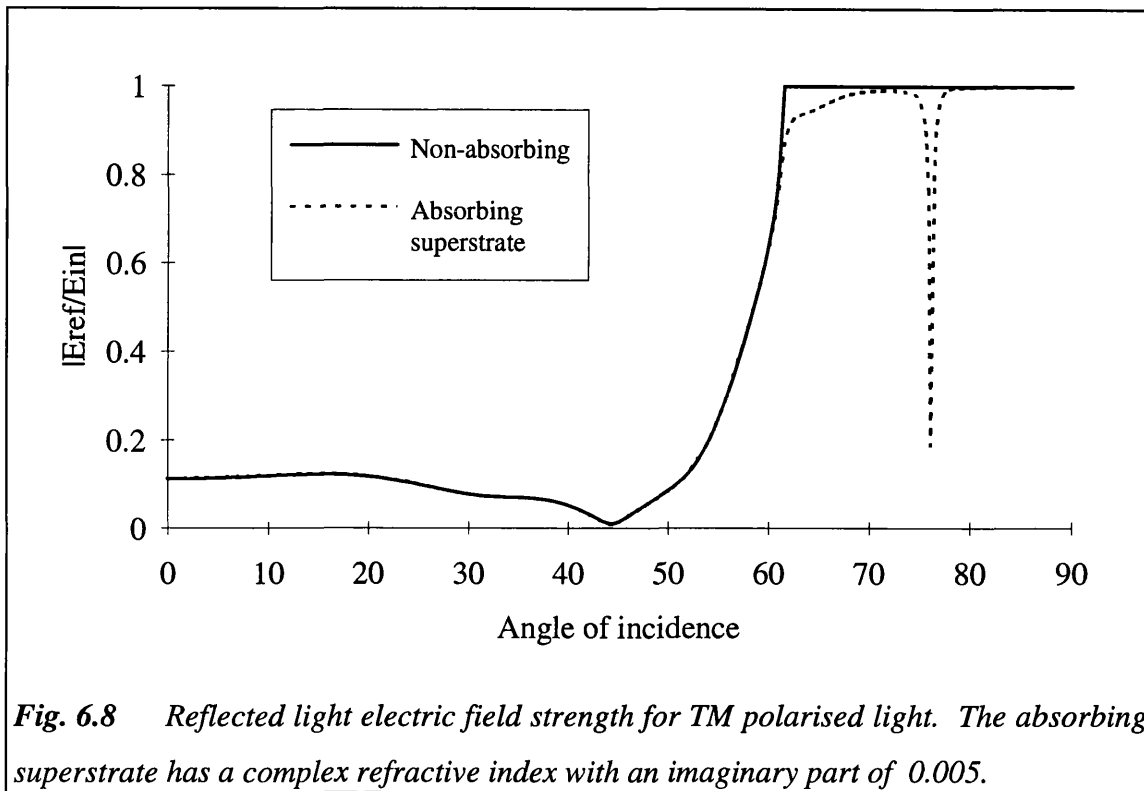
**Fig. 6.6** Evanescent electric field strength as a function of the exciting light angle of incidence.

fig. 6.5. The graph shows a stronger resonant peak for the TE polarisation but, as will be shown later in this chapter, this is highly dependent on the waveguide layer thickness and an equally strong resonance can be obtained from the TM polarised light at a different waveguide layer thickness.

Light energy is concentrated in the waveguide layer at the resonant angle of incidence as illustrated in fig. 6.7 for both the TM and TE polarisations. Note that, due to the boundary conditions, the electric field strength for the TM polarised light is discontinuous across the interfaces and that, because of different resonance conditions in this case, the TE polarised wave exhibits a stronger resonance and a lower penetration depth.

Any light incident on the multilayer structure at an angle of incidence greater than the critical angle for the waveguide/superstrate interface is not transmitted, but undergoes total reflection. However, if an absorbing layer is present, the light energy can be absorbed. This absorption becomes significant, resulting in a trough in the





**Fig. 6.8** Reflected light electric field strength for TM polarised light. The absorbing superstrate has a complex refractive index with an imaginary part of 0.005.

reflected light intensity, at the resonant angle of incidence as shown in fig. 6.8, where an absorbing superstrate layer has been added.

#### 6.1.4.1 Thin film thickness dependence

The choice of materials that could be used in the fabrication of the thin films was limited by the requirement for spin coating. This served to limit the range of refractive indices that could be obtained. In addition, the substrate and superstrate (solution) refractive indices were fixed at 1.517 and 1.331 respectively. However, the thicknesses of the two thin film layers could be easily varied, using the spin-coating technique, over a wide range. The requirement for the multilayer system was to produce a strong evanescent field in the solution layer and a low evanescent field penetration depth, and this section deals with the modelling of the multilayer thin film structure with respect to optimising the thin film thicknesses.

Fig. 6.9 illustrates the dependence of the evanescent field electric field strength on

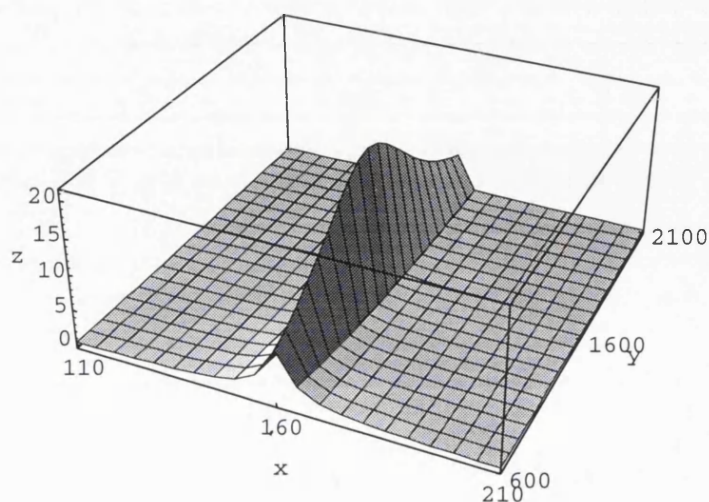


**Fig. 6.9** The dependence of the evanescent field strength on the buffer and waveguide layer film thicknesses. 'x' = waveguide thickness (nm), 'y' = buffer thickness (nm), 'z' =  $|E_{out}/E_{in}|$ , and the angle of incidence is  $76.1^\circ$ .

the waveguide and buffer layer thicknesses when observed at a fixed angle of incidence. This shows that the resonance is weakly dependent on the buffer layer thickness but strongly dependent on the waveguide layer thickness. This can be expected as the resonant wave is present in the waveguide layer whereas the buffer layer acts as damper system in the coupling of light energy into and out of the waveguide layer.

Given a buffer and waveguide layer thickness, there will exist an angle of incidence which will give a peak in the evanescent field strength. Figs. 6.10 - 6.12 show the maximum evanescent field strength and the angle of incidence required for the maximum field as a function of the buffer and waveguide layer thicknesses respectively. Note that:

- the angle of incidence required for resonance is independent of the buffer layer thickness (over a buffer thickness of  $\sim 500\text{nm}$ ).

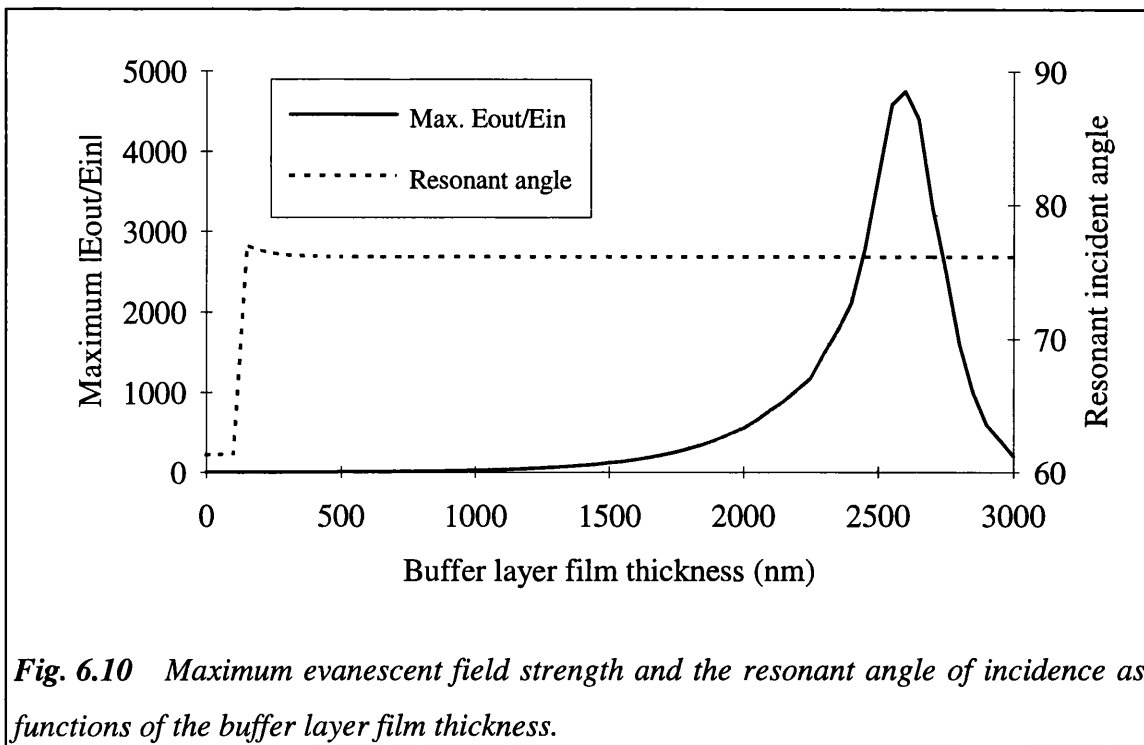


**Fig. 6.10** Maximum evanescent field strength and the resonant angle of incidence as functions of the buffer layer film thickness.

- the resonance collapses as the angle of incidence required for resonance approaches 90°.
- several resonant modes exist (dependent on the waveguide layer thickness).

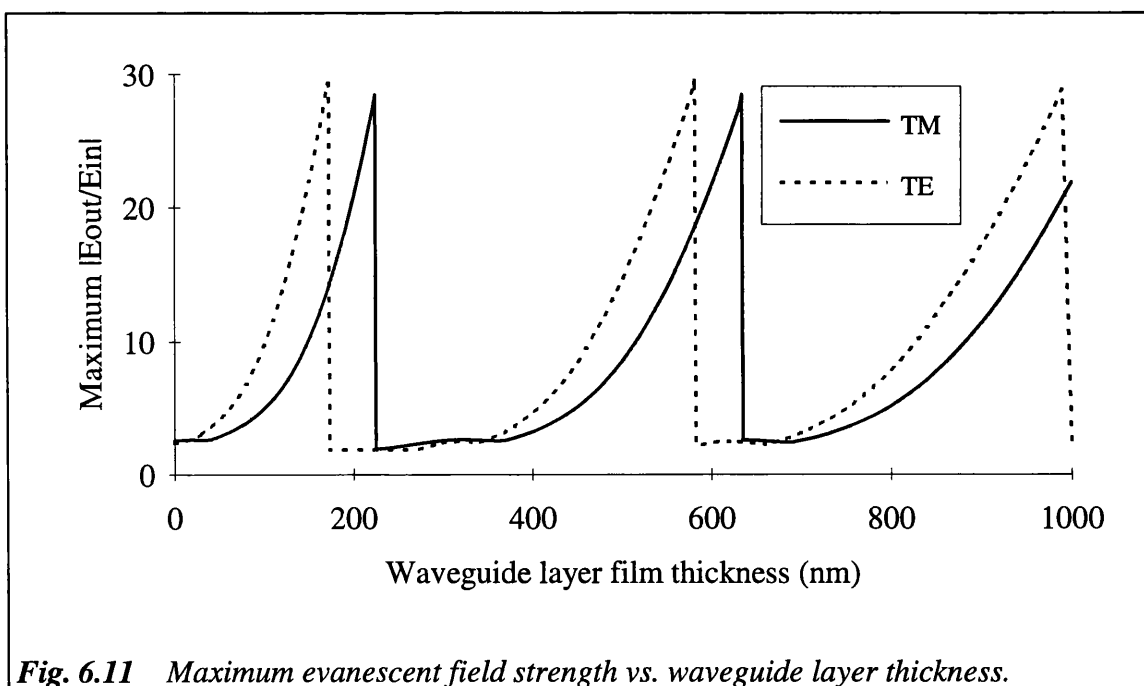


**Fig. 6.11** Maximum evanescent field strength vs. waveguide layer thickness.

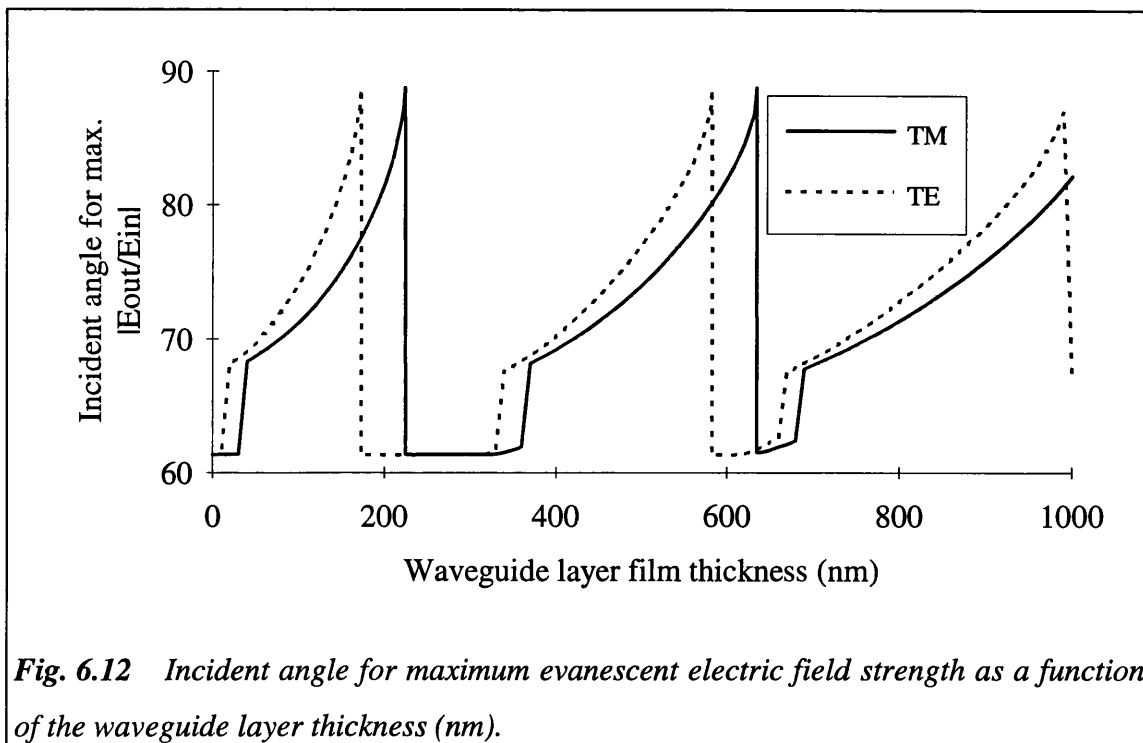
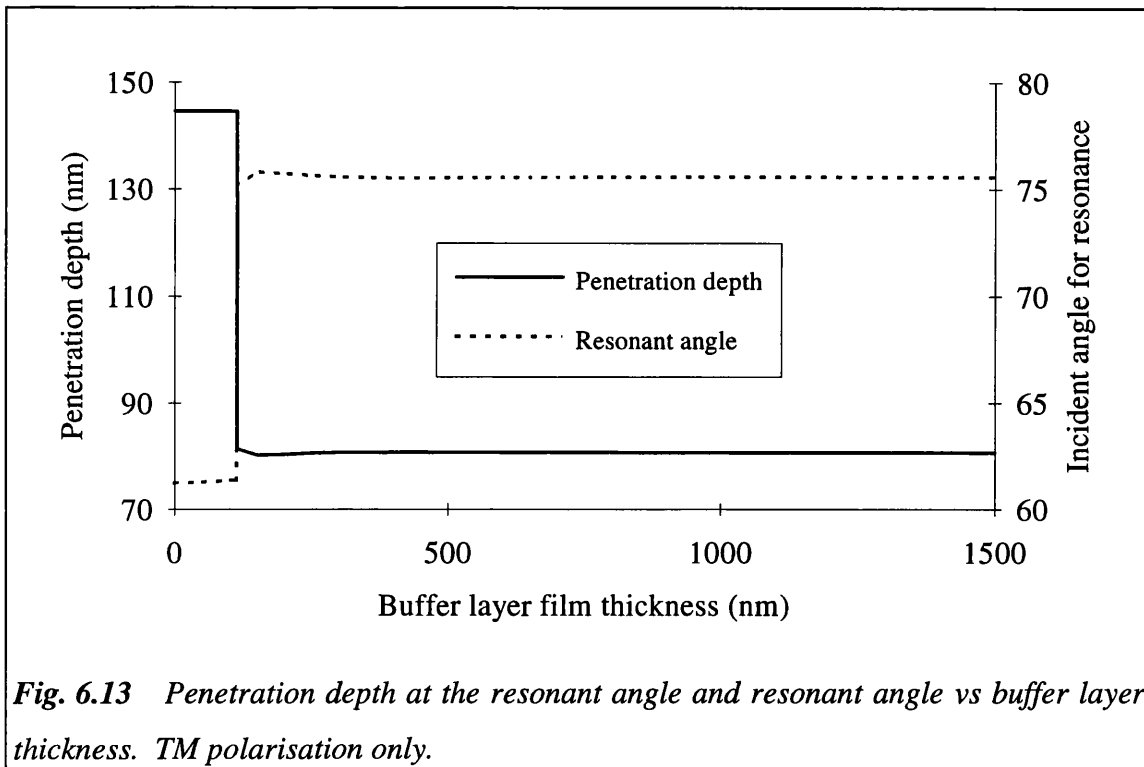


**Fig. 6.12** Incident angle for maximum evanescent electric field strength as a function of the waveguide layer thickness (nm).

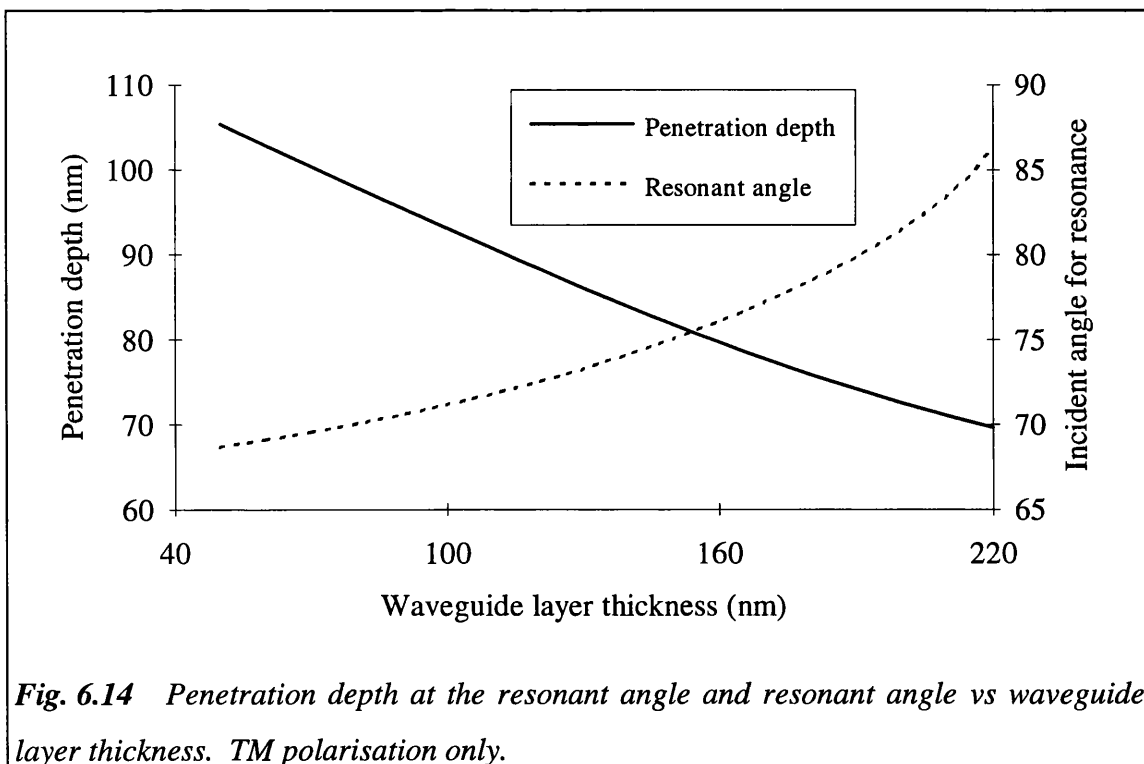
It can be seen from fig. 6.11 that the multilayer system gives similar overall evanescent electric field enhancements for both TE and TM polarisations but that the resonant angles (fig. 6.12) and enhancement magnitudes differ for a given waveguide layer thickness.

The discontinuities in the graph of fig. 6.12 occur due to the use of a maximum search routine. This routine will find the absolute maximum evanescent field strength which, in the absence of a resonant peak, will occur at the critical angle of incidence (see fig. 6.2) for total internal reflection at the waveguide/superstrate interface. It is also possible for a number of local maxima to be present at angles just above the critical angle and the maximum search routine may occasionally return one of these angles in the absence of a resonant peak. When a resonant peak is present with an evanescent field strength greater than that at the critical angle, the maximum search routine will return the resonant angle of incidence.

Figs. 6.10 - 6.12 show the electric field strength as a function of the angle of incidence. It was also necessary to know the dependence, if any, of the penetration



depth on the buffer and waveguide thin film thicknesses. Figs. 6.13 and 6.14 show the penetration depth vs. the buffer and waveguide layer thicknesses respectively.

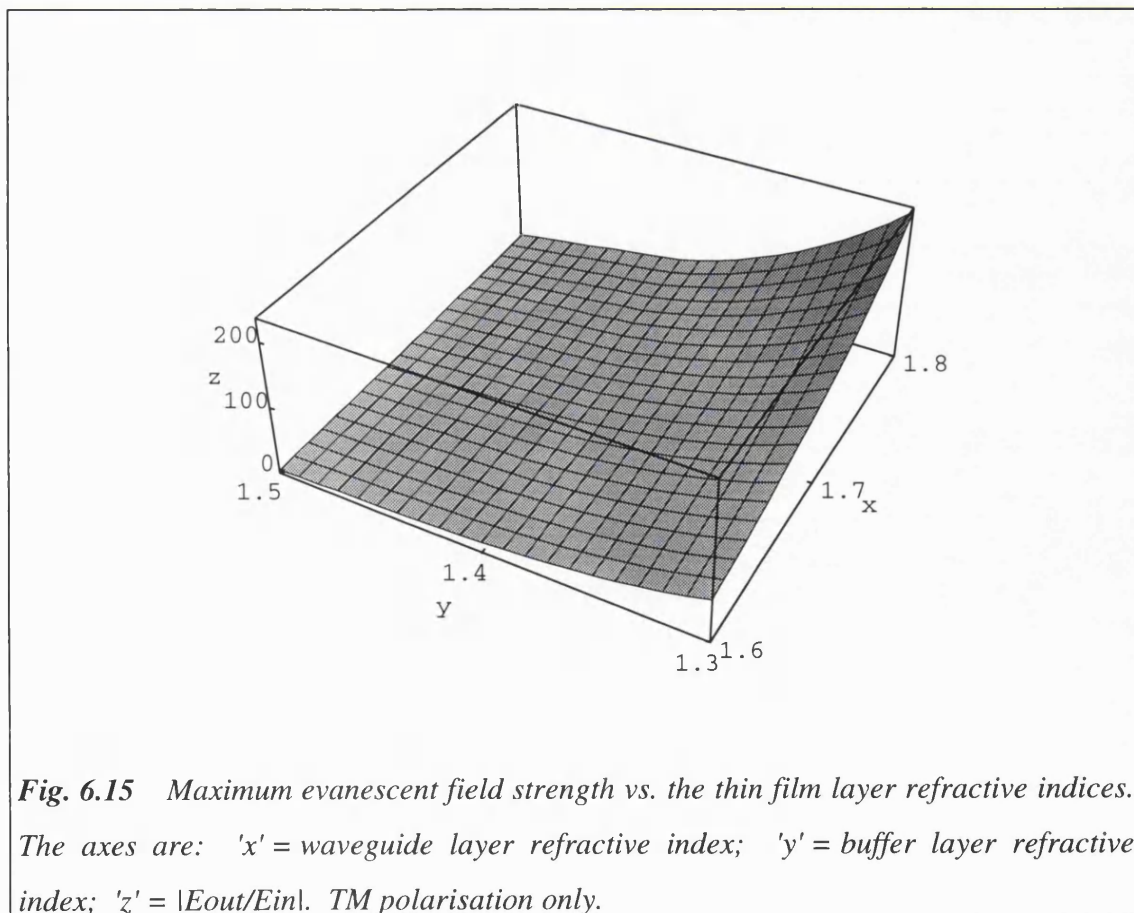


Note that the penetration depth has been calculated for exciting light incident at the resonant angle of incidence. The figures illustrate that the penetration depth of the evanescent field is independent of both the buffer and waveguide layer thicknesses, but that it is dependent on the angle of incidence of the exciting light.

#### 6.1.4.2 Thin film refractive index dependence

Refractive indices from about 1.4 to 1.9 can be achieved by using a range of different materials (eg. sol-gel silica and titania, phosphate glasses) which can be spin coated onto glass substrates. The dependence of the resonance and the penetration depth of the evanescent field on the refractive indices of the thin film layers was thus modelled to ascertain the best combination of refractive indices for the thin films.

Figs. 6.15 and 6.16 show the dependence of the resonance magnitude and angle of



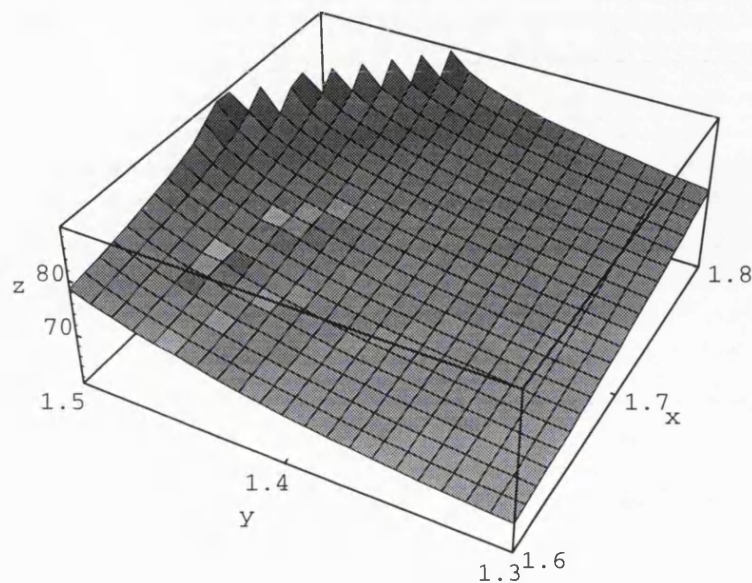


**Fig. 6.16** Incident angle for maximum  $E_{out}/E_{in}$  vs. the thin film layer refractive indices. The axes are: 'x' = waveguide layer refractive index; 'y' = buffer layer refractive index; 'z' = Incident angle for maximum  $|E_{out}/E_{in}|$ . TM polarisation only.

incidence on the thin film refractive indices. Fig. 6.15 suggests that a large waveguide layer to buffer layer refractive index ratio is required for strong resonance. When the refractive index of the buffer layer approaches the substrate refractive index (1.517), the angle of incidence required for TIR at the substrate/buffer interface approaches  $90^\circ$  and the resonance can collapse (see fig. 6.16).

Fig. 6.17 shows the dependence of the penetration depth of the evanescent field on the refractive indices of the thin film layers when the exciting light is incident at the resonant angle of incidence as given in fig. 6.16. It can be seen, as with the dependence of the penetration depth on the thin film layer thicknesses (figs. 6.13 and 6.14), that the penetration depth is independent of the thin film refractive indices but is inversely proportional to the angle of incidence of the exciting light. The sudden increase in the penetration depth (visible in fig. 6.17) occurs due to the collapse of resonance at the indicated thin film refractive index combinations, resulting in the maximum evanescent

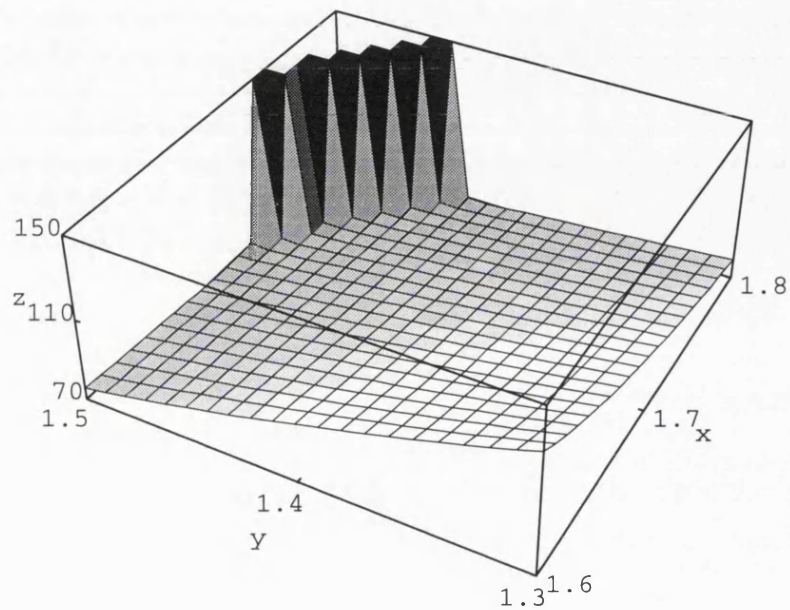


**Fig. 6.17** Penetration depth of the evanescent field vs the thin film layer refractive indices. The penetration depth is for exciting light incident at the resonant angle. The axes are: 'x' = waveguide layer refractive index; 'y' = buffer layer refractive index; 'z' = Penetration depth (nm). TM polarisation only.

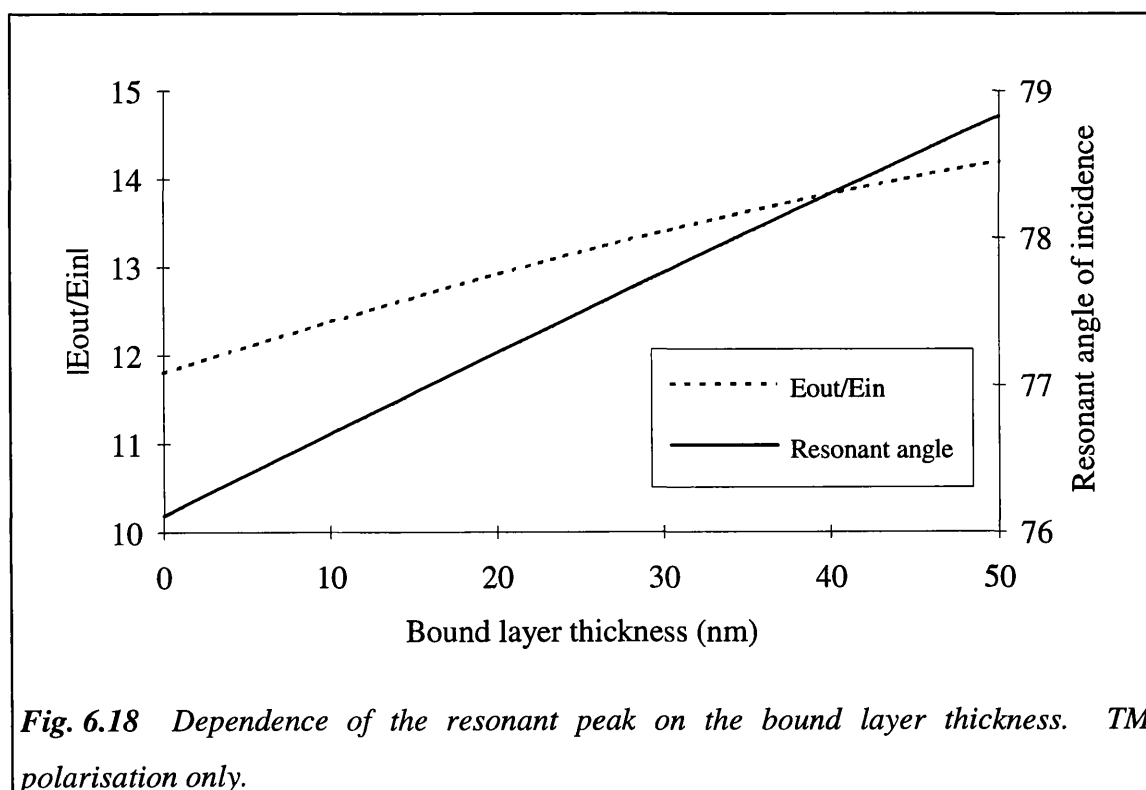
field strength occurring at an angle of incidence close to the critical angle.

### 6.1.5 The five layer resonant system

Although so far only a four-layer system has been considered, a practical multilayer thin film immunosensor would also have a fifth layer - the bound layer (ie. capture antibody, analyte and bound labelled antibody). The thickness of this layer is very dependent on the size of the analyte but is, typically, about 5 - 30 nm thick if a protein is assumed to be the analyte. Refractive index values of 1.46 - 1.56 have been used by various researchers [4, 7, 8] for the bound protein layer, whereas values of between 1.53 - 1.68 have been obtained for the refractive indices of different serum

proteins [9, 10]. A value of 1.5 was used in this case to model a protein/solution layer.

Surface plasmon resonance (SPR) sensors use changes in the refractive index and thickness of the bound layer (due to the binding of the analyte) to measure the analyte concentration by measuring the shift in the resonant angle of incidence [11, 12]. The modelling of the four layer system suggested that the resonant angle of incidence in the multilayer system would be dependent on the bound protein layer. Fig. 6.18 shows the resonant angle of incidence as a function of the bound protein layer thickness (it is assumed that the bound layer is a mixture of protein and solution). Although the changes in the resonant angle of incidence are smaller than can be obtained for SPR systems [11, 12], the sharp resonant peaks of the multilayer sensor should give a comparable sensitivity performance. However, the expected accuracy of the thickness of the spin-coated thin films ( $\sim 10\%$  between separate substrates and  $\sim 3\%$  across any single film) means that the multilayer sensor is unlikely to give a good performance when used as an SPR type sensor. *Fisons'* multilayer sensor overcomes this problem by using a more expensive, but more accurate, CVD thin film fabrication technique, and by



using a more sensitive interferometric phase measurement [5].

### 6.1.6 Discussion

The modelling illustrated in section 6.1 has allowed a suitable multilayer device to be designed for fluorescence immunosensing.

The requirements for a high evanescent field strength are:

- thick buffer layer (of the order of  $\mu\text{m}$ ).
- an appropriate waveguide layer thickness (depending on refractive index, exciting light wavelength, etc.).
- high waveguide layer to buffer layer refractive index ratio.

The penetration depth was neither dependent on the waveguide or buffer layer thicknesses nor on their refractive indices. The requirements for a low evanescent field penetration depth are:

- high substrate to superstrate refractive index ratio.
- high exciting light angle of incidence.

#### **Indirect fluorescence immunoassay or direct SPR type immunoassay?**

Section 6.1.5 showed that a direct mass loading immunoassay similar to SPR could be performed with the multilayer system. However, the lack of uniformity in the fabrication of the thin films was likely to render any direct immunoassay measurements highly inaccurate. Fig. 6.18 indicates that a change in the thickness of the bound layer from 10nm to 30nm (a large change) gives a shift in the angle of resonance by about  $1^\circ$  but, a 3% variation in a waveguide layer film thickness of 160nm will give a variation of  $0.5^\circ$  (from fig. 6.12) in the angle of resonance (an error of 50%). However, the same film thickness variation gives only a  $\sim 5\%$  variation in the evanescent field strength.

Thus, although direct SPR type sensing is possible, the multilayer system would be better utilised as a fluorescence immunosensor given the fabrication accuracies that can be obtained.

**TE or TM polarisation?** The resonance peaks occur at different angles of incidence for the two polarisations and, thus, both polarisations cannot be used together without the use of complex optics to ensure that each polarisation is incident at the correct angle on the same device. Unpolarised light can be used, and an angular scan performed, to obtain both TE and TM resonance peaks but there may be a large background signal due to scattering of the polarisation which is not at resonance. It was mentioned in chapter 4, section 4.2.3 that TM polarised light may excite greater fluorescence due to the rotation of the evanescent electric field vector. Hence, in the immunosensing experiments, it was decided to use the TM polarisation.

**Angle of incidence.** The highest evanescent field strengths and lowest penetration depths occur at the high angles of incidence (depending on waveguide layer film thickness). However, there are practical limitations to using a high incident angle - usually due to the beam size of the incident light and the finite size of the multilayer device (see chapter 5, section 5.2.8). This constraint on the angle of incidence will, essentially, determine the waveguide layer thickness (given its refractive index).

A multilayer device suitable for fluorescence immunosensing was now designed

Layer (material)	Thickness (nm)	Refractive index
Substrate (float glass)	-	1.517
Buffer (silica)	750	1.44
Waveguide (iron phosphate)	160	1.70
Superstrate (buffer solution)	-	1.334
Resonant angle of incidence = $\sim 76^\circ$		

*Table 6.1 Multilayer thin film immunosensor parameters*

based on the modelling described and the constraints discussed above (table 6.1). The limitation on the buffer layer thickness and the measurement of the thin film layer refractive indices are discussed later in this chapter.

## 6.2 MULTILAYER THIN FILM SYSTEM CHARACTERISATION

### 6.2.1 Sol-gel silica spin coating

The spin coating technique, used for the inexpensive fabrication of thin films, has been investigated previously [13, 14], and various mathematical models to describe the film thickness as a function of spin speed, solution viscosity, spin time, etc., have been described. The simplest of the models uses an inverse exponential fit [13] of the form:

$$h = h_1 \omega^{-u} \quad (6.3)$$

where  $h$  = film thickness,  $\omega$  = spin speed, and  $h_1$  and  $u$  are constants.

Fig. 6.19 illustrates the dependence of the sol-gel silica film thickness on the spin speed. Two curves are shown: one for the initial deposition onto PERMABLOC float glass and a second subsequent coat onto a previously deposited silica film. Note that the second coating produces a thicker film than the first coating. The reasons for this are unclear and have not been investigated, but it may be due to the micro-porosity of the underlying silica film which allows the second coat of sol-gel silica to adhere more strongly to the surface. A similar increase in film thickness was also observed for iron phosphate films deposited on silica films as opposed to deposition on PERMABLOC float glass - this will be discussed later in this chapter.

It was found that, even with spin speeds as low as 400rpm, a single coat of sol-gel silica did not yield a film of thickness greater than ~600nm (using undiluted

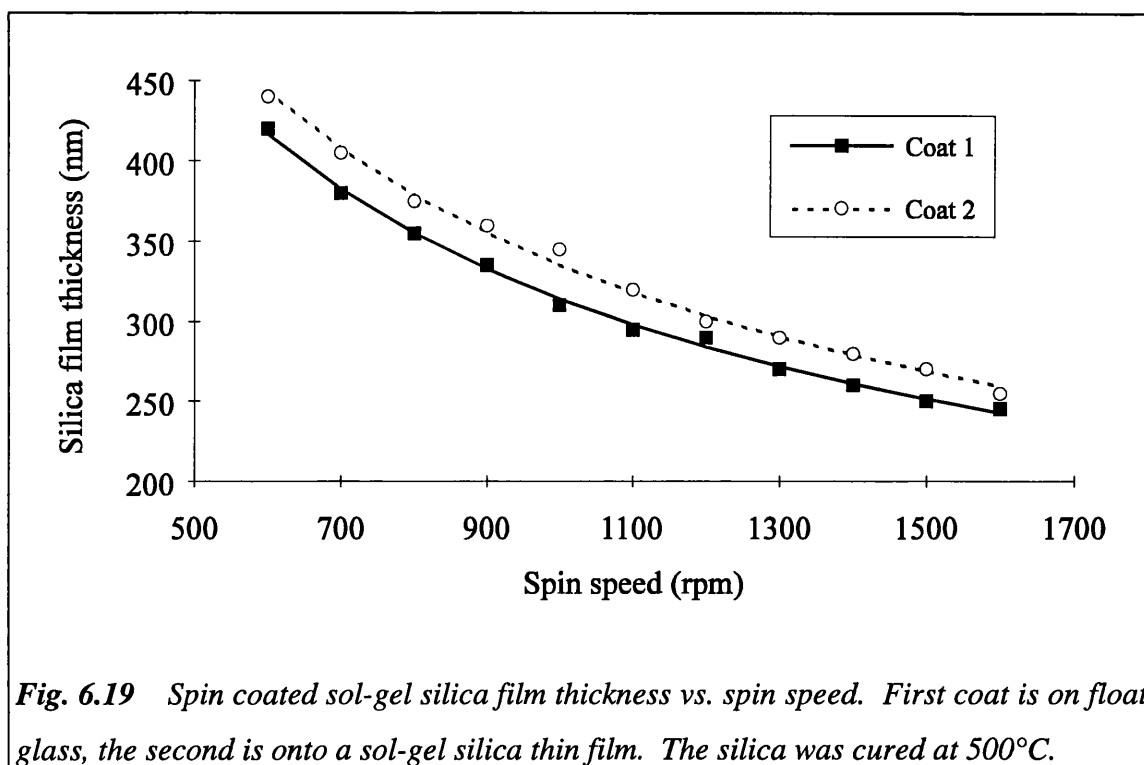
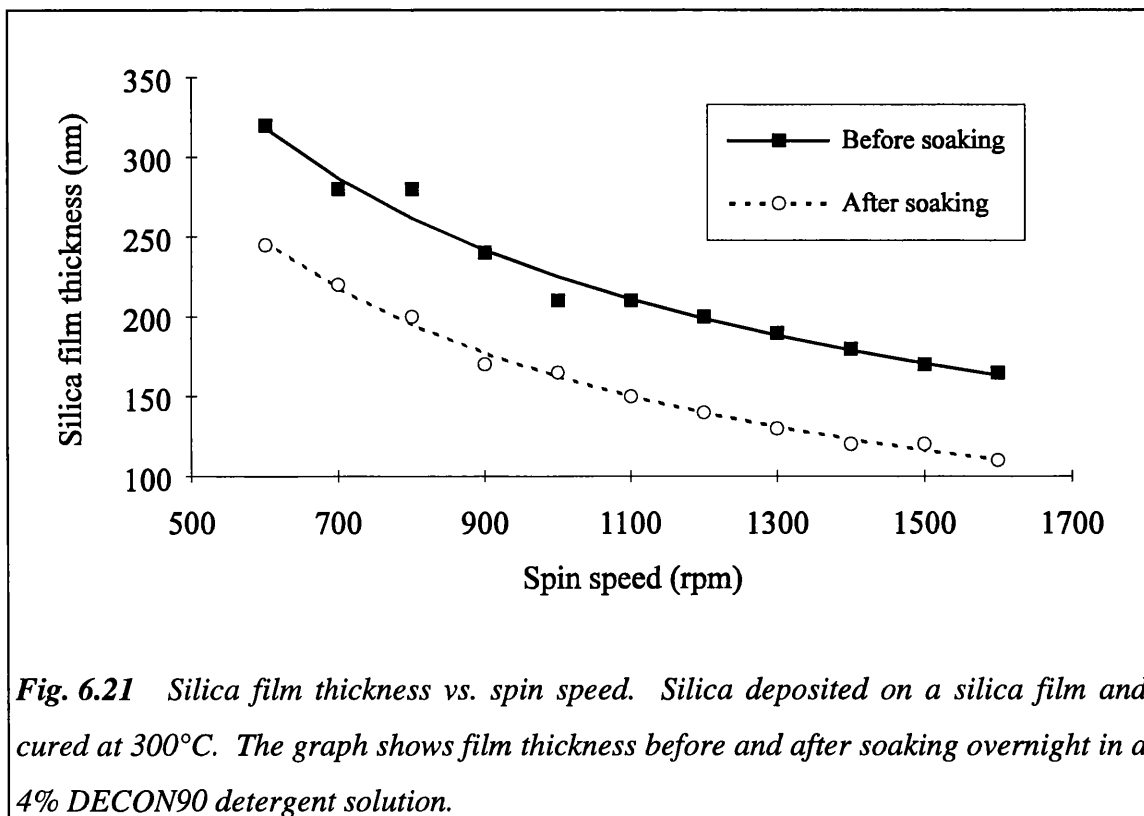
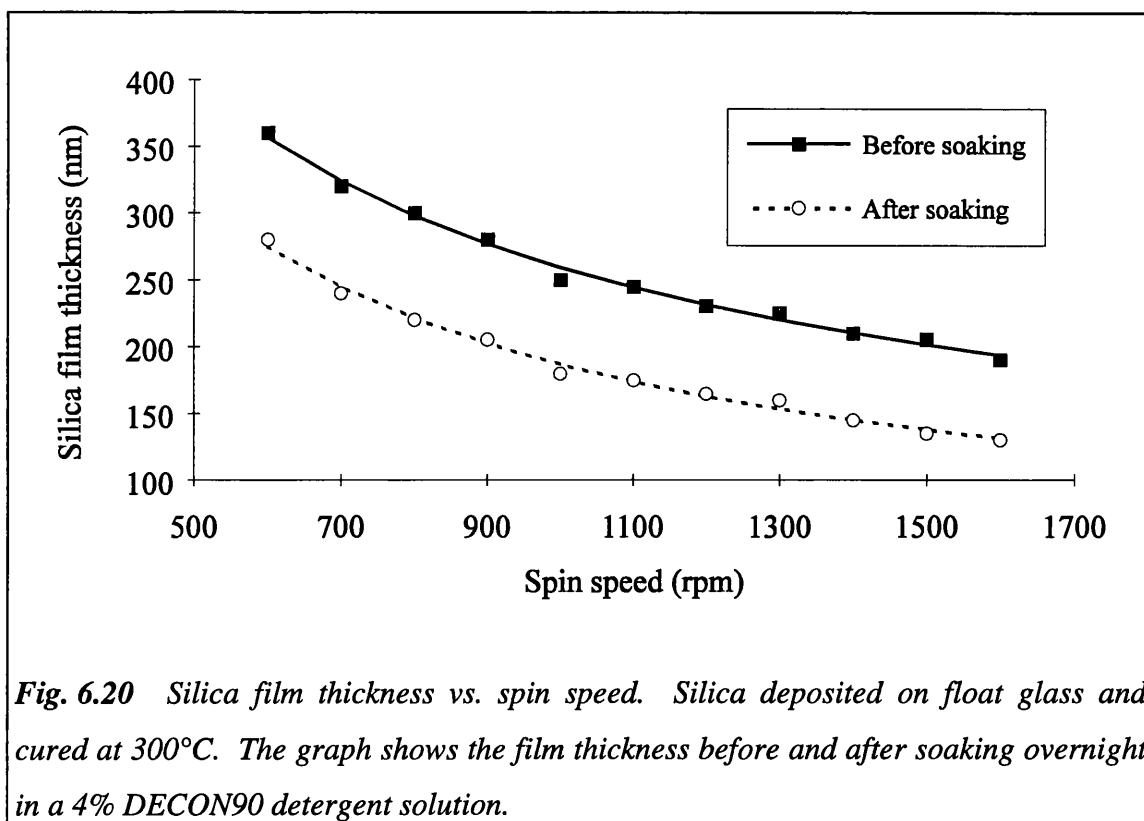


*Fig. 6.19 Spin coated sol-gel silica film thickness vs. spin speed. First coat is on float glass, the second is onto a sol-gel silica thin film. The silica was cured at 500°C.*

LIQUICOAT Si, *Merck Ltd, Germany*), and a second coat was required to increase the thickness. However, there was an upper limit to the silica film thickness. Above a thickness of approximately 750 - 800nm the films exhibited a slight, but visible, opacity and, on examination under a microscope, the films had a crazed appearance. This became more significant as the film thickness increased, and above about 1000nm the films became rough to the touch and the surface of the film began to flake off. The most likely cause of this is the difference in the thermal expansion coefficients of the silica film and float glass substrates. The difference becomes significant at high silica film thicknesses, causing the film to craze or flake. The degradation of a thin film due to expansion coefficient differences has been observed before [15]. A possible solution would be to cure the film at a lower temperature, but this would result in a more porous film [16, 17].

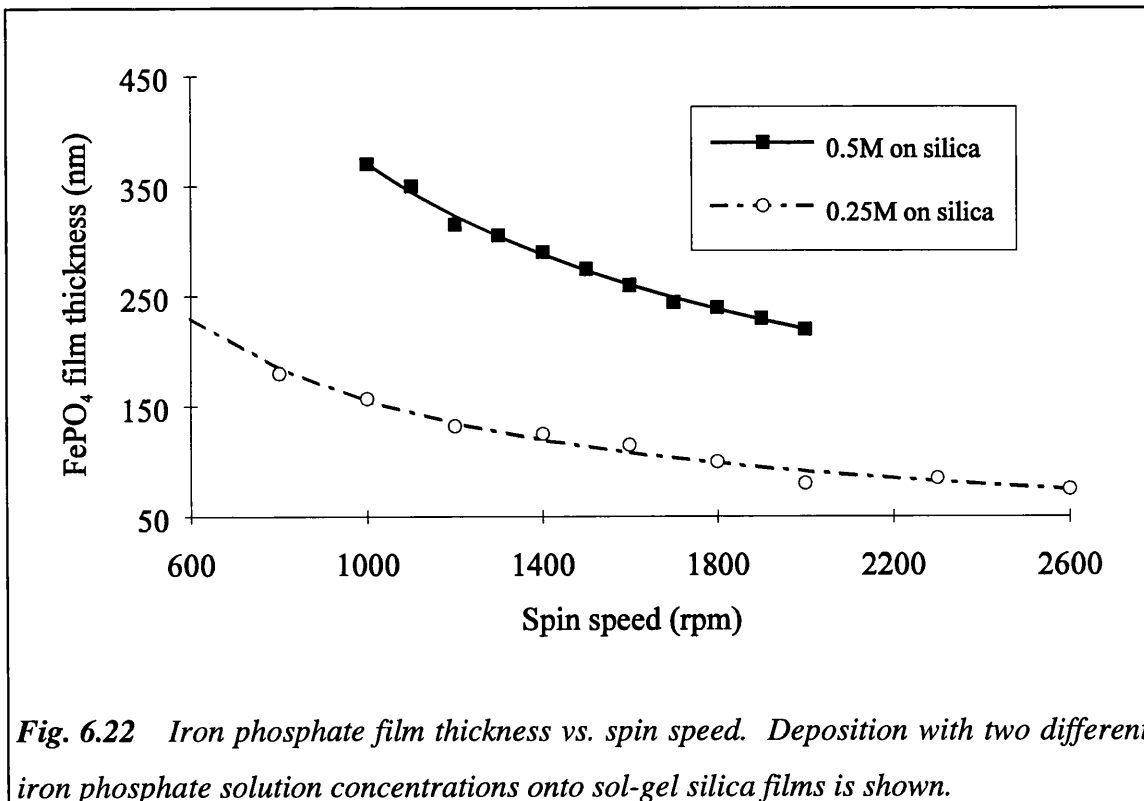
Figs. 6.20 - 6.21 show how the silica film thickness depends on spin speed when the silica is cured at 300°C. At this temperature, the second deposition of silica gives a thinner film than the initial deposition onto float glass. The reasons for this were not investigated.

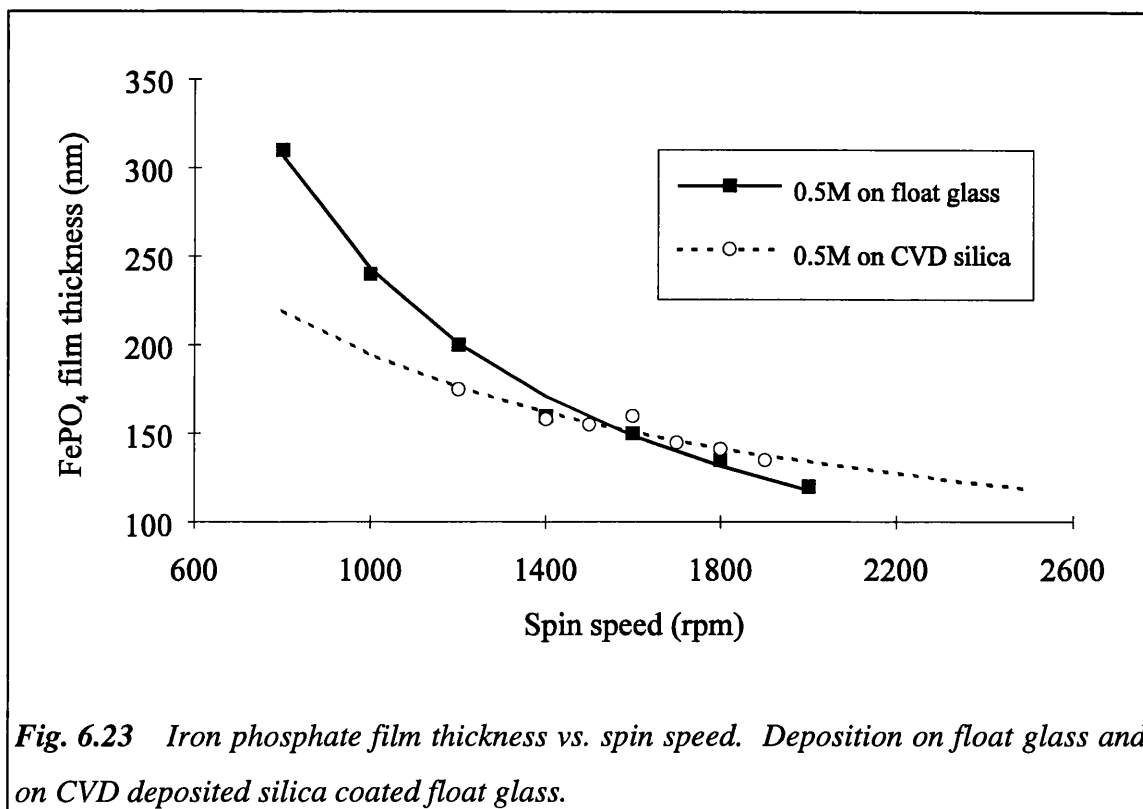


It can be seen from the graphs that sol-gel silica cured at 300°C is etched by long-term exposure to an alkaline solution (a 4% DECON90 solution has a pH of ~10.5 - 11). Etching of the silica film was not observed when the film was cured at 500°C. When cured at 300°C, the sol-gel silica film is not fully densified and remains porous [16, 18]. Full densification is achieved only at temperatures of over 900°C, although near-full densification is achieved at 500°C [18]. It is known that strong alkaline solutions dissolve silica and the porous nature of the sol-gel silica cured at 300°C may present a large surface area allowing it to be etched more rapidly than a dense film. However, there was no indication that either the 300°C or 500°C cured silica film was etched by a short exposure (~5mins) to the aluminium etchant used to remove the iron phosphate film.

**6.2.2 Iron phosphate film spin coating**

Iron phosphate (for the waveguide layer) was deposited onto the silica film (the





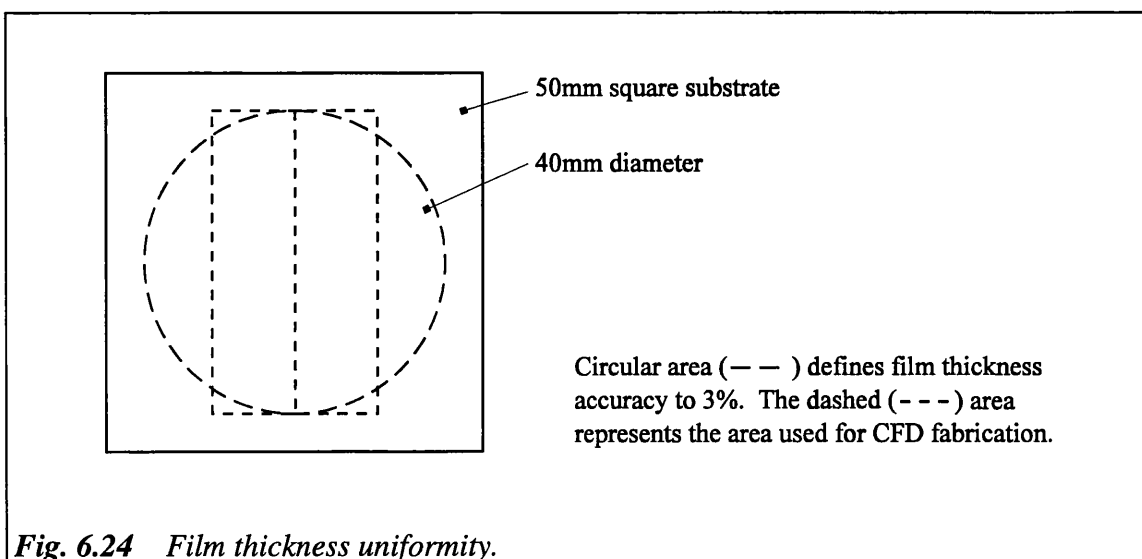
buffer layer). The simple equation 6.3 that describes the relationship between film thickness and spin speed for spin coated films applies to the iron phosphate films.

Figs. 6.22 - 6.23 show the iron phosphate film thickness as a function of spin speed and how the film thickness varies depending on the substrate that the film is deposited on. Iron phosphate films deposited on sol-gel silica coated substrates produced thicker films than deposition onto uncoated float glass. The reasons for this, as with silica layer deposition, are unclear and may be related to the micro-porous nature of the sol-gel deposited silica layer. This argument is partially supported by fig. 6.23 where iron phosphate deposition on a silica film deposited by a CVD process shows similar film thickness to iron phosphate deposited onto float glass. However, the deposition onto the CVD silica coated substrate shows a lower gradient.

### 6.2.3 Film thickness uniformity

Generally, the film thickness could be maintained to within about 3% across the surface of a 50mm square substrate (this area is shown in fig. 6.24). Note that, due to edge effects, this accuracy did not apply within 5mm of the edge of the substrate.

However, there was also a film thickness uniformity problem related to the spinner chuck on which the substrates were placed during spin-coating. Fig. 6.25 shows the surface of the spinner chuck which has a series of concentric circular grooves connected by radial grooves to a hole in the centre of the chuck. A vacuum is applied through this hole to hold the substrate securely on the chuck. It was found, through experiments conducted by *Dr. A Sloper*, that a spin coated film thickness dropped by between 5 - 10% in the area that was immediately above the radial grooves during spinning. This suggested that the coating solution lying immediately above the grooves was more fluid than elsewhere on the substrate, and that, because of the outward flow of solution during spinning, film thickness non-uniformities occurred only above the radial grooves. When a PTFE chuck cover was used, the film thickness non-uniformity due to the radial grooves fell to less than 5%. This suggested that thermal conduction through the chuck may be responsible. Heat transfer through the glass substrate is greater where the substrate is in contact with the metal chuck and less where the substrate is not in



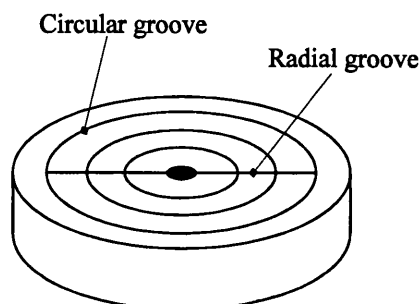


**Fig. 6.25** *Surface of spinner chuck.*

contact (ie. above the grooves). A lower rate of heat transfer from the chuck to the solution above the grooves allows the solution to remain more fluid (due to a lower solvent evaporation rate) and, therefore, produce a drop in film thickness.

A PTFE chuck cover was available for use with 90mm square substrates, but not for use with the 50mm square substrates on which all the films used for the immunosensor experiments were deposited. To minimise the effect of the thickness non-uniformity, the substrates were carefully aligned on the spinner chuck such that the radial grooves on the chuck ran lengthways along the capillary cells (see fig. 6.24) and, thus, would lie below the central divider in the dual cell CFD.

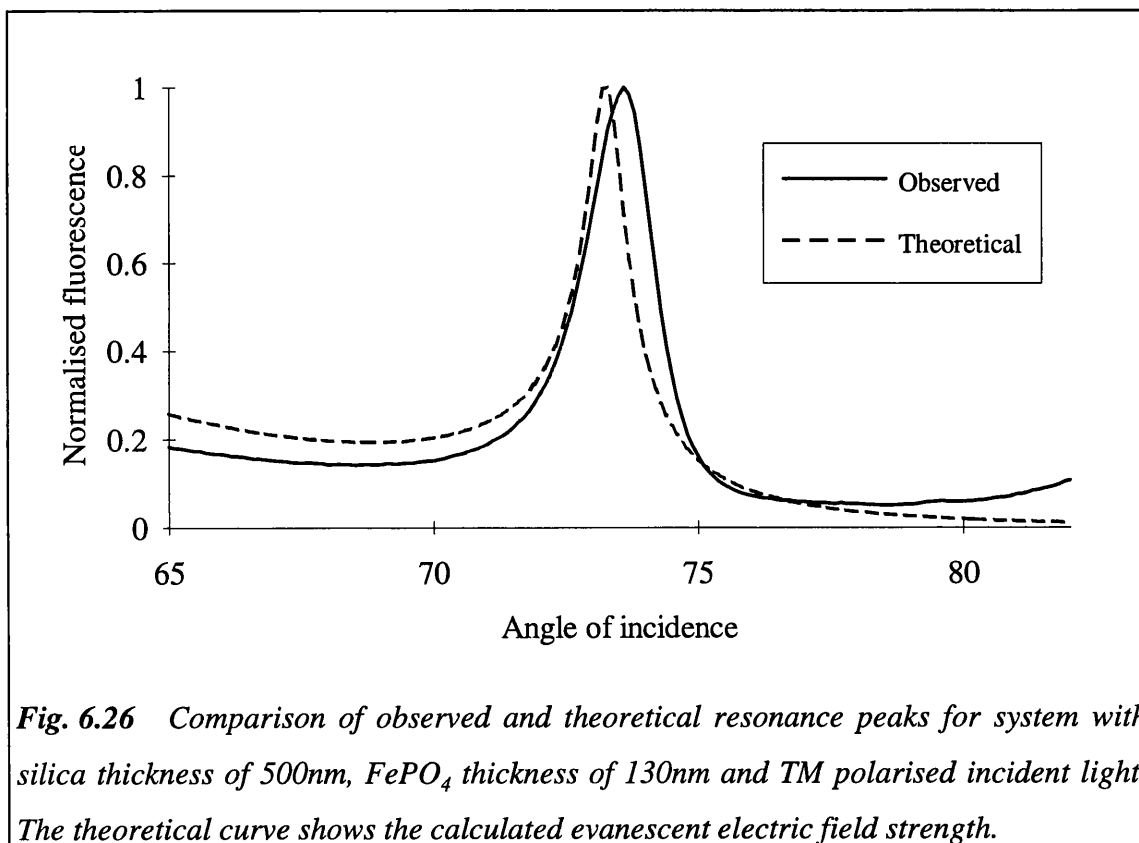
#### **6.2.4 Optical resonance in the four layer system**

It was now possible to perform some measurements on the four layer system (substrate, silica buffer, iron phosphate waveguide and superstrate/solution layers). It was decided to use a fluorescent solution as the superstrate/solution layer in the four layer system. This would allow the measurement of the evanescent field in the superstrate/solution layer, and the observation of the resonance characteristics of the system. Thus, single cell CFD's were fabricated (as described in chapter 5) from substrates having had silica and iron phosphate thin films of varying thicknesses deposited on them. The CFD's could then be filled with a fluorescent solution of a

complex of Nile blue and bovine serum albumin, and a scan over a range of exciting light angles of incidence could be performed to obtain the resonance peak.

Fig. 6.26 shows a typical angular scan and how it compares with a theoretical curve for an 'ideal' resonant system with the same thin film thicknesses. There is a good agreement between the shapes of the two curves in Fig. 6.26 but the observed resonance peak is slightly broader than the theoretical peak. The deviation from theory can be expected because the iron phosphate film thickness uniformity could vary by up to 5% and because the incident light had a slight convergence of  $\sim 0.12^\circ$ . Note that the theoretical curve has been calculated using estimated silica and iron phosphate refractive indices - the method of estimation is described in Chapter 5 and in Section 6.3.

The experimental apparatus and the prism/CFD mount ensured that the incident light convergence remained identical between measurements, but variations in the sharpness of the resonant peaks, due to iron phosphate film thickness non-uniformities,



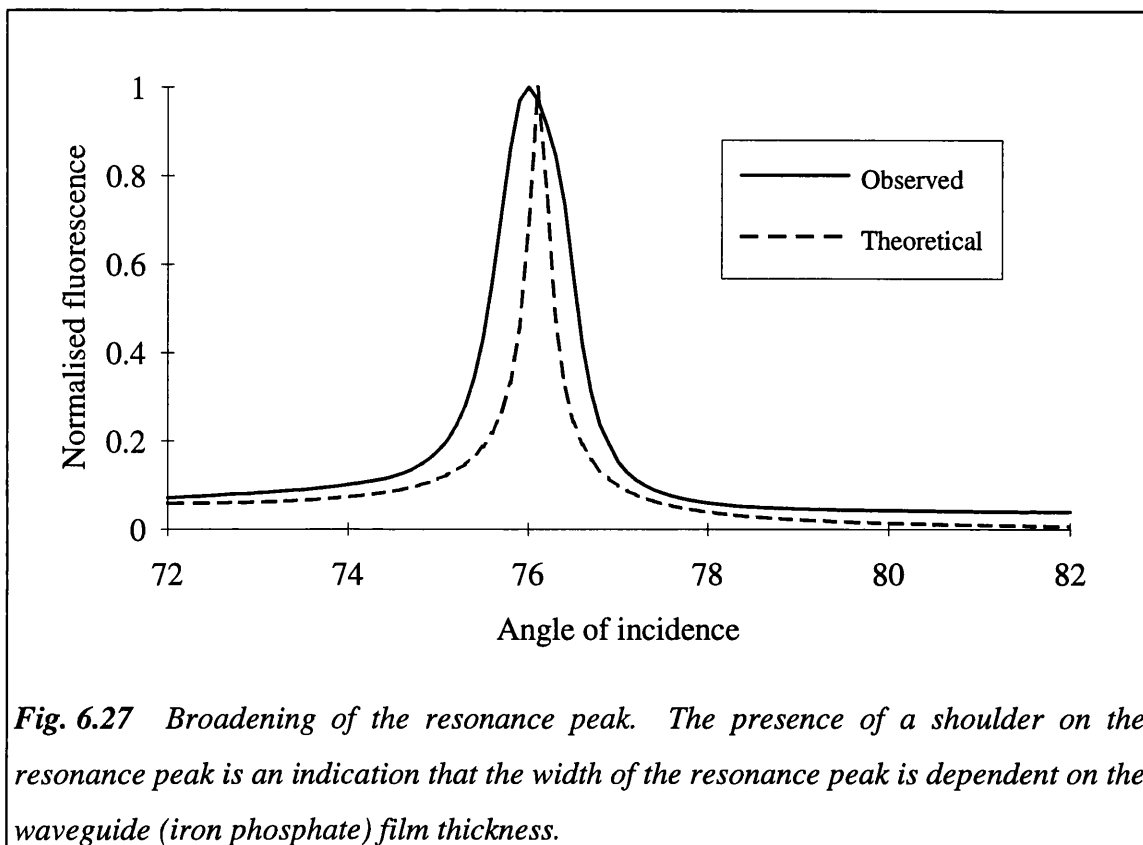


**Fig. 6.27** Broadening of the resonance peak. The presence of a shoulder on the resonance peak is an indication that the width of the resonance peak is dependent on the waveguide (iron phosphate) film thickness.

could be observed (fig. 6.27). An indication that the differences in the width of the resonant peaks between devices may be film thickness related is given by the presence of a shoulder on some observed resonance peaks. Variations in the divergence or convergence of the incident light would give a smooth, but broad, peak, whereas the presence of a localised thickness non-uniformity would allow a localised resonant wave to be established at a slightly different angle of incidence to the general resonance peak. This would show as a shoulder on the overall resonance peak.

### 6.3 THIN FILM REFRACTIVE INDICES ESTIMATION

The refractive indices of the sol-gel silica and iron phosphate thin film layers were estimated by fitting the multilayer theory described in chapter 4 (and illustrated in section 6.1) to measurements of the resonant angle of incidence for multilayer systems

with varying silica and iron phosphate film thicknesses. Resonant multilayer devices were fabricated with silica film thicknesses between 500 - 800 nm and iron phosphate film thicknesses between 70 - 190 nm, from which single cell capillary fill devices were then assembled. Angular scans were then performed to obtain the angle of incidence required for maximum fluorescence emission.

The theoretical resonant angles of incidence were calculated for each film thickness using estimated silica and iron phosphate refractive indices. A constrained least squares minimisation using unweighted data points on the observed resonant angles was performed to fit the theory to the available data and, thus, obtain the silica and iron phosphate refractive indices. A 'simplex' minimisation routine [2] was used to perform the non-linear regression. The regression yielded values of 1.439 and 1.702 for the silica and iron phosphate thin films respectively. Figs. 6.28 - 6.30 show the fitting graphically. Note that, due to the dependence of the resonant angle on the silica layer thickness, the fit in fig. 6.30 is not a smooth curve (caused by small variations in the silica thickness).

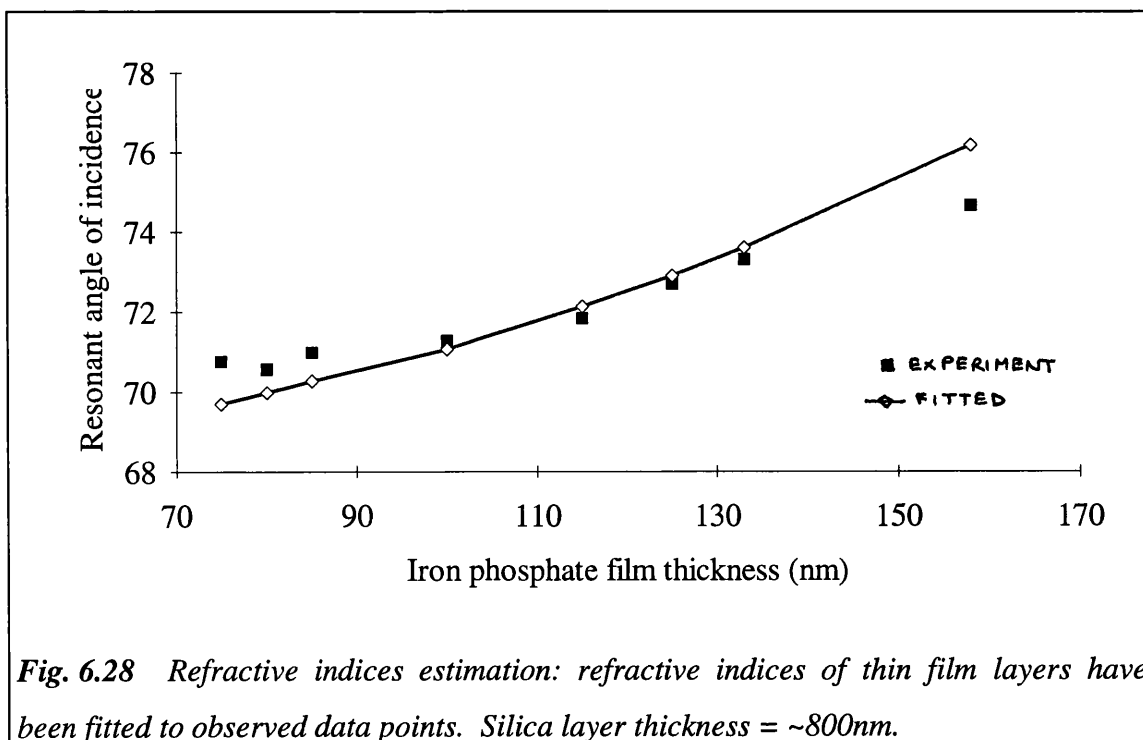


**Fig. 6.28** Refractive indices estimation: refractive indices of thin film layers have been fitted to observed data points. Silica layer thickness = ~800nm.

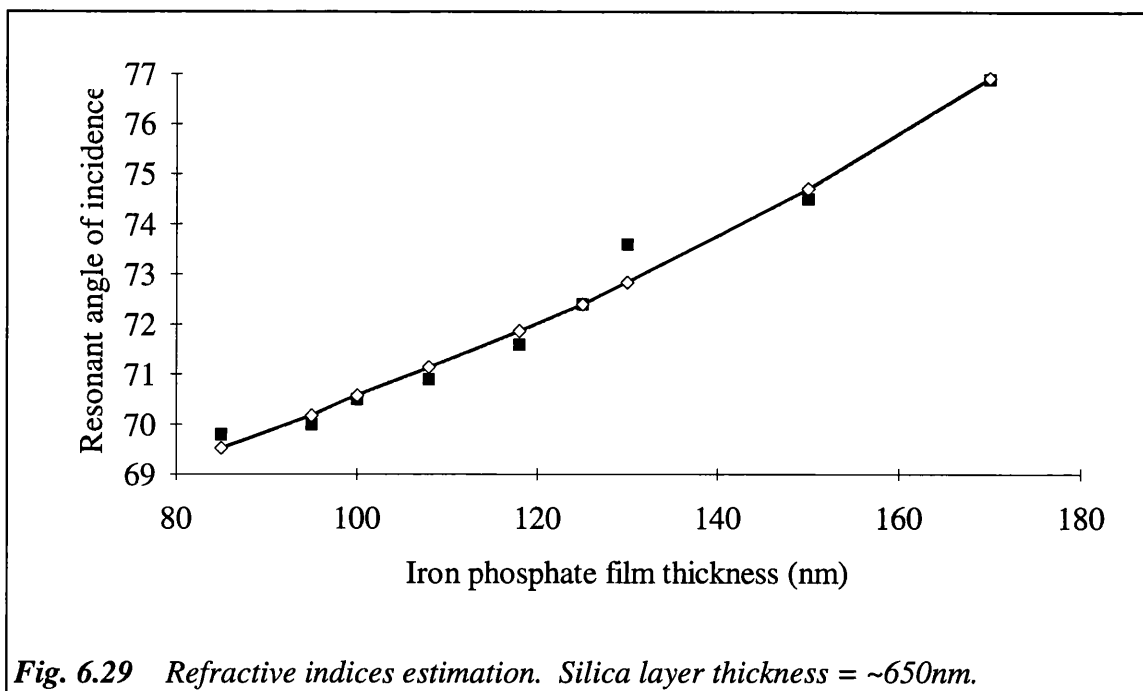


Fig. 6.29 Refractive indices estimation. Silica layer thickness = ~650nm.

The manufacturer's (*Merck Ltd.*) data on LIQUICOAT™ Si [17] suggests a refractive index of 1.4 for sol-gel derived silica. This is contradicted by *Hewak & Lit* [18] who, also using LIQUICOAT™ products, obtained a sol-gel silica refractive index of 1.465 (at a wavelength of 633nm) when cured at 500°C. However, the former value

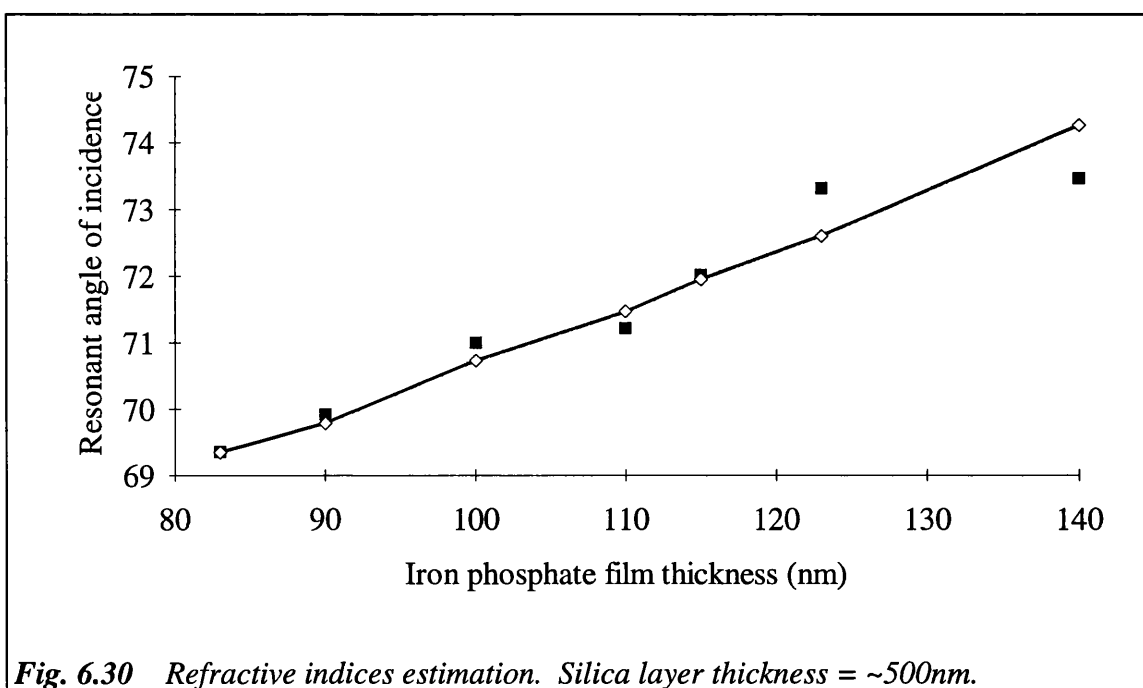
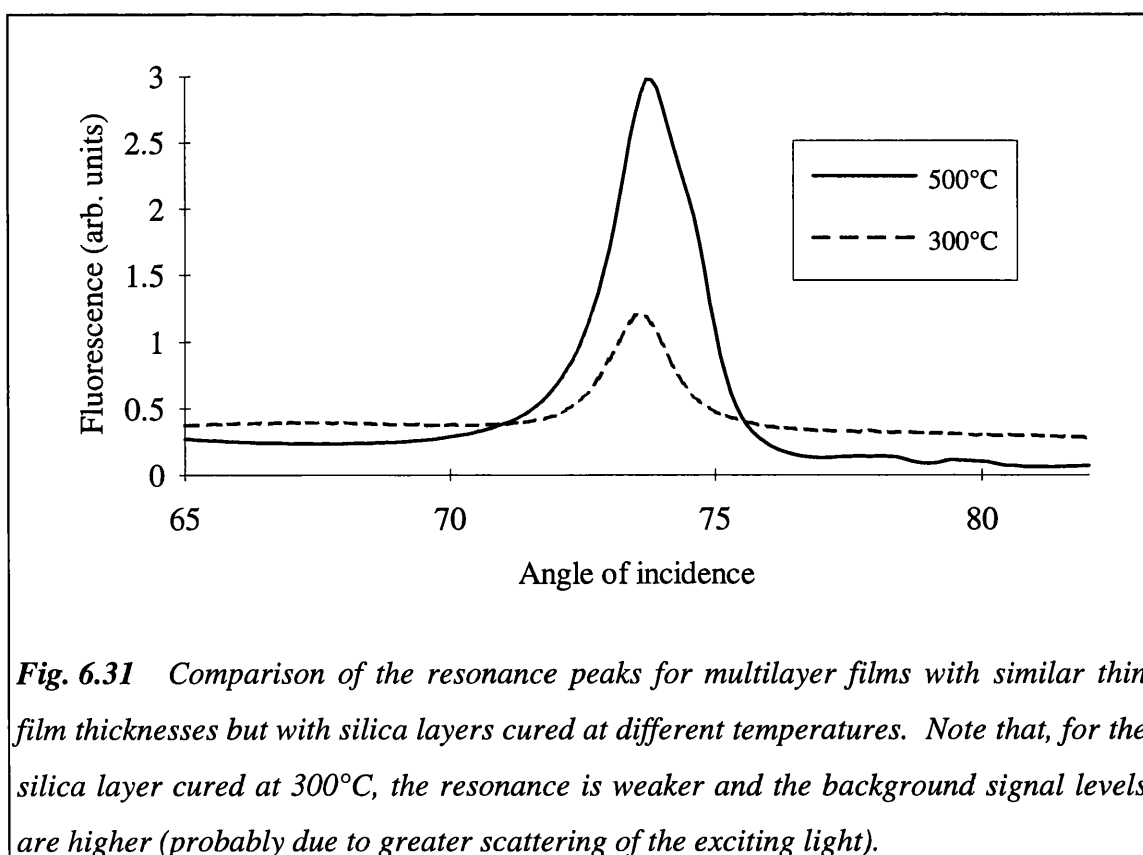


Fig. 6.30 Refractive indices estimation. Silica layer thickness = ~500nm.

seems low and the latter seems high when considering that the refractive index of dense, bulk silica is 1.457 [19]. The silica layer refractive index of 1.44 obtained from the resonant angle fitting lies in between the values quoted by *Merck* and *Hewak & Lit* and can be reasonably assumed to be a good estimate of the true refractive index.

*Sloper & Flanagan* [20] obtained an iron phosphate refractive index of 1.72 when deposited on a PERMABLOC float glass substrate and cured at 200°C, whereas, a value of 1.70 was obtained for deposition on sol-gel silica in the multilayer system. The difference between the two values may be caused by the porosity of the underlying sol-gel derived silica layer. The porous surface of the silica layer will absorb some of the coating solution immediately before and during spinning, creating a transition layer with a refractive index varying between the silica and iron phosphate refractive indices. Thus, when fitting the observed data to the multilayer theory, the presence of a transition layer may increase the estimated silica refractive index and decrease the estimated iron phosphate refractive index. This was confirmed when the multilayer theory was fitted to



**Fig. 6.31** Comparison of the resonance peaks for multilayer films with similar thin film thicknesses but with silica layers cured at different temperatures. Note that, for the silica layer cured at 300°C, the resonance is weaker and the background signal levels are higher (probably due to greater scattering of the exciting light).

the resonant angles for devices fabricated with a silica layer cured only at 300°C. The lower curing temperature would leave a more porous silica layer with a lower refractive index than curing at 500°C. The refractive indices for a silica layer cured at 300°C were 1.47 and 1.57 for the silica and iron phosphate layers respectively. The large drop in the iron phosphate layer refractive index as compared to the relatively small rise in the silica layer refractive index may be explained by comparing the thicknesses of the two films. The silica layer was between 500 - 800nm thick whereas the iron phosphate layer was between 60 - 135nm thick. Therefore, the presence of a transition layer due to the absorption of iron phosphate into the pores in the silica layer, would have a more significant effect on the estimated iron phosphate refractive index than on the silica refractive index. The low iron phosphate to silica refractive index ratio should produce a weak resonance peak and this is confirmed in fig. 6.31.

## 6.4 DISCUSSION

The theoretical analysis of the multilayer resonant system provided a number of requirements for the maximisation of the evanescent field strength:

- a large waveguide layer to buffer layer refractive index ratio.
- a buffer layer thickness of  $\sim 2\mu\text{m}$  when a silica layer is used. Thicker buffer layers produce, theoretically, very sharp resonance peaks and, therefore practically, the shape of the resonance peak may become highly dependent on the waveguide layer thickness non-uniformities (eg. multiple peaks).
- a waveguide layer thickness of  $\sim 200\text{nm}$  when an iron phosphate layer is used.

Minimisation of the penetration depth of the evanescent field simply required the exciting light to be incident at a high angle of incidence.

However, practical considerations and experimental work put limits on the conclusions obtained from the theoretical work:

- The waveguide layer to buffer layer refractive index ratio was limited by the ready availability of materials that could be spin-coated.
- The thickness of the silica layer was limited to less than 800nm to preserve the quality of the thin film.
- The angle of incidence was limited to less than 80° to prevent the exciting beam from striking the ends of the capillary fill devices, thus limiting the thickness of the iron phosphate layer.
- The observed resonance peaks were weaker and broader than the theoretical peaks due to the convergence of the exciting beam and to film thickness non-uniformities.

The agreement between theory and experiment was, however, sufficient to allow the theory to be used in the estimation of the silica and iron phosphate thin film refractive indices. The theory still requires improvement to match the experimental conditions more closely and to obtain a better correlation between experimental data and theory. This was done when modelling the immunosensor and will be discussed in chapter 8.

The experimental and theoretical work described in this chapter allowed the parameters of the multilayer devices for immunosensing to be ascertained:

- A silica layer thickness of ~750nm.
- An iron phosphate layer thickness of between 150 - 170nm which would give resonant angles of incidence between 75° - 77°.

The following chapter describes the immunosensing work that was performed using the multilayer devices.

## REFERENCES

- 1 THORNE A P, Spectrophysics, *Chapman and Hall, London, 1988, 2nd ed., 1-92.*
- 2 PRESS W H *et al*, Numerical recipes in C, *Cambridge University Press, Cambridge, 1992, 2nd ed., 408-412.*
- 3 NELDER J A, MEAD R, A simplex method for function minimization, *Computer Journal, 1965, 7, 308-313.*
- 4 ATTRIDGE J W *et al*, Sensitivity enhancement of optical immunosensors by the use of a surface plasmon resonance fluoroimmunoassay, *Biosensors & Bioelectronics, 1991, 6, 201-214.*
- 5 CUSH R *et al*, The resonant mirror: a novel optical sensor for direct sensing of biomolecular interactions. Part I: principle of operation and associated instrumentation, *Biosensors & Bioelectronics, 1993, 8, 347-353.*
- 6 BUCKLE P E *et al*, The resonant mirror: a novel optical sensor for direct sensing of biomolecular interactions. Part II: applications, *Biosensors & Bioelectronics, 1993, 8, 355-363.*
- 7 FONTANA E, PANTELL R H, STROBER S, Surface plasmon immunoassay, *Applied Optics, 1990, 29(31), 4694-4704.*
- 8 CULLEN D C, BROWN R G W, LOWE C R, Detection of immuno-complex formation via surface plasmon resonance on gold-coated diffraction gratings, *Biosensors, 1987/88, 3, 211-225.*
- 9 ARWIN H, Optical properties of thin layers of bovine serum albumin, gamma-globulin, and haemoglobin, *Applied Spectroscopy, 1986, 40, 313-318.*
- 10 PUTZEYS P, BROSTEAUX J, L'indice de réfraction des protéides, *Bulletin de la Société de Chimie Biologique, 1936, 18(11), 1681-1703.*
- 11 KOOYMAN R P H, KOLKMAN H, VAN GENT J, GREVE J, Surface plasmon resonance immunosensors: sensitivity considerations, *Analytica Chimica Acta, 1988, 213, 35-45.*
- 12 DANIELS P B, DEACON J K, EDDOWS M J, PEDLEY D G, Surface plasmon resonance applied to immunosensing, *Sensors and Actuators, 1988, 15, 11-18.*
- 13 GIVENS F L, DAUGHTON W J, On the uniformity of thin films: a new technique applied to polyimides, *Journal of the Electrochemical Society, 1979, 126(2), 269-272.*
- 14 WASHO B D, Rheology and modelling of the spin coating process, *IBM Journal of Research and Development, 1977, 21(1), 190-198.*
- 15 SAKKA S, YOKO T, Sol-gel derived coating films and applications, in REISFELD R, JØRGENSEN C K EDS., Structure and Bonding 77, *Springer-Verlag, Berlin, 1992, 90-118.*
- 16 NELLEN Ph M, LUKOSZ W, Integrated optical input grating couplers as direct affinity sensors, *Biosensors & Bioelectronics, 1993, 8, 129-147.*
- 17 LIQUICOAT™ solutions information, *Merck Ltd., Germany.*
- 18 HEWAK D W, LIT J W Y, Standardization and control of a dip-coating procedure for optical thin films prepared from solution, *Canadian Journal of Physics, 1988, 66, 861-867.*

- 19 **MALITSON I H**, Interspecimen comparison of the refractive index of fused silica, *Journal of the Optical Society of America*, 1965, **55**(10), 1205-1209.
- 20 **SLOPER A N, FLANAGAN M T**, Novel iron phosphate optical waveguides fabricated by a low temperature process, *Electronics Letters*, 1988, **24**(6), 353-355.

## CHAPTER 7

### MULTILAYER THIN FILM OPTICAL IMMUNOSENSORS

*Multilayer thin film immunosensor devices are described in this chapter. The devices were fabricated as capillary fill devices and were characterised using a sandwich assay for mouse IgG in phosphate buffered saline. The performance of the multilayer thin film immunosensor was assessed by comparison with a simple single spot total internal reflection (TIR) immunosensor. The performance of both the multilayer thin film and TIR immunosensors using 633nm HeNe laser and 650nm laser diode light sources are assessed and contrasted.*

#### 7.1 DEVICES FOR IMMUNOSENSING

##### 7.1.1 Multilayer thin film sensor specification

Improvements in the performance, in terms of sensitivity and accuracy, of a sensor can be achieved by improving the signal-to-noise ratio or the signal-to-background ratio.

Noise can be defined as the variability (eg. standard deviation) of the measured signal for repeated measurements at the same analyte concentration (see chapter 2, fig. 2.3) and it affects both sensor accuracy and sensitivity. The noise in the response of a sensor can be attributed to a number of causes, of which a few examples are listed below:

- electrical noise eg. noise in the detector, amplifiers, etc.
- variations between individual devices or between batches eg. variations in

thin film characteristics, film thickness non-uniformities or capture antibody activity.

- variations in the sample solution eg. pH or metabolite content.
- user error eg. poor equipment maintenance, use of unclean devices.

The last of the above list is unpredictable and, therefore, is difficult to incorporate into any assessments of sensor performance.

Unlike noise, the background signal is relatively stable between measurements and is typically due to detector dark current, ambient background light contamination or fluorescence excited from unbound labelled antibodies. Exciting light scattering is one problem that can contribute to both the noise and background signals depending on where the scattering arose (scattering from the substrate may be relatively stable, whereas scattering from the capture layer may be highly variable between devices).

Hence, sensor accuracy can be improved by increasing the signal-to-noise ratio, whereas, sensor sensitivity can be improved by either increasing the signal-to-noise ratio or the signal-to-background ratio or both. Assuming that production variations between devices can be minimised, the signal-to-noise ratio can be improved by increasing the signal strength (eg. by increasing the exciting light intensity), but at the cost of increased scattering which compromises the signal-to-background ratio. Assuming that the detector dark current and ambient light can be minimised, the signal-to-background ratio can be improved by increasing the discrimination of the bound layer fluorescence to the unbound layer fluorescence (eg. by reducing the evanescent field penetration depth).

The fluorescence signal strength can be increased by using a more powerful exciting light source, but this would have the effect of increasing the noise and background signal sources (eg. scattering and phosphorescence) in proportion with the exciting light source intensity throughout the whole device. The multilayer device, by concentrating the light energy in the waveguide layer, increases the background and noise signals only in the waveguide and adjacent layers but not in the rest of the device.

The strongest resonance, in a multilayer system, occurs at high exciting light angles of incidence and this offers a second advantage over a TIR system. The combination of a strong evanescent field and a low penetration depth (at a high angle of incidence) should offer an improved signal-to-background ratio and therefore an improved sensitivity.

Discussed, at the end of chapter 6, were the requirements for a multilayer system with silica and iron phosphate thin films that would offer the best combination of evanescent field strength and penetration depth. However, due to practical limitations, these requirements could not be met. Thus, the system that was adopted for use as an immunosensor had a silica film (buffer) thickness of  $750\pm 50\text{nm}$  and an iron phosphate film (waveguide) thickness of  $160\pm 10\text{nm}$ . The iron phosphate film thickness gives a resonant exciting light angle of incidence of  $\sim 76^\circ \pm 1^\circ$ . Although a higher angle of incidence would give a lower penetration depth,  $76^\circ$  was chosen to allow the performance of the multilayer immunosensor to be assessed at off-resonance angles of incidence on both sides of the resonant angle of incidence. Note that the maximum angle of incidence, limited by the size of the device and the experimental apparatus, was  $\sim 82^\circ$ .

### **7.1.2 Total internal reflection sensor specification**

The total internal reflection sensor system was used as a comparison for the multilayer system. This comparison, due to the inherent similarities between the two systems, was simple and easy to achieve by replacing the multilayer device in the experimental apparatus with a TIR device.

The TIR device used was fabricated in a similar manner to the multilayer device, but without any thin film layers, thus ensuring that resonance could not be excited.

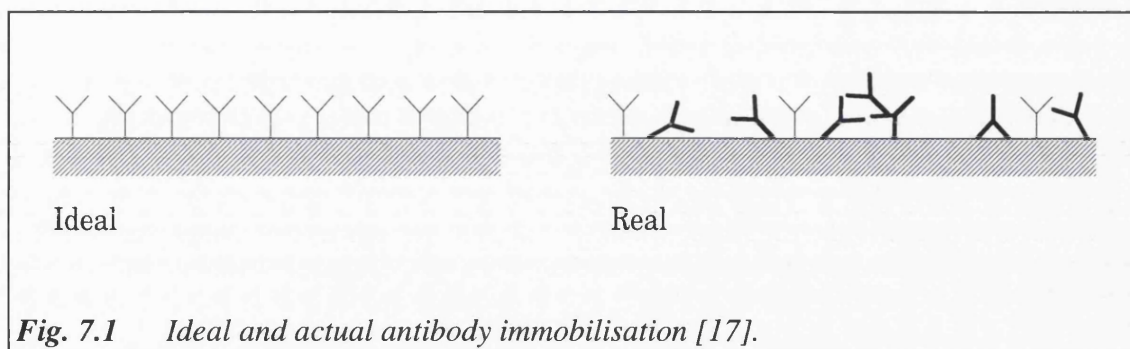
### **7.1.3 The capillary fill device**

The capillary fill device (CFD) [1, 2] provides an excellent means by which a small, well defined volume of sample solution can be introduced into the immunosensing device. Looking towards the commercial exploitation of immunosensor devices, the CFD can also be used such that a sandwich assay, which requires the addition of a reagent, can appear reagentless to the user [1] and, therefore, simpler to use.

The immunosensing devices used were all fabricated as dual cell CFD's (see chapter 5, fig. 5.7). A dual cell CFD was used to allow a reference measurement to be taken along with the sample measurement to account for fabrication differences between devices. A commercial biosensor may require a similar reference measurement to account for fabrication differences, sample solution dependence, non-specific binding, etc..

## **7.2 CAPTURE ANTIBODY IMMOBILISATION**

The immunosensors described in this thesis require the immobilisation of the capture antibody onto a solid, glass support. The requirements for an immobilisation technique are that it provides a high density of stable, active binding sites [3] distributed evenly over the surface of the sensor and that the capture layer thickness remains well within the penetration depth of the evanescent field. A high density of binding sites increases the amount of analyte binding to the capture layer, increases the analyte/capture antibody binding rate and increases the analyte concentration that can be measured before the sensor saturates, thus increasing the dynamic range of the sensor. The capture layer thickness is required to be less than the penetration depth so that there is a strong evanescent field strength available to excite fluorescence from the labelled antibody. Another requirement is that the capture antibody is bound strongly to the solid



support so that the density of active binding sites is less sensitive to sample solution variations (eg. pH). Ideally, a technique that gives the maximum density of active binding sites and zero non-specific binding sites is preferable, but this, as with most immobilisation techniques is not the case, as is shown in fig. 7.1.

The more common immobilisation methods employed are:

- binding to gel-matrices [7, 13]. This is a more complex method than adsorption, but antibody activity remains high and the process is reversible, thus allowing the immunosensor devices to be re-used. The gel-matrix usually forms a thick layer (~400nm [7]) so that many analyte binding sites may be outside the penetration depth of the evanescent field. Immobilisation needs to be performed shortly before use as these techniques do not offer a long shelf-life.
- adsorption onto the support [4]. A simple method but the antibodies are bound only weakly to the support and antibody activity may be reduced due to steric hindrance (see fig. 7.1). A single layer of capture antibodies can be immobilised (~10nm thick). Long shelf-life is possible by depositing a humectant (eg. sucrose) coating over the immobilised layer.
- covalent binding directly to the solid support [5]. The antibodies are strongly bound, hence the process is irreversible but antibody activity may be reduced due to steric hindrance (fig. 7.1). Long shelf-life is possible by coating with a humectant layer.

Techniques that employ the binding of the antibody to a gel-matrix have been used by *Pharmacia* in their BIAcore system [6] and also by *Fisons* [7]. However, these devices are re-usable and require the user to perform the immobilisation of the capture antibody. Considering the market of single-use disposable biosensor devices (as discussed in chapters 1 - 3), a gel-matrix technique of immobilising antibodies would be inappropriate due to the limited shelf-life and the requirement for the user to perform the immobilisation. Adsorption techniques, currently used by many researchers [8, 9], lend themselves easily to a mass production system because of the simplicity of the technique. However, the drawback is that the nature of the binding of the antibody to the support is unpredictable and that the binding may be weak and, thus, more sensitive to the sample solution properties.

Covalent coupling of the capture antibody to the solid support provides a layer of capture antibodies that are chemically bound more strongly than adsorption [10] and also have a longer shelf-life than binding to a gel-matrix. However, the density of available analyte binding sites when using covalent coupling is lower than for immobilisation using a gel-matrix [7]. Theoretically, (assuming antibodies are spherical with a 10nm diameter and that they are hexagonally close packed) an active binding site density of 38.5 fmol/mm<sup>2</sup> is possible.

Covalent coupling of the capture antibodies was used as the immobilisation technique for the immunosensors described in this thesis using a standard coupling method described in chapter 5. The method is based on the derivatisation of hydroxyl groups on a glass surface using glycidyl oxypropyltrimethoxysilane followed by the formation of a peptide link between the silane complex and the protein.

The above method has been used previously in this department by *Dr. A Sloper* for immobilisation onto phosphate glasses and PERMABLOC™ float glass [11]. Figures of 3.05±0.41 and 3.32 fmol/mm<sup>2</sup> were obtained for the number of active binding sites for immobilisation onto indium phosphate and iron phosphate thin films respectively by using a commercially available ELISA test. A similar figure of 2.86±0.57 fmol/mm<sup>2</sup>

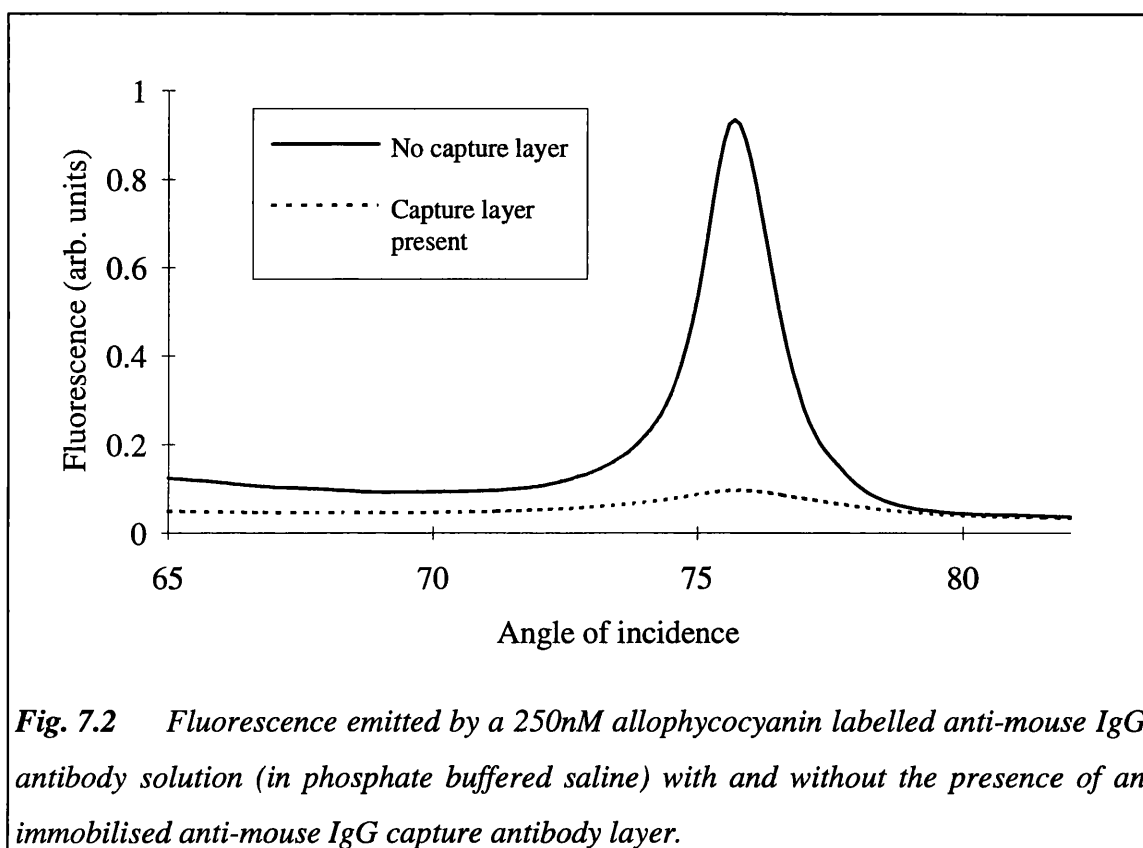


**Fig. 7.2** Fluorescence emitted by a 250nM allophycocyanin labelled anti-mouse IgG antibody solution (in phosphate buffered saline) with and without the presence of an immobilised anti-mouse IgG capture antibody layer.

was obtained for immobilisation onto PERMABLOC float glass. A Comparison of these figures with the theoretical density of active binding sites suggests that less than 10% of the possible number of active binding sites can be realistically achieved. It is likely that near full coverage of the sensor surface with capture antibodies is achieved but, as shown in fig. 7.1, most of the capture antibody binding sites are either inactive or inhibited from binding due to steric hindrance. This is confirmed in fig. 7.2 where the fluorescence from a multilayer device is much greater when a capture antibody layer is not present. The lack of a capture antibody layer allows the labelled antibody to bind non-specifically directly onto the iron phosphate (waveguide) layer, thus bringing the fluorophore within the evanescent field and greatly increasing the fluorescent signal. The large fluorescence signal difference between the two curves in fig. 7.2 suggests that the capture antibody covers much more than 10% of the surface of the iron phosphate layer. The no capture layer to capture layer fluorescence signal ratio was highly variable between a minimum of ~10 to a maximum of ~50 indicating that adsorption and non-specific binding directly to the iron phosphate layer were greatly variable.

In a capillary cell with a capillary gap of  $\sim 130\mu\text{m}$ , the measured density of active binding sites would give a saturation analyte concentration at equilibrium of  $\sim 25\text{nM}$  (assuming that all the analyte binds to the capture antibodies). It is, however, unlikely that all the analyte will bind to the capture antibody and, therefore, quite probable that signal saturation will occur at a much higher analyte concentration than  $25\text{nM}$ . The immunosensors described in this thesis used a polyclonal antibody, for which the binding constants were not known, thus making it difficult to estimate what fraction of the available analyte would bind to the capture layer.

### **7.3 THE MODEL IMMUNOASSAY**

The immunoassay chosen to assess the performance of the multilayer and TIR immunosensors was a sandwich assay for mouse IgG in a phosphate buffered saline (pH 7.5) medium. The immobilised capture layer was polyclonal sheep anti-mouse IgG antibody and the mouse IgG analyte solution was obtained by diluting mouse serum calibrated for IgG content. The labelled antibody was either allophycocyanin conjugated polyclonal goat anti-mouse IgG antibody or CY5.18 (a sulphoindocyanine dye) labelled polyclonal sheep anti-mouse IgG antibody. The capture and labelled antibodies were affinity purified and were specific for both the heavy and light chains on the mouse IgG molecule.

Although the chosen assay is not representative of the types of immunoassay or analytes that a high-sensitivity multilayer immunosensor may be used for, it does serve the purpose for the comparison of the multilayer and TIR immunosensor technologies.

#### **7.3.1 Fluorescence excitation, collection and measurement**

A single laser (5mW, 632.8nm Helium-Neon) was available for much of the

multilayer characterisation work described in chapter 6, but, before the immunosensor work commenced, a visible wavelength laser diode (1mW, 650nm) became available. The use of a laser diode is essential (due to the reduced size and cost) in a commercial optical biosensor instrument and, thus, both the HeNe and diode lasers were used in the immunosensing experiments to compare their relative performances. Excitation of the fluorophores (allophycocyanin and CY5.18) was possible with either the 633nm or 650nm diodes (as described in chapter 5).

The commercial availability of appropriate interference filters in the red region of the visible spectrum is rather limited and the combination of filters used in the collection of the fluorescence signal (see chapter 5) represents the best compromise that could be made. Dyes such as allophycocyanin and CY5.18 require appropriately matched interference filters due to their small Stokes' shifts (the difference between the peak absorption and emission wavelengths) of 10nm and 20nm respectively. Hence, when exciting the fluorophore at the peak absorption wavelength, collection of the fluorescence at the peak emission wavelength is not possible due to the inadequate filtering of any scattered exciting light.

### **7.3.2 The sample and reference solutions**

Chapter 5 described the requirement for and the use of the dual cell capillary fill devices. These were necessary to allow a reference measurement to be taken for each sample measurement to compensate for variations in signal strength between devices.

#### **7.3.2.1 The sample solution**

The sample solutions were prepared by diluting mouse serum with 0.1M phosphate buffer containing 0.1M saline (PBS) to give a mouse IgG concentration within the range 1nM to 96nM. The required dilution ratios ranged from 100 to over 10000 and it can thus be assumed that the solution was essentially in a PBS medium.

The labelled anti-mouse IgG antibody concentration, in a sandwich assay, is determined by the affinity of the labelled antibody for the analyte - the greater the affinity, the lower the required labelled antibody concentration. The basic requirement is to push the reaction equilibrium such that all the analyte binds to a labelled antibody which requires a labelled antibody concentration greater than the maximum analyte concentration. The affinities of the labelled polyclonal antibodies used in these experiments were not known and, therefore, a labelled antibody to maximum analyte concentration ratio of 10 was chosen for experimental convenience and to ensure that most of the analyte would bind to the labelled antibody. Using the figure quoted in section 7.2 for the maximum analyte concentration (25nM), the labelled antibody concentration in the immunosensor experiments was 250nM. The sample solution was obtained by premixing the solution of mouse IgG with the labelled antibody solution to give the required concentrations. The solution was then equilibrated for at least ten minutes before being used in the immunosensor.

### **7.3.2.2 The reference solution**

The reference solution was chosen to be a 250nM solution of the labelled antibody. This solution would essentially provide the zero measurement for each device and allow signal variations between devices to be compensated for.

### **7.3.2.3 Signal normalisation**

Each dual cell CFD gave two signals: the sample signal; and the reference signal. A normalised signal was obtained from these by:

$$N = (S - R)/R \quad (7.1)$$

where: N, S and R are the normalised, sample and reference signals respectively.

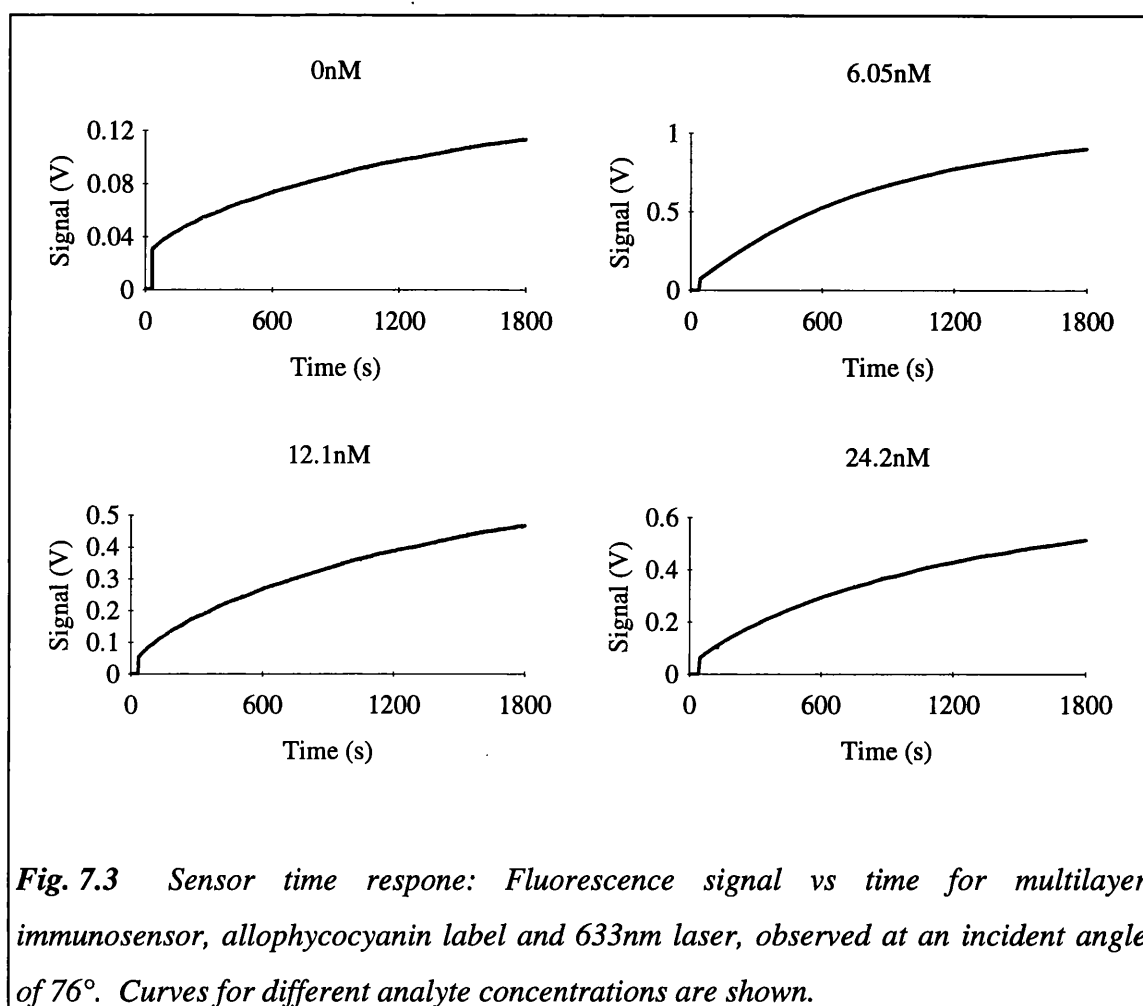
## **7.4 MULTILAYER THIN FILM IMMUNOSENSORS**

The immunosensing measurements were performed as described in chapter 5. The sample and reference solutions and the immunosensing device were allowed to reach room temperature by equilibrating for 10 minutes prior to use. The dual cell device was then filled, the timer started, and the device was inserted into the experimental apparatus described in chapter 5. The similarity between the TIR and multilayer immunosensor devices allowed one to be directly substituted for the other in the experimental apparatus without modification of either the apparatus or devices.

### **7.4.1 Immunosensor signal time response**

Figs. 7.3 - 7.4 show the time response of the multilayer immunosensor for the allophycocyanin and CY5.18 labels respectively, and fig. 7.5 shows the kinetic response of the TIR sensor. Measurements using the TIR sensor and the CY5.18 label were not performed. Note that when time = 0, the device was filled with the sample solution and that there was a short time gap before the first fluorescence signal measurement.

In a sandwich assay format evanescent field fluorescence immunosensor, the fluorescence signal increases with time until it saturates when an equilibrium is established [12]. The time required for signal saturation can vary from a few minutes to a few tens of minutes [11 - 13]. However, in the immunosensor experiments that were performed, only when the CY5.18 labelled antibody was used did the fluorescence signal reach saturation (fig. 7.4), usually after 15mins.. The slow reaction rate for both the TIR and multilayer immunosensor may be due to two factors: a) the use of polyclonal capture and labelled antibodies which may have a low average affinity for the analyte; and b) the large size and molecular weight (~254000 daltons) of the allophycocyanin labelled antibody conjugate which would diffusion limit the reaction rate [12]. Although, the lack of an equilibrium signal does not allow a reaction kinetics analysis, the latter of the above reasons is more likely and may explain the particularly



slow reaction rate of the allophycocyanin system (half-life >1000s) as compared to the CY5.18 system (half-life ~250-300s) for which the molecular weight of the CY5.18 labelled antibody conjugate is ~155000. The reaction time could not be extended beyond ~30mins. because evaporation of the solutions from the ends of the capillary cells increased the probability of the formation of air bubbles within the cells.

#### 7.4.1.1 Immunosensor signal levels

It can be seen from fig. 7.3 that the signal levels do not bear an obvious relationship with the analyte concentration. This was observed with both the allophycocyanin and CY5.18 systems when using the multilayer immunosensor and illustrates one of the problems of observing reaction kinetics on such a resonant

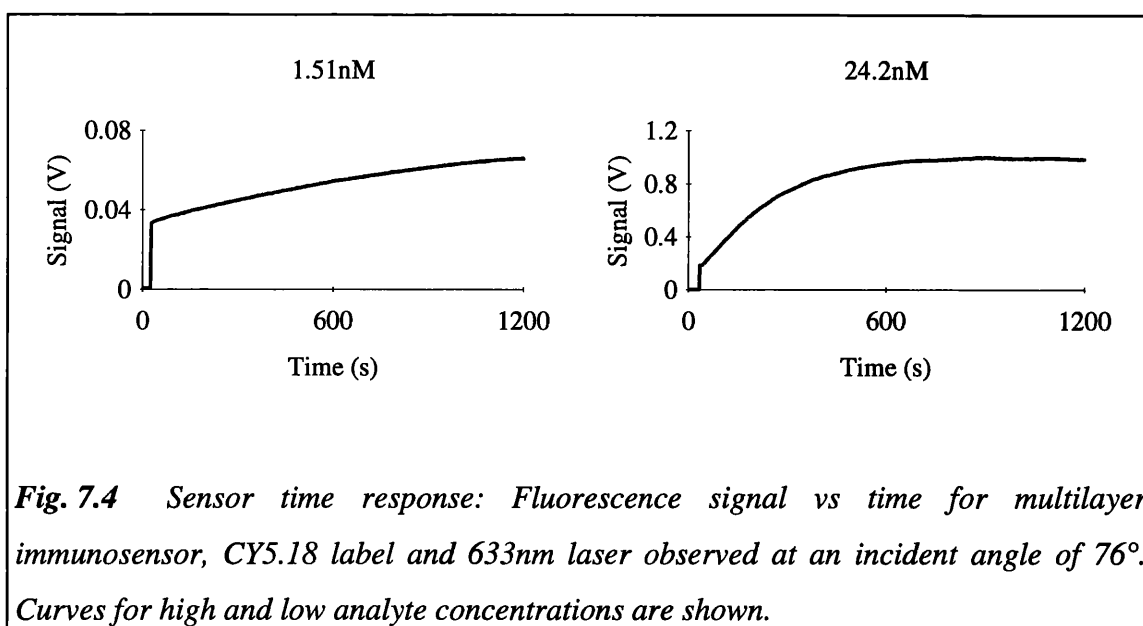


**Fig. 7.4** Sensor time response: Fluorescence signal vs time for multilayer immunosensor, CY5.18 label and 633nm laser observed at an incident angle of  $76^\circ$ . Curves for high and low analyte concentrations are shown.

multilayer system. To obtain comparable signal levels between devices, the exciting light angle of incidence at which the reaction is observed would need to be the resonant angle. Minor differences from this resonant angle would produce signal levels that were well below the possible peak. It has already been mentioned (in chapter 5 and in section 7.1.1) that, due to thin film thickness variations, the resonant angle of incidence may lie between  $75^\circ$  and  $77^\circ$ , whereas all the reaction kinetics were observed at a fixed angle of incidence of  $76^\circ$ . It is conceivable that the angle of incidence could be adjusted at the beginning by looking for the angle of incidence that gives the maximum fluorescence signal. However, this is difficult in practice because the fluorescence signal is increasing most rapidly at the start of the reaction.

An important observation can be made from the graphs of figs. 7.3 - 7.5 by considering the fluorescence signal at zero time. A crude extrapolation of the fluorescence signal curve to zero time reveals that the signal starts at the same level whether a multilayer or TIR sensor is used, and whether the fluorescent label is allophycocyanin or CY5.18. It is also independent of whether the observation is made at the resonant angle or off the resonant angle. This initial signal is between approximately 0.02 - 0.03 V based on 12 reaction kinetics observations. This suggests that there is a constant background signal, probably due to the dark current of the

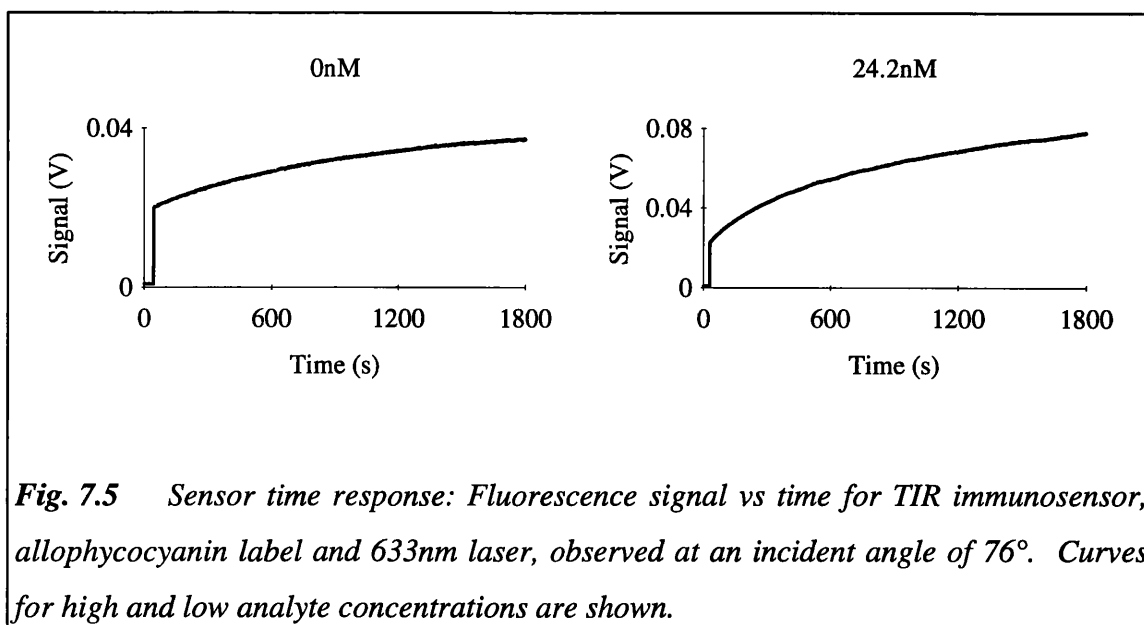


**Fig. 7.5** Sensor time response: Fluorescence signal vs time for TIR immunosensor, allophycocyanin label and 633nm laser, observed at an incident angle of  $76^\circ$ . Curves for high and low analyte concentrations are shown.

photomultiplier tube, an offset in the signal amplifiers, exciting light scattering or a combination of the three. This observation is also discussed in section 7.4.2.1.

## 7.4.2 Immunosensor angular scans

The angular scans were taken, as described in chapter 5, after allowing 30mins. for the allophycocyanin system and 20mins. for the CY5.18 system after the reaction was started. Angular scans using both the 633nm Helium-Neon and the the 650nm laser diode were performed and are shown in figs. 7.6 - 7.14.

### 7.4.2.1 Multilayer thin film immunosensor

Angular scans performed using the multilayer sensor are shown in figs. 7.6 - 7.11. The differences between the shapes of the curves (eg. peak sharpness and the presence of a shoulder), and the variability of the peak signal level (eg. in fig. 7.6, the 1.5125nM curve gave a stronger signal than the 3.025nM curve) highlight the need for a reference measurement which will compensate for such variations. There are also differences in the resonant angle of incidence which ranges from  $75^\circ$  to  $77^\circ$  (mean =  $75.8^\circ$ ,

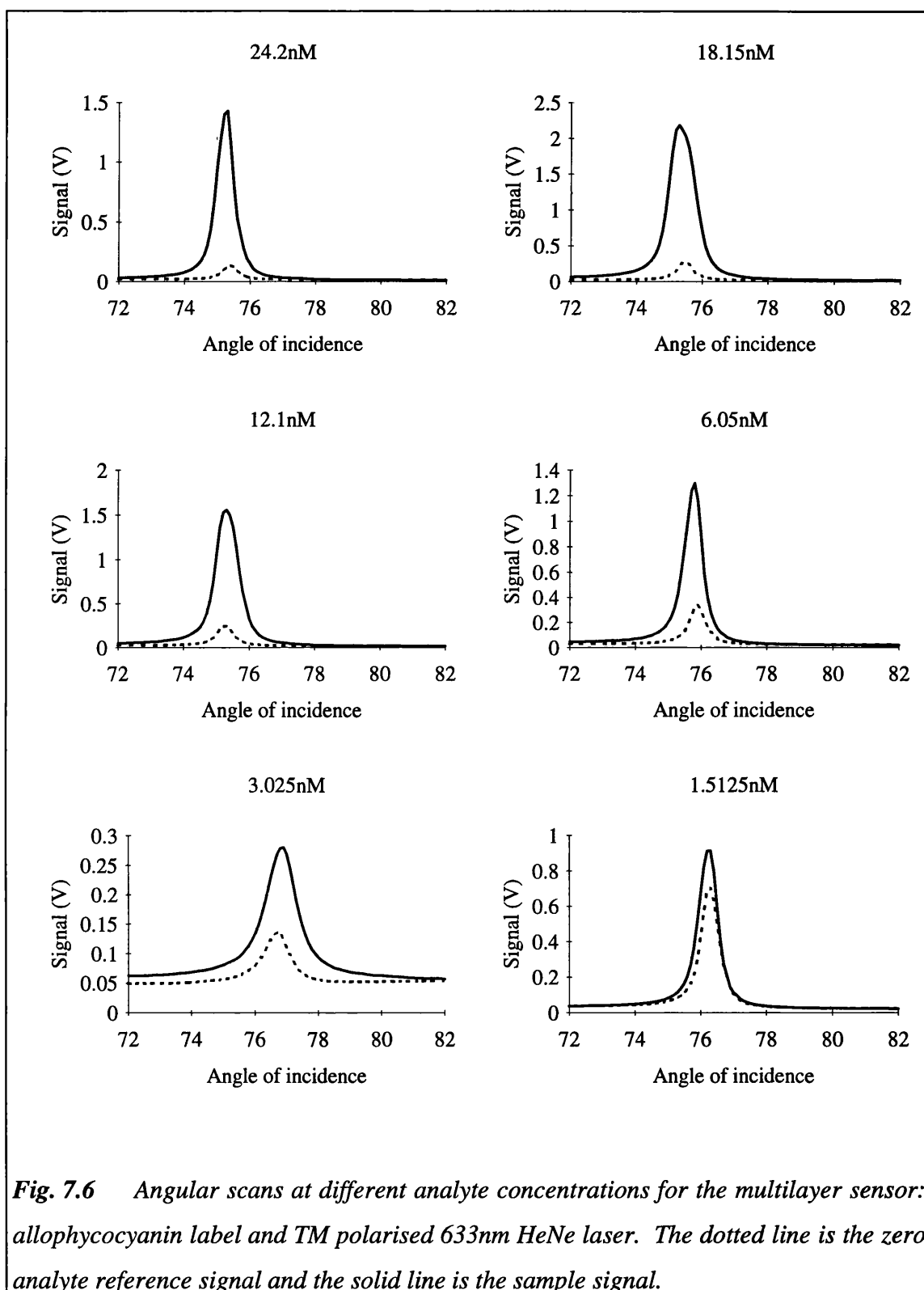


**Fig. 7.6** Angular scans at different analyte concentrations for the multilayer sensor: allophycocyanin label and TM polarised 633nm HeNe laser. The dotted line is the zero analyte reference signal and the solid line is the sample signal.

st.dev. =  $0.6^\circ$ ). Resonant angle differences (within  $\pm 0.3^\circ$ , st.dev. =  $0.1^\circ$ ) were also observed for sample and reference curves taken from the same dual cell CFD. The

differences in the resonant peaks are most likely due to variations in the thin film parameters (eg. refractive index and thickness). For example, a 5% variation in the iron phosphate (waveguide) layer thickness could, theoretically, produce a  $0.8^\circ$  difference in the resonant angle between the sample and reference curves.

A large variation in the peak reference signal strength between devices was observed. Table 7.1 gives the mean and standard deviations of the peak reference signals for the different multilayer sensor systems. The causes of these large reference signal differences between devices were not investigated but possible reasons may be variations in scattering or exciting light input coupling efficiency.

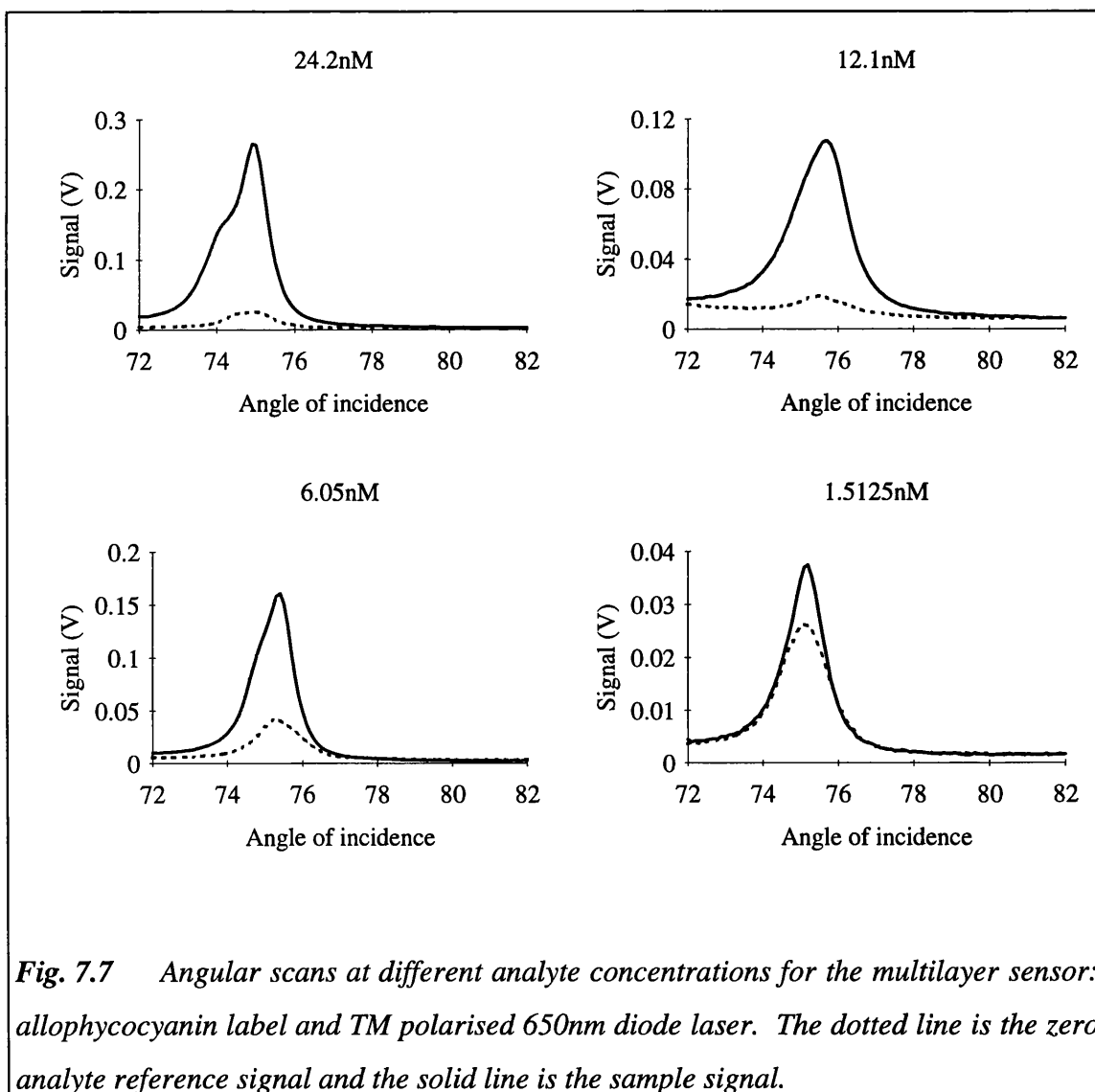


**Fig. 7.7** Angular scans at different analyte concentrations for the multilayer sensor: allophycocyanin label and TM polarised 650nm diode laser. The dotted line is the zero analyte reference signal and the solid line is the sample signal.

Laser:	633nm		650nm	
Label	Mean	Std. deviation	Mean	Std. deviation
Allophycocyanin	0.288	0.176	0.0337	0.0143
CY5.18	0.0498	0.0276	0.0164	0.0095

**Table 7.1** Peak reference signals (Volts) for multilayer immunosensor.

### Differences between 633nm and 650nm lasers

The angular scans were taken first with the 633nm HeNe laser source followed immediately by the 650nm laser diode source. Hence, in figs. 7.6 - 7.14 comparisons can be made between the laser sources knowing that the devices were identical for each laser, the only difference being that there was a longer reaction time before the angular scan with the 650nm laser.

The first observation is that the resonant angle is lower for the 650nm source, mean difference =  $0.4^\circ$  which compares favourably with a theoretical difference (for an iron phosphate film thickness of 160nm) of  $0.43^\circ$ . The resonant peaks for the 650nm source are broader than those for the 633nm source due to the greater divergence ( $\sim 0.5^\circ$  as opposed to  $0.12^\circ$ ) of the laser diode light beam and also possibly due to the greater spread of output wavelengths from the diode source. The signal levels (allophycocyanin system) for the 650nm source are, approximately a factor of 10 lower than for the 633nm source. This is because the TM polarised optical power available from the 650nm source is approximately 10 times lower than that from the 633nm source. However, the equivalent difference for the CY5.18 system is only a factor of about 4. The reasons for this are discussed in the following paragraphs.

### Differences between the allophycocyanin and CY5.18 labels

Note that the angular range for the CY5.18 label system was  $65^\circ$ - $82^\circ$  whereas for the allophycocyanin label system it was  $72^\circ$ - $82^\circ$ . The most obvious difference here is

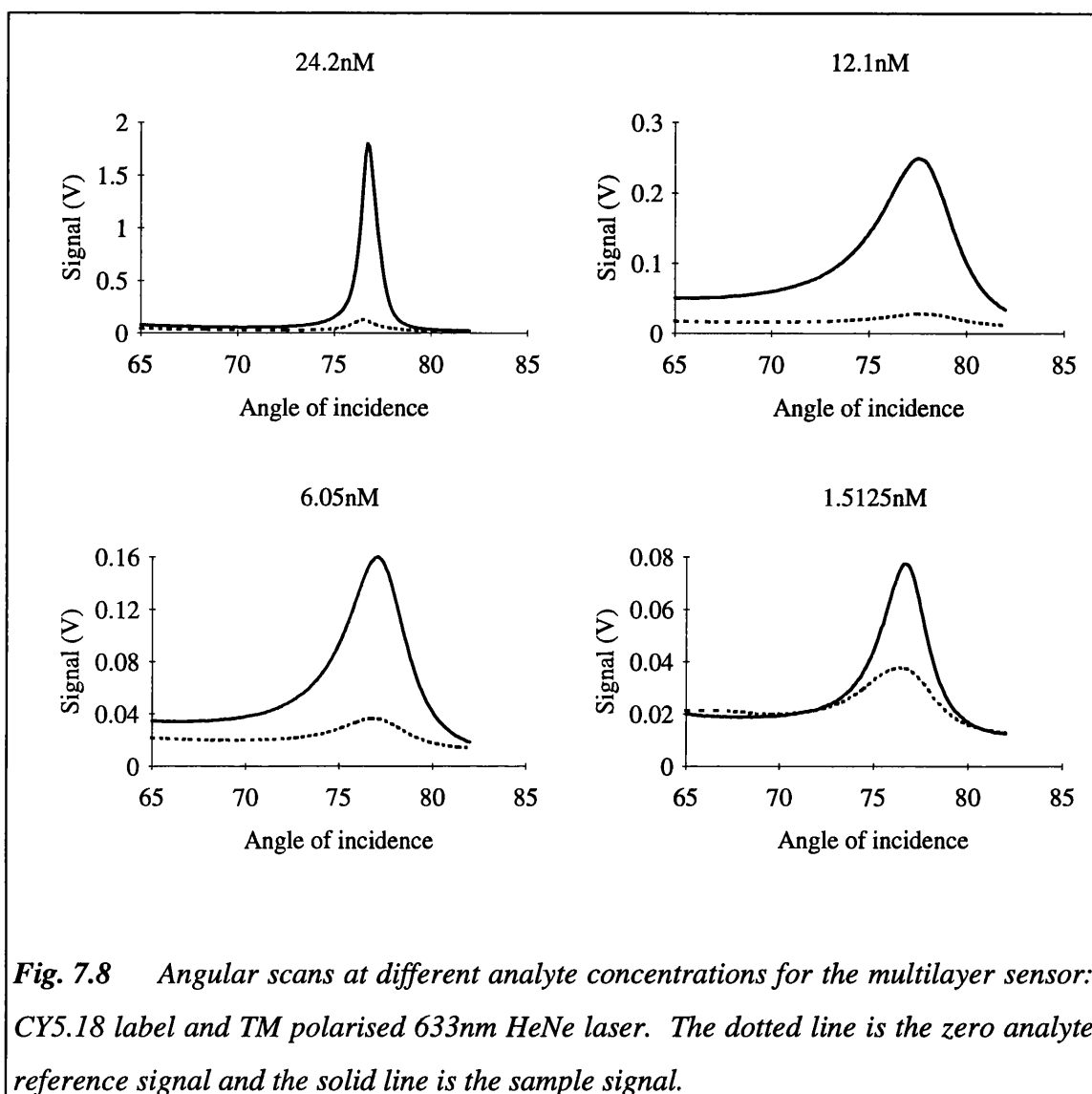


**Fig. 7.8** Angular scans at different analyte concentrations for the multilayer sensor: CY5.18 label and TM polarised 633nm HeNe laser. The dotted line is the zero analyte reference signal and the solid line is the sample signal.

the broad resonant peaks of the CY5.18 label system as compared to the allophycocyanin label system which makes the direct comparison of the two labels difficult. The reasons for the broad peaks can only be attributed to differences in the fabrication of the two sets of multilayer thin film devices, particularly in the thickness of the iron phosphate waveguide layer. The angular position of the resonant peak is similar for both the APC and CY5.18 systems suggesting that the mean iron phosphate thickness is the same, but the broad peaks suggest that there is a loss of film thickness uniformity in the devices used in the CY5.18 system. The broad peaks for the CY5.18 system mean that the peak signal levels are lower and that the difference between the signal levels for the 633nm and 650nm source is less than for the APC system.

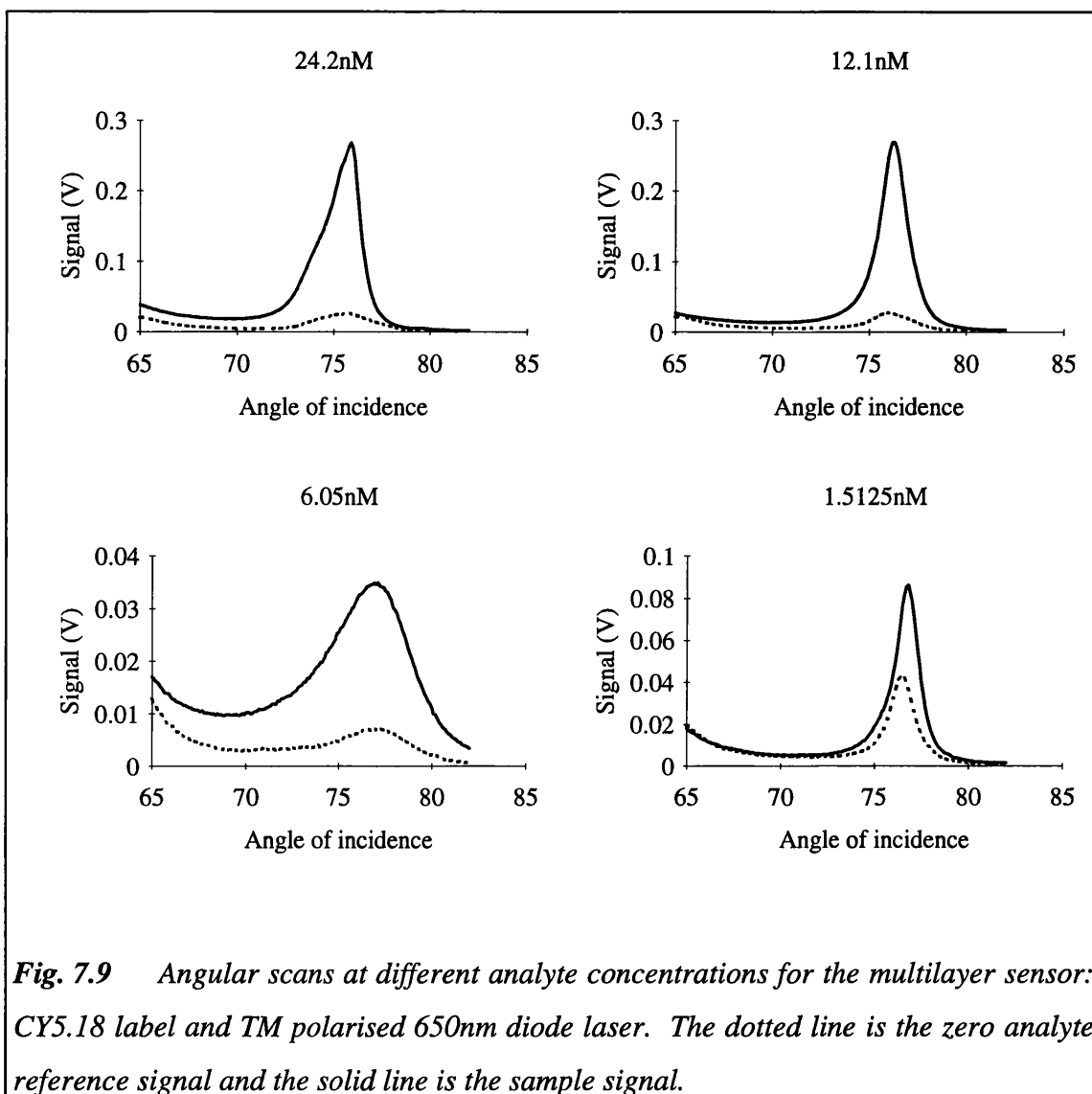


**Fig. 7.9** Angular scans at different analyte concentrations for the multilayer sensor: CY5.18 label and TM polarised 650nm diode laser. The dotted line is the zero analyte reference signal and the solid line is the sample signal.

**Signal normalisation**

The sample and reference signals required normalisation (equation 7.1) to compensate for the large variations in observed signal levels. Figs. 7.10 and 7.11 show how the normalised signal varies with the exciting light angle of incidence. Note that, to obtain a meaningful graph, the reference signal angular scans were shifted such that the reference and the sample resonant angles were equal.

The normalised signal is a maximum at, or near, the resonant angle of incidence suggesting that the signal-to-background ratio is improved by the presence of a resonant

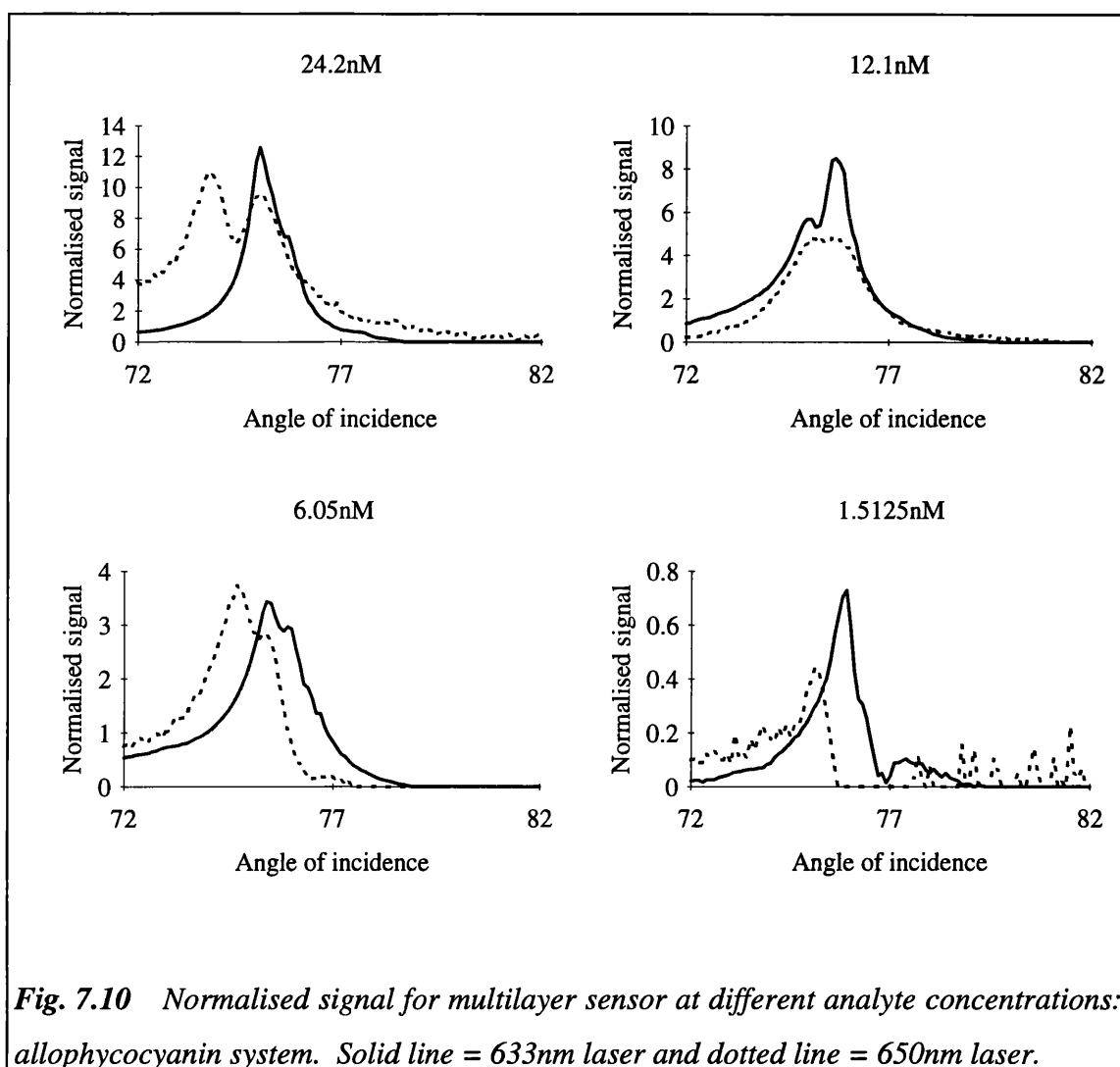


**Fig. 7.10** Normalised signal for multilayer sensor at different analyte concentrations: *allophycocyanin* system. Solid line = 633nm laser and dotted line = 650nm laser.

peak. Many of the graphs contain two local maxima on either side of the resonant angle of incidence. This is due to minor differences in the shapes of the reference and sample signal curves (figs. 7.6 - 7.9). Near the resonant angle, the signals are changing rapidly and if the sample resonant peak is broader than the reference resonant peak, a normalised signal with a double maximum is obtained. If the reference peak is broader than the sample peak, a single, broad peak is obtained in the normalised signal. Note, also, that there is little difference in the peak normalised signal levels due to the 633nm and the 650nm sources. However, due to the lower signal levels, the signal-to-noise ratio is lower when using the 650nm laser source. This leads to greater fluctuations, that are particularly noticeable at low sample concentrations, in the normalised signal curves for the 650nm laser.

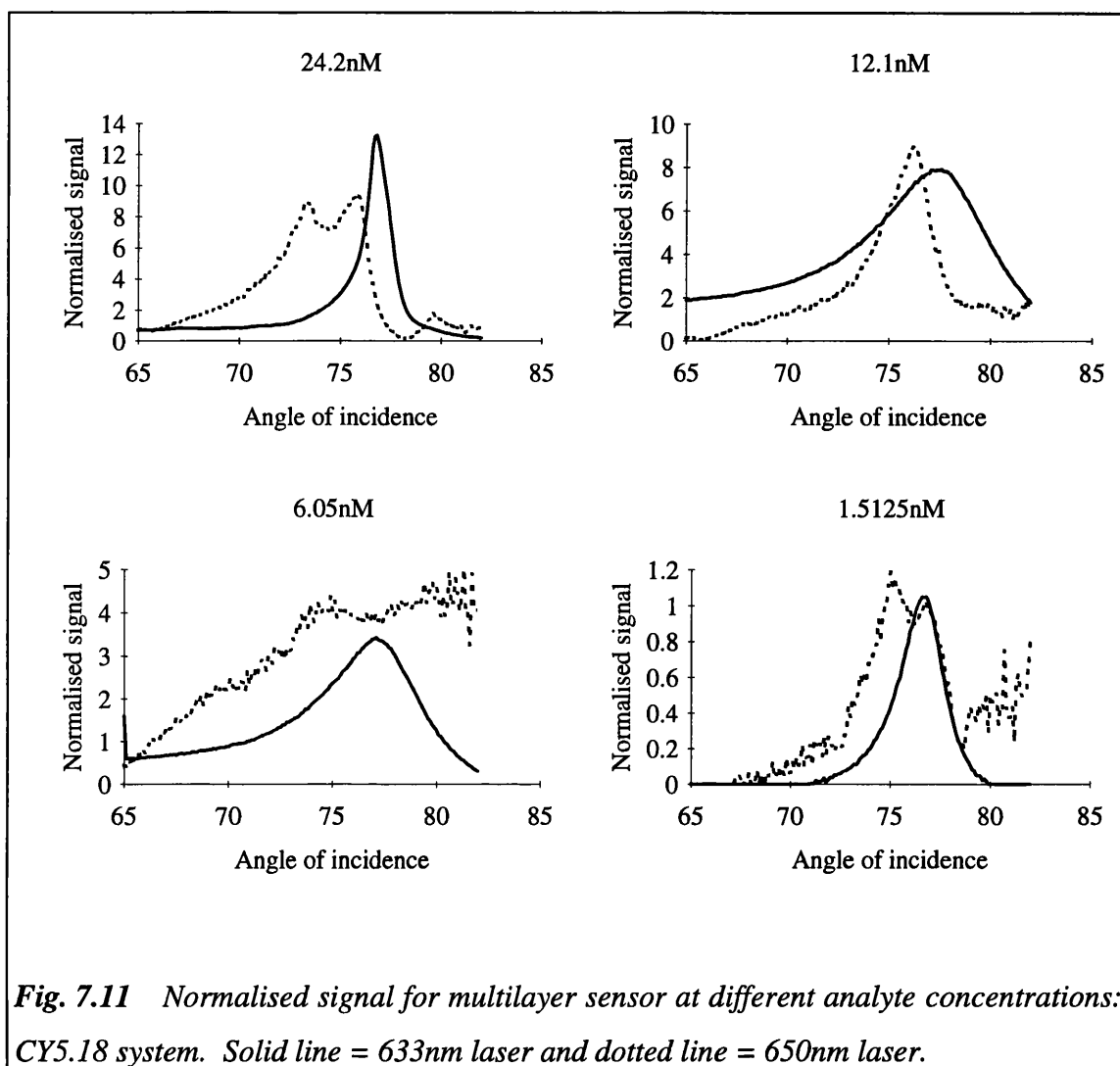


**Fig. 7.11** Normalised signal for multilayer sensor at different analyte concentrations: CY5.18 system. Solid line = 633nm laser and dotted line = 650nm laser.

### Signal without fluorophores

It was noted in section 7.4.1 that there was a minimum signal ( $\sim 0.02V$ ) that was independent of the exciting light angle of incidence or the type of sensor (multilayer or TIR). An angular scan (fig. 7.12) was, therefore, performed on a multilayer sensor device using a phosphate buffered saline solution that did not contain any fluorophores, labelled antibodies or analyte antibodies to ascertain the background signal. Note that the background signal (PBS solution) remains relatively constant with angle of incidence, exhibits only a very minor resonance peak and has a signal level comparable to that mentioned in section 7.4.1 (signal at zero time on the kinetics graphs,  $0.02V$ ). It is difficult to estimate, from fig. 7.12, what proportion of the background signal is due

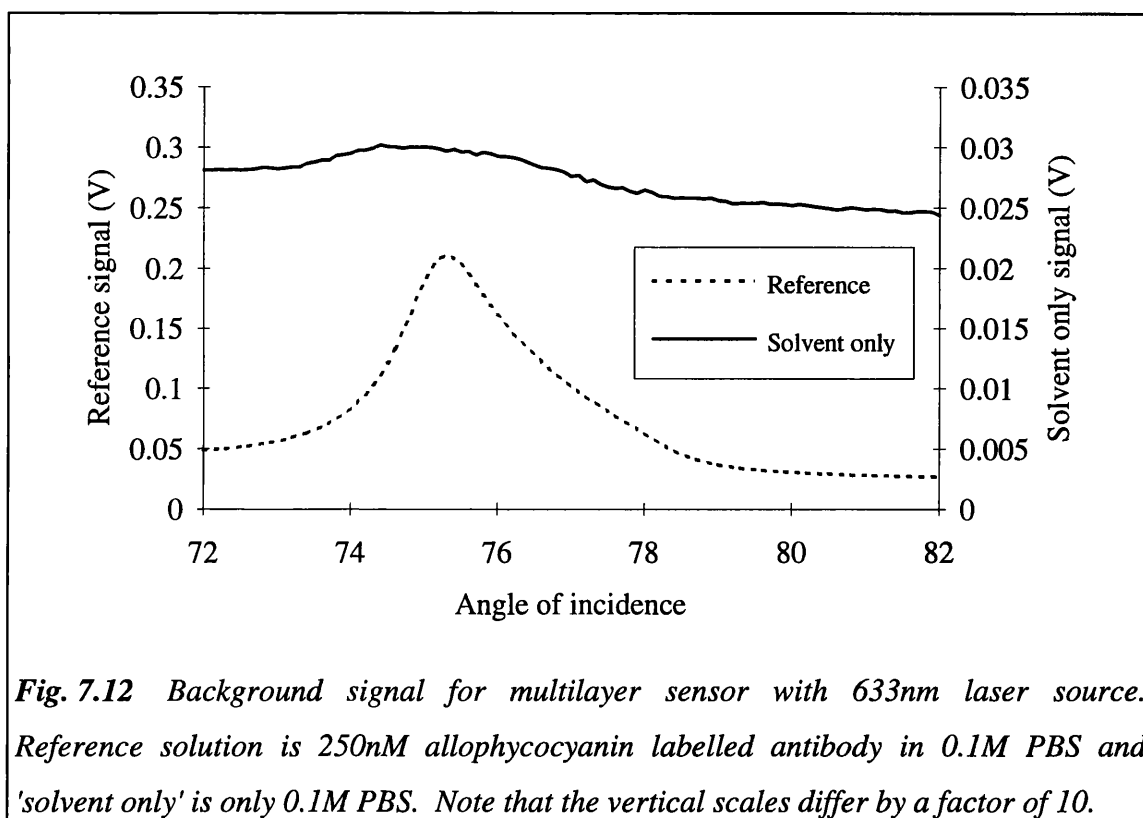


**Fig. 7.12** Background signal for multilayer sensor with 633nm laser source. Reference solution is 250nM allophycocyanin labelled antibody in 0.1M PBS and 'solvent only' is only 0.1M PBS. Note that the vertical scales differ by a factor of 10.

to a photomultiplier dark current, an offset in the amplifying electronics, or scattering of exciting light. However, it is possible to state that exciting light scattering from the iron phosphate waveguide layer, the capture antibody layer or the area of the silica buffer layer in close proximity to the waveguide layer is low in comparison to the other layers, as otherwise the resonant peak would be more pronounced. This observation is also discussed in chapter 8.

### Non-specific binding

The increase in the fluorescence signal with time as illustrated in the 0nM reaction kinetics curve of fig. 7.3 shows that non-specific binding of the labelled antibody to the capture antibody layer does occur. To check how dependent the sample fluorescence signals were on non-specific binding of the analyte to the capture and labelled antibodies, a solution where the mouse IgG analyte was replaced by rabbit IgG was used. Fig. 7.13 shows the reference and sample solution fluorescence signals as a function of the angle of incidence. Despite the high rabbit IgG concentration (87.5nM),

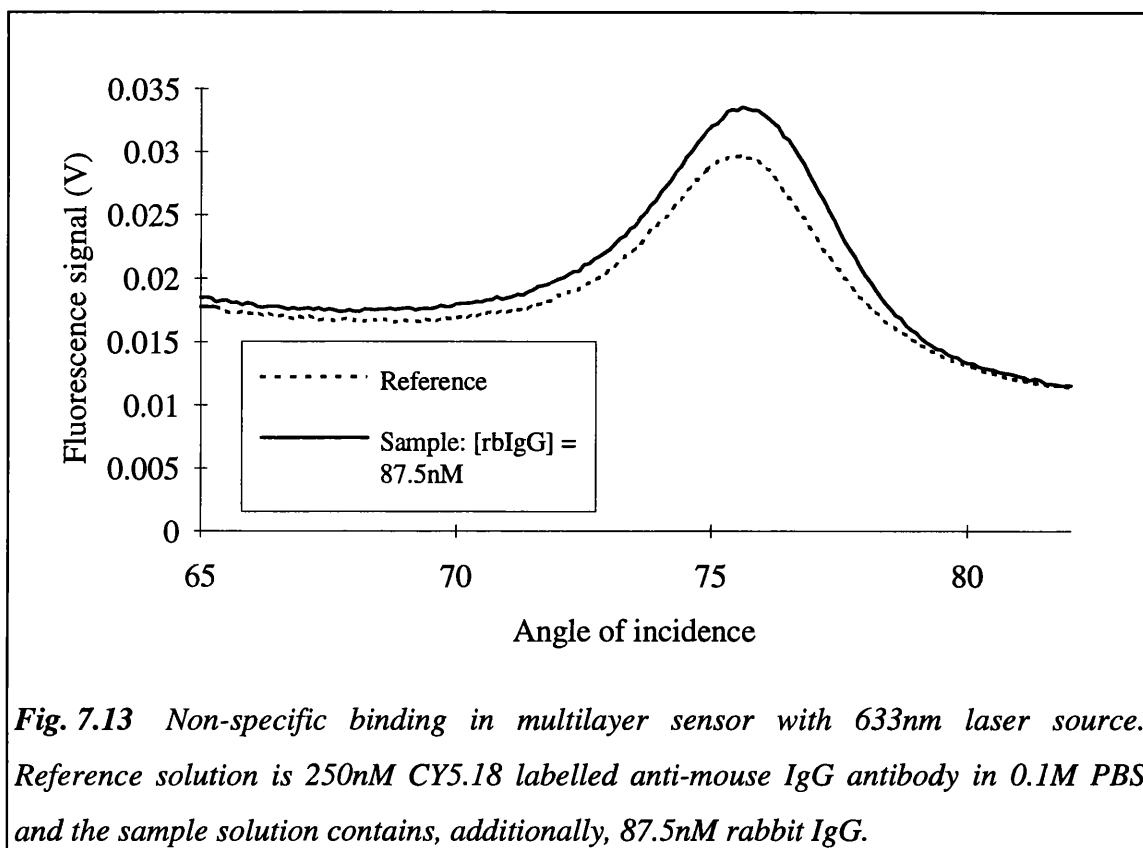


**Fig. 7.13** Non-specific binding in multilayer sensor with 633nm laser source. Reference solution is 250nM CY5.18 labelled anti-mouse IgG antibody in 0.1M PBS and the sample solution contains, additionally, 87.5nM rabbit IgG.

the sample solution fluorescence is only marginally greater than the reference solution fluorescence and in sample solutions with rabbit IgG concentrations below ~50nM, there was no significant difference observable between the reference and sample solution fluorescence signals.

#### 7.4.2.2 Total internal reflection immunosensor

Angular scans (figs. 7.14 - 7.16) were made on the TIR sensor in an identical manner to those for the multilayer sensor (as described in chapter 5). However, measurements were only made using the allophycocyanin label system.

The signal levels fall off, as expected, with increasing exciting light angle of incidence (above the critical angle of ~62°). The signal levels are much lower (by a factor of ~10) than the corresponding peak multilayer signal whereas the reference signal is only about a factor of approximately 2 down on the peak multilayer reference

signal. The reference sample signals became indistinguishable at concentrations of approximately 6nM as shown in figs. 7.14 and 7.15 clearly indicating that the TIR sensor had a higher detection limit than the multilayer sensor which could measure down to ~1.5nM.

The signals were normalised using equation 7.1 and these graphs are shown in fig. 7.16. It can be seen from these graphs that the normalised signal (equivalent to the signal-to-background ratio) remains constant or falls gradually with increasing angle of incidence, in contrast to the multilayer system where a peak in the normalised signal was obtained. Noise is also more evident on these graphs due to the low signal levels.

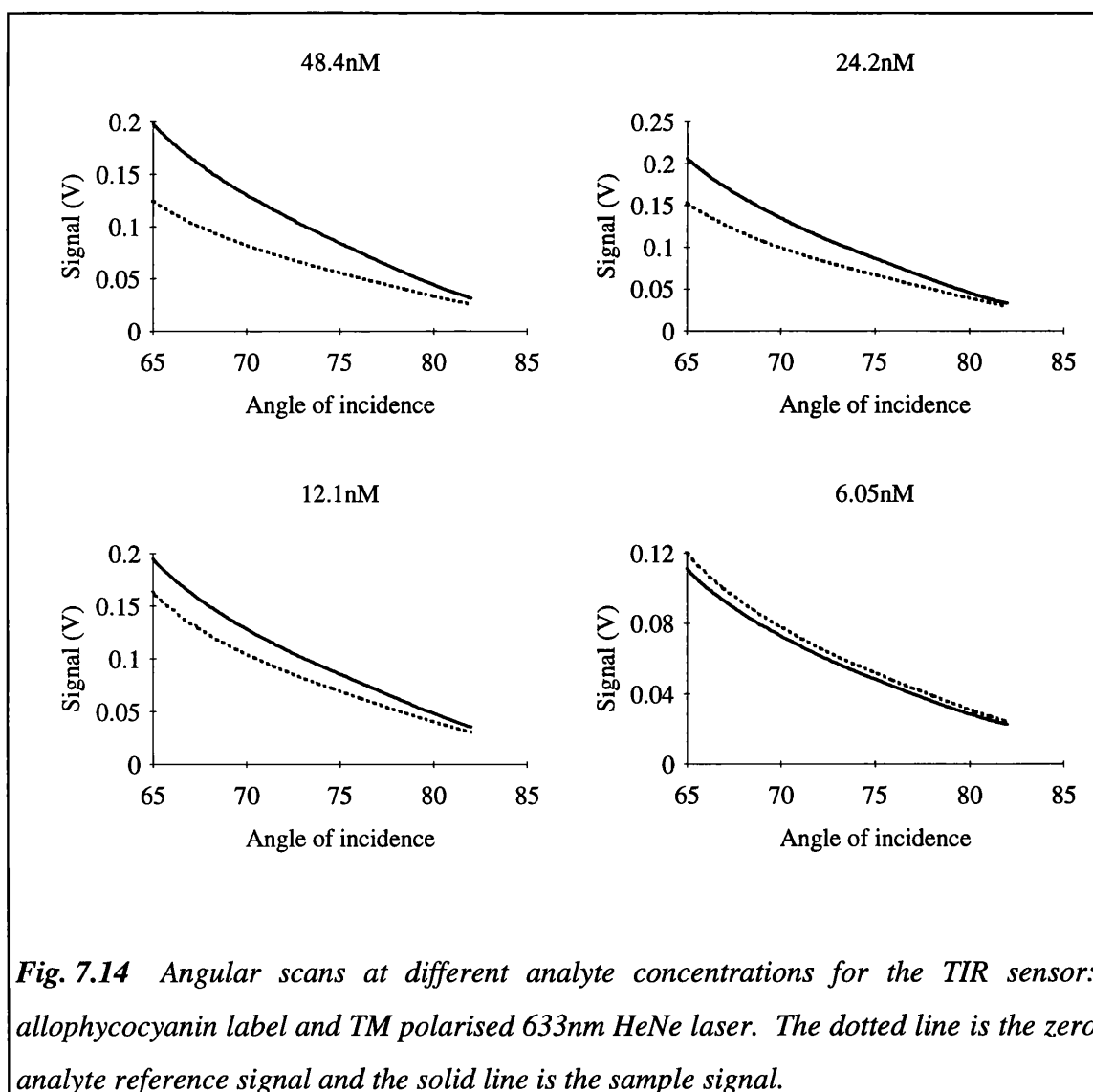


**Fig. 7.14** Angular scans at different analyte concentrations for the TIR sensor: allophycocyanin label and TM polarised 633nm HeNe laser. The dotted line is the zero analyte reference signal and the solid line is the sample signal.

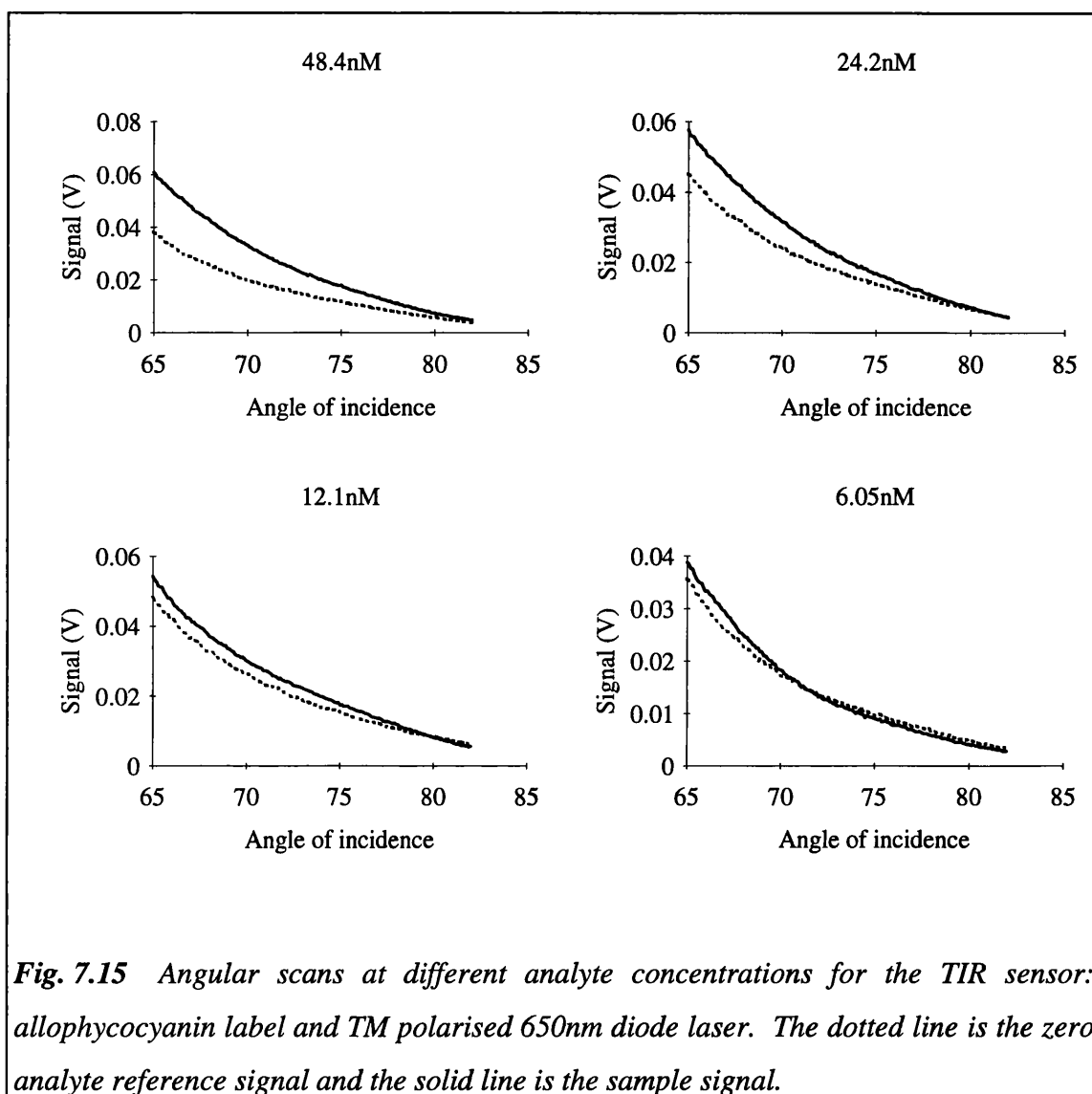


**Fig. 7.15** Angular scans at different analyte concentrations for the TIR sensor: allophycocyanin label and TM polarised 650nm diode laser. The dotted line is the zero analyte reference signal and the solid line is the sample signal.

The evanescent field strength and the penetration depth of the evanescent field of a totally reflected beam drop with increasing angle of incidence (see chapter 6, fig. 6.4). Thus, it is possible to deduce that, for a TIR sensor system, any signal-to-background improvement that can be obtained by reducing the penetration depth is offset by a corresponding reduction in the signal levels. The penetration depth (referring to chapter 6, fig. 6.4) for the TIR system is  $\sim 150\text{nm}$  at an incident angle of  $65^\circ$  and  $\sim 80\text{nm}$  at  $80^\circ$ , whereas the capillary gap of the CFD's is  $\sim 130\mu\text{m}$  which is of the order of a 1000 times greater than the penetration depth. Assuming that any unbound, labelled antibody is evenly distributed throughout the capillary gap, a decrease in the penetration depth does not significantly decrease the background signal.

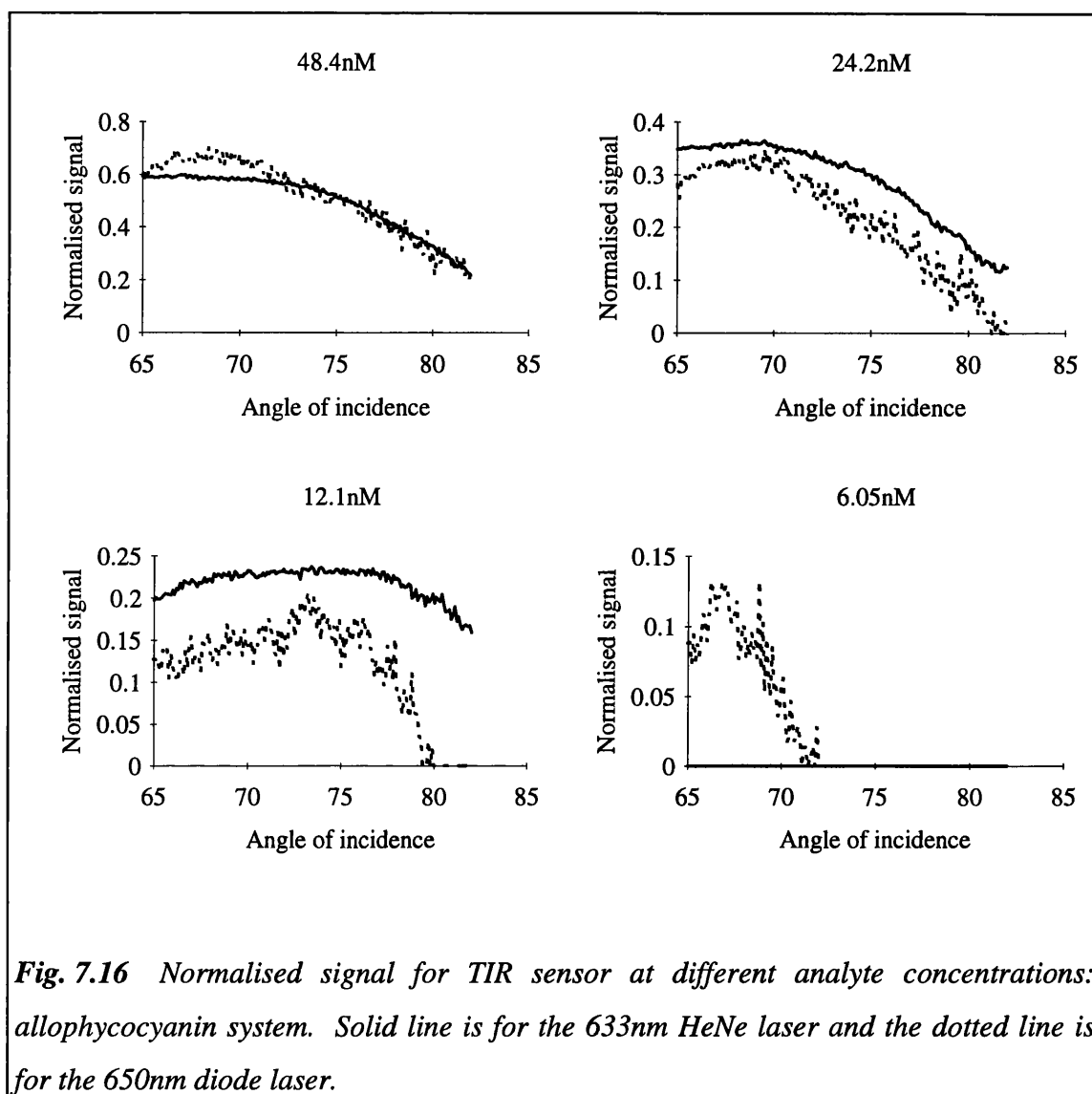


**Fig. 7.16** Normalised signal for TIR sensor at different analyte concentrations: allophycocyanin system. Solid line is for the 633nm HeNe laser and the dotted line is for the 650nm diode laser.

### 7.4.3 Immunosensor dose response

Figs. 7.17 - 7.19 show the variation of the normalised signal with the analyte (mouse IgG) concentration. The figures all show straight line fits to the data points. Signal normalisation was performed by dividing the peak sample signal by the peak reference signal (with the TIR sensor, the sample and reference signals at an exciting light angle of incidence of 65° were used).

The sensitivity of the immunosensors can best be described by *Ekins'* definition [14] (see chapter 2, section 2.4 and fig. 2.3). However, due to the limited number of

devices available, repeated measurements at each analyte concentration point could not be performed and, thus, a modified method has been used in this thesis. Firstly, the standard deviation of the difference between the observed and fitted data points was calculated. The detection limit signal was then assumed to be the zero analyte signal plus two standard deviations. The sensitivity was then equal to the analyte concentration that gave the detection limit signal on the fitted straight line. The sensitivities for the immunosensors described in this chapter are listed in table 7.2.

Figs. 7.17 - 7.19 show a surprising similarity in the results obtained using the 633nm HeNe and the 650nm diode lasers, despite an almost ten-fold optical power difference. However, in fig. 7.18, there is an outlying point at 24nM that alters the straight line fit for the 650nm laser immunosensor response. The reasons for the presence of this outlier point are unknown, but its inclusion in the sensitivity calculations changes the sensitivity from a possible 0.635nM to 7.790nM (table 7.2).

There is some variation in the sensitivity that can be obtained depending on the type of sensor system that is used (see table 7.2). The sensitivity for the multilayer

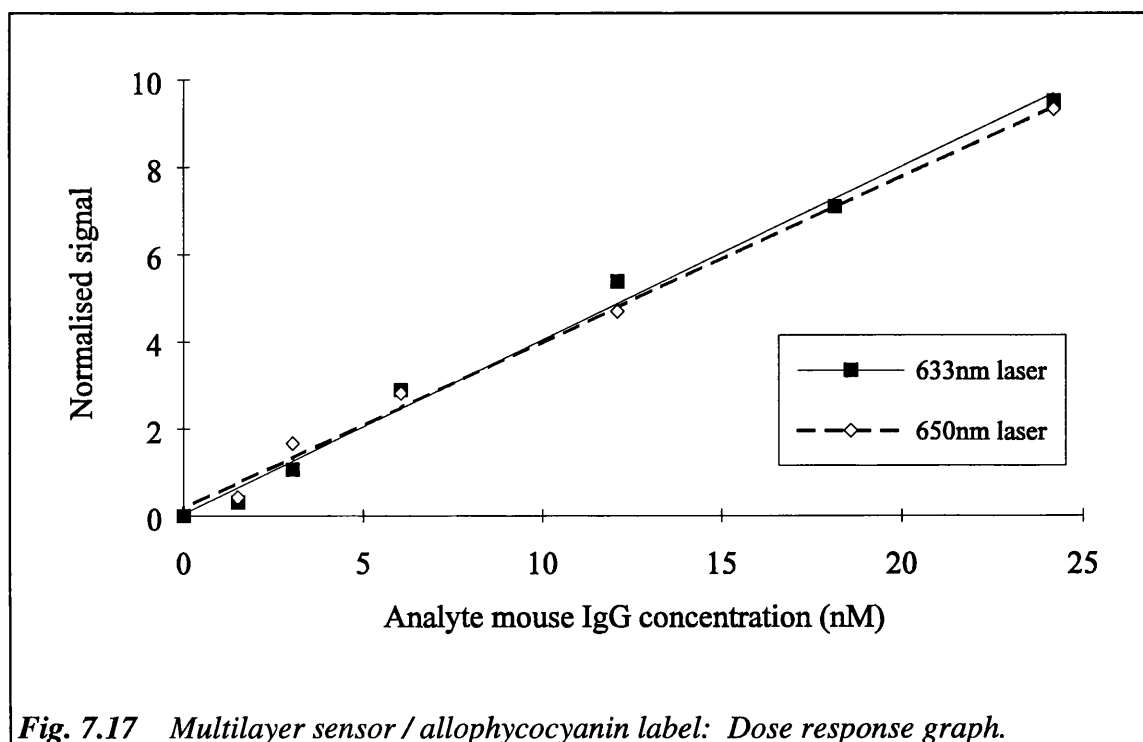


Fig. 7.17 Multilayer sensor / allophycocyanin label: Dose response graph.

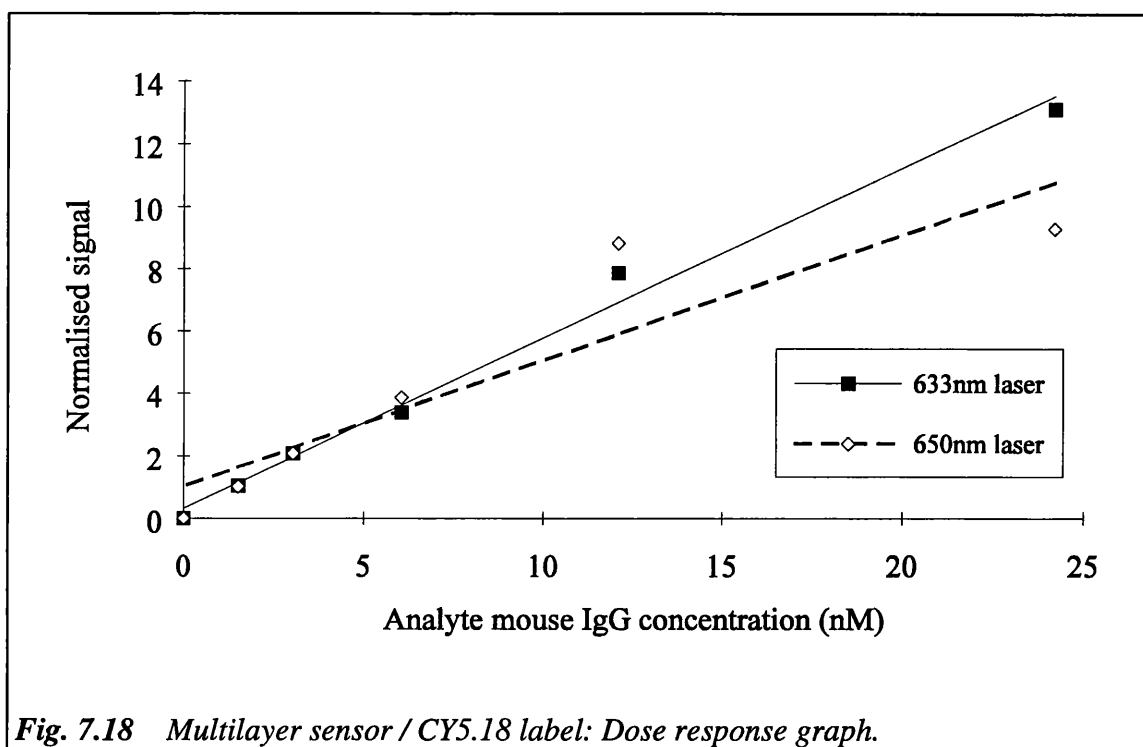


Fig. 7.18 Multilayer sensor / CY5.18 label: Dose response graph.

sensor using the 650nm laser and CY5.18 fluorescent label is affected by the presence of an outlier point. The sensitivity for the TIR sensor using the 650nm laser is probably much better than can realistically be obtained. It was mentioned earlier (section 7.4.2.2) that measurements below an analyte concentration of  $\sim 6$ nM using the TIR sensor produced a sample signal level equal to that of the reference signal level. Hence, it can reasonably be assumed that the figure of 2.342 nmol/l for the TIR sensor sensitivity is rather optimistic, but this can only be confirmed by performing a greater number of measurements at each analyte concentration. Generally, however, the multilayer sensor gave a sensitivity improvement over the TIR sensor by a factor of between 6 to 8.

The performance of an immunosensor can be described in terms of its sensitivity, precision and dynamic range (see chapter 2, section 2.4). These parameters are in turn dependent on the signal variation (or the standard deviation) of repeated measurements taken at the required analyte concentration. Variations between repeated signal measurements are obtained because of fabrication differences between devices (eg. thin film thickness, activity of the immobilised capture layer), sample solution differences (eg. pH, metabolite content), instrument differences or user practices. It has been shown

Sensor:	Multilayer		TIR	
Label	633nm laser	650nm laser	633nm laser	650nm laser
Allophycocyanin	1.732	1.421	11.132	2.342
CY5.18	1.809	7.790 (0.635)	N/A	N/A

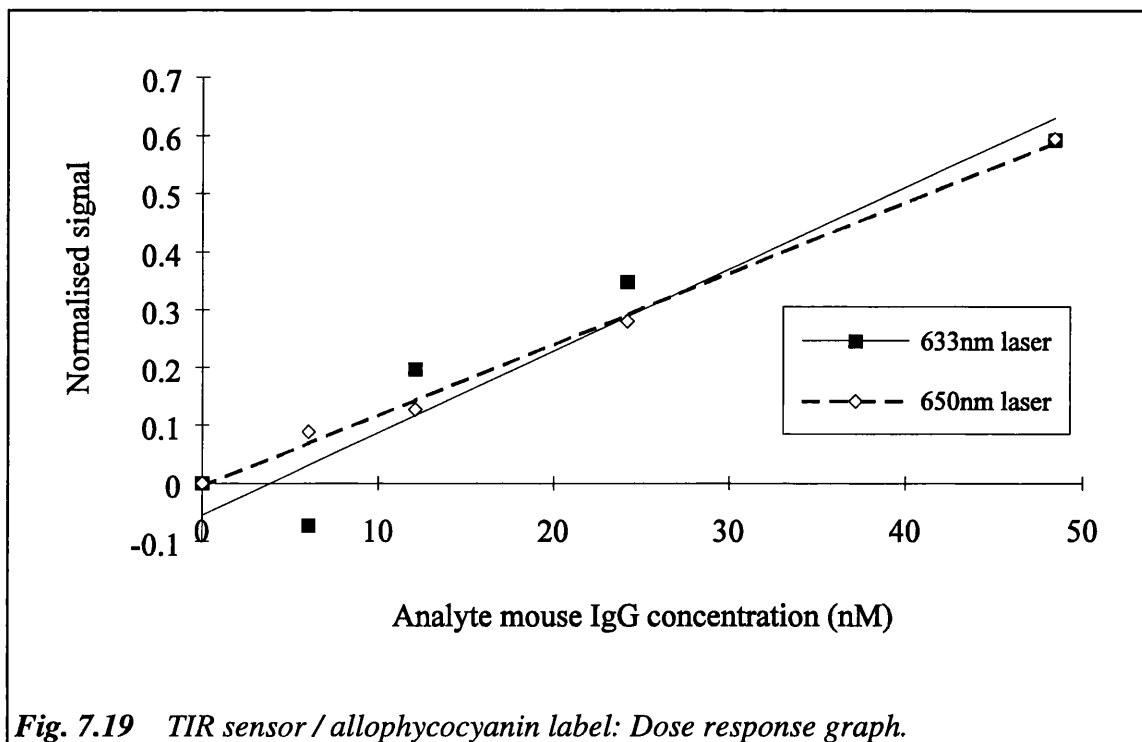
*Table 7.2 Immunosensor sensitivities (nmol/l). Note: the value in brackets is the sensitivity when an outlying point is not included in the calculation.*

in this chapter that there is some variability in the fabrication of the multilayer devices, particularly in the thin film thickness which may vary by up to 10% between devices and by up to 5% across a single device. This leads to variations in the observed sample signal level, thus requiring a reference measurement to be taken. However, a single reference measurement may be insufficient in the case of the multilayer sensors because of the 5% variation in the film thickness on a single device. The signal variations that are the result of thickness non-uniformities increase the detection limit and therefore compromise the sensitivity and the precision of the sensors. A distinct advantage of the TIR sensors is that, because there are no thin films, one of the sources of signal variability is not present. Hence, it is possible to postulate that further improvements in the sensitivity of the multilayer sensor over the TIR sensor are possible, but only with the use of improved thin film fabrication techniques.

## 7.5 DISCUSSION

It is possible to draw some conclusions from the immunosensing results presented in sections 7.4.1 - 7.4.3.

The reaction kinetics graphs of section 7.4.1 showed that the binding of the analyte, the labelled antibody and the capture antibody progressed slowly with the reaction not being complete (in the APC label case) even after 30mins.. A reaction time



of 30mins. or longer is clearly inadequate for any commercial biosensor instrument aimed at the doctor's surgery/patient's bedside market which, realistically, will need to produce a result in less than 10mins [15, 16]. The two most obvious explanations for the slow reactions are the relatively low affinity of the polyclonal antibodies that were used and, in the case of the allophycocyanin label, the large size and molecular weight of the labelled antibody that would diffusion-limit the reaction. The latter explanation is confirmed by the faster reaction times (~20mins) obtained when the lower molecular weight CY5.18 fluorescent label was used.

The graphs illustrating the dependence of the normalised fluorescence signal on the exciting light angle of incidence (figs. 7.10 and 7.11) showed clearly that the signal-to-background ratio of the multilayer immunosensors was increased at the resonant angle of incidence, whereas, for the TIR sensors, the signal-to-background ratio remained constant or fell with increasing angle of incidence (fig. 7.16). The shapes of the normalised signal vs. angle of incidence curves and the differences in the resonant angle of incidence indicated the variability in the fabrication of the multilayer immunosensors. These variations are most probably due to thin film thickness

differences on individual devices and between devices but this requires confirmation. An interesting observation of the angular scans was that illustrated in fig. 7.12. This showed that, in the absence of fluorophores in the solution, the measured signal remained relatively constant over angle of incidence and exhibited only a very minor resonance peak, thus suggesting that exciting light scattering from the waveguide (iron phosphate) layer may not be highly significant.

The dose response graphs presented in section 7.4.3 showed the similarity of the results obtained using the 633nm and 650nm laser sources. This indicated that the diode lasers may give equal performance to helium-neon lasers in optical biosensing equipment, although, to fully confirm this, further work would be needed to ascertain how the sensitivity and precision may be dependent on the type of laser used. Finally, the sensitivity figures of table 7.2 showed that the multilayer sensor improved on the performance of the TIR sensor, although this improvement is probably insufficient to justify the increased expense of fabricating the multilayer sensor. However, it is likely that much better performance from the multilayer sensors can be obtained than has been done in the experiments described above. An obvious area for improvement is in the fabrication of the thin films to obtain more uniform film thicknesses - a possible cost-effective solution may be the use of CVD techniques to grow the thin films.

## REFERENCES

- 1 **BADLEY R A, et al**, Optical biosensors for immunoassays: the fluorescence capillary fill device, *Philosophical Transactions of the Royal Society of London B*, 1987, **316**, 143-160.
- 2 **ROBINSON G A, ATTRIDGE J W, DEACON J K, WHITELEY S C**, The fluorescent capillary fill device, *Sensors and Actuators B*, 1993, **11**, 235-238.
- 3 **AHLUWALIA A et al**, A comparative study of protein immobilization techniques for optical immunosensors, *Biosensors & Bioelectronics*, 1991, **7**, 207-214.
- 4 **ANDRADE J D**, Principles of protein adsorption, in **ANDRADE J D ed.**, Surface and interfacial aspects of biomedical polymers, Vol.2, Protein adsorption, *Plenum Press, New York*, 1985, *Chap.1*.
- 5 **ALARIE J P, SEPANIAK M J, VO-DINH T**, Evaluation of antibody immobilization techniques for fiber optic-based fluoroimmunosensing, *Analytica Chimica Acta*, 1990, **229**, 169-176..
- 6 **O'SHANNESY D J, BRIGHAM-BURKE M, PECK K**, Immobilisation chemistries suitable for use in the BIAcore surface plasmon resonance detector, *Analytical Biochemistry*, 1992, **205**, 132-136.
- 7 **BUCKLE P E et al**, The resonant mirror: a novel optical sensor for direct sensing of biomolecular interactions. Part II: Applications, *Biosensors & Bioelectronics*, 1993, **8**, 355-363.
- 8 **STAMM Ch, LUKOSZ W**, Integrated optical difference interferometer as refractometer and chemical sensor, *Sensors & Actuators B*, 1993, **11**, 177-181.
- 9 **ZHOU Y et al**, Multichannel evanescent fluorescence immunosensing using potassium and sodium ion-exchanged waveguides, *Journal of Molecular Electronics*, 1991, **7**, 135-149.
- 10 **SCOUTEN W H**, A survey of enzyme coupling techniques, in **MOSBACH K ed.**, Immobilised enzymes and cells, Part B, *Methods in Enzymology*, 1987, **135**, 57-60.
- 11 **SLOPER A N, DEACON J K, FLANAGAN M T**, A planar indium phosphate monomode waveguide evanescent field immunosensor, *Sensors & Actuators*, 1990, **B1**, 589-591.
- 12 **SADANA A, SHI D**, Binding kinetics of antigen by immobilized antibody: Influence of reaction order and external diffusional limitations, *Biosensors & Bioelectronics*, 1992, **7**, 559-568.
- 13 **KARLSSON R, MICHAELSSON A, MATTSSON L**, Kinetic analysis of monoclonal antibody-antigen interactions with a new biosensor based analytical system, *Journal of Immunological Methods*, 1991, **145**, 229-240.
- 14 **EKINS R**, Immunoassay design and optimisation, in **PRICE C P, NEWMAN D J eds.**, Principles and practice of immunoassay, *Stockton Press, New York*, 1991, *1st ed.*, 96-153.
- 15 **ROBINSON G A**, Optical immunosensing systems - meeting the market needs, *Biosensors & Bioelectronics*, 1991, **6**, 183-191.
- 16 **MANNING B, MALEY T**, Immunosensors in medical diagnostics - major hurdles to commercial success, *Biosensors & Bioelectronics*, 1992, **7**, 391-395.
- 17 **VADGAMA P**, Designing biosensors, *Chemistry in Britain*, March 1992, 249-252.

## CHAPTER 8

### THEORETICAL MODELLING OF THE IMMUNOSENSOR

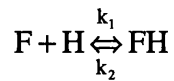
*The theory described in chapter 4 largely dealt with a near ideal situation, where there is a plane uniform wave incident on a stratified system with smooth, planar boundaries. The real case is, however, very different: the incident light beam is not a plane wave, the thin film thicknesses are not uniform, the boundaries are neither smooth nor planar and the materials may scatter the incident light. Additionally, there is the binding of the analyte, capture antibody and labelled antibody to consider because this clearly affects how much of the fluorescent label is brought within the strong evanescent field close to the waveguide layer. This chapter extends the theory of chapter 4 to include thin film thickness non-uniformities and the presence of a bound protein layer and applies this to the immunosensor measurements presented in chapter 7. The modelling presented is neither mathematically complex nor comprehensive, but the results provide some insight into the various sources (eg. scattering from the thin film layers, fluorescence, etc.) that combine to produce the observed signal.*

#### 8.1 ANTIBODY-ANALYTE BINDING

##### 8.1.1 Theory

The theory will not be discussed in any depth in this section, and, therefore, a reader requiring further information is referred to *Day* [1].

The binding of an antibody to its antigen is a reversible reaction described by:



where F and H are, respectively, the antibody and antigen and  $k_1$  and  $k_2$  are, respectively, the forward and reverse reaction rate constants. At equilibrium, the association constant K is given by:

$$K = \frac{k_1}{k_2} = \frac{[FH]}{[F][H]} \quad (8.1)$$

where  $[x]$  signifies 'the concentration of x'. It can thus be shown that, at equilibrium and assuming that both antibody and antigen are univalent (ie. have only one binding site), the fraction ( $\bar{p}$ ) of antibody bound to antigen is:

$$\bar{p} = \frac{[FH]}{[F] + [FH]} = \frac{K[H]}{1 + K[H]} \quad (8.2)$$

Similarly, the fraction ( $\bar{q}$ ) of antigen bound to antibody is:

$$\bar{q} = \frac{[FH]}{[H] + [FH]} = \frac{K[F]}{1 + K[F]} \quad (8.3)$$

The above equations assume that the antibody is homogeneous (ie. monoclonal, with a single association constant). When considering a heterogeneous antibody (ie. polyclonal with a range of association constants), a modification to the equations is required. A typical method is to use a Sips distribution [1] by replacing  $K[x]$  with  $(K[x])^a$  where  $a$  is the Sipsian heterogeneity constant. For a homogeneous antibody,  $a = 1$  and, for a heterogeneous antibody,  $a < 1$ .

The equations become considerably more complex when considering the binding of two or more antibodies to the same antigen (eg. a sandwich immunoassay).

However, it was assumed, for the purposes of the modelling presented here, that the binding of a labelled antibody did not significantly affect the binding of the capture antibody. It was also assumed that the capture and labelled antibodies bound to different binding sites on the analyte and that this binding sterically hindered the second binding site of the antibodies, thus making all reaction components univalent.

### 8.1.2 Application to observed data

The antibody binding equations could now be applied to the observed data. Consider:

$F_s$	peak sample fluorescence.
$F_r$	peak reference fluorescence.
$C$	initial effective concentration, in solution, of capture antibody.
$L$	initial labelled antibody concentration.
$A$	initial analyte concentration.
$K_1$	association constant of capture antibody.
$K_2$	association constant of labelled antibody.
$F_b$	fluorescence from totally saturated capture antibody layer.
$\bar{p}$	fraction of capture antibody bound to analyte.
$\bar{q}$	fraction of analyte bound to labelled antibody.
$a$	heterogeneity constant for capture antibody.
$b$	heterogeneity constant for labelled antibody.

The sample fluorescence is now:

$$F_s = F_b \bar{p} \bar{q} + \frac{F_r (L - C \bar{p} \bar{q})}{L} \quad (8.4)$$

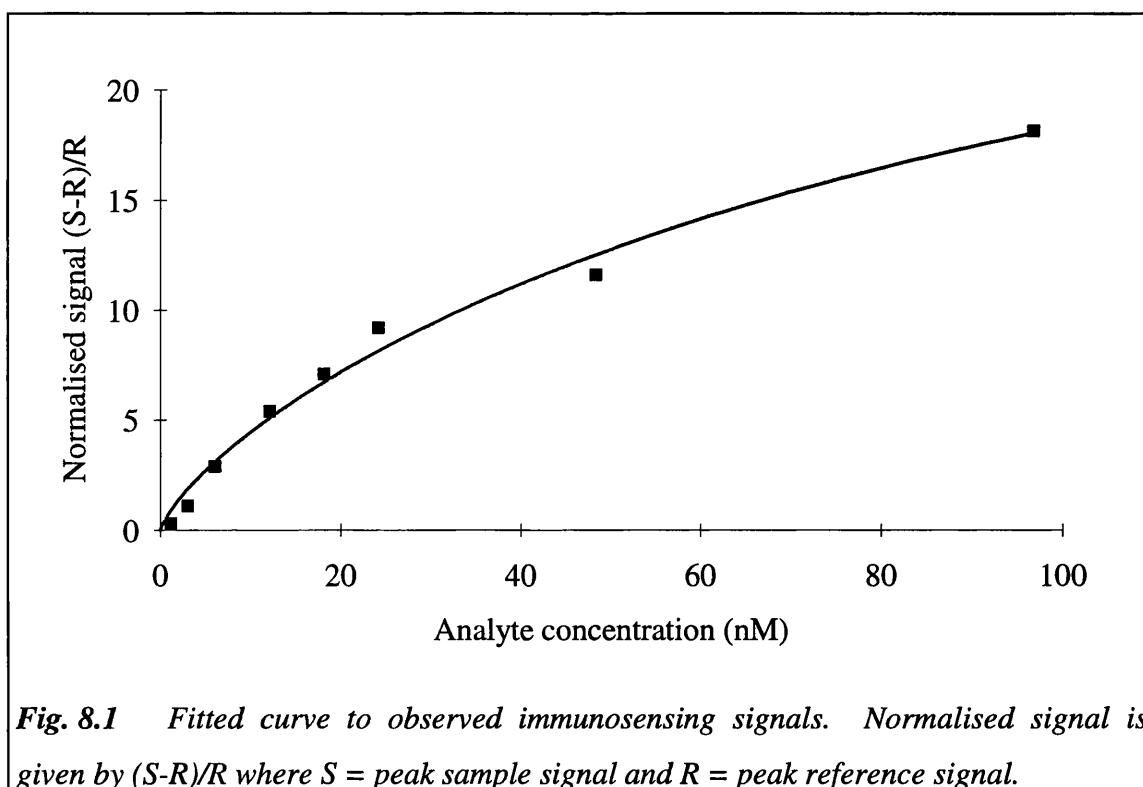
$$\Rightarrow \frac{F_s - F_r}{F_r} = \bar{p}\bar{q} \left( F_{br} - \frac{C}{L} \right) \quad (8.5)$$

where  $F_{br} = F_b/F_r$ , and  $\bar{p}$  and  $\bar{q}$  are given, from equations 8.3 and 8.4, by:

$$\bar{p} = \frac{(K_1\Lambda)^a}{1 + (K_1\Lambda)^a} \quad (8.6)$$

$$\bar{q} = \frac{(K_2M)^b}{1 + (K_2M)^b} \quad (8.7)$$

where  $\Lambda = A - C\bar{p}$  and  $M = L - A\bar{q}$ . The left-hand-side of equation 8.5 is equivalent to the normalised signal as used in the dose response graphs in chapter 7 (figs. 7.18 and 7.19).



The parameter  $\bar{p}$  can be obtained by performing a bisection root search for  $y = 0$  on the equation:

$$y = \log \bar{p} - a \log [K_1 (A - C\bar{p})] + \log \left\{ 1 + [K_1 (A - C\bar{p})]^a \right\} \quad (8.8)$$

which is a re-arrangement of equation 8.6.  $\bar{q}$  can be obtained in a similar manner.

Equation 8.5 can now be fitted to the observed dose response data with five unknown variables:  $a$ ,  $b$ ,  $K_1$ ,  $K_2$  and  $F_{br}$ . The results obtained from fitting equation 8.5 (using least-squares minimisation by the Simplex method [2]) to the immunosensing data from the 633nm laser, allophycocyanin system are given below and illustrated in figs. 8.1 and 8.2.

Capture antibody association constant,  $K_1$ :  $5.68 \times 10^9 \text{ M}^{-1}$ .

Capture antibody Sipsian heterogeneity index,  $a$ : 0.73.

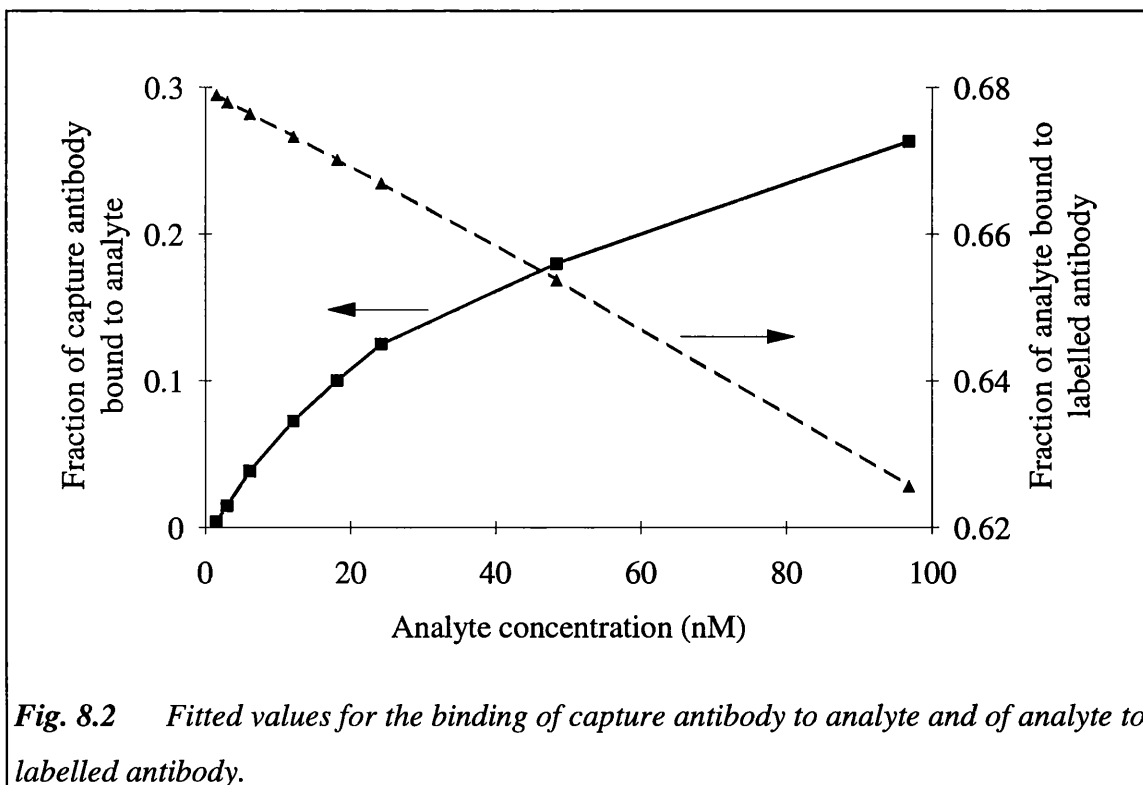


Fig. 8.2 Fitted values for the binding of capture antibody to analyte and of analyte to labelled antibody.

Labelled antibody association constant, $K_2$ :	$2.63 \times 10^8 \text{ M}^{-1}$ .
Labelled antibody Sipsian heterogeneity index, $b$ :	0.86.
Maximum fluorescence signal, $F_{br}$ :	110.3.

The values for  $\bar{p}$  (fraction of active capture antibody bound to analyte) and  $\bar{q}$  (fraction of analyte bound to labelled antibody) were used in the theoretical modelling of the immunosensor system that will be described in the following sections. Note that the theory requires that the antibody-antigen binding reaction is at equilibrium. This, however, was not strictly true as indicated by the binding kinetics graphs (see chapter 7) which show that binding of the analyte to the capture antibody was still occurring when the final fluorescence signals were measured.

## 8.2 THEORETICAL CONSIDERATIONS

### 8.2.1 The incident light beam

Although a lens arrangement was used to broaden and collimate the incident exciting laser light (see chapter 5), the incident beam did have a small convergence

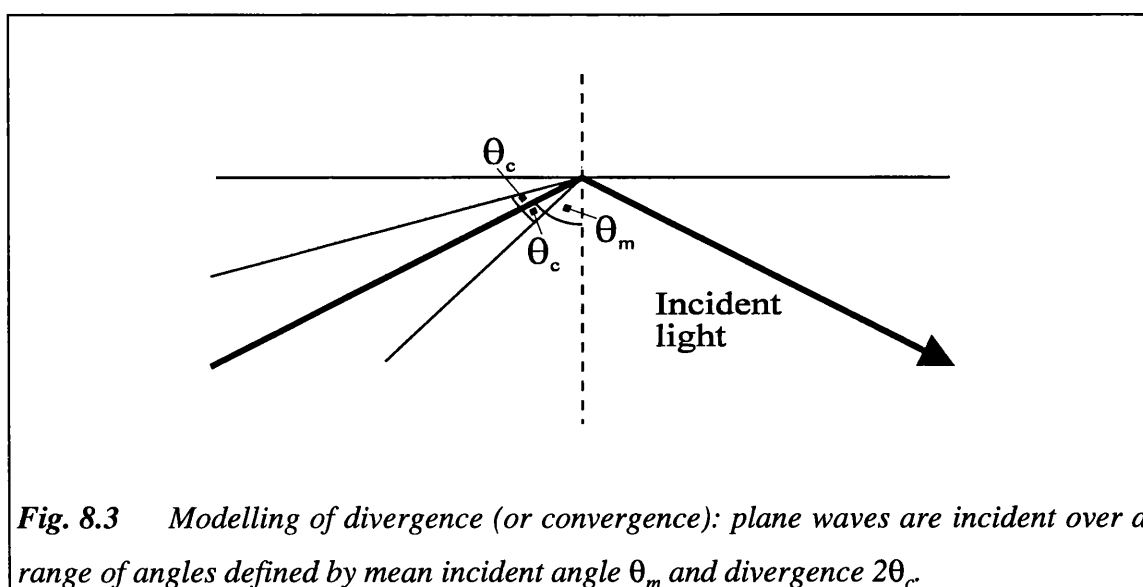


**Fig. 8.3** Modelling of divergence (or convergence): plane waves are incident over a range of angles defined by mean incident angle  $\theta_m$  and divergence  $2\theta_c$ .

(Helium-Neon:  $\sim 0.12^\circ$ , laser diode:  $\sim 0.5^\circ$ ). This convergence was modelled as a plane wave incident over a range of angles equal to the convergence (fig. 8.3). Thus the optical intensity at any point, relative to the incident intensity, was obtained (assuming that intensity is proportional to the square of the electric field strength) by:

$$\frac{I}{I_0} = \frac{1}{n} \sum_{i=1}^n E_i E_i^* \quad (8.9)$$

where:  $I_0$  = Incident optical intensity.

$E_i$  = the complex electric field strength at angle of incidence  $\theta_i$  and the asterisk denotes the complex conjugate.

and:  $\theta_m - \theta_c < \theta_i < \theta_m + \theta_c$ , where  $\theta_m$  is the mean incident angle and  $\theta_c$  is half the convergence angle. The number of points ( $n$ ) were spaced evenly over the range of incident angles.

## 8.2.2 The multilayer immunosensor system

The multilayer system described in chapters 4 and 6 was too simplistic and required modification to include the bound protein layer and to take account of film thickness variations in the waveguide layer. The basic system is illustrated in fig. 8.4.

### 8.2.2.1 The solution layer

The solution layer was defined by the thickness of the capillary cell gap ( $130\mu\text{m}$ ) and by the refractive index of the solution. The refractive index was complex due to the presence, in solution, of the optically absorbing fluorescent label. The real part was given by the measured value ( $n_{so} = 1.334$ ) and the imaginary part was calculated using Beer's law:

Thickness	Layer	Refractive index
variable	Solution	$n_{so} + jm_{so}$
	Bound	$n_{bo} + jm_{bo}$
$t_w$	Waveguide (FePO <sub>4</sub> )	$n_{wa} = 1.70$
750nm	Buffer (SiO <sub>2</sub> )	$n_{bu} = 1.44$
	Substrate	$n_{su} = 1.517$

**Fig. 8.4** Multilayer system for immunosensor modelling.

$$\log_{10} \frac{I_0}{I} = c\epsilon x \tag{8.10}$$

- where:
- $I_0$  = light intensity at zero distance.
  - $I$  = light intensity at distance  $x$ .
  - $c$  = concentration of absorbing material (mol/l).
  - $\epsilon$  = extinction coefficient (l/molcm).
  - $x$  = distance (cm).

and the complex equations describing the propagation of an electromagnetic wave (see appendix 1, chapter 4 or refs. [3, 4]):

$$E = E_0 e^{-j(n+jm)\frac{2\pi}{\lambda_0}x} = E_0 e^{-jn\frac{2\pi}{\lambda_0}x} e^{m\frac{2\pi}{\lambda_0}x} \tag{8.11}$$

- where:
- $E_0$  = complex electric field strength at zero distance.
  - $E$  = complex electric field strength at distance  $x$ .
  - $n + jm$  = complex refractive index of absorbing material.
  - $\lambda_0$  = free space wavelength of light (cm).
  - $x$  = distance (cm).

The part,  $e^{\frac{m}{\lambda_0}x}$ , is the decay in the field strength as the wave propagates through the absorbing medium (note that, with the above notation,  $m$  must be negative to be physically meaningful). Hence, assuming that  $I \propto EE^*$ , the following relation was obtained:

$$m = \frac{c\epsilon\lambda_0}{4\pi} \ln 10 \quad (8.12)$$

Note that steps to obtain the time averaged real magnitude of the electric field strength have been omitted, for clarity, in the above derivation.

### 8.2.2.2 The protein layer

The bound protein layer for a sandwich assay was sub-divided into two separate layers: a) the immobilised capture antibody; and b) the bound analyte/labelled antibody complex (see fig. 8.5). It was assumed that the capture antibodies and the analyte/labelled antibody complex could be modelled as spheres [5] with radii depending on the molecular weight and specific volume of the proteins, and with a refractive index of  $\sim 1.6$  [6, 7] (see chapter 6, section 6.1.5).

#### The immobilised capture layer

This was assumed to be a dense, hexagonally close packed array of spheres of radius  $R_{Cab}$  to give a layer thickness of  $2R_{Cab}$ , where the radius was given by:

$$r = \left( \frac{3M_{Cab}S_{Cab}}{4\pi N_A} \right)^{\frac{1}{3}} \quad (8.13)$$

where:  $r$  = radius of protein molecule.

and:  $M_{Cab}$  = Molecular weight of the capture antibody.

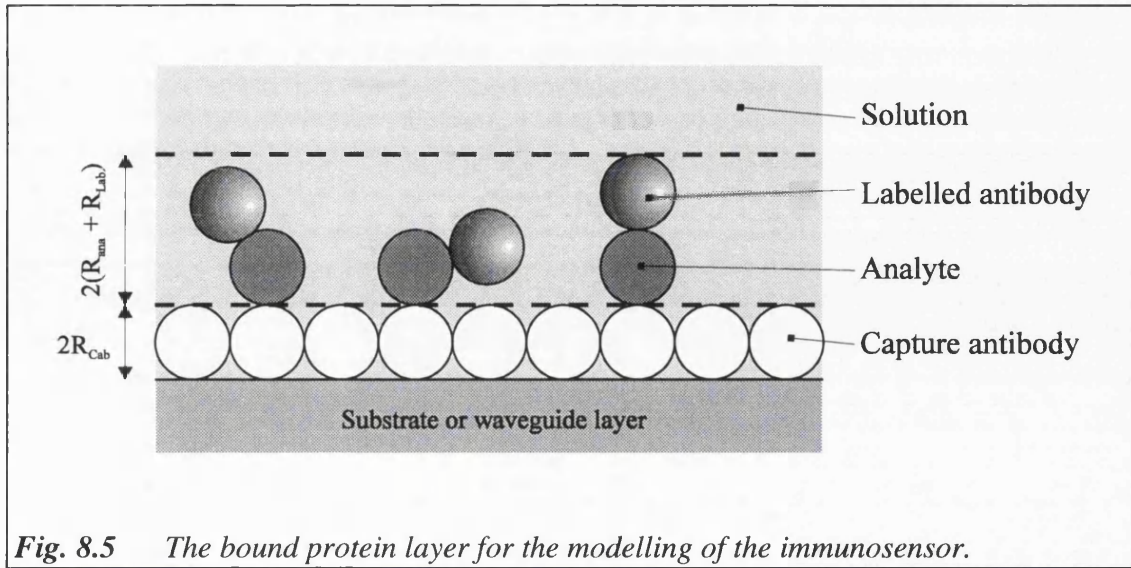


**Fig. 8.5** The bound protein layer for the modelling of the immunosensor.

$S_{Cab}$  = Specific volume of the capture antibody.

$N_A$  = Avogadro's number.

The capture layer consists of antibody molecules with the solvent filling in the gaps. The refractive index of this layer was calculated by using the Clausius-Mossotti relationship [5, 8] which states that the molar refractivity of a compound is the sum of the molar refractivities of the component molecules:

$$R_c = \frac{(n_c^2 - 1)}{(n_c^2 + 2)} V_c = \sum_i^N \frac{(n_i^2 - 1)}{(n_i^2 + 2)} V_i \quad (8.14)$$

where:  $R_c$  = molar refractivity of compound.

$n_c$  = refractive index of compound.

$n_i$  = refractive index of the  $i$ th component.

$N$  = number of components.

$V_c = M_c/\rho_c$  = molar volume of compound.

$V_i = M_i/\rho_i$  = molar volume of the  $i$ th component.

$M$  = molar mass.

$\rho$  = density.

Thus, the capture antibody layer refractive index,  $n_c$ , is given by calculating the right hand sum and rearranging equation 8.14.

Although the capture layer was assumed to be densely packed, the surface concentration of active capture antibody was estimated (chapter 7) to be  $\sim 330$  fmol/cm<sup>2</sup>.

### The bound analyte layer

The characteristics of this layer, thickness  $2(R_{ana} + R_{Lab})$  where  $R_{ana}$  is the radius of the analyte molecule and  $R_{Lab}$  is the radius of the labelled antibody molecule (both calculated using equation 8.13), will vary with the concentration of the analyte in the sample solution. It was assumed that there was no non-specific binding so that this layer consisted of only the solvent at zero analyte concentration and a mixture of bound analyte and solvent at increasing analyte concentrations. The reason for considering the analyte/labelled antibody complex as a single layer was that it was not known in which orientation the complex binds to the capture layer (fig. 8.4). Thus, it was possible that the fluorescent label may be lying immediately above the capture layer or be bound some distance from the capture layer. It was therefore decided that the analyte and labelled antibody layers were best considered as one layer with the fluorescent label being uniformly distributed through this layer. It was also assumed that only one analyte molecule binds to each capture antibody, the second binding site being inhibited by the binding of the large analyte/labelled antibody complex. The real part of the refractive index of this layer was calculated using equation 8.14, and the imaginary part (necessary because of the presence of the absorbing fluorophore) was obtained using equation 8.12.

The amount of analyte bound to the capture layer and the labelled antibody bound to the analyte were calculated using the values for  $\bar{p}$  and  $\bar{q}$  (see section 8.1).

#### 8.2.2.3 The waveguide layer thin film thickness

The multilayer modelling results presented in chapter 6 showed how the

transmitted electric field depended on the thin film layer thicknesses. It was shown that at a buffer layer thickness of ~750nm, neither the resonant angle nor the transmitted field strength were significantly dependent on small variations of the buffer layer thickness. However, this was not true for small variations in the waveguide layer thickness. The most likely result of such thickness non-uniformities would be a decrease in the resonant field strength and an increase in the broadness of the resonant peak when compared to the ideal theoretical resonant peak. To incorporate waveguide layer thickness variations adequately into the theoretical model, two parameters were required: a) the mean waveguide layer thickness and b) a measure of the thickness variation (eg. standard deviation). These measurements, due to the limited size of the substrates from which the devices were fabricated, could not be taken. It was thus decided that estimates of the mean waveguide layer thickness and variation would be obtained from the immunosensing measurements.

Firstly, it was assumed that the waveguide thicknesses were normally distributed with a mean thickness  $t_0$ , and standard deviation  $\sigma$ , where the normal (or Gaussian) distribution function is given by:

$$f(t) = \frac{1}{\sigma\sqrt{2\pi}} e^{-\frac{1}{2}\left(\frac{t-t_0}{\sigma}\right)^2} \quad (8.15)$$

The mean thickness,  $t_0$ , was obtained by cubic spline interpolation to give the waveguide layer thickness such that the theoretical resonance angle matched the observed resonance angle. The theoretical resonance angle was calculated assuming a waveguide layer thickness standard deviation of 1nm.

The standard deviation,  $\sigma$ , was also obtained by cubic spline interpolation such that the width of the observed resonant peak matched the width of the theoretical resonant peak. The width of the resonant peak was taken to be that at half-height (half the difference between the maximum and minimum signals). The mean waveguide thickness was that obtained from the first interpolation as described earlier.

The optical intensity at a given point can now be obtained by summing over a range of waveguide thicknesses with mean  $t_0$  and standard deviation  $\sigma$ :

$$\frac{I}{I_0} = \sum_i (E_i E_i^*) g(t_i) \quad (8.16)$$

where  $I$  and  $E$  have been defined before and  $g(t_i)$  is the Gaussian factor given by:

$$g(t_i) = \int_{t_i - \delta t/2}^{t_i + \delta t/2} f(t) dt \quad (8.17)$$

and:  $f(t)$  = the Gaussian function (equation 8.7) with parameters  $t_0$  and  $\sigma$ .

$t_i$  = the waveguide layer film thickness.

$\delta t$  = the spacing between adjacent  $t_i$ .

The inclusion of the protein layer and the summing of the optical intensity over the light beam convergence angle and waveguide layer film thickness distribution allowed the theoretical model to take into account:

- the convergence of the incident exciting light beam.
- the presence of an optically absorbing solution layer.
- the presence of an optically absorbing analyte/labelled IgG layer.
- the presence of a capture antibody layer.
- the variation in the waveguide layer film thickness.

The model is not comprehensive - eg. the assumptions that there is no non-specific binding and that there is only a single layer of capture antibodies. However, the lack of sufficient experimental data does not support, or justify, a more comprehensive model.

### **8.2.3 The TIR immunosensor system**

Note, also, that the theoretical aspects concerning the solution and bound protein layers and the exciting light divergence/convergence presented in this chapter are as applicable to the TIR sensor as they are to the resonant multilayer sensor. Only the aspects concerning the waveguide layer thickness non-uniformity need to be omitted.

### **8.2.4 Fitting theory to the observed data**

#### **8.2.4.1 The immunosensor signal components**

##### **The dark signal**

The dark signal was measured by preparing the apparatus as when making an immunosensing measurement but leaving the laser off. This gave a combined measurement of the dark signal of the photomultiplier tube (PMT) and associated electronics and of any stray light entering the PMT. The dark signal, of 0.975mV, could then be subtracted from the immunosensing signals prior to fitting.

##### **Scattering and fluorescence**

Having removed the dark signal component from the measured signals, the remainder of the signal was assumed to have been due to scattering of the exciting laser light and fluorescence excited from the fluorescent label. The various origins of the measured signal could be split conveniently between the different layers of the multilayer system as shown in table 8.1. An important assumption, that both scattering and fluorescence are proportional to the optical intensity at a given point, was now made. It is possible that each layer has more than one component (scattering, fluorescence, phosphorescence, etc.) that may contribute to the final measured signal. However, given the aforementioned assumption, it would be impossible to distinguish

Layer	Signal component		Parameter
	Reference	Sample	
Substrate	Scattering	Scattering	$a_1$
Buffer (silica)	Scattering	Scattering	$a_2$
Waveguide (iron phosphate)	Scattering	Scattering	$a_3$
Capture antibody	Scattering	Scattering	$a_4$
Bound analyte/labelled antibody	<i>No component</i>	Fluorescence	$a_5$
Solution	Fluorescence	Fluorescence	$a_6$

**Table 8.1** Signal components in the multilayer sensor. The parameters  $a_1 - a_6$  are discussed later.

between the various components contributing to the signal from each of the layers. Hence, only the assumed strongest component for each layer has been listed in table 8.1.

The origins of the TIR immunosensor signal can also be split between the various layers of the TIR sensor system. Hence, the signal components will be the same as listed in table 8.1 but without the buffer and waveguide components (see table 8.2).

Layer	Signal component		Parameter
	Reference	Sample	
Substrate	Scattering	Scattering	$a_1$
Capture antibody	Scattering	Scattering	$a_4$
Bound analyte/labelled antibody	<i>No component</i>	Fluorescence	$a_5$
Solution	Fluorescence	Fluorescence	$a_6$

**Table 8.2** Signal components in the TIR sensor. The parameters  $a_1$  and  $a_4 - a_6$  are discussed later.

### 8.2.4.2 The theoretical immunosensing signal

Assuming that scattering and fluorescence are proportional to the optical intensity, the output signal of the immunosensor can be modelled as a volume integral:

$$S = \iiint_V a(x, y, z) I(x, y, z) dx dy dz \quad (8.18)$$

where:  $S$  = immunosensor signal.

$I(x, y, z)$  = optical intensity at point  $(x, y, z)$  obtained as described in section 8.2.

$a(x, y, z)$  = distribution of scattering or fluorescing points.

$V$  = volume of device.

Equation 8.18 can be simplified by assuming: a) that the distribution of scattering or fluorescence points is uniform in any given layer and b) that the optical intensity is uniform in the x-y plane. Thus considering a unit surface on the x-y plane (see fig. 8.6), equation 8.18 reduces to:

$$S = \sum_{i=1}^n \left( a_i \int I dz \right) \quad (8.19)$$

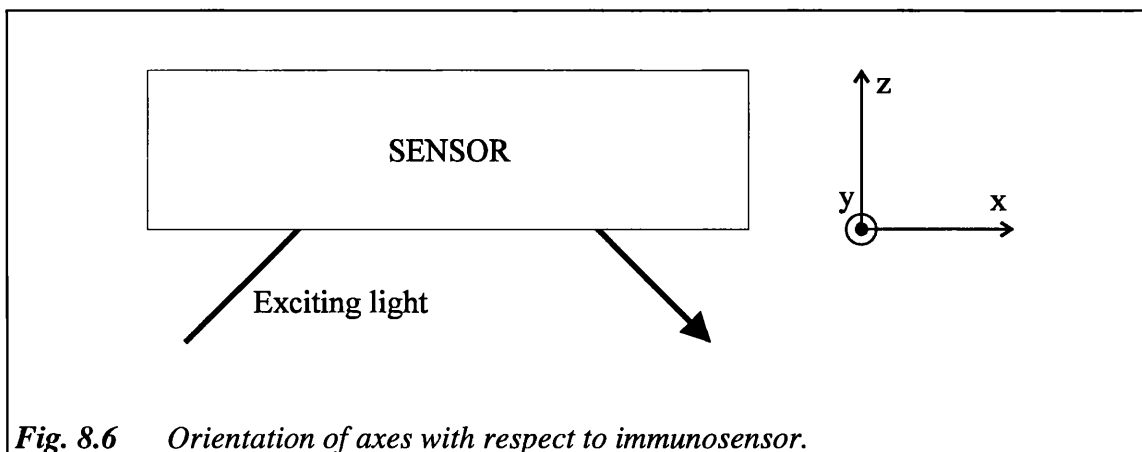


**Fig. 8.6** Orientation of axes with respect to immunosensor.

where:  $i$  = layer and  $n$  = number of layers.

$a_i$  = distribution of scattering or fluorescence points in layer  $i$ .

and note that the integral is taken only between the boundaries of layer  $i$ .

Equation 8.19 can now be fitted to the measured immunosensor signals with the unknown parameters being the various  $a_i$  as defined in table 8.1 and 8.2.

### 8.2.5 Constraints on the distribution of scattering/fluorescing points

The unknown parameters in the fitting ( $a_i$  - the distribution of scattering or fluorescing points in a given layer,  $i$ ) are not all independent and, thus, it is possible to constrain some so that the number of unknowns in the fitting can be reduced.

#### 8.2.5.1 Constraints between the reference and sample cells

Each device consisted of a reference and a sample cell fabricated from a single substrate. It would, therefore, be reasonable to assume that the distribution of scattering points will be uniform and equal between the reference and sample cells. This means that parameters  $a_1$  to  $a_4$  (as defined in table 8.1) are equal between the two cells.

The only difference between the reference and sample cells arises due to the differences in the concentration of the fluorescent label in the bound analyte and solution layers. However, assuming that there is only a fluorescent signal from the bound analyte and solution layers, the following relationships for the sample cell can be established:

$$a_{5,\text{sam}} = \frac{[\text{lab}]_{\text{ana}}}{[\text{lab}]_{\text{sol,ref}}} a_{6,\text{ref}} \quad (8.20)$$

$$a_{6,\text{sam}} = \frac{[\text{lab}]_{\text{sol,sam}}}{[\text{lab}]_{\text{sol,ref}}} a_{6,\text{ref}} \quad (8.21)$$

where: the subscripts 'sam' and 'ref' refer to the sample and reference cells respectively.

$[\text{lab}]_{\text{ana}}$  = concentration of fluorescent label in the bound analyte layer.

$[\text{lab}]_{\text{sol}}$  = concentration of label in the solution layer.

The concentration of the fluorescent label was calculated from the results of the analysis of antibody-antigen binding presented in section 8.1.

### 8.2.5.2 Constraints between separate devices

The substrate (PERMABLOC float glass) on which the multilayer devices were fabricated was mass produced and, therefore, it was assumed that there was almost no intra-batch variation in its characteristics. This essentially fixes the substrate scattering parameter,  $a_1$ , to be constant between devices. The same argument applies for the reference solution, which was prepared from a single stock solution of the labelled antibody. This, again, fixes the solution fluorescence parameter,  $a_6$  (reference cell), to be constant between devices.

The argument for constraining the scattering and fluorescence parameters between devices need not end at the substrate and solution layers. The buffer (silica) and waveguide (iron phosphate) layers were fabricated using the same solutions and methods between devices and, therefore, it is reasonable to assume that any variations in the characteristics of these layers will be minimal.

### 8.2.5.3 Exciting light input coupling efficiency

The theory presented thus far requires one pre-condition: the exciting light power incident on the immunosensing device is always the same. Variations in the input

coupling efficiency would produce different measured signal levels between devices. This signal variation, in fact, can be observed in the immunosensing results presented in chapter 7, and is probably the most important factor in the argument for the inclusion of a reference (or calibration) measurement on each device.

The absolute input coupling efficiency is difficult to determine, especially using the experimental apparatus that was used for the immunosensing measurements. Instead, only a relative input coupling efficiency can be estimated by comparing the differing reference signal levels between devices. The coupling efficiency variation was accommodated into the theory by including a variable factor for each device by which the the theoretically obtained signals could be scaled.

### **8.3 FITTING TO THE MULTILAYER IMMUNOSENSOR DATA**

This section presents and discusses the results of fitting the theoretical model of the multilayer immunosensor to the available multilayer immunosensing data. Although the results from fitting to both the 633nm and 650nm excitation sources will be presented, the bulk of the following discussion will concern the 633nm excitation source and the allophycocyanin fluorescent label.

#### **8.3.1 Fitting results**

The unknown parameters in the fitting were:

- the scattering parameters  $a_1$  to  $a_4$ , fixed between reference and sample cells and between devices.
- the solution fluorescence parameter  $a_{6,ref}$ , fixed between all reference cells.

The parameters  $a_5$  and  $a_{6,sam}$  for the sample cells were derived from  $a_{6,ref}$

using equations 8.20 and 8.21.

- a factor,  $e$ , for each device to account for exciting light input coupling variations.

### 8.3.1.1 Helium-Neon (633nm) laser, allophycocyanin label

The fitting was performed on the data sets from four devices at analyte concentrations of 6.05, 12.1, 18.15 and 24.2 nM. There were, therefore, eight unknown parameters: five scattering/fluorescence and three light input coupling efficiency factors, the fourth (for the 6.05nM data) being the reference factor.

Layer	Component	Parameter	
Substrate	Scattering	$a_1$	13.26
Buffer (silica)	Scattering	$a_2$	9.96
Waveguide (iron phosphate)	Scattering	$a_3$	6.38
Capture antibody	Scattering	$a_4$	$9.15 \times 10^4$
Solution (reference cell only)	Fluorescence	$a_{6,ref}$	$5.56 \times 10^4$

a) Fitted parameters  $a_1 - a_4$  and  $a_{6,ref}$  (fixed between cells and devices).

Sample cell	Parameter	Analyte concentration (nM)			
		6.05	12.1	18.15	24.2
Bound analyte	$a_5$	$1.98 \times 10^6$	$3.71 \times 10^6$	$4.88 \times 10^6$	$6.34 \times 10^6$
Solution	$a_{6,sam}$	$5.55 \times 10^4$	$5.54 \times 10^4$	$5.53 \times 10^4$	$5.52 \times 10^4$
Light coupling	$e$	1.0	0.790	0.980	0.322

b) Fitted sample cell fluorescence parameters,  $a_5$ ,  $a_{6,sam}$  (calculated from  $a_{6,ref}$ ) and relative exciting light input coupling efficiency,  $e$ .

**Table 8.3** Results of fitting to multilayer immunosensor (633nm laser, allophycocyanin label).

Table 8.3 and figs. 8.7 and 8.8 give the results of fitting to the multilayer immunosensor. The parameters,  $a_1 - a_6$ , as explained before, can be considered as being the density of scattering or fluorescing points in a given layer.

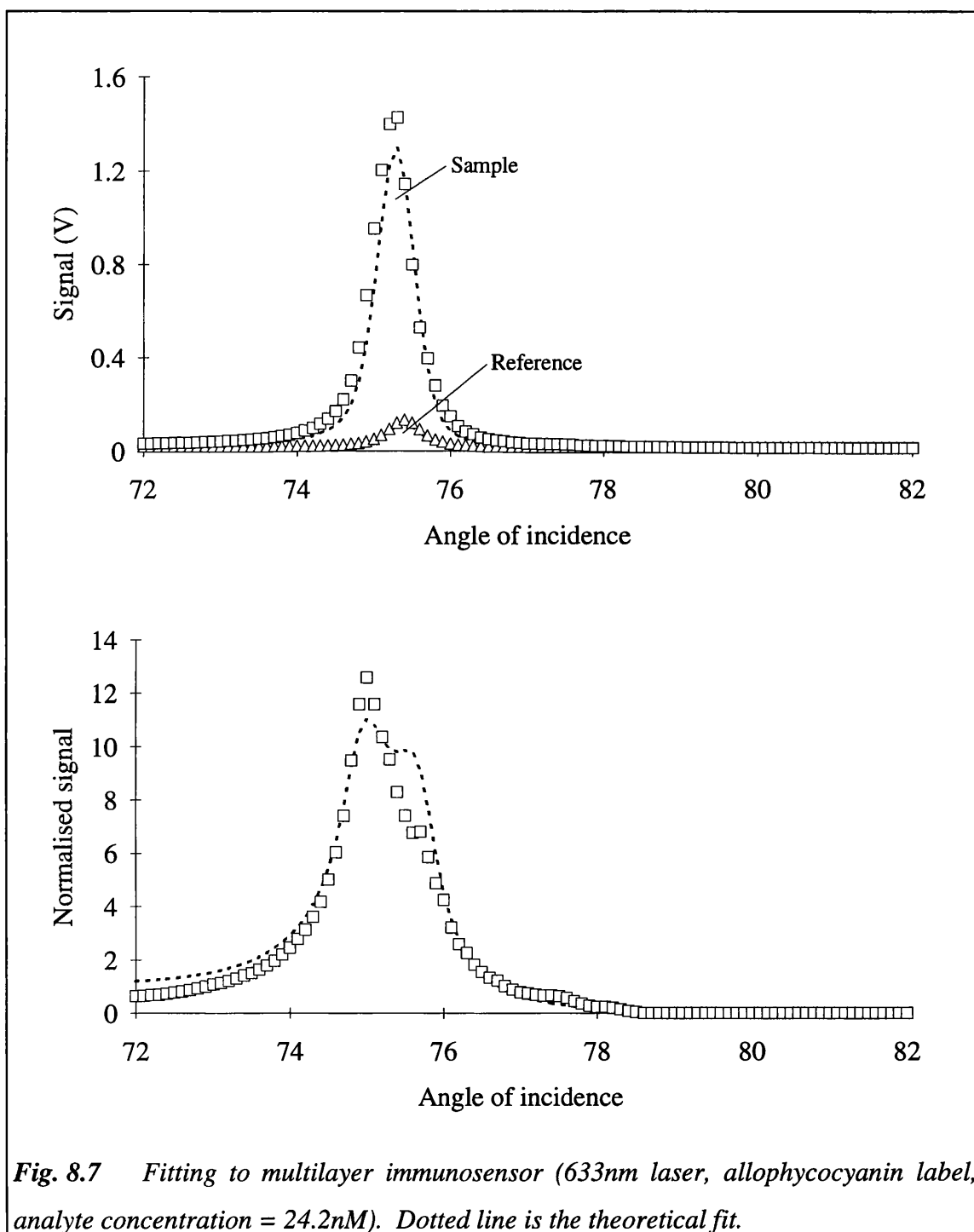


**Fig. 8.7** Fitting to multilayer immunosensor (633nm laser, allophycocyanin label, analyte concentration = 24.2nM). Dotted line is the theoretical fit.

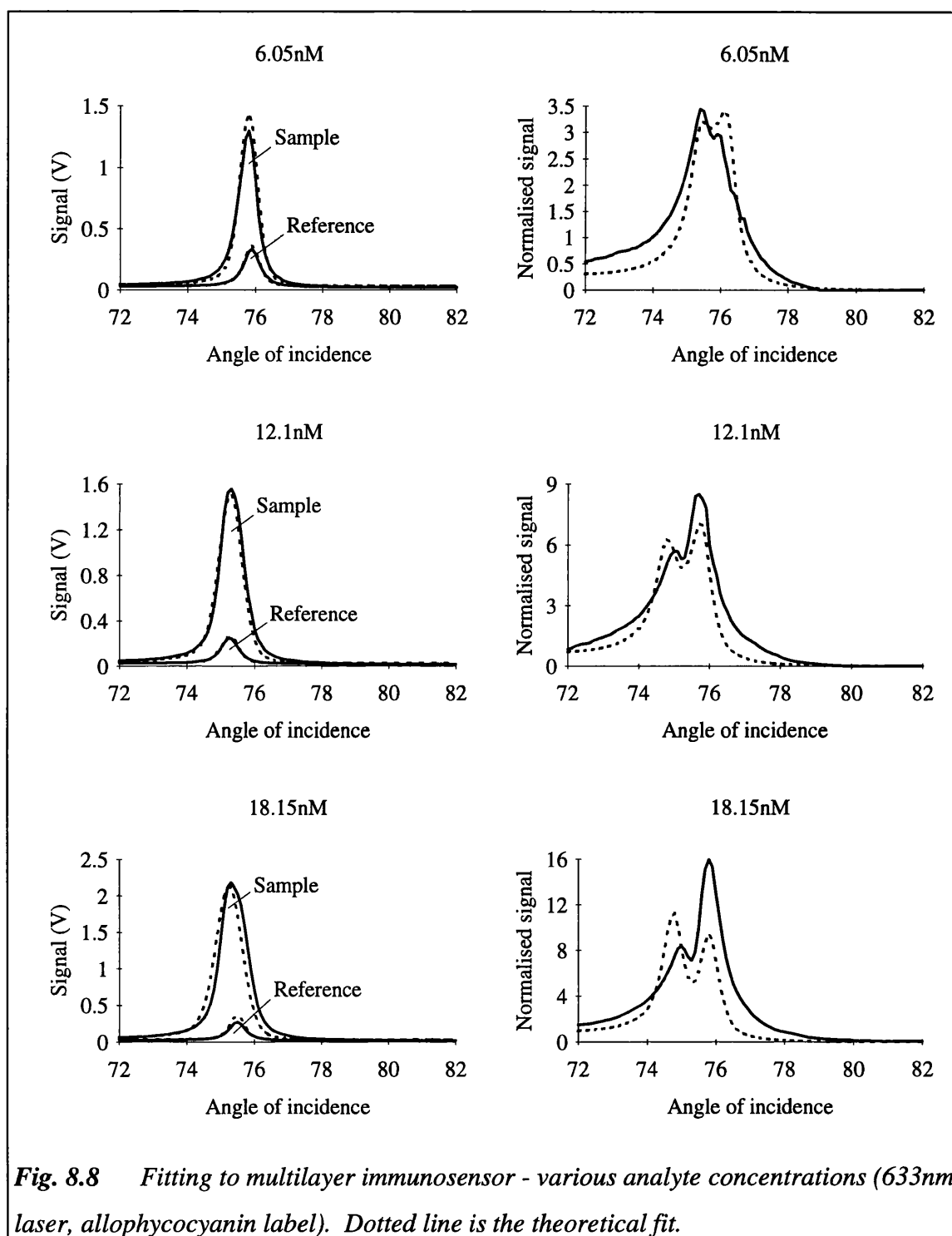


**Fig. 8.8** Fitting to multilayer immunosensor - various analyte concentrations (633nm laser, allophycocyanin label). Dotted line is the theoretical fit.

An immediate observation from the data in table 8.3 is that the distribution of scattering/fluorescence points is much greater in the capture antibody, bound analyte and solution layers than in the other layers. It can also be seen that the scattering parameter is greater for the substrate layer than for the buffer or waveguide layers. It is unlikely

that the commercially manufactured float glass substrate is more scattering than the buffer or waveguide layers, and this parameter may be artificially high so that any stray light (whose intensity is independent of the angle of incidence of the exciting light) entering the detector can be accounted for.

The distribution of scattering/fluorescence points allow comparisons between multilayer and TIR sensors (discussed later in this chapter), to be made. However, for an analysis of the sources of the measured signal we need to see what proportion of the theoretical signal can be attributed to each layer in the multilayer system. Table 8.4 shows what percentage of the total theoretical sample signal can be attributed to arising from each layer in the multilayer system.

The proportion of the signal from the bound analyte layer is the most important in terms of sensor performance. Increasing the proportion that originates from this layer,

	At resonance				Off resonance (angle = 72°)			
[Analyte] (nM)	6.05	12.1	18.15	24.2	6.05	12.1	18.15	24.2
Layer								
Substrate	2.23	1.68	1.49	0.80	55.65	26.16	19.45	19.67
Buffer	0.01	0.01	0.01	0.00	0.00	0.00	0.00	0.00
Waveguide	0.01	0.00	0.00	0.00	0.00	0.00	0.00	0.00
Capture antibody	2.32	1.38	1.08	0.86	1.12	1.01	0.87	0.70
Bound analyte	77.76	86.32	89.12	91.77	34.78	64.65	73.07	74.07
Solution	17.67	10.61	8.31	6.58	8.45	8.18	6.61	5.56
<b>Signal (%)</b>	77.76	86.32	89.12	91.77	34.78	64.65	73.07	74.07
<b>Background (%)</b>	22.24	13.68	10.89	8.24	65.22	35.35	26.93	25.93

*Table 8.4 Percentage of theoretical sample signal arising in each layer of the multilayer sensor (both at and off the resonant peak). "Signal" is the percentage from the bound analyte layer and "Background" is the total from the other layers.*

increases the signal-to-background ratio and, therefore, improves the sensor performance. It can be seen, from table 8.4, that the signal-to-background ratio drops with decreasing analyte concentration and it is this drop that eventually determines the sensor sensitivity.

It can be seen, from table 8.4, that the majority of the signal, at resonance, originates from the bound analyte layer with the remainder originating mainly from the solution. This is distinctly different from the off-resonance situation where a significant proportion of the signal is from the substrate layer. Two conclusions can be drawn from these observations. Firstly, there is a distinct advantage, in terms of signal-to-background ratio, in operating the multilayer sensor at resonance. This advantage can be seen in the normalised signal graphs of figs. 8.7 and 8.8. Secondly, when off resonance, a greater proportion of the signal originates from the substrate than from the solution. When off resonance, the multilayer sensor resembles a simple TIR sensor and, therefore, it would be reasonable to assume that the aforementioned observation will also be true of TIR sensors. Thus, previous researchers' [9 - 11] conclusions, that the majority of the background signal is due to unwanted fluorescence from the solution which can be reduced by decreasing the penetration depth of the evanescent field, may not be wholly correct. This point will be discussed again in section 8.4 when the results from the TIR sensor modelling will be presented.

### **8.3.2.2 Laser diode (650nm), allophycocyanin label**

Fitting to the 650nm laser diode data was performed on four data sets at analyte concentrations of 3.025, 6.05, 12.1 and 24.2 nM. The fitting procedure was different from that adopted for the 633nm Helium-Neon laser data. The scattering/fluorescence parameters,  $a_1 - a_6$ , should not be significantly different from those obtained from fitting to the 633nm laser data because of the similarity of the multilayer devices. However, the exciting light input coupling efficiency factor,  $e$ , should be significantly different because the 650nm laser diode has a lower optical power output. Thus, a good fit to the 650nm laser diode data should be obtained by maintaining the

	Parameter	Analyte concentration (nM)			
		3.025	6.05	12.1	24.2
<b>Light coupling</b>	e	0.505	0.184	0.103	0.125

*Table 8.5 Results of fitting to multilayer immunosensor (650nm laser diode, allophycocyanin label).*

scattering/fluorescence parameters as given in table 8.3 and allowing the light input coupling factor to vary. Hence, the fitting to the laser diode data had only four unknowns: the four exciting light input coupling efficiency factors - one for each data set. Note that this factor is only relative - with respect to the input coupling efficiency factor for the 6.05nM data set for the 633nm Helium-Neon laser.

Tables 8.5 and 8.6 and figures 8.9 and 8.10 present the results of fitting to the

Layer	Analyte concentration (nM)			
	3.025	6.05	12.1	24.2
Substrate	11.85	3.86	3.07	1.68
Buffer	0.02	0.01	0.01	0.00
Waveguide	0.01	0.01	0.00	0.00
Capture antibody	4.05	2.26	1.35	0.85
Bound analyte	52.32	75.95	84.95	90.72
Solution	31.75	17.91	10.61	6.75
<b>Signal (%)</b>	52.32	75.95	84.95	90.72
<b>Background (%)</b>	47.68	24.05	15.05	9.28

*Table 8.6 Percentage of theoretical sample signal arising in each layer of the multilayer sensor (650nm laser diode). "Signal" is the percentage from the bound analyte layer and "Background" is the total from the other layers.*

650nm laser diode data.

The exciting light input coupling efficiency factor,  $e$ , for the laser diode is, on average, about 30% of the average for the helium-neon laser. However, this is not as

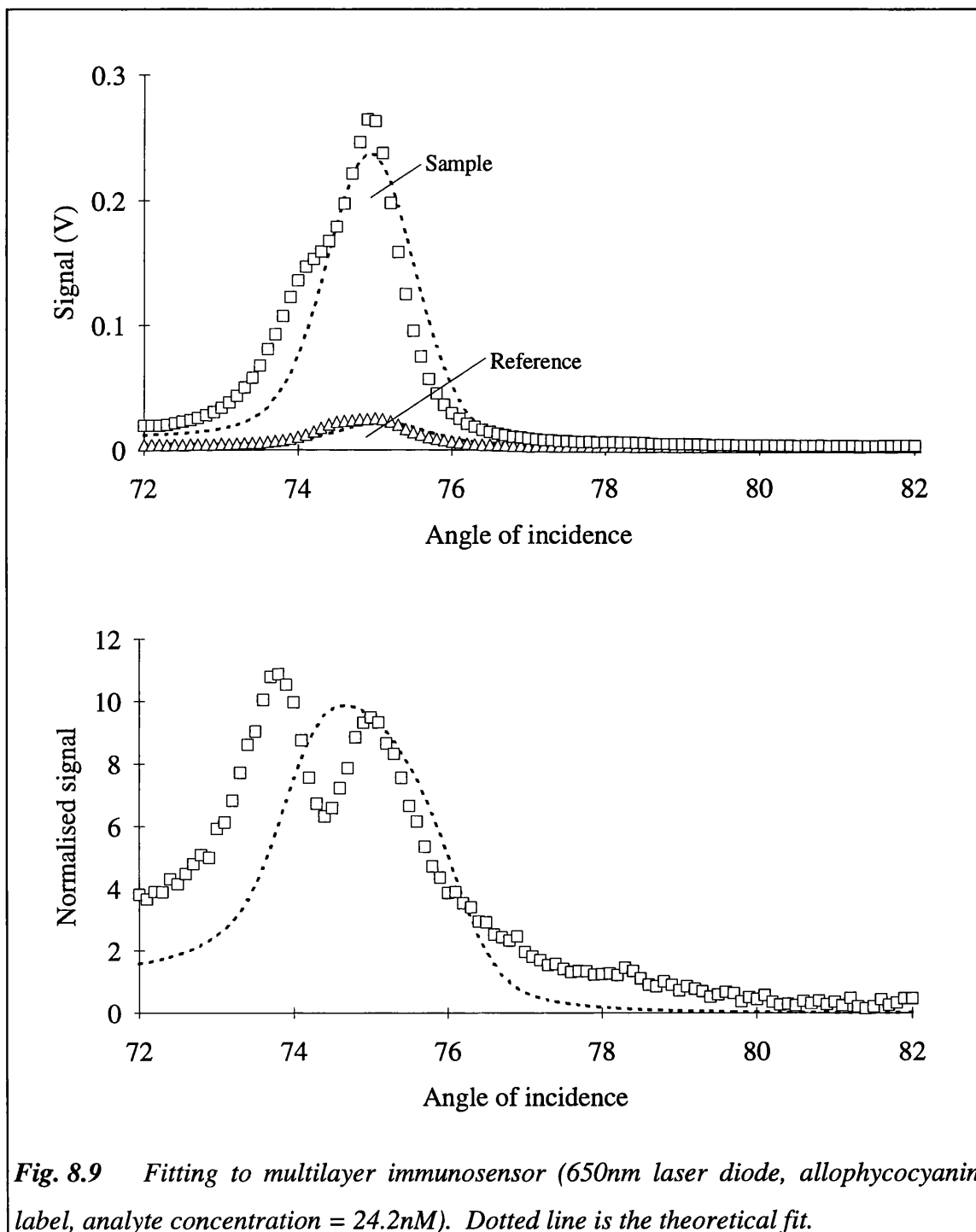
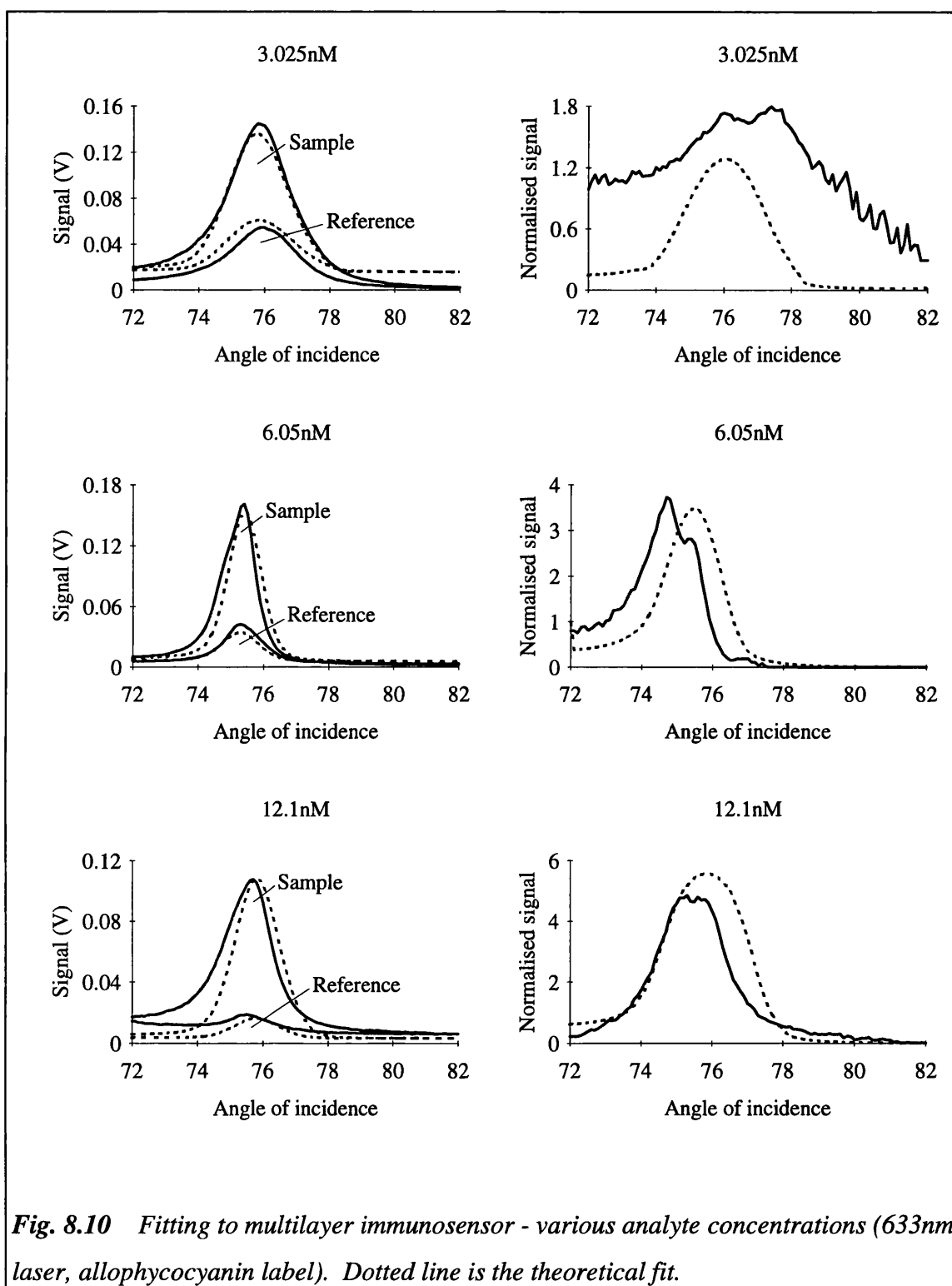


**Fig. 8.9** Fitting to multilayer immunosensor (650nm laser diode, allophycocyanin label, analyte concentration = 24.2nM). Dotted line is the theoretical fit.



low as anticipated (~10%) and may be due to the high signal strength of the 3.025nM data (laser diode) and the low signal strength of the 24.2nM data (HeNe laser).

Figs. 8.9 and 8.10 indicate that the fits to the laser diode data are not as good as the fits to the HeNe laser data. However, the similarity of the theoretical and observed reference and sample signal levels (despite having the scattering/fluorescence parameters fixed) suggests that the theoretical model is generally correct but lacks fine tuning, as clearly indicated in fig. 8.9. The graph shows a shoulder on the observed sample signal curve indicating that the waveguide (iron phosphate) film thickness is not symmetrically distributed about a mean value. This is in direct contrast to the assumptions made for the theoretical model.

## 8.4 FITTING TO THE TIR IMMUNOSENSOR DATA

Fitting to the TIR sensor data was done in a similar manner to that for the multilayer sensor data (as described in section 8.3.1) with the one difference: that there was neither a buffer nor waveguide thin film layer. Thus, the scattering and fluorescence parameters are as defined in table 8.2 with the parameters  $a_5$  and  $a_{6,sam}$  being derived from  $a_{6,ref}$  using equations 8.20 and 8.21. These parameters were also constrained between reference and sample cells and between devices as described in section 8.3.1.

### 8.4.1 Fitting results

The unknown parameters in the fitting were:

- the scattering parameters  $a_1$  and  $a_4$  fixed between reference and sample cells and between devices.
- the solution fluorescence parameter  $a_{6,ref}$  fixed between all reference cells. The parameters  $a_5$  and  $a_{6,sam}$  for the sample cells were derived from  $a_{6,ref}$  using equations 8.20 and 8.21.

- a factor,  $e$ , for each device to account for exciting light input coupling variations.

#### 8.4.1.1 Helium-Neon (633nm) laser, allophycocyanin label

The fitting was performed on four data sets at analyte concentrations of 6.05, 12.1, 24.2 and 48.4 nM. There were, thus, six unknown parameters: three scattering/fluorescence and three light input coupling efficiency factors. The results are given in tables 8.7 and 8.8 and figs. 8.11 and 8.12.

There are a couple of similarities between the results for the TIR sensor and those for the multilayer sensor given in table 8.3: the substrate scattering and solution fluorescence factors ( $a_1$  and  $a_{6,ref}$ ) are very similar and within an order of magnitude.

Layer	Component	Parameter	
Substrate	Scattering	$a_1$	8.16
Capture antibody	Scattering	$a_4$	$3.67 \times 10^6$
Solution (reference cell only)	Fluorescence	$a_{6,ref}$	$1.10 \times 10^4$

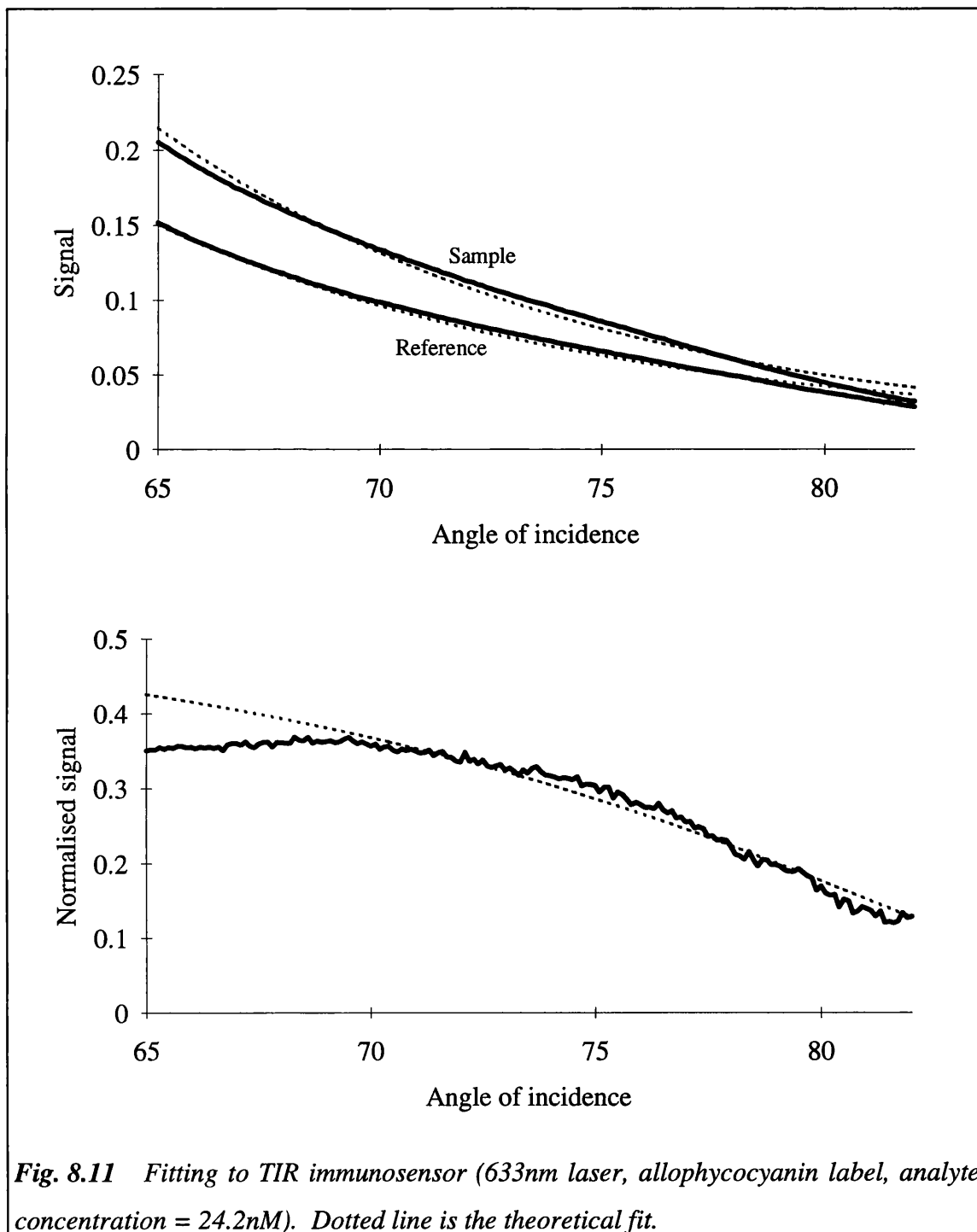
a) Fitted parameters  $a_1$ ,  $a_4$  and  $a_{6,ref}$  (fixed between cells and devices).

Sample cell	Layer	Parameter	Analyte concentration (nM)			
			6.05	12.1	24.2	48.4
Bound analyte		$a_5$	$3.90 \times 10^5$	$7.30 \times 10^5$	$1.25 \times 10^6$	$1.58 \times 10^6$
Solution		$a_{6,sam}$	$1.09 \times 10^4$	$1.09 \times 10^4$	$1.09 \times 10^4$	$1.08 \times 10^4$
Light coupling		$e$	1	1.485	1.390	1.219

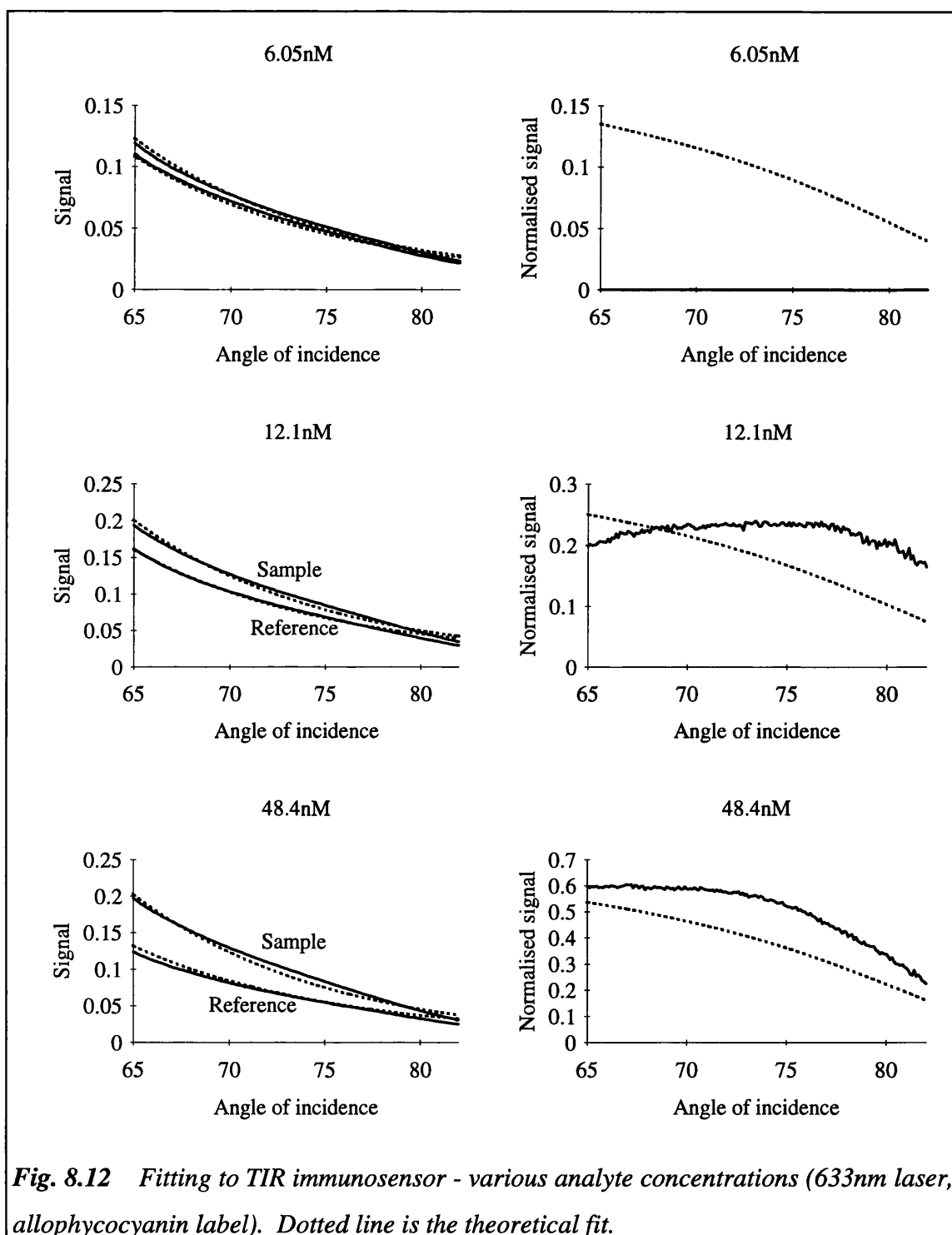
b) Fitted sample cell fluorescence parameters,  $a_5$ ,  $a_{6,sam}$  (calculated from  $a_{6,ref}$ ) and relative exciting light input coupling efficiency,  $e$ .

Table 8.7 Results of fitting to TIR immunosensor (633nm laser, allophycocyanin label).

However, there is a large difference between the capture antibody layer scattering factors with the TIR sensor factor being about two orders of magnitude greater than the multilayer sensor factor. This suggests that there is a significant difference between the two capture antibody layers whereby the TIR sensor capture layer is either more



**Fig. 8.11** Fitting to TIR immunosensor (633nm laser, allophycocyanin label, analyte concentration = 24.2nM). Dotted line is the theoretical fit.



**Fig. 8.12** Fitting to TIR immunosensor - various analyte concentrations (633nm laser, allophycocyanin label). Dotted line is the theoretical fit.

scattering or encourages greater non-specific binding than the multilayer sensor capture layer.

The figures of table 8.8 show that the high capture antibody layer scattering

Layer	Analyte concentration (nM)			
	6.05	12.1	24.2	48.4
Substrate	16.07	14.59	12.80	11.88
Capture antibody	67.27	61.09	53.60	49.76
Bound analyte	11.68	19.80	29.66	34.72
Solution	4.98	4.51	3.94	3.65
<b>Signal (%)</b>	11.68	19.80	29.66	34.72
<b>Background (%)</b>	88.32	80.20	70.34	65.28

*Table 8.8 Percentage of theoretical sample signal arising in each layer of the TIR sensor (633nm HeNe laser, incident angle = 65°). "Signal" is the percentage from the bound analyte layer and "Background" is the total from the other layers.*

parameter has translated into a large proportion of the TIR immunosensor sample signal arising in the capture layer. This major difference between the multilayer and TIR sensors makes their comparison difficult and suggests that there is a significant difference between immobilising onto an iron phosphate layer and onto PERMABLOC float glass.

Looking at the contribution that arises from the solution layer to the total sample signal, it can be seen that it is still significantly less than the contribution from the substrate. This confirms the figures of table 8.4 and the observations of section 8.3.2.1, which was that unwanted solution fluorescence may not be the most significant background signal contributor in a TIR fluorescence immunosensor.

Table 8.8 also shows clearly the reasons for the improved performance and increased sensitivity of the multilayer sensor over the TIR sensor. It can be seen that the background contribution to the TIR sensor signal is much greater than that from the bound analyte layer whereas the opposite was true for the multilayer sensor. A more direct comparison of the TIR and multilayer sensor is somewhat hampered by the

	Parameter	Analyte concentration (nM)			
		6.05	12.1	24.2	48.4
<b>Light coupling</b>	e	0.261	0.365	0.323	0.318

**Table 8.9** Results of fitting to TIR immunosensor (650nm laser diode, allophycocyanin label).

obvious differences between the immobilised capture layers between the two devices.

#### 8.4.1.2 Laser diode (650nm), allophycocyanin label

The fitting to the laser diode data was done in a similar manner to that described in section 8.3.2.2. The scattering/fluorescence parameters were fixed as obtained for the HeNe laser fitting (table 8.7) and only the exciting light input coupling efficiency factor was allowed to vary. Tables 8.9 and 8.10 and figs. 8.13 and 8.14 illustrate the results.

The fit in this case is not good and obviously becomes worse with decreasing

Layer	Analyte concentration (nM)			
	6.05	12.1	24.2	48.4
Substrate	16.03	14.55	12.76	11.84
Capture antibody	67.13	60.96	53.47	49.63
Bound analyte	11.70	19.84	29.71	34.77
Solution	5.14	4.65	4.06	3.76
<b>Signal (%)</b>	11.70	19.84	29.71	34.77
<b>Background (%)</b>	88.30	80.16	70.29	65.23

**Table 8.10** Percentage of theoretical sample signal arising in each layer of the TIR sensor (650nm laser diode). "Signal" is the percentage from the bound analyte layer and "Background" is the total from the other layers.

analyte concentration (or decreasing signal levels) - something that can also be observed with the fit to the multilayer sensor (laser diode data). This indicates that the theoretical model is inadequate at low signal levels.

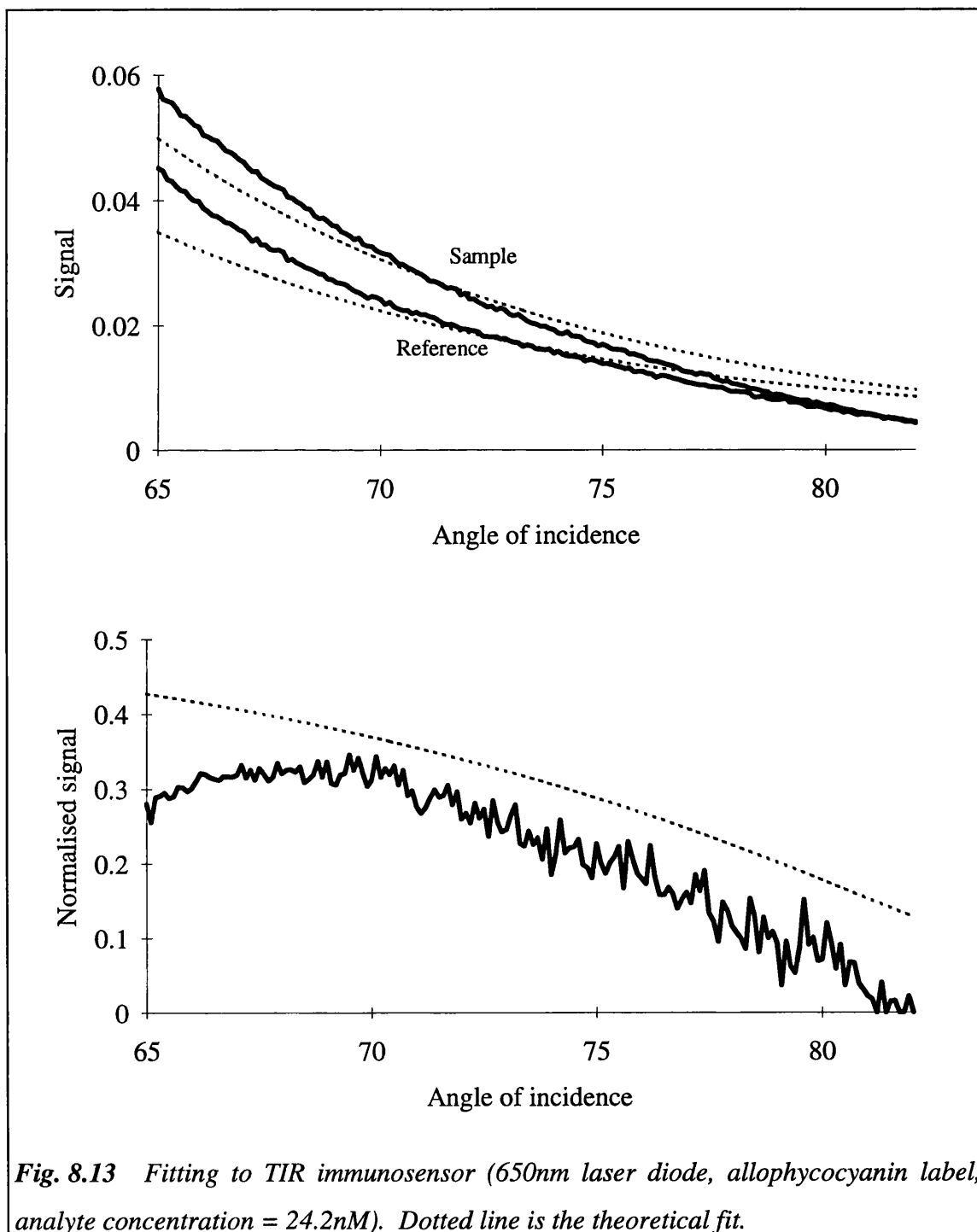
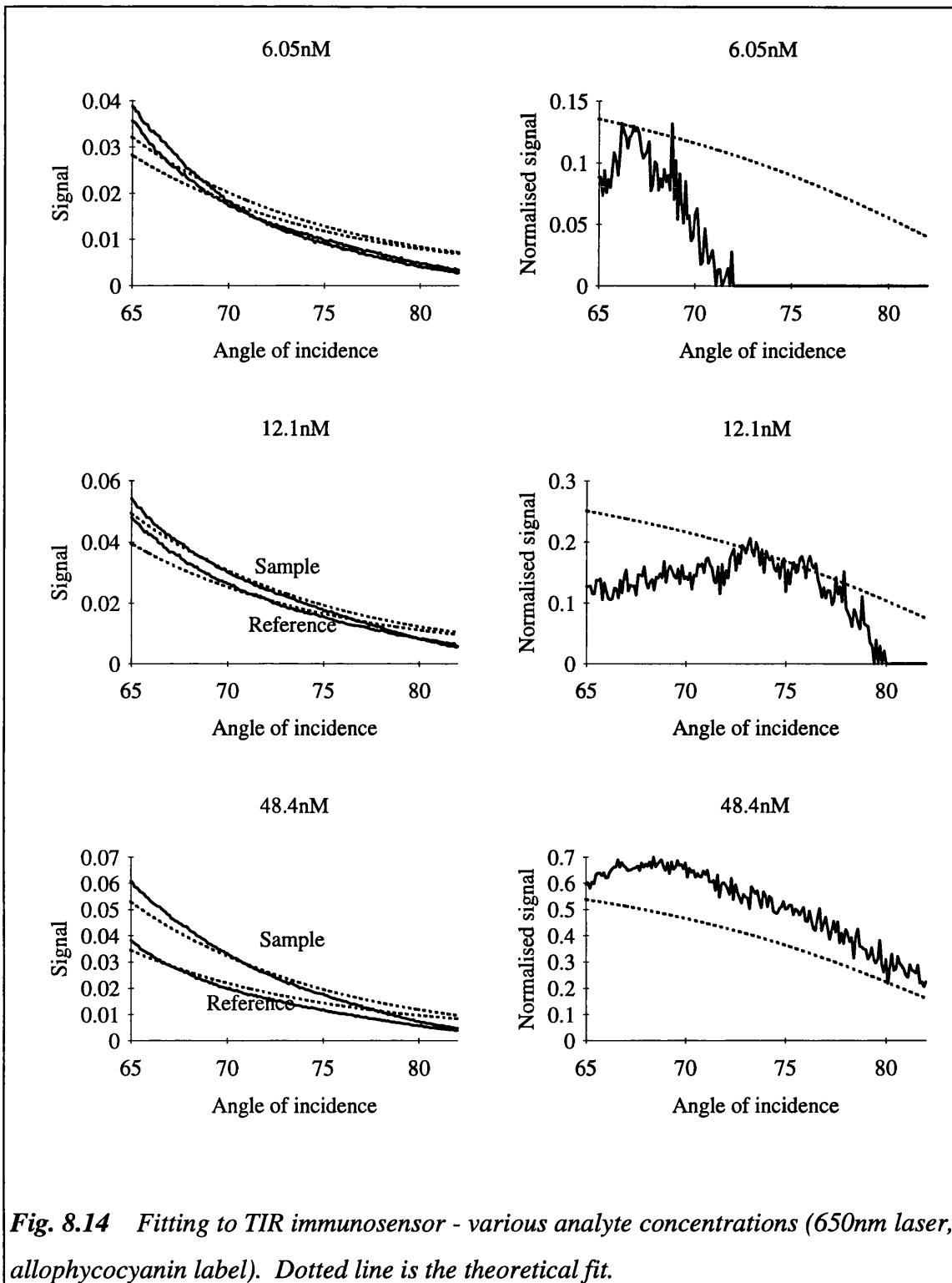


**Fig. 8.13** Fitting to TIR immunosensor (650nm laser diode, allophycocyanin label, analyte concentration = 24.2nM). Dotted line is the theoretical fit.



## 8.5 RE-DESIGNING THE IMMUNOSENSOR

Once a suitable agreement between the observed immunosensor measurements and the theoretical modelling results have been achieved, the model can be used to test the effect of design changes to the immunosensors. The multilayer sensor can be altered in many different ways:

- increasing the immobilised capture layer antibody activity.
- increasing or decreasing the waveguide layer thickness.
- increasing or decreasing the buffer layer thickness.
- increasing or decreasing the waveguide layer thickness variations.

The TIR sensor can only be altered by increasing the capture layer antibody activity.

Consider first, the multilayer sensor using the example of the 6.05nM analyte concentration measurement using the 633nm laser source. The various parameters that were obtained from the theoretical modelling presented earlier are given in table 8.11 (the estimated buffer layer thickness is 750nm and the estimated capture antibody activity is 10% - see chapter 7). Table 8.12 shows the possible normalised signals predicted by the theoretical model when various changes are made to the design of the multilayer sensor.

It can be seen that, by far, the best improvement in the normalised signal (or

Cell	Waveguide layer	
	Thickness (nm)	Standard deviation (nm)
Reference	153.7	1.76
Sample	152.7	2.02

*Table 8.11 Fitted parameters to multilayer sensor (633nm laser source, allophycocyanin label and 6.05nM analyte concentration.*

Design changes	Reference signal	Sample signal	Normalised signal	% change
Observed measurement			2.87	-
Capture layer antibody activity = 50%	0.354	7.278	19.59	583
Buffer layer thickness = 500nm	0.164	0.646	2.93	2.1
Buffer layer thickness = 1000nm	0.468	1.889	3.04	5.9
Waveguide layer thickness = 120nm	0.256	1.020	2.98	3.8
Waveguide layer thickness = 190nm	0.300	1.227	3.09	7.7
Waveguide layer thickness standard deviation = 4.0nm	0.211	0.893	3.23	12.5
Waveguide layer thickness standard deviation = 0.5nm	0.556	2.496	3.50	22.0

*Table 8.12 Effect of design changes on multilayer sensor. '% change' is the percentage improvement in the theoretical normalised signal over the observed measurement.*

signal-to-background ratio) is obtained by increasing the activity of the immobilised capture layer which again emphasises the importance of the bio-specific layer in the performance of a biosensor. Relatively minor normalised signal improvements are obtained with changes to the thin film layer thicknesses. This suggests that fabrication tolerances on the thin film thickness variations between devices can be relaxed without greatly compromising the signal-to-background ratio. However at low buffer and waveguide layer thicknesses, both reference and sample signal levels are lower and, thus, will be more affected by noise (eg. electrical noise). Significant increases in both the signal levels and the normalised signal can be obtained if the waveguide layer film

thickness is highly uniform (ie. the standard deviation is low). This will not only require tightly controlled thin film fabrication procedures, but also tightens the requirements of the exciting light beam which will now need to hit a sharper resonance peak. The fact that normalised signal improvements have been obtained despite lower reference and sample signal levels (eg. when waveguide layer thickness = 120nm) suggests that a key factor to improving the sensor performance is ensuring thin film uniformity between the reference and sample cells. This observation is based on the results of modelling film thickness and thickness standard deviation changes to the waveguide layer which gave normalised signal improvements even if the actual reference and sample signal levels fell.

Combining some of the design changes listed in table 8.12, it is possible to achieve normalised signal improvements of approximately 1000% over the observed measurement. This can be compared to the TIR sensor where the only possible change is an increase in the capture antibody activity. A 50% increase in activity gives an approximately 600% improvement in the normalised signal.

## **8.6 DISCUSSION**

### **8.6.1 Antibody-analyte binding**

The results of the analysis presented in section 8.1 illustrate one of the major problems associated with immunosensing devices. The fraction of capture antibody bound to the analyte was very low, which meant that at an analyte concentration of 1.5125nM, only about 10% of the analyte was bound to the capture antibody. Obviously, to improve the signal-to-background ratio, this figure would need to be much higher, ideally approaching 100%.

The problems lie, largely, with the immobilised capture layer. Current covalent binding or adsorption techniques of immobilisation result in an antibody activity that is

less than 10% of the possible maximum [12] and is one of the reasons why both *Pharmacia* and *Fisons* chose an alternative method of immobilisation for their commercial optical immunosensing instruments [14, 15]. However, for immunosensor devices, which feature minimal user manipulation, immobilisation techniques that offer a long shelf-life are necessary. Currently, covalent binding and adsorption are the simplest and most suitable techniques that can offer a long shelf-life.

### **8.6.2 Thin film fabrication**

The thin film layers on the multilayer devices were fabricated under non-ideal conditions (no clean room environment, spinner chuck problems, etc.) and one concern prior to the modelling was that film non-uniformities (eg. dust particles, film thickness variations, etc.) would have a significant effect on the sensor performance.

A clear indication from the modelling presented in this chapter is that the silica buffer and iron phosphate waveguide layers contribute almost nothing to the observed signal suggesting that scattering from these layers is insignificant (see chapter 7, section 7.4.2). In fact the only problem seems to arise from the film thickness variations in the waveguide layer which can largely be attributed to heat conduction from the spinner chuck (see chapter 6, section 6.2.3). This has the effect of broadening the resonance peak and thus reducing the possible maximum sample signal - to - reference signal ratio and of also causing minor differences between the resonance angles of the sample and reference cells. Fig. 8.15 shows that the waveguide layer film thickness variations lie within the expected fabrication limits of about 5% (note that the waveguide layer film thickness was between 145 - 160 nm).

### **8.6.3 Comparison of multilayer and TIR immunosensors**

A direct comparison of the two types of sensor is not possible because of the

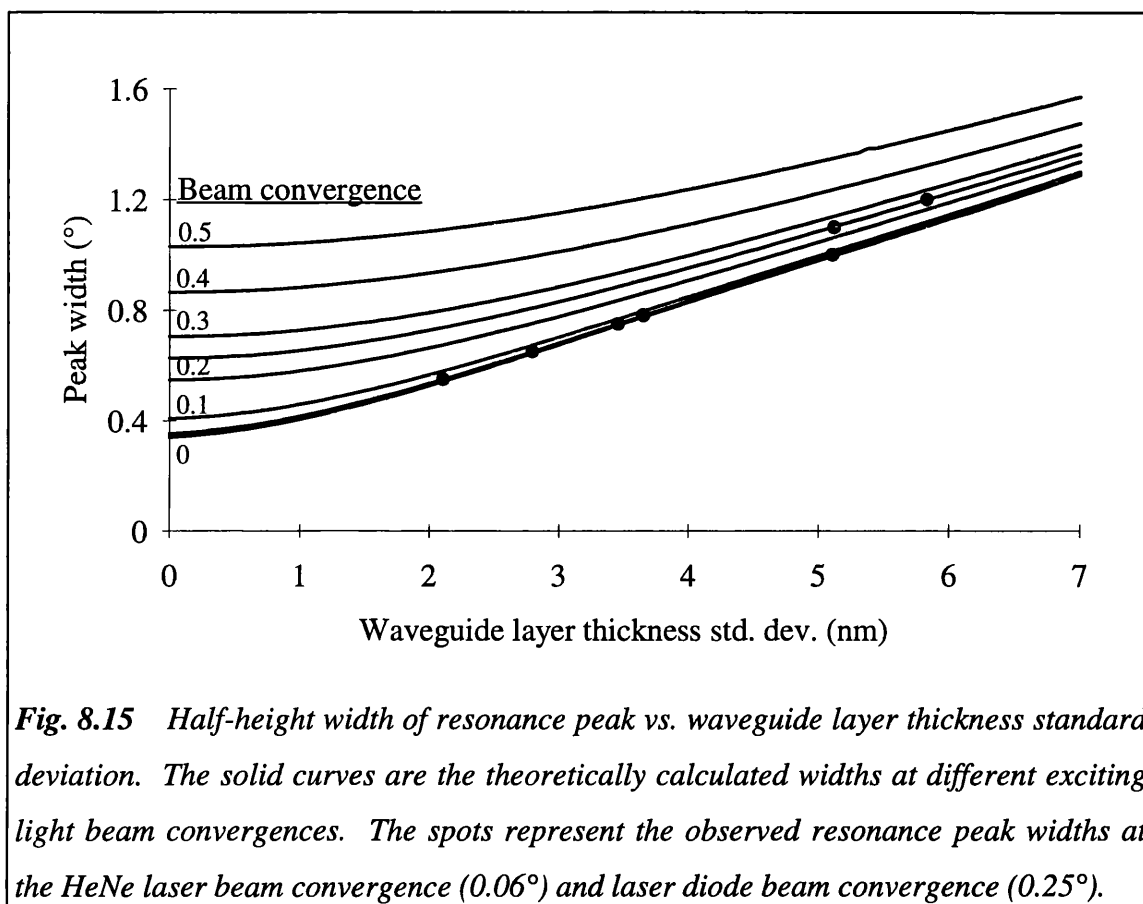


**Fig. 8.15** Half-height width of resonance peak vs. waveguide layer thickness standard deviation. The solid curves are the theoretically calculated widths at different exciting light beam convergences. The spots represent the observed resonance peak widths at the HeNe laser beam convergence ( $0.06^\circ$ ) and laser diode beam convergence ( $0.25^\circ$ ).

differences between the capture antibody layers of the sensors. However, it is still possible to draw some conclusions.

The multilayer sensor showed a sample signal - to - reference signal ratio improvement at the resonance angle which was confirmed by the theory, thus suggesting that the presence of a resonance peak does improve the signal-to-background ratio. The most significant contribution to the background signal (at resonance) was from the solution layer. The multilayer sensor, therefore, will require a minimisation of the penetration depth of the evanescent field to enhance performance.

This compares with the TIR sensor where, ignoring the contribution from the capture layer, the most significant contribution is from the substrate. This was also true of the multilayer sensor when observed off the resonant angle. These results suggest that the TIR sensor performance is less dependent on reducing the penetration depth

than has been previously claimed [9 - 11].

#### **8.6.4 Comparison between 633nm and 650nm lasers**

The theoretical model was clearly not as effective for the 650nm laser diode data sets as it was for the 633nm laser data. This may be due partly to the fact that the scattering/fluorescing parameters were fixed, but also because the model seemed to have more problems when fitting to the lower signal levels obtained when using the 650nm laser diode.

#### **8.6.5 Scope of the theoretical model**

The theoretical model presented in this chapter is not comprehensive, for example, scattering and fluorescence have not been rigorously, but have been assumed to be proportional to the optical intensity at any given point. However, the model was intended to be used to analyse the origins of the observed signals with an aim towards identifying where design modifications may be necessary to improve the performance of the sensors. In this respect, the model has provided some insight:

- highlighting the differences between TIR and multilayer immunosensors.
- illustrating that there is no significant background signal contribution from the buffer and waveguide thin film layers.
- demonstrating that there is a definite improvement in the signal-to-background ratio improvement at the resonant angle of incidence.
- showing that thin film thickness fabrication tolerances are within the expected limits.
- showing the differences in the dependence on the penetration depth between the TIR sensor and the multilayer sensor operating at resonance.
- demonstrating the high dependence of the signal-to-background ratio on the

activity of the capture layer antibodies.

## REFERENCES

- 1 DAY E D, Advanced immunochemistry, *Wiley-Liss Inc., New York, 1990, 2nd ed., 259-350.*
- 2 NELDER J A, MEAD R, A simplex method for function minimization, *Computer Journal, 1965, 7, 308-313.*
- 3 LEE D L, Electromagnetic principles of integrated optics, *J Wiley & Sons, New York, 1986, 1st ed., 13-67.*
- 4 LORRAIN P, CORSON D R, LORRAIN F, Electromagnetic fields and waves, *WH Freeman & Co., New York, 1988, 3rd ed., 492-593.*
- 5 FRICKE H, A mathematical treatment of the electric conductivity and capacity of disperse systems, 1. The electric conductivity of a suspension of homogeneous spheroids, *The Physical Review, 1924, 24, 575-588.*
- 6 ARWIN H, Optical properties of thin layers of bovine serum albumin, gamma-globulin, and haemoglobin, *Applied Spectroscopy, 1986, 40, 313-318.*
- 7 PUTZEYS P, BROSTEAUX J, L'indice de réfraction des protéides, *Bulletin de la Société de Chemie Biologique, 1936, 18(11), 1681-1703.*
- 8 ATKINS P W, Physical chemistry, *Oxford University Press, Oxford, 1982, 2nd. ed., 766-79.*
- 9 SUTHERLAND R M *et al*, Optical detection of antibody-antigen reactions at a glass-liquid interface, *Clinical Chemistry, 1984, 30(9), 1533-1538.*
- 10 SHRIVER-LAKE L C, OGERT R A, LIGLER F S, A fiber-optic evanescent-wave immunosensor for large molecules, *Sensors and Actuators B, 1993, 11, 239-243.*
- 11 MacCRAITH B D, Enhanced evanescent wave sensors based on sol-gel-derived porous glass coatings, *Sensors and Actuators B, 1993, 11, 29-34.*
- 12 SLOPER A N, Optical waveguide biosensors, *PhD Thesis, April 1991, University of London, 187-191.*
- 13 O'SHANNESY D J, BRIGHAM-BURKE M, PECK K, Immobilisation chemistries suitable for use in the BIAcore surface plasmon resonance detector, *Analytical Biochemistry, 1992, 205, 132-136.*
- 14 BUCKLE P E *et al*, The resonant mirror: a novel optical sensor for direct sensing of biomolecular interactions Part II: applications, *Biosensors & Bioelectronics, 1993, 8, 355-363.*

## **CHAPTER 9**

### **DISCUSSION**

#### **9.1 INTRODUCTION**

Optical immunosensors are seen as having an excellent potential for development to the commercial stage [1, 2]. Evanescent wave optical techniques offer a particularly suitable means of developing wash-free immunoassay systems [1-5]. Firstly, a sensing technique is required that can offer the precision, sensitivity and dynamic range for a given analyte or a panel of analytes. Secondly, the sensing technique, device and instrument need to be developed to provide an integrated product suitable for the market it is being aimed at. Finally, all this needs to be accomplished at a cost that can be recovered through the sale of the product. Previously, researchers have tended to concentrate on the discovery of new techniques or the application of old techniques in new ways whilst losing sight of the other objectives [6].

There are two major types of evanescent field optical sensors: a) surface plasmon resonance (SPR) [7-12] and b) optical waveguides (which includes multiple internal reflection [13], optical fibre [5, 13-18] and planar waveguide [19-28] sensors). There are also two major types of sensing [29]: a) direct detection and b) indirect detection that can be used with the above sensors.

Direct detection is inherently simple and often relies on refractive index changes in the bound protein layer (due to the binding of the analyte to the capture antibody) to produce a measurable signal [7-12, 23-28]. Direct detection is typically employed in

SPR systems, the grating coupler sensor [20, 23, 24, 30], Mach-Zehnder interferometer sensors [25, 26] and also in *Fisons'* multilayer sensor (*IA<sup>3</sup>ys*) [27, 28]. However, direct detection systems are likely to be affected by non-specific binding, and signals can be sample solution dependent [2, 4, 30], which compromises the sensitivities they can attain. Some researchers have thus attempted to magnify the signal levels and increase the signal-to-background ratio at low analyte concentrations by using high refractive index labels (eg. gold particles [28]) or fluorescent labels [31]. However, this removes one of the advantages of direct detection, which was that it does not require the addition of a labelled reagent.

Although indirect detection methods introduce an extra level of complexity (by requiring a labelled reagent), they are less affected, especially in sandwich (or two-site) immunoassays, by non-specific binding [32]. It is also less sample solution dependent because the measured signal is produced by a particular characteristic (eg. fluorescence) of the label. Indirect detection is typically employed with optical waveguide systems (optical fibre, planar waveguide and multiple TIR), and in the multilayer system described in this thesis.

Planar waveguide sensors have a number of advantages over optical fibre sensors. The planar geometry allows for a more rugged sensor that is easier to manipulate and handle by the user. Sample presentation, particularly in the form of a capillary fill device [19, 33], is also easier and is an important consideration concerning the user-friendliness of a device. When using thin film planar waveguide devices, it is possible to envisage the processing of the thin film layer by standard integrated optics techniques [4]. The thin film layer can be patterned (eg. etching [21, 34], embossing [20, 23, 24, 34] and photolithography [4, 34]) during device manufacture to incorporate multiple stripe waveguides, which would allow referencing and multiple analyte measurement to be performed on a single device. Similar incorporation of diffraction grating structures may also allow some optical processing to be performed on the device (eg. input/output coupling [20, 23], optical wavelength selection, etc.). However, a major disadvantage of planar thin film waveguides is their low exciting light input coupling efficiency [21].

Input coupling is more efficient into optical fibre waveguides and are also easier to fabricate (using existing fibre drawing techniques). Also, because both excitation and collection of fluorescence is done evanescently in optical fibres, both scattering and bulk solution fluorescence are greatly reduced, thus increasing the signal-to-background ratio.

## 9.2 MULTILAYER THIN FILMS

The advantages of thin film waveguide immunosensors (strong evanescent fields) may be combined with the advantages of TIR or multiple-TIR immunosensors (high exciting light input coupling efficiency) by employing resonant multilayer thin film devices. The drawbacks of resonant devices are: a) the requirement for the exciting light to be coupled at the resonant angle of incidence; and b) increased device fabrication costs (because of the requirement of two thin films of very different refractive indices).

### 9.2.1 Design considerations

The design of the multilayer thin film immunosensor requires some careful consideration.

#### 9.2.1.1 Thin film refractive indices

Ideally, the difference between the refractive indices of the thin films should be large. The buffer layer refractive index should be low (eg.  $\text{MgF}_2$ , RI = 1.38) and the waveguide layer refractive index should be high (eg.  $\text{ZrO}_2$ , RI = 2.05) to give a strong resonance peak, low evanescent field penetration depth, and a low critical angle of incidence (thus giving a wider angular working range).

### 9.2.1.2 Thin film layer thicknesses

The ideal thin film thicknesses will largely be determined by the refractive indices of the materials chosen, and the polarisation state and wavelength of the exciting light. Given an optical wavelength of 632nm, the low refractive index buffer layer will need to be relatively thick (of the order of 1 $\mu$ m) whereas the high refractive index waveguide layer will be relatively thin (of the order of 100 - 200 nm).

Given a pair of materials for the buffer and waveguide layers, the film thicknesses can be varied to optimise the performance of the sensor. Ideally, a strong resonance is required at a high angle of incidence (eg.  $>80^\circ$  to minimise the evanescent field penetration depth). The strength of the resonance can be optimised by choosing an appropriate buffer layer thickness, and the resonance strength and resonant angle of incidence increased by choosing an appropriate waveguide layer thickness. However, as the waveguide layer thickness increases, the resonance strength and resonant angle become highly sensitive to variations in the waveguide layer thickness. Thus, maximising resonant strength and angle will also put more stringent limits on the accuracy and uniformity of the thickness of the waveguide layer.

## 9.2.2 Fabrication considerations

### 9.2.2.1 Thin film materials

The most important criterion in fabricating a single-use disposable device is cost. Magnesium fluoride and zirconium dioxide were suggested, in section 9.2.1.1, as two possible materials for the buffer and waveguide layers respectively. However, they require expensive deposition techniques, such as CVD. Alternative materials that are relatively inexpensive and can be deposited by cheaper methods (eg. dip-coating) are the sol-gel glasses [20, 23, 24, 35-37] and the metal phosphate glasses [21, 34, 38, 39].

Sol-gel materials are commercially available and, using a silica-titania combination, it is possible to obtain thin films with refractive indices in the range 1.4 to 1.9 [36]. Sol-gel films can be spin coated (as described in this thesis) or dip-coated with sufficient film thickness uniformity and reproducibility [36]. However, silica and titania sol-gel films are micro-porous, and require expensive high temperature curing ( $>900^{\circ}\text{C}$ ) for full densification. Low temperature curing is possible, but the resulting porous films [40] will absorb the sample solution and may cause a signal drift (as observed by *Nellen & Lukosz* [24]). A sol-gel silica buffer layer was used in the sensors described in this thesis. It was shown that when the film was cured at  $300^{\circ}\text{C}$  it remained noticeably porous, but less so when cured at  $500^{\circ}\text{C}$ . However, any lingering porosity of the sol-gel silica (cured at  $500^{\circ}$ ) was only significant in determining the strength of the resonance peak but did not affect the immunosensor measurements. This was because the silica layer was coated with the waveguide layer of iron phosphate which has been shown to be fully densified and non-porous when cured at temperatures as low as  $200^{\circ}\text{C}$  [34, 39].

Phosphate glasses offer many advantages for the inexpensive fabrication of thin films [34]: a) inexpensive materials and preparation; b) inexpensive deposition methods (eg. dip coating and spin coating); c) low curing temperatures; d) wide range of refractive indices; e) chemical stability; f) non-porous films and g) suitability for surface patterning. These properties and characteristics make phosphate thin films particularly attractive for use in optical immunosensor devices. Among the phosphate glasses investigated by *Sloper and Flanagan* [34], aluminium phosphate had the lowest refractive index (1.457) and iron(III) phosphate had the highest (1.720). They could not be used together in the multilayer sensor, however, as it was found to be difficult to deposit iron phosphate on aluminium phosphate.

It may be possible to use a sol-gel silica buffer layer (RI = 1.44) and a sol-gel titania waveguide layer (RI = 1.9) to obtain a large refractive index difference between the two layers. The problem of the porosity of the titania layer can be avoided by coating it with a thin layer of iron phosphate of about 10 to 20 nm thick.

### 9.2.2.2 Film thickness variations

A totally uniform thin film thickness combined with a perfectly collimated exciting light beam would give the strongest resonant peaks. However, these resonant peaks would be narrow (with a half-height width of  $\sim 0.3^\circ$ ), thus requiring accurate coupling of the exciting light at the resonant angle of incidence. This would not present a problem if the film thicknesses could be accurately reproduced between devices and the instrument configured appropriately. However, it may be more cost-effective, in terms of device fabrication and instrument production, to allow the resonance peaks to be broader. This can be achieved in two ways: a) by reducing the waveguide layer film thickness uniformity and b) by adding a small divergence to the exciting light beam. It is more cost-effective to collimate the exciting light beam than to improve film thickness uniformity. Although the broadening of the resonant peak will decrease the signal strength and, therefore, also decrease the signal-to-background ratio, the decreased fabrication costs may be advantageous.

### 9.2.2.3 Thin film deposition

The most important consideration in fabricating the thin films is one of cost. The technique employed for the fabrication of the thin films in this thesis was spin coating. Although spin coating is cheap in small fabrication volumes, it is not particularly suited to large production volumes, due to the limited substrate size and a reliance on manual labour. Dip coating is the most cost-effective alternative and both sol-gel and phosphate glasses lend themselves to dip coating methods [36, 38]. However, the film thickness uniformity and reproducibility that can be obtained with dip coating (particularly concerning phosphate glasses) needs to be investigated.

It was noted in chapter 6 that the buffer layer was required to be greater than  $1.5\mu\text{m}$  thick to greatly increase the resonant evanescent field strength and also of the difficulty in fabricating a sol-gel silica layer of this thickness. The difficulty is mainly due to the differences in the expansion coefficients between the substrate and thin film

materials [41], and because of the stresses induced in the sol-gel film as it shrinks during heating [44]. Thicker silica films can be obtained by using more expensive deposition methods such as CVD [42] and sputtering [43]. A wide variety of different sol-gel materials can be deposited by spin or dip coating methods [44], and it may be worthwhile investigating whether another material may be more suitable for use as the buffer layer in the multilayer system.

### **9.3 MULTILAYER THIN FILM OPTICAL IMMUNOSENSORS**

#### **9.3.1 The immobilised capture layer**

The characteristics of the immobilised capture antibody layer is critical to the performance of the immunosensor device. The requirements for the capture layer are [46, 47, 54]: a) high specificity and affinity for the analyte of interest; b) high level of antibody activity; and c) a long shelf-life. The shelf-life requirement can be achieved by coating the capture layer with a soluble humectant and storing at a low temperature and a low humidity [21].

The analysis presented in chapter 8, section 8.1 suggested that the affinity of the capture antibodies was not greatly affected by the covalent binding immobilisation technique that was used. However, it has been shown that both covalent binding and adsorption immobilisation techniques result in an antibody activity of approximately 10 - 20 % of the possible theoretical maximum [21, 28]. This low capture antibody activity means that, at low analyte concentrations, as little as 10% of the analyte may be bound to the capture layer, thus reducing signal levels and sensor sensitivity. If, as shown in chapter 8, section 8.5, the capture antibody activity was 50%, a corresponding five-fold increase in the sensitivity can be obtained.

Although adsorption or covalent binding immobilisation techniques are most

suited to single-use, disposable immunosensor fabrication, the antibody activity offered is far from ideal. The activity of the antibody layer may be increased by suitably orienting the antibodies immediately prior to immobilisation such that the binding sites are not sterically hindered after immobilisation. The Langmuir-Blodgett method [47, 48] is a possibility that may also ensure that a monolayer of capture antibody is immobilised. Another method involves the use of protein A (a cell wall component of the *Staphylococcus aureus* bacterium), which binds specifically to the Fc portion of the IgG of various animals [49]. The limit to the adoption of a particular technique will largely be dependent on whether the immobilisation method can be sufficiently cost-effective to allow its use in the fabrication of disposable immunosensor devices.

### 9.3.2 Immunosensor performance

#### 9.3.2.1 Sensor response

The long immunosensor response times that were observed (in excess of 30mins. for the allophycocyanin label case) are unacceptable for any commercial biosensor instrument [2, 50]. The most immediate reason for the long response time is the sizes and molecular weights (MW) of the analyte and the fluorescent label. The MW of the analyte (mouse IgG) was ~150000, the MW of the allophycocyanin labelled antibody was ~254000 and the MW of the CY5.18 labelled antibody was 155000. When the allophycocyanin label was used, the equilibrium time was in excess of 30mins., but this dropped to about 20mins. when the CY5.18 label was used. Thus, if a low molecular weight analyte (eg. human pregnancy hormone hCG, MW = 39000 [51]) was being detected using a CY5.18 labelled antibody, a response time of a few minutes could be expected.

#### 9.3.2.2 Sensor sensitivity

The multilayer immunosensor gave stronger signal levels and higher

Analyte	Dynamic range	Units	Sample solution
Glucose	1-20	mM	Serum
Chlorpromazine [62]	350-700	$\mu$ M	Serum
Phenobarbital [62]	65-170	$\mu$ M	Serum
Streptomycin [62]	26-34	$\mu$ M	Serum
Theophylline [63]	14-238	$\mu$ M	Serum
Lidocaine [62]	6-21	$\mu$ M	Serum
Methotrexate [64]	1-1000	$\mu$ M	Serum
Erythromycin [62]	500-3000	nM	Serum
Thyroxine [65]	129-165	nM	Serum
Cortisol [63]	28-1930	nM	Serum
Digitoxin [63]	20-33	nM	Serum
Progesterone [65]	13.3-19.7	nM	Serum
Hydrocortisone [64]	3-3000	nM	Serum
Triiodothyronine [65]	2.77-3.62	nM	Serum
Digoxin [62]	1-2.6	nM	Serum
Clonidine [62]	900-9000	pM	Serum
Androstenedione [63]	350-35000	pM	Serum
Prolactin (PRL) [63]	136-6800	pM	Serum
Testosterone [63]	69-5530	pM	Serum
Human growth hormone (hGH) [63]	23.2-2320	pM	Serum
Human interleukin-2 (IL-2) [66]	19.4-10700	pM	Serum
Insulin [63]	17.5-2100	pM	Serum
Human chorionic gonadotropin (hCG) [67]	14-1400	pM	Serum
Human chorionic gonadotropin (hCG) [67]	70-2400	pM	Urine
Calcitonin [63]	1.1-22.5	pM	Serum

*Table 9.1 Dynamic ranges of some clinical analytes.*

sample-signal to reference-signal ratios than the TIR immunosensor. This translated into a greater than 6-fold improvement in the sensitivity of the multilayer sensor over the TIR sensor. However, the sensitivity achieved by the multilayer sensor ( $\sim 1.7$ nM as

Immunoassay method	Analyte	Sensitivity (nM)	Sample solution	Source
<b>Fluorescence immunosensors</b>				
Multilayer	IgG	1.7	PBS	This work
Total Internal Reflection (TIR)	IgG	11.1	PBS	This work
Thin film waveguide	hCG	0.83	Serum	[21]
TIR	hCG	2.6	Serum	[21]
Multiple-TIR: Glass plate	IgG	18.8	PBS	[13]
Multiple-TIR: Optical fibre	IgG	9.4	PBS	[13]
Multiple-TIR: Optical fibre	Digoxin	0.64	Serum	[5]
Glass plate	IgG	66	PBS	[19]
<b>Other optical immunosensors</b>				
Surface Plasmon Resonance	$\alpha$ -feto protein	5	PBS	[10]
Grating coupler	IgG	2	BSA	[68]
Mach-Zehnder interferometer	hCG	0.05	PBS	[26]
<b>Optical immunosensor based instruments</b>				
SPR ( <i>Pharmacia</i> - BIACore)	Various		Various	[69]
Resonant Mirror ( <i>Fisons</i> - IASys)	IgG	~1	PBS	[28]
<b>Electrochemical immunoassay</b>				
Potentiometric, homogeneous	IgG	0.3	Saline	[70]
<b>Conventional immunoassays</b>				
Particle	hCG	0.01	Urine	[71]
Radio-isotopic	hGH	30pM	Urine	[72]

**Table 9.2** Comparison of some immunoassay methods.

opposed to ~11nM for the TIR sensor) still falls short of the sensitivity requirement for many analytes of clinical interest as indicated in table 9.1.

Table 9.2 compares the multilayer thin film immunosensor with other immunosensor and immunoassay technologies. It can be seen that the sensitivity performance of the multilayer sensor falls short of many of the other technologies.

However, many of the highly sensitive methods listed in table 9.2 employ washing steps, large sample volumes and signal stabilisation routines prior to the measurement. This will have the effect of improving sensitivity and is particularly true of the Mach-Zehnder interferometer sensor [26] and the immunosensor based instruments [28, 69]. The multilayer sensor compares well with the other single-step optical immunosensing methods such as the thin film waveguide [21], optical fibre [5] and grating coupler [68] sensors. Some of the reasons for the relatively poor performance of the multilayer sensor lie in the design and fabrication of the device. The modelling of the immunosensor presented in chapter 8, section 8.5 showed how certain design alterations (eg. capture layer activity and thin film thicknesses) to the multilayer immunosensor affected the sample signal - to - reference signal ratio. It can be expected that improvements to this ratio will result in corresponding improvements in the sensor sensitivity. Thus, a theoretical sensitivity of  $\sim 170\text{pM}$  for the multilayer sensor (which lies well within the requirements for many clinical analytes) is possible if all the design improvements of table 8.15 (chapter 8) were implemented. This can be contrasted with the TIR sensor where the only possible improvement in the design is to increase the activity of the immobilised capture layer, giving a theoretically possible sensitivity of  $\sim 1\text{ nM}$ .

There are two other factors affecting sensitivity: a) instrument design and b) device fabrication. The apparatus used to make signal measurements would require improvement for commercialisation purposes. The optical filters used to remove stray exciting light need to be better matched to the fluorescent labels being used in the assay, so that reference signals can be reduced. The means of delivering the exciting laser light to the device needs to be improved (eg. by minimising the number of optical components between the laser output and the device) to ensure maximum exciting light intensity within the device. The prism coupling method used in the experiments presented in this thesis gives a highly variable input coupling efficiency (as indicated by the modelling presented in chapter 8), and may even be variable between the reference and sample cells on a single device. Finally, the nature of the device fabrication process introduces a high degree of variability that would not be expected from a mass

production process (particularly in the immobilisation of the capture antibody). It is not possible to state what the sensitivity improvements would be if the above recommendations were to be incorporated without further experimental data.

### 9.3.2.3 Signal referencing

The modelling presented in chapter 8 and the variability of the measured signal strengths highlighted the need for the adequate referencing of all measurements. The most variable factor in many optical systems (particularly those relying on fluorescence excitation) is the exciting light input coupling efficiency [21, 33, 52]. Typical methods of referencing include:

- measurement of the initial signal at time = 0 [15, 20, 21].
- the use of a reference cell [52] as adopted in this thesis.

Many glasses, including soda-lime float glass, emit phosphorescence when excited at ultra-violet wavelengths. This phosphorescence is highly stable because of the mass-produced nature of the glass and, therefore, can be used as a reference for the exciting light input coupling efficiency. However, phosphorescence measurements do not allow for other variations (eg. thin film thickness, sample solution, non-specific binding) between devices. The use of a separate reference cell or reference zone can be used to compensate for these variations. Ideally, a combination of substrate glass phosphorescence measurement together with the use of a reference cell would provide the best reference signal.

### 9.3.3 Comparison of exciting laser light sources

The commercialisation of an optical biosensor instrument will require the incorporation of a diode laser (as opposed to a HeNe laser) light source due to its low size and cost. The sensitivities obtained for the multilayer sensors described in this

thesis were similar regardless of whether a laser diode or a helium-neon light source was used. However, the signal levels were much lower thus making the noise more visible on the signals obtained using the laser diode. An average 9-fold difference between the peak signal strengths with the helium-neon and laser diode sources was obtained despite only a five-fold difference between the power output of the lasers. This was due to the greater divergence of the laser diode beam ( $0.5^\circ$  as opposed to  $0.12^\circ$ ) and also due the lack of availability of optical components suitable for use at the 650nm wavelength (eg. optical filters and polarisers).

Development of an appropriately designed exciting light delivery system and the use of appropriately matched fluorescent labels and optical filters should allow a much better utilisation of the laser diode source than has been possible in this work.

#### **9.3.4 Comparison of the fluorescent labels**

The two fluorescent labels used in this work were selected for the similarity of their excitation and emission wavelengths and their suitability for use with both the 632nm helium-neon laser and the currently available 650nm laser diode light sources. The only clear difference observable between the two labels can be attributed to the size and molecular weight of the labels. The lower molecular weight of the CY5.18 label (MW = 937) as opposed to the allophycocyanin label (MW = 104000) allowed the antibody antigen binding reactions to reach equilibrium quicker in the case of the CY5.18 label.

#### **9.3.5 General use of multilayer sensor**

The use of the multilayer sensor is not restricted to fluorescence sandwich immunoassay. The similarities between the multilayer and surface plasmon resonance sensors suggest that the multilayer sensor can be used as a direct evanescent field immunosensor. However, only relatively small resonant angle changes are possible,

which would be insufficient for a high sensitivity immunosensor. A phase sensitive method as adopted by *Fisons* [27] would be a much more sensitive alternative. It is expected, for reasons mentioned before, that direct sensing will be prone to a higher background signal and, therefore, a compromised sensitivity. The multilayer sensor can also be used with a competitive immunoassay format or with other bio-recognition components as required for the measurement of the analyte under test.

## 9.4 IMMUNOSENSOR MODELLING

### 9.4.1 Scope of model

The commercial development of an immunosensor will require more work than the simple demonstration of the feasibility of a particular technology. Mathematical modelling, on computer, of the immunosensor provides an attractive and cost-effective means of checking and improving upon the design of the immunosensor device. The modelling presented in chapter 8 of this thesis was performed not only with this intent, but also to examine the major differences between the multilayer and TIR immunosensors.

The model was not comprehensive and gave no absolute values for parameters such as scattering, phosphorescence, fluorescence or light input coupling efficiency. However, it was possible to obtain relative values that allowed the comparison of separate devices and multilayer and TIR technologies. The model is not restricted to the immunosensors described in this thesis but, with modifications, the ideas used to build the model can be used to analyse most optical immunosensor technologies, particularly towards tracing the origins of the background signal sources.

There are many possible improvements that can be envisaged for the model. One clear area is the modelling of scattering. It was assumed that scattering was proportional

to the optical intensity at any point. A more comprehensive model would incorporate non-homogeneous layers with point non-uniformities and non-planar surfaces and surface boundaries. The model also could not differentiate between fluorescence, scattering or phosphorescence. Thus, by incorporating a better analysis of the scattering and the distribution of fluorophores, it may be possible to differentiate between the different signal sources. However, a more detailed model is not useful without more experimental data against which the model can be assessed.

#### **9.4.2 Results of immunosensor modelling**

Modelling of the immunosensor served to point out many of the features and drawbacks of the immunosensors described in this thesis. One aspect that is particularly important and which was highlighted by the modelling was the requirement of a reference measurement largely to account for exciting light input coupling variations.

##### **9.4.2.1 Antibody-antigen binding**

The modelling of the antibody-antigen binding using a gaussian distribution [53] highlighted one of the major problems of immunosensor design - the capture layer antibody activity [28, 46, 54]. The results presented in chapter 8, section 8.5 showed how an increase in the capture layer activity can dramatically increase the signal levels and, thus, the sensitivity of the immunosensor. A higher antibody activity would also help to reduce non-specific binding and, therefore, further improve sensitivity.

##### **9.4.2.2 Signal sources**

A key requirement for improving the design of the multilayer immunosensor is a knowledge of the various background signal contributions in the measured signal. This would help in identifying the parts of the multilayer system that required most attention. The modelling provided this information.

**Substrate.** Background signals emanating from the substrate layer were found to be a significant contributor to the total signal from the immunosensor. This was particularly true for the TIR immunosensor, where the signal from the substrate was greater than the signal from the solution layer. The model does not differentiate between background signals emanating from the substrate or from external sources (eg. the input coupling prism or coupling fluid between the prism and the substrate) which were not included in the model. It may be possible that such sources of background signals may be reduced by design alterations to the measurement apparatus.

**Thin film layers.** It was expected that the thin film layers would be significant background signal contributors because of film non-uniformities and rough surfaces that would be combined with a strong optical intensity at resonance. This, however, proved not to be the case with background signal contribution from these layers being negligible. These results were encouraging and suggested that resonant multilayer optical systems could be employed without increasing the background signal overhead.

**Capture layer.** It was expected that the capture layer would also be a significant contributor to the background signal because this layer would be non-homogeneous and rough and, therefore, highly scattering. This was proved to be true as the capture layer returned the highest scattering parameters among the substrate, thin film and capture layers. This did not translate to a large proportion of the background signal emanating from the capture layer in the case of the multilayer immunosensor. However, in the case of the TIR immunosensor, the contribution from the capture layer was very high and very significant. This clearly indicated that there were significant differences between immobilising the capture antibody on an iron phosphate surface as opposed to a PERMABLOC float glass surface. The reasons for the differences have not been investigated.

**Solution.** The high resonant evanescent field strengths associated with the multilayer sensor led to a large background signal contribution from the solution layer. It would be difficult to reduce this contribution significantly by increasing the resonant angle of

incidence. For example, an angle of incidence of  $75^\circ$  has an associated evanescent field intensity penetration depth of  $\sim 80\text{nm}$  whereas at  $85^\circ$  it is  $\sim 70\text{nm}$ , a decrease of only  $\sim 12\%$ . The contribution from the solution layer of the TIR immunosensor was much less than that in the case of the multilayer sensor because of the lower evanescent field strengths and was, in fact, lower than the contribution from the substrate layer. Although it is difficult to state whether this directly contradicts other conclusions [13] that fluorescence excited from the solution layer is the most significant background signal contributor, it can be said that other background signal sources do exist and that further work is required to ascertain the significance of these sources.

#### 9.4.3 Achievements of modelling the immunosensor

The work of modelling the immunosensor has helped to ascertain some of the areas in the immunosensor design that will require further work if a commercial exploitation of the immunosensor is to be attempted:

- the large background contribution from the substrate layer. This may be improved by better instrument or measurement apparatus design.
- the importance of the capture layer to the sensitivity of the immunosensor. An increase in the activity of the capture layer will greatly improve the signal-to-background ratio and, therefore, the sensitivity.
- the low background contribution from the thin film layers.
- the relatively low background contribution from the solution layer (in the TIR sensor) suggesting that sensitivity may not be as dependent on the penetration depth of the evanescent field as it was thought.

## 9.5 RECOMMENDATIONS AND FURTHER WORK

### 9.5.1 Planar thin film architecture

*Sloper & Flanagan* [4, 21, 34, 39] noted some of the advantages of a planar thin film architecture in immunosensor design. Some of these advantages are applicable to multilayer sensors.

**Strip waveguides.** The thin film may be processed (eg. by photolithography) to obtain two or more strip waveguides (in the case of the multilayer sensor, the iron phosphate waveguide layer can be processed in this manner). These individual strips can act as separate zones for multi-analyte measurement (by depositing different bio-recognition components) or be used for referencing. This factor alone may tip the balance in favour of commercial viability.

**Integrated diffraction gratings.** The use of photolithographic procedures or embossing techniques can be used to incorporate gratings into the thin films. This would allow input/output coupling without the use of a prism. Further applications are wavelength selectivity (eg. to differentiate exciting light and excited fluorescence) and beam focussing (thus removing the requirement for lenses). An aspect that may be particularly applicable to multilayer sensors is the incorporation of a grating between the buffer and waveguide layers to facilitate input coupling or on the surface of the waveguide layer to vary the characteristics of the resonance peak.

### 9.5.2 Immobilised capture antibody

The full exploitation of the multilayer immunosensor, or other immunosensors, relies to a large extent on the effectiveness of the immobilised capture antibody. It has been shown in this work that this is one of the major obstacles to improving the sensitivity. Further work is required to increase the activity of the immobilised

antibody, which would help to increase signals, and also improve the sensitivity and dynamic range of the immunosensor. A higher capture antibody activity would also help to reduce non-specific binding.

### 9.5.3 The immunoassay

One aspect of the immunoassay that could be improved lies in the choice of the fluorescent label. The labels used in this work had small Stokes' shifts (10nm for allophycocyanin and 20nm for CY5.18) and thus effective filtering of the exciting light and maximisation of fluorescence collection was difficult. This can be overcome by using highly selective optical filters with sharp cut-off wavelengths or fluorescent labels with greater Stokes' shifts. The effective Stokes' shift can be greatly enhanced by using energy transfer immunoassay methods [55, 56] which would also help in reducing the background signal from the solution layer. This may be particularly effective in the multilayer sensor where a significant proportion of the background signal emanates from the solution layer.

Polarisation or time resolved fluorescence immunoassays can also be used with the multilayer system. Polarisation immunoassay would help to reduce the background signal from the solution layer [57] whereas time resolved immunoassay would reduce contamination by stray exciting laser light [58].

### 9.5.4 The multilayer immunosensor

The resonant angle of incidence is dependent on factors such as the wavelength or polarisation of the exciting light. It may, therefore, be possible to use more than one laser source at different resonant angles to excite different fluorescent labels, thus facilitating multi-analyte detection and measurement. Different polarisation modes may each be used as a reference measurement for the other mode because of the differing

resonant angles for TE and TM polarised waves. It may also be possible, by using the differing behaviour of the two polarisation, to make measurements of the thickness of the immobilised capture layer and also of the fraction of the sensor surface that has been covered by the immobilised layer. This could be used to compare different immobilisation methods.

The use of different cost-effective materials in the fabrication of the thin film layers need to be investigated. Only solution deposition of sol-gel silica and iron phosphate materials has been used in this work but deposition methods such as CVD may prove equally cost-effective with other materials that cannot be deposited from solution.

A problem of using sol-gel has been the porosity of the fabricated thin film, particularly when the film is cured at low temperatures (eg.  $<500^{\circ}$ ). Although a non-porous film is required for the immunosensors described in this thesis, it is possible to envisage the use of porous films in other sensing applications. Some researchers have succeeded in entrapping enzymes in porous sol-gel glasses without significantly reducing the activity of the enzyme [59-61]. Fine tuning of the sol-gel pore size would then allow the substrate to be selectively transported to the entrapped enzyme, thus reducing one of the background sources. A porous sol-gel layer incorporating entrapped enzymes could be incorporated as the waveguide layer in a resonant multilayer system. The very high optical intensities at resonance in this waveguide layer would lead to a greatly magnified signal that may give a high sensitivity. Such a system could be used to measure the emitted fluorescence or be used in a simple optical absorption type measurement - for example by looking at a dip in the reflected light intensity.

## REFERENCES

- 1 **SETHI R S**, Transducer aspects of biosensors, *Biosensors & Bioelectronics*, 1994, **9**, 243-264.
- 2 **ROBINSON G A**, Optical immunosensing systems - are they meeting the market needs?, *Biosensors & Bioelectronics*, 1993, **8**, xxxvii-xxxx.
- 3 **KRONICK M N, LITTLE W A**, A new immunoassay based on fluorescence excitation by internal reflection spectroscopy, *Journal of Immunological Methods*, 1975, **8**, 235-240.
- 4 **FLANAGAN M T, SLOPER A N, ASHWORTH R H**, From electronic to opto-electronic biosensors: an engineering view, *Analytica Chimica Acta*, 1988, **213**, 23-33.
- 5 **BLUESTEIN B I, WALCZAK I M, CHEN S-Y**, Fiber optic evanescent wave immunosensors for medical diagnostics, *TIBTECH*, 1990, **8**, 161-168.
- 6 **GRIFFITHS D, HALL G**, Biosensors - what real progress is being made?, *TIBTECH*, 1993, **11**, 122-130.
- 7 **HALL E A H**, Biosensors, *Open university press, Milton Keynes*, 1990, 1st ed., pp 320-330.
- 8 **FLANAGAN M T, PANTELL R H**, Surface plasmon resonance and immunosensors, *Electronics Letters*, 1984, **20**(23), 968-970.
- 9 **CULLEN D C, BROWN R G W, LOWE C R**, Detection of immuno-complex formation via surface plasmon resonance on gold-coated diffraction gratings, *Biosensors*, 1987/88, **3**, 211-225.
- 10 **DANIELS P B et al**, Surface plasmon resonance applied to immunosensing, *Sensors and Actuators*, 1988, **15**, 11-18.
- 11 **FONTANA E, PANTELL R H, STROBER S**, Surface plasmon immunoassay, *Applied Optics*, 1990, **29**(31), 4694-4704.
- 12 **ANONYMOUS**, Label-free biosensor technology visualizes biomolecular interactions in real time, *Biosensors & Bioelectronics*, 1993, **8**, xi-xiv.
- 13 **SUTHERLAND R M et al**, Optical detection of antibody-antigen reactions at a glass-liquid interface, *Clinical Chemistry*, 1984, **30**(9), 1533-1538.
- 14 **EENINK R G et al**, Fibre fluorescence immunosensor based on evanescent wave detection, *Analytica Chimica Acta*, 1990, **238**, 317-321.
- 15 **WALCZAK I M et al**, The application of evanescent wave sensing to a high-sensitivity fluoroimmunoassay, *Biosensors & Bioelectronics*, 1992, **7**, 39-48.
- 16 **CARLYON E E et al**, A single mode fibre-optic evanescent wave biosensor, *Biosensors & Bioelectronics*, 1992, **7**, 141-146.
- 17 **GRAHAM C R, LESLIE D, SQUIRRELL D J**, Gene probe assays on a fibre-optic evanescent wave biosensor, *Biosensors & Bioelectronics*, 1992, **7**, 487-493.
- 18 **ANDERSON G P, GOLDEN J P, LIGLER F S**, A fiber optic biosensor: combination tapered fibers designed for improved signal acquisition, *Biosensors & Bioelectronics*, 1993, **8**, 249-256.

- 19 **BADLEY R A et al**, Optical biosensors for immunoassays: the fluorescence capillary-fill device, *Philosophical Transactions of the Royal Society of London B*, 1987, **316**, 143-160.
- 20 **NELLEN Ph M, TIEFENTHALER K, LUKOSZ W**, Integrated optical input grating couplers as biochemical sensors, *Sensors and Actuators*, 1988, **15**, 285-295.
- 21 **SLOPER A N, DEACON J K, FLANAGAN M T**, A planar indium phosphate monomode waveguide evanescent field immunosensor, *Sensors and Actuators*, 1990, **B1**, 589-591.
- 22 **ZHOU Y et al**, Multichannel evanescent fluorescence immunosensing using potassium and sodium ion-exchanged patterned waveguides, *Journal of Molecular Electronics*, 1991, **7**, 135-149.
- 23 **LUKOSZ W et al**, Output grating couplers on planar optical waveguides as direct immunosensors, *Biosensors & Bioelectronics*, 1991, **6**, 227-232.
- 24 **NELLEN Ph M, LUKOSZ W**, Integrated optical input grating couplers as direct affinity sensors, *Biosensors & Bioelectronics*, 1993, **8**, 129-147.
- 25 **FATTINGER Ch, KOLLER H, SCHLATTER D, WEHRLI P**, The difference interferometer: a highly sensitive optical probe for quantification of molecular surface concentration, *Biosensors & Bioelectronics*, 1993, **8**, 99-107.
- 26 **HEIDEMAN R G, KOOYMAN R P H, GREVE J**, Performance of a highly sensitive optical waveguide Mach-Zehnder interferometer immunosensor, *Sensors and Actuators B*, 1993, **10**, 209-217.
- 27 **CUSH R et al**, The resonant mirror: a novel optical biosensor for direct sensing of biomolecular interactions. Part I: principle of operation and associated instrumentation, *Biosensors & Bioelectronics*, 1993, **8**, 347-353.
- 28 **BUCKLE P E et al**, The resonant mirror: a novel optical sensor for direct sensing of biomolecular interactions. Part II: applications, *Biosensors & Bioelectronics*, 1993, **8**, 355-363.
- 29 **MIYAI K**, Classification of immunoassay, in **PRICE C P, NEWMAN D J eds.**, Principles and practice of immunoassay, *Stockton Press, New York*, 1991, 1st ed., pp 246-264.
- 30 **HUBER W et al**, Direct optical immunosensing (sensitivity and selectivity), *Sensors and Actuators B*, 1992, **6**, 122-126.
- 31 **ATTRIDGE J W et al**, Sensitivity enhancement of optical immunosensors by the use of a surface plasmon resonance fluoroimmunoassay, *Biosensors & Bioelectronics*, 1991, **6**, 201-214.
- 32 **SIDDLE K**, Properties and applications of monoclonal antibodies, in **COLLINS W P ed.**, Alternative immunoassays, *John Wiley & Sons Ltd., Chichester*, 1985, 1st ed., 13-38.
- 33 **ROBINSON G A et al**, The fluorescence capillary fill device, *Sensors and Actuators B*, 1993, **11**, 235-238.
- 34 **SLOPER A N, FLANAGAN M T**, Metal phosphate planar waveguides for biosensors, *Applied Optics*, 1994, **33(19)**, 4230-4240.
- 35 **BRINKER C J, FRYE G C, HURD A J, ASHLEY C S**, Fundamentals of sol-gel dip coating, *Thin Solid Films*, 1991, **201**, 97-108.
- 36 **HEWAK D W, LIT J W Y**, Standardization and control of a dip-coating procedure for optical thin

- films prepared from solution, *Canadian Journal of Physics*, 1988, **66**, 861-867.
- 37 **OZER N, DEMIRYONT H, SIMMONS J H**, Optical properties of sol-gel spin-coated TiO<sub>2</sub> films and comparison of the properties with ion-beam-sputtered films, *Applied Optics*, 1991, **30(21)**, 3661-3666.
- 38 **ROTHON R N**, Solution-deposited metal phosphate coatings, *Thin Solid Films*, 1981, **77**, 149-153.
- 39 **SLOPER A N, FLANAGAN M T**, Novel iron phosphate optical waveguides fabricated by a low temperature process, *Electronics Letters*, 1988, **24(6)**, 353-355.
- 40 **BRINKER C J, SCHERER G W**, Sol → gel → glass: I. Gelation and gel structure, *Journal of Non-Crystalline Solids*, 1985, **70**, 301-322.
- 41 **VOROTILOV K A, ORLOVA E V, PETROVSKY V I**, Sol-gel silicon dioxide films, *Thin Solid Films*, 1992, **209**, 188-194.
- 42 **KERN W, BAN V S**, Chemical vapour deposition of inorganic thin films, in **VOSSSEN J L, KERN W** eds., Thin film processes, *Academic Press, New York*, 1978, 1st ed., 258-320.
- 43 **YIN Z, GARSIDE B K**, Low-loss GeO<sub>2</sub> optical waveguide fabrication using low deposition rate rf sputtering, *Applied Optics*, 1982, **21**, 4324-4328.
- 44 **SAKKA S, YOKO T**, Sol-gel derived coating films and applications, in **REISFELD R, JØRGENSEN C K** eds., Structure and bonding 77, *Springer-Verlag, Berlin*, 1992, 90-118.
- 45 **ASTON W J**, Manufacturing biosensors, *Biosensors & Bioelectronics*, 1992, **7**, 161-163.
- 46 **VADGAMA P**, Designing biosensors, *Chemistry in Britain*, March 1992, 249-252.
- 47 **AHLUWALIA A et al**, A comparative study of protein immobilization techniques for optical immunosensors, *Biosensors & Bioelectronics*, 1991, **7**, 207-214.
- 48 **DUBROVSKY T B et al**, Fluorescent and phosphorescent study of Langmuir-Blodgett antibody films for application to immunosensors, *Biosensors & Bioelectronics*, 1993, **8**, 377-385.
- 49 **OWAKU K, GOTO M**, Optical immunosensing for IgG, *Sensors and Actuators B*, 1993, **13-14**, 723-724.
- 50 **MANNING B, MALEY T**, Immunosensors in medical diagnostics - major hurdles to commercial success, *Biosensors & Bioelectronics*, 1992, **7**, 391-395.
- 51 **YEN S S C, JAFFE R B**, Reproductive endocrinology, *W B Saunders & Co. Ltd.*, 1978, 1st ed., 525-527.
- 52 **ROBINSON G A et al**, The calibration of an optical immunosensor - the FCFD, *Biosensors & Bioelectronics*, 1993, **8**, 371-376.
- 53 **DAY E D**, Advanced immunochemistry, *Wiley-Liss Inc., New York*, 1990, 2nd ed., 259-350.
- 54 **ALARIE J P, SEPANIAK M J, VO-DINH T**, Evaluation of antibody immobilization techniques for fiber optic-based fluoroimmunosensing, *Analytica Chimica Acta*, 1990, **229**, 169-176.
- 55 **MORRISON L E**, Time-resolved detection of energy transfer: theory and application to

- immunoassays, *Analytical Biochemistry*, 1988, **174**, 101-120.
- 56 **LAKOWICZ J R et al**, Fluorescence lifetime energy-transfer immunoassay quantified by phase-modulation fluorometry, *Sensors and Actuators B*, 1993, **12**, 65-70.
- 57 **TSURUOKA M, TAMIYA E, KARUBE I**, Fluorescence polarization immunoassay employing immobilized antibody, *Biosensors & Bioelectronics*, 1991, **6**, 501-505.
- 58 **PAPANASTASIOU-DIAMANDI A, SHANKARAN P, KHOSRAVI M J**, Immunoassay of triiodothyronine in serum by time-resolved fluorometric measurement of europium chelate complexes in solution, *Clinical Biochemistry*, 1992, **25**, 255-261.
- 59 **ROTTMAN C et al**, Doped sol-gel glasses as pH sensors, *Materials Letters*, 1992, **13**, 293-298.
- 60 **ELLERBY L M et al**, Encapsulation of proteins in transparent porous silicate glasses prepared by the sol-gel method, *Science*, Feb. 1992, **255**, 1113-1115.
- 61 **YAMANAKA S A et al**, Enzymatic activity of glucose oxidase encapsulated in transparent glass by the sol-gel method, *Chemistry of materials*, 1992, **4**(3), 495-497.
- 62 **BOCHNER F et al**, Handbook of clinical pharmacology, *Little, Brown & Co., Boston*, 1983, 2nd ed..
- 63 Various immunoassay methods, *Biogenesis*.
- 64 **GUTIERREZ M C GOMEZ-HENS A, PEREZ-BENDITO D**, Immunoassay methods based on fluorescence polarization, *Talanta*, 1989, **36**(12), 1187-1201.
- 65 Serozyme, ELISA immunoassays, *Serono Diagnostics Ltd.*
- 66 Various immunoassay methods, *Genzyme Corporation*.
- 67 **YEN S S C, JAFFE R B**, Reproductive endocrinology, *W B Saunders & Co. Ltd.*, 1978, 1st ed., 525-527.
- 68 **NELLEN Ph M, LUKOSZ W**, Integrated optical input grating couplers as chemo- and immunosensors, *Sensors and Actuators*, 1990, **B1**, 285-295.
- 69 **KARLSSON R, MICHAELSSON A, MATTSO L**, Kinetic analysis of monoclonal antibody-antigen interactions with a new biosensor based system, *Journal of Immunological Methods*, 1991, **145**, 229-240.
- 70 **TAYLOR R F, MARENCHIC I G, SPENCER R H**, Antibody- and receptor-based biosensors for detection and process control, *Analytica Chimica Acta*, 1991, **249**, 67-70.
- 71 **van HELL H et al**, Particle immunoassays, in **COLLINS W P ed.**, Alternative immunoassays, *J Wiley & Sons Ltd., Chichester*, 1985, 1st ed., 55.
- 72 **EDWARDS R**, Radiolabelled immunoassay, in **PRICE C P, NEWMAN D J**, Principles and practice of immunoassay, *Stockton Press, New York*, 1991, 1st ed., 265-294.

## APPENDIX 1

### ELECTROMAGNETIC WAVE THEORY OF PLANE WAVES

*This appendix provides a brief introduction to Maxwell's equations and to plane electromagnetic waves as a background to the theory presented in chapter 4.*

#### A1.1 ABBREVIATIONS

<b>E</b>	electric field vector.
<b>H</b>	magnetic field vector.
<b>D</b>	electric displacement.
<b>B</b>	magnetic induction.
<b>J</b>	electric current density.
$\rho$	electric charge density.
$\mu$	magnetic permeability.
$\epsilon$	electric permittivity.
<b>r</b>	position vector of a point in space.
<b>t</b>	time.
$\omega$	circular frequency.
$\hat{x}$	unit vector in x-direction.
$\nabla$	$= \left( \frac{\partial}{\partial x} + \frac{\partial}{\partial y} + \frac{\partial}{\partial z} \right)$ a vector operator.

**A1.2 BASIC ELECTROMAGNETIC THEORY****A1.2.1 Maxwell's equations**

Maxwell's equations describe the behaviour of electromagnetic fields in a medium and are defined as follows:

$$\nabla \times \mathbf{E}(\mathbf{r}, t) = -\frac{\partial}{\partial t} \mathbf{B}(\mathbf{r}, t) \quad (\text{A1.1})$$

$$\nabla \times \mathbf{H}(\mathbf{r}, t) = -\frac{\partial}{\partial t} \mathbf{D}(\mathbf{r}, t) + \mathbf{J}(\mathbf{r}, t) \quad (\text{A1.2})$$

$$\nabla \cdot \mathbf{D}(\mathbf{r}, t) = \rho(\mathbf{r}, t) \quad (\text{A1.3})$$

$$\nabla \cdot \mathbf{B}(\mathbf{r}, t) = 0 \quad (\text{A1.4})$$

The current and charge sources ( $\mathbf{J}$  and  $\rho$ ) are related by:

$$\nabla \cdot \mathbf{J}(\mathbf{r}, t) + \frac{\partial}{\partial t} \rho(\mathbf{r}, t) = 0 \quad (\text{A1.5})$$

There are two further equations - the constitutive or material equations:

$$\mathbf{B} = \mu \mathbf{H} \quad (\text{A1.6})$$

$$\mathbf{D} = \epsilon \mathbf{E} \quad (\text{A1.7})$$

**A1.2.2 Time harmonic electromagnetic fields**

A time harmonic electromagnetic field takes the following form (where  $x$  denotes that this is the field component in the  $x$ -direction):

$$A_x(\mathbf{r}, t) = A_x(\mathbf{r}) \cos[\omega t + \phi_x(\mathbf{r})] \quad (\text{A1.8})$$

$$\Rightarrow A_x(\mathbf{r}, t) = \text{Re} \left[ A_x(\mathbf{r}) e^{j\phi_x(\mathbf{r})} e^{j\omega t} \right] \quad (\text{A1.9})$$

$$\Rightarrow A_x(\mathbf{r}, t) = \text{Re} \left[ \underline{A}_x(\mathbf{r}) e^{j\omega t} \right] \quad (\text{A1.10})$$

where 'Re' signifies the real part and:

$$\underline{A}_x(\mathbf{r}) = A_x(\mathbf{r}) e^{j\phi_x(\mathbf{r})} \quad (\text{A1.11})$$

The field vectors are now described generally by:

$$\mathbf{A}(\mathbf{r}, t) = \text{Re} \left[ \underline{\mathbf{A}}(\mathbf{r}) e^{j\omega t} \right] \quad (\text{A1.12})$$

Expressing the field in the complex notation greatly simplifies Maxwell's equations, giving:

$$\nabla \times \mathbf{E}(\mathbf{r}) = -j\omega \mathbf{B}(\mathbf{r}) \quad (\text{A1.13})$$

$$\nabla \times \mathbf{H}(\mathbf{r}) = j\omega \mathbf{D}(\mathbf{r}) + \mathbf{J}(\mathbf{r}) \quad (\text{A1.14})$$

$$\nabla \cdot \mathbf{D}(\mathbf{r}) = \rho(\mathbf{r}) \quad (\text{A1.15})$$

$$\nabla \cdot \mathbf{B}(\mathbf{r}) = 0 \quad (\text{A1.16})$$

Note that  $\mathbf{E}$ ,  $\mathbf{H}$ ,  $\mathbf{B}$ ,  $\mathbf{D}$ ,  $\mathbf{J}$  and  $\rho$  are now complex quantities.

### A1.2.3 The electromagnetic wave equation

Assuming a source free region (ie  $\mathbf{J}(\mathbf{r}) = \mathbf{0}$ ) and an isotropic medium, substituting the material equations (A1.6), (A1.7) into equations (A1.13) and (A1.14) gives:

$$\nabla \times \mathbf{E}(\mathbf{r}) = -j\omega\mu\mathbf{H}(\mathbf{r}) \quad (\text{A1.17})$$

$$\nabla \times \mathbf{H}(\mathbf{r}) = j\omega\epsilon\mathbf{E}(\mathbf{r}) \quad (\text{A1.18})$$

Eliminating  $\mathbf{H}(\mathbf{r})$  from the above equations yields the wave equation:

$$\nabla^2 \mathbf{E}(\mathbf{r}) + \omega^2 \mu \epsilon \mathbf{E}(\mathbf{r}) = \mathbf{0} \quad (\text{A1.19})$$

Thus, the x-component of the electric field is given by:

$$\left( \frac{\partial^2}{\partial x^2} + \frac{\partial^2}{\partial y^2} + \frac{\partial^2}{\partial z^2} \right) E_x(\mathbf{r}) + \omega^2 \mu \epsilon E_x(\mathbf{r}) = 0 \quad (\text{A1.20})$$

Substitution of a trial solution of the form

$$E_x(\mathbf{r}) = E_{x0} e^{-j(k_x x + k_y y + k_z z)} \quad (\text{A1.21})$$

where  $E_{x0}$  is an arbitrary complex constant, into equation (A1.19) yields the dispersion relation:

$$k_x^2 + k_y^2 + k_z^2 = \omega^2 \mu \epsilon = k^2 \quad (\text{A1.22})$$

where  $k$  is called the wave number. The dispersion relation applies also to the y- and z-components of the electric field. The wave vector  $\mathbf{k}$  can now be defined as:

$$\mathbf{k} = k_x \hat{\mathbf{x}} + k_y \hat{\mathbf{y}} + k_z \hat{\mathbf{z}} \quad (\text{A1.23})$$

which points in the direction of propagation of the electromagnetic wave. The electric field can now be conveniently expressed as:

$$\mathbf{E}(\mathbf{r}) = \mathbf{E}_0 e^{-j\mathbf{k} \cdot \mathbf{r}} \quad (\text{A1.24})$$

The time variant factor  $e^{j\omega t}$  has been dropped for clarity.

#### **A1.2.4 Plane wave solutions**

A plane wave has a planar wavefront that is perpendicular to the direction of propagation of the wave. The phase and amplitude of the field vectors can be assumed to be constant across the wavefront. Thus, Maxwell's equations can be simplified further by eliminating the spatial dependence term. Hence, for the field described by equation (A1.24):

$$\nabla \times \mathbf{E}(\mathbf{r}) = -j\mathbf{k} \times \mathbf{E}(\mathbf{r}) \quad (\text{A1.25})$$

$$\nabla \cdot \mathbf{E}(\mathbf{r}) = (-j\mathbf{k} \cdot \mathbf{E}) e^{-j\mathbf{k} \cdot \mathbf{r}} \quad (\text{A1.26})$$

Maxwell's equations now simplify to:

$$\mathbf{k} \times \mathbf{E} = \omega \mathbf{B} \quad (\text{A1.27})$$

$$\mathbf{k} \times \mathbf{H} = -\omega \mathbf{D} \quad (\text{A1.28})$$

$$\mathbf{k} \cdot \mathbf{D} = 0 \quad (\text{A1.29})$$

$$\mathbf{k} \cdot \mathbf{B} = 0 \quad (\text{A1.30})$$

Equations (A1.28) and (A1.29) simplify further for an isotropic material for which the material equations (A1.6) and (A1.7) hold:

$$\mathbf{k} \times \mathbf{E} = \omega \mu \mathbf{H} \quad (\text{A1.31})$$

$$\mathbf{k} \times \mathbf{H} = -\omega \epsilon \mathbf{E} \quad (\text{A1.32})$$

It can be seen from the above equations that  $\mathbf{E}$ ,  $\mathbf{H}$  and  $\mathbf{k}$  are mutually

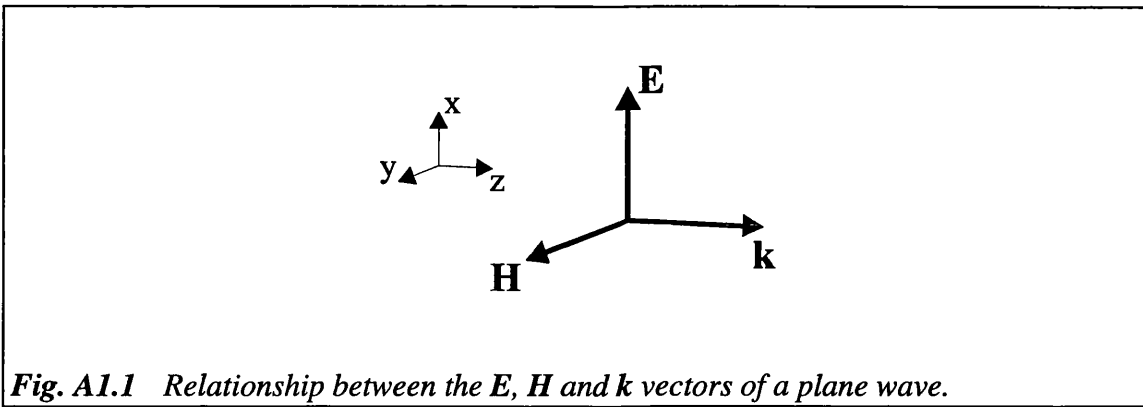


**Fig. A1.1** Relationship between the  $\mathbf{E}$ ,  $\mathbf{H}$  and  $\mathbf{k}$  vectors of a plane wave.

perpendicular (see fig. A1.1). It can also be seen that:

$$|\mathbf{H}| = \frac{1}{\omega\mu} |\mathbf{k}||\mathbf{E}| \quad (\text{A1.33})$$

$$\frac{|\mathbf{E}|}{|\mathbf{H}|} = \eta = \sqrt{\frac{\mu}{\epsilon}} \quad (\text{A1.34})$$

where  $\eta$  is defined as the characteristic impedance of the medium.

### A1.2.5 Power flow in an electromagnetic wave

Poynting's theorem, which deals with power flow in an electromagnetic wave, will simply be stated in this section. A full derivation may be obtained from a number of texts on electromagnetic wave theory.

The Poynting vector is defined as:

$$\mathbf{S} = \mathbf{E} \times \mathbf{H} \quad (\text{A1.35})$$

or in complex form:

$$\mathbf{S} = \mathbf{E} \times \mathbf{H}^* \quad (\text{A1.36})$$

(where \* denotes the complex conjugate) and has the units of power per unit area, pointing in the direction of power flow. The time averaged power flowing out of an enclosed volume is given by integrating the Poynting vector over the surface area of the enclosed volume:

$$P_{\text{out}} = \oiint_A (\mathbf{E} \times \mathbf{H}) \cdot \hat{\mathbf{n}} dA \quad (\text{A1.37})$$

where  $\hat{\mathbf{n}}$  is a unit vector normal to the surface.

### A1.3 REFLECTION AND TRANSMISSION AT AN INTERFACE

#### A1.3.1 Boundary conditions at a dielectric interface

The boundary conditions are obtained directly from Maxwell's equations for a source free region of space and will only be stated here. The boundary conditions state that for a source-free boundary, the tangential components of the electric and magnetic fields must be continuous across the boundary. This holds at all points along the interface.

#### A1.3.2 Reflection and transmission

Consider a plane wave incident on an interface between medium 1 ( $\epsilon_1, \mu_1$ ) and medium 2 ( $\epsilon_2, \mu_2$ ) as shown in fig. A1.2. The incident, reflected and transmitted waves have electric fields of the following form:

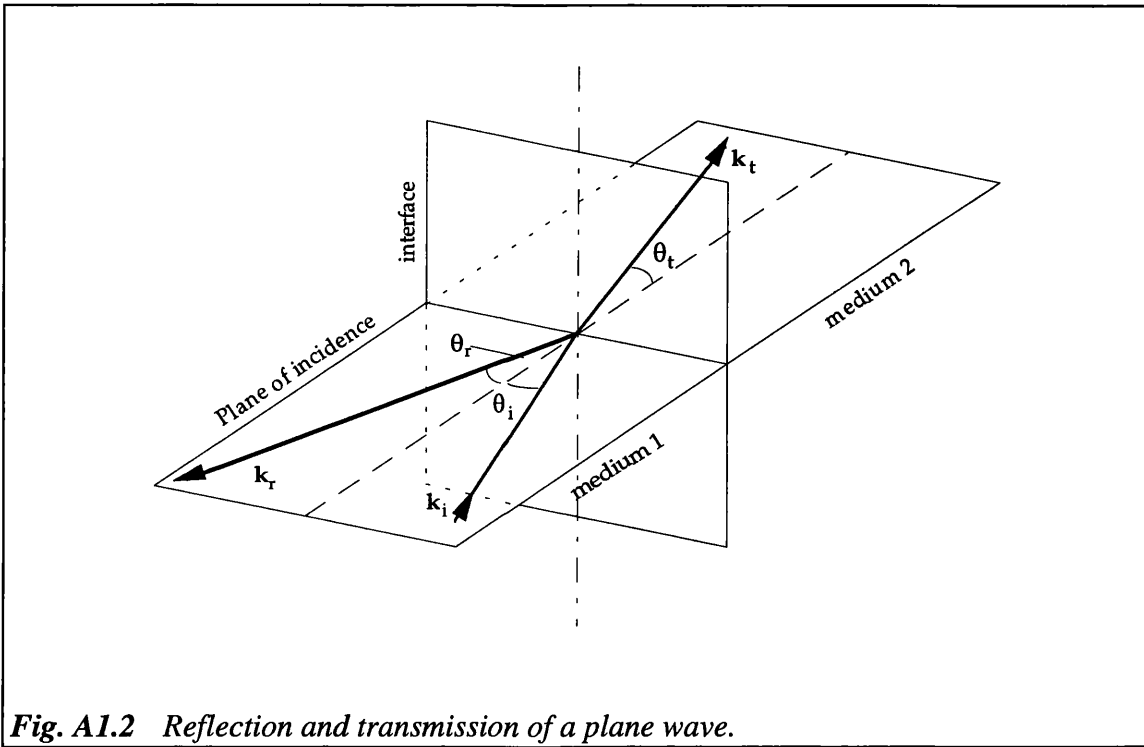


Fig. A1.2 Reflection and transmission of a plane wave.

$$\mathbf{E}_i(\mathbf{r}) = \mathbf{A}_i e^{-j(\mathbf{k}_i \cdot \mathbf{r})} \tag{A1.38}$$

$$\mathbf{E}_r(\mathbf{r}) = \mathbf{A}_r e^{-j(\mathbf{k}_r \cdot \mathbf{r})} \tag{A1.39}$$

$$\mathbf{E}_t(\mathbf{r}) = \mathbf{A}_t e^{-j(\mathbf{k}_t \cdot \mathbf{r})} \tag{A1.40}$$

where  $\mathbf{A}_i$ ,  $\mathbf{A}_r$ ,  $\mathbf{A}_t$  are, respectively, the incident, reflected and transmitted field amplitudes. Assuming  $\hat{\mathbf{z}}$  is perpendicular to the interface, the boundary conditions require that:

$$\left[ \mathbf{A}_i e^{-jk_{ix}x} e^{-jk_{iy}y} + \mathbf{A}_r e^{-jk_{rx}x} e^{-jk_{ry}y} \right]_{\tan} = \left[ \mathbf{A}_t e^{-jk_{tx}x} e^{-jk_{ty}y} \right]_{\tan} \tag{A1.41}$$

which is satisfied if:

$$\begin{aligned} k_{ix} &= k_{rx} = k_{tx} = k_x \\ k_{iy} &= k_{ry} = k_{ty} = k_y \end{aligned} \tag{A1.42}$$

This implies that the incident, reflected and transmitted waves lie in the same plane - the plane of incidence (see fig. A1.2). It is now possible to write  $k_{ix}$ , etc in terms of the angles  $\theta_i$ ,  $\theta_r$  and  $\theta_t$ :

$$\begin{aligned} k_{ix} &= k_1 \sin \theta_i & k_{iz} &= k_1 \cos \theta_i \\ k_{rx} &= k_1 \sin \theta_r & k_{rz} &= k_1 \cos \theta_r \\ k_{tx} &= k_2 \sin \theta_t & k_{tz} &= k_2 \cos \theta_t \end{aligned} \quad (\text{A1.43})$$

$$k_1 = \omega \sqrt{\mu_1 \epsilon_1} \quad k_2 = \omega \sqrt{\mu_2 \epsilon_2} \quad (\text{A1.44})$$

It must be noted that the z-component of the  $\mathbf{k}_r$  vector is negative. The above equations yield the relations:

$$\sin \theta_i = \sin \theta_r \quad (\text{A1.45})$$

and

$$k_1 \sin \theta_i = k_2 \sin \theta_t \quad (\text{A1.46})$$

$$\Rightarrow \frac{\sin \theta_i}{\sin \theta_t} = \sqrt{\frac{\mu_2 \epsilon_2}{\mu_1 \epsilon_1}} \quad (\text{A1.47})$$

Equation (A1.47) is a more general form of Snell's law.

### A1.3.3 The reflection and transmission coefficients

The reflection and transmission coefficients (or Fresnel coefficients) provide information on the amplitude and phase of the reflected and transmitted waves relative to the incident wave amplitude and phase. However, before continuing with the

derivation of the reflection and transmission coefficients, it is convenient to decompose the waves into TE (transverse electric) and TM (transverse magnetic) waves. A TE wave has its electric field, and a TM wave has its magnetic field, polarised perpendicular to the plane of incidence (fig. A1.3). Any arbitrarily polarised plane wave is a linear combination of a TE and a TM wave.

Considering a TE wave in detail (see fig.3) with the electric field polarised in the  $\hat{y}$ -direction, the incident, reflected and transmitted fields can be written as:

$$\mathbf{E}_i = \hat{y}A_i e^{-jk_{iz}z} e^{-jk_{ix}x} \tag{A1.48}$$

$$\mathbf{E}_r = \hat{y}rA_i e^{+jk_{rz}z} e^{-jk_{rx}x} \tag{A1.49}$$

$$\mathbf{E}_t = \hat{y}tA_i e^{-jk_{tz}z} e^{-jk_{tx}x} \tag{A1.50}$$

and

$$k_{ix} = k_{rx} = k_{tx} = k_x \tag{A1.51}$$

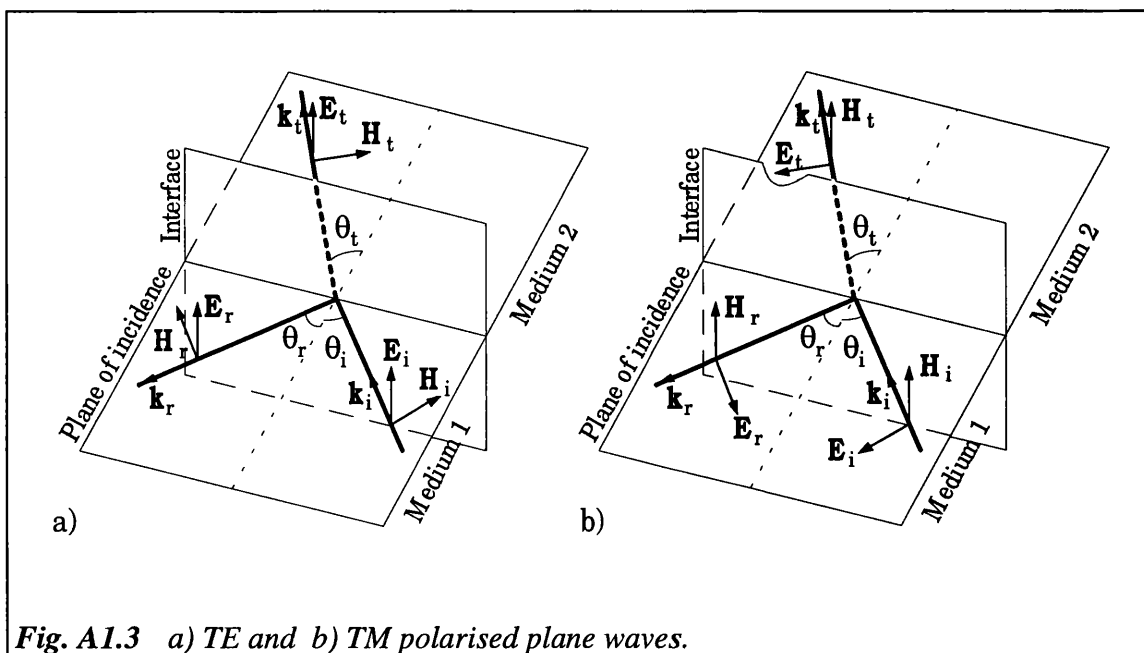


**Fig. A1.3** a) TE and b) TM polarised plane waves.

where  $r$  and  $t$  are complex constants.

The magnetic field  $\mathbf{H}$  is obtained by using the relation (A1.31) derived earlier for plane waves:

$$\mathbf{k} \times \mathbf{E} = \omega\mu\mathbf{H}$$

Thus,  $\mathbf{H}_i$  is given by:

$$\mathbf{H}_i = \frac{1}{\omega\mu_1} (\hat{\mathbf{x}}k_x + \hat{\mathbf{z}}k_{iz}) \times \hat{\mathbf{y}}A_i e^{-jk_{iz}z} e^{-jk_x x} \quad (\text{A1.52})$$

$$\Rightarrow \mathbf{H}_i = \frac{A_i}{\omega\mu_1} (-\hat{\mathbf{x}}k_{iz} + \hat{\mathbf{z}}k_x) e^{-jk_{iz}z} e^{-jk_x x} \quad (\text{A1.53})$$

Similarly,  $\mathbf{H}_r$  and  $\mathbf{H}_t$  are given by:

$$\mathbf{H}_r = \frac{rA_i}{\omega\mu_1} (\hat{\mathbf{x}}k_{iz} + \hat{\mathbf{z}}k_x) e^{+jk_{iz}z} e^{-jk_x x} \quad (\text{A1.54})$$

$$\mathbf{H}_t = \frac{tA_i}{\omega\mu_2} (-\hat{\mathbf{x}}k_{iz} + \hat{\mathbf{z}}k_x) e^{-jk_{iz}z} e^{-jk_x x} \quad (\text{A1.55})$$

Satisfying the boundary conditions for the tangential components of  $\mathbf{E}$  and  $\mathbf{H}$  at  $z = 0$  yields:

$$1 + r = t \quad (\text{A1.56})$$

$$1 - r = \frac{k_{iz}}{k_{iz}} \frac{\mu_1}{\mu_2} t \quad (\text{A1.57})$$

Hence, using  $k_{iz} = k_{iz}$  and solving for  $r$  and  $t$ , the reflection and transmission

coefficients for a TE wave incident on a dielectric interface are:

$$\left( \frac{E_r}{E_i} \right)_{\text{TE}} \equiv r_{\text{TE}} = \frac{\mu_2 k_{iz} - \mu_1 k_{tz}}{\mu_2 k_{iz} + \mu_1 k_{tz}} \quad (\text{A1.58})$$

$$\left( \frac{E_t}{E_i} \right)_{\text{TE}} \equiv t_{\text{TE}} = \frac{2\mu_2 k_{iz}}{\mu_2 k_{iz} + \mu_1 k_{tz}} \quad (\text{A1.59})$$

where,  $E_i$ ,  $E_r$  and  $E_t$  are the complex amplitudes of the incident, reflected and transmitted wave electric field strengths respectively.

The coefficients for a TM wave are obtained in a similar manner:

$$\left( \frac{H_r}{H_i} \right)_{\text{TM}} \equiv r_{\text{TM}} = \frac{\epsilon_2 k_{iz} - \epsilon_1 k_{tz}}{\epsilon_2 k_{iz} + \epsilon_1 k_{tz}} \quad (\text{A1.60})$$

$$\left( \frac{H_t}{H_i} \right)_{\text{TM}} \equiv t_{\text{TM}} = \frac{2\epsilon_2 k_{iz}}{\epsilon_2 k_{iz} + \epsilon_1 k_{tz}} \quad (\text{A1.61})$$

where,  $H_i$ ,  $H_r$  and  $H_t$  are the complex amplitudes of the incident, reflected and transmitted wave magnetic field strengths respectively.

Using equation (A1.34), the ratios of the the reflected and transmitted electric field strengths to the incident electric field strength are obtained for a TM wave:

$$\left( \frac{E_r}{E_i} \right)_{\text{TM}} = r_{\text{TM}} \quad \left( \frac{E_t}{E_i} \right)_{\text{TM}} = \frac{\eta_2}{\eta_1} t_{\text{TM}} \quad (\text{A1.62})$$

### A1.3.4 Total internal reflection

It is clear from equations (A1.32) and (A1.33) that when a plane wave in medium 1 is incident on an interface with an optically less dense medium 2, (fig. 3) there exists a range of incident angles such that:

$$\sin \theta_t = \frac{k_1}{k_2} \sin \theta_i > 1 \quad (\text{A1.63})$$

Hence, the transmitted  $\mathbf{k}$  vector splits into an imaginary  $z$ -component and a real  $x$ -component given respectively by:

$$k_{tz} = k_2 \cos \theta_t = \pm j\alpha_{tz} \quad (\text{A1.64})$$

$$k_{tx} = k_2 \sin \theta_t = \beta_{tx} \quad (\text{A1.65})$$

where

$$\frac{\alpha_{tz}}{k_{iz}} = \frac{\sqrt{\sin^2 \theta_i - \left(\frac{\epsilon_2}{\epsilon_1}\right)}}{\cos \theta_i} \quad (\text{A1.66})$$

and it can be seen that  $|r_{TE}| = |r_{TM}| = 1$ . Hence, all the incident power is reflected when the incident angle exceeds the critical angle defined by equation (A1.39). However, the field in medium 2 does not disappear. Substituting equations (A1.64) and (A1.65) into equation (A1.50) for a TE wave, the transmitted electric field is obtained:

$$\mathbf{E}_t = \hat{\mathbf{y}}tA_i e^{-jk_{ix}x} e^{-\alpha_{tz}z} \quad (\text{A1.67})$$

The sign for  $\alpha_{tz}$  has been chosen such that  $E_t$  remains finite with increasing  $z$ . It can be seen, that in medium 2, the field amplitude decreases exponentially away from the

interface (see chapter 4, fig. 4.2), and the penetration depth  $d_{\text{pen}}$  (the distance at which the field strength falls to  $1/e$  of its value at the boundary) is:

$$d_{\text{pen}} = \frac{1}{\alpha_{\text{tz}}} \quad (\text{A1.68})$$

The wave in medium 2 is described as an evanescent wave and it is also non-uniform - ie. the planes of constant phase and constant amplitude are not co-incident. In this case, the planes of constant phase are perpendicular to the interface and the planes of constant amplitude are parallel to the interface.

### **A1.3.5 Power flow across the interface**

It is useful to know the power that is transferred from medium 1 into medium 2 and, to calculate this, it is required to calculate the power flow perpendicular to the interface.

The Poynting vectors for the incident, reflected and transmitted TE waves are:

$$\mathbf{S}_i = \frac{|A_i|^2}{\omega\mu_1} (\hat{\mathbf{z}}k_{iz} + \hat{\mathbf{x}}k_{ix}) \quad (\text{A1.69})$$

$$\mathbf{S}_r = \frac{|r_{\text{TE}}A_i|^2}{\omega\mu_1} (-\hat{\mathbf{z}}k_{iz} + \hat{\mathbf{x}}k_{ix}) \quad (\text{A1.70})$$

$$\mathbf{S}_t = \frac{|t_{\text{TE}}A_i|}{\omega\mu_2} (\hat{\mathbf{z}}k_{iz} + \hat{\mathbf{x}}k_{ix}) e^{-j(k_z - k'_z)x} \quad (\text{A1.71})$$

and the ratios of the reflected and transmitted power flowing normal to the interface relative to the incident power flow are given, respectively, by:

$$\mathfrak{R}_{\text{TE}} = \frac{-\hat{\mathbf{z}} \cdot \mathbf{S}_r}{\hat{\mathbf{z}} \cdot \mathbf{S}_i} = |r_{\text{TE}}|^2 \quad (\text{A1.72})$$

$$\mathfrak{S}_{\text{TE}} = \frac{-\hat{\mathbf{z}} \cdot \mathbf{S}_t}{\hat{\mathbf{z}} \cdot \mathbf{S}_i} = \frac{\mu_1 k_{tz}^*}{\mu_2 k_{iz}} |t_{\text{TE}}|^2 \quad (\text{A1.73})$$

Similarly, for a TM wave:

$$\mathfrak{R}_{\text{TM}} = |r_{\text{TM}}|^2 \quad (\text{A1.74})$$

$$\mathfrak{S}_{\text{TM}} = \frac{\epsilon_1 k_{tz}^*}{\epsilon_2 k_{iz}} |t_{\text{TM}}|^2 \quad (\text{A1.75})$$

$\mathfrak{R}$  and  $\mathfrak{S}$  are known as the reflectivity and the transmittivity respectively. The law of conservation of energy means:  $\mathfrak{R} + \mathfrak{S} = 1$ .